Fibre Microstructure and Mechanics of Atherosclerotic Plaques

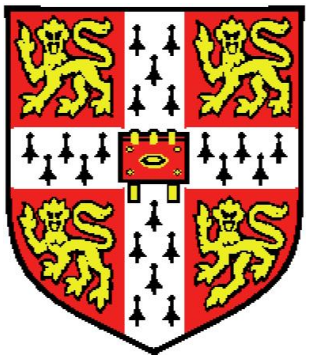

Graeham Rees Douglas

Hughes Hall

Department of Engineering

University of Cambridge

This dissertation is submitted for the degree of

Doctor of Philosophy

February 2017

To health from knowledge.

Declaration

This dissertation is the result of my own work and includes nothing which is the outcome of work done in collaboration except as declared in the Acknowledgements and specified in the text.

It is not substantially the same as any that I have submitted, or, is being concurrently submitted for a degree or diploma or other qualification at the University of Cambridge or any other University or similar institution except as declared in the Preface and specified in the text. I further state that no substantial part of my dissertation has already been submitted, or, is being concurrently submitted for any such degree, diploma or other qualification at the University of Cambridge or any other University or similar institution except as declared in the Preface and specified in the text

It does not exceed 65,000 words including appendices, bibliography, footnotes, tables and equations and has fewer than 150 figures.

Graeham Rees Douglas
1 February 2017

Acknowledgements

I would like to thank my supervisors, Dr. Michael Sutcliffe and Dr. Zhongzhao Teng, for their guidance. Additional advice has been welcome from Dr. Timothy Fletcher, Dr. Yuan Huang, Dr. Chen Yen Ooi, Aziz Tokgoz, Dr. Joe Bird, Dr. Vikram Deshpande, and others.

Technical assistance and fabrication of experimental equipment was provided by Gary Bailey and Simon Marshall (Engineering Department). Access and training on a scanning electron microscope (SEM) and multiphoton microscope were provided by Dr. Jeremy Skepper and Dr. Kevin O'Holleran (Cambridge Advanced Imaging Centre). Dr. Skepper also prepared the SEM samples. Nicola Figg (Cardiovascular Medicine) prepared samples used in histology imaging.

Laboratory facilities and access in Addenbrookes Hospital were arranged by Prof. Martin Bennett (Cardiovascular Medicine) and Prof. Jonathan Gillard (Radiology Department). Tissue samples are provided by the surgical staff of Surgical Theatre 6 in the Addenbrookes Hospital. Tissue collection was arranged by Dr. Umar Sadat (Radiology Department) and Dr. Martin Bennett.

Personal funding was provided by the National Science and Engineering Research Council (NSERC) of Canada through the PGS-D programme, and the WD Armstrong Trust Graduate Studentship in the Application of Engineering in Medicine. Funding for materials is acknowledged from a CUED Engineering for Clinical Practice Grant and the British Heart Foundation.

I would like to thank the communities I have been a part of during my PhD studies including Hughes Hall, Cambridge University Swim and Water Polo Club, and Cambridge University Eco-Racing for their support, encouragement, and things I have learned from them.

I am grateful for my family's support, encouragement, and inspiration.

Abstract

Atherosclerosis is characterised by the progressive growth of a plaque, where a fibrous cap covers a lipid-rich core. Rupture of this fibrous cap can lead to thrombosis and a heart attack or stroke. This dissertation considered the role of plaque microstructure in the mechanics and rupture risk of atherosclerotic plaques. Fibre structures in human atherosclerotic plaques were characterised through scanning electron microscopy, histology, and image processing. Local primary fibre orientation and the fibre dispersion were calculated. Plaque shoulder regions, where rupture is most frequent, had higher fibre dispersion and were more misaligned with the lumen wall.

Comparative FE models were made from the plaque geometries and fibre structures found by image processing: one with evenly dispersed fibres (isotropic) and one with a preferred fibre orientation (anisotropic). The isotropic and anisotropic FE models predicted significantly different stresses. Stresses were often highest in the shoulder regions. Anisotropic stresses were calculated relative to fibres: axial stresses were highest, shear stresses were intermediate, and transverse stresses were low. Since the tissue is strongest in the fibre direction (axially), axial and shear failure modes should be considered.

Material tests (uniaxial tension, trouser tear, and notched specimen) were used to characterise material properties in healthy porcine arteries. Fibre structures were evaluated by histology, multiphoton microscopy, and image processing. Samples were stiffer circumferentially and toughest against radial tears. Fractures progressed between fibres, rather than by breaking them. Material properties and fracture mechanisms were explained by fibre structures. In summary, atherosclerosis altered the fibre structure of the arteries, in ways that were mechanically significant and that explained clinical observations.

Summary of Key Findings

Factor	Effect and Justification	Source
Triangle of Fibres at Shoulder	Potential for high stresses deeper into tissue Possible delamination plane (shearing) Seam closer to lumen may be higher risk	Figures 2.1, 3.8, 4.2, 4.5
Plaque Type on Stresses	Coronary smaller than carotid Some significantly different stresses Shoulders more at risk in coronary Shoulders and fibrous cap similar risk in carotid	Tables 3.1, 4.4, 4.5
Plaque Geometry on Stresses	Geometry more important for coronary Coronary: sharp shoulder curvature ($R^2 \approx 0.4$) Carotid: fibrous cap thickness ($R^2 \approx 0.15$)	Tables 4.8, 4.9
Fibre Structure on Stresses	Coronary: fibre structure a limited factor Carotid: fibre misalignment ($R^2 \approx 0.2$-0.3) Interactions and coupling with geometry	Table 4.10
Isotropic FE Models	Explain about half ($R^2 \approx 0.3$-0.7) of variability in stresses from anisotropic FE models	Table 4.11
Shear Failure	Probable failure mode: shear between fibres Shear stresses higher than transverse Fissures between fibres observed in SEM images Tearing $\approx 3\times$ tougher across then between fibres	Figures 2.2, 4.10, 4.11, 5.9
Anisotropy on Tearing	Toughness probably decreases with anisotropy Anisotropy: stiffness and fibre structure	Figures 5.15, 5.16
Stretch on Fibre Structure	Fibres rearrange to direction of applied loads Primary fibre orientation and dispersion change May explain strain-stiffening of material	Figures 6.5, 6.6, 6.8, 6.9
Fibre Toughening Mechanisms	Fibres recruited near and bridge over crack tips Fibre cross-links fail, not fibres themselves Mechanisms dependent on initial fibre structure	Figures 6.12-6.16

Contents

List of Figures

List of Tables

Nomenclature

List of Abbreviations

AC	Axial-circumferential tissue plane
AR	Axial-radial tissue plane
CA	Circumferential-axial tissue plane
CR	Circumferential-radial tissue plane
EVG	Verhoeff's Van Gieson histology stain
FC	Fibrous cap, a plaque region
FE	Finite element
GEX	Global excluding lipid plaque region, all fibrous tissues
H&E	Hematoxylineosin histology stain
IEL	Internal elastic lamella, a tissue layer between the intima and media
IT	Intimal thickening, a plaque region
IVUS	Intravascular ultrasound, clinical imaging technique
MIP	Maximum intensity projection, for rendering a 3D volume in 2D images.
MRI	Magnetic resonance imaging, clinical imaging technique
OCT	Optical coherence tomography, clinical imaging technique

SEM	Scanning electron microscopy
SH	Shoulder, a plaque region
SHG	Second harmonic generation signal from collagen
TPF	Two photon fluorescence signal from collagen and elastin

Experiments Symbols

α	The material anisotropy ratio between tangent modulus in the axial and circumferential directions
$\bar{F}$	Average tearing force in trouser tear tests
B	Trouser tear strip thickness (or length of crack front)
E_a	Tangent modulus for axial strips
E_c	Tangent modulus for circumferential strips
J_C	Tearing toughness, material property
l_0	Unstretched length of a uniaxial tensile test strip
$P(\theta)_2$	Orientation density distribution for a two-family fibre system
$P_m(\theta)_2$	von Mises model for a two-family orientation density distribution
t_0	Unstretched thickness of a uniaxial tensile test strip
w_0	Unstretched width of a uniaxial tensile test strip
x	Displacement applied to one end of a uniaxial tensile test strip
κ_2	Fibre dispersion for each family in a two-family fibre system
σ_c	Approximate circumferential stress from physiological blood pressure
θ_1	First primary orientation of a two-family fibre system
θ_2	Second primary orientation of a two-family fibre system

θ_o	Angle between the sample direction and the mid-point between θ_1 and θ_2 in a two-family fibre system
θ_s	Angle between θ_o and θ_1 or θ_2 in two-family fibre system
λ_1	Stretch in a uniaxial tensile test strip, in the direction being stretched
σ_1	Cauchy stress in a uniaxial tensile test strip
F	Tensile force in a uniaxial tensile test strip

Finite Element Modelling Symbols

C_{10}	Material parameter for the matrix stiffness in fibrous tissue
J	Material compressibility; det($\mathbf{F}$)
k_1	Material parameter for the linear component of fibre stiffness
k_2	Material parameter for the exponential component of fibre stiffness
K_{10}	Material parameter for the linear component of lipid stiffness
K_{20}	Material parameter for the quadratic component of lipid stiffness
λ_a	Stretch ratio in the axial direction
λ_c	Stretch ratio in the circumferential direction
λ_r	Stretch ratio in the radial direction
$\mathbf{C}$	Right Cauchy-Green deformation tensor
$\mathbf{F}$	Deformation gradient in the material
$\overline{\mathbf{C}}$	Distortion component of the right Cauchy-Green deformation tensor
$\overline{I}_1$	First invariant of $\overline{\mathbf{C}}$
$\overline{I}_4$	Invariant describing fibre orientation
$\overline{\psi}_f$	Strain energy density function for fibrous tissue

$\overline{\psi}_l$	Strain energy density function for lipid tissue
$\sigma_{1,a}$	Maximum principal stress, in the anisotropic FE models
$\sigma_{1,i}$	Maximum principal stress, in the isotropic FE models
σ_{11}	Axial stress, in the anisotropic FE models
σ_{12}	Shear stress, in the anisotropic FE models
σ_{22}	Transverse stress, in the anisotropic FE models
θ_σ	Stress transformation angle, in the anisotropic FE models
R^2_{adj}	R^2, adjusted to down-weight models with more predictor variables

Plaque Geometry Symbols

$\%_{li}$	Lipid fraction, [%]
$\%_{pb}$	Plaque burden, [%]
A_{li}	Lipid area, [mm^2]
A_{lu}	Lumen area, [mm^2]
A_{pl}	Plaque area, [mm^2]
t_{fc}	Fibrous cap thickness, [mm]
t_{li}	Lipid thickness, [mm]
ρ	Shoulder radius of curvature, [mm]
ρ_{norm}	Normalised shoulder radius of curvature, [unitless]
θ_{li}	Lipid arc, [°]

Imaging and Microstructure Symbols

$P(\theta)$	Normalised orientation density function

$P_m(\theta)$	Orientation density function for a von Mises distribution with spherical normalisation
κ	Fibre dispersion for a one-family fibre system
θ_μ	Local mean fibre orientation relative to the image coordinate system
θ_i	Local mean fibre orientation relative to the artery coordinate system
A	Slope of the predictor variable in a linear regression model
b	Concentration parameter for a von Mises distribution
R^2	Coefficient of determination in a linear regression model

Chapter 1

Introduction

1.1 Motivation and Objectives

Cardiovascular disease is responsible for most deaths in the United Kingdom and worldwide. In 2011, 74,000 UK deaths were from coronary heart disease and 43,500 were from stroke [BHF, 2013; NHS, 2013]. Worldwide, there are about nineteen million deaths per year from cardiovascular disease.

Atherosclerotic plaque disruption (through rupture or erosion) is responsible for 75% of acute coronary events [Falk, 1991; Falk et al., 1995], and is presumed to be responsible for many carotid and cerebral events as well [Halvorsen et al., 2008]. These disruptions cause thrombosis, which can lead to severe narrowing or occlusion of an artery [Halvorsen et al., 2008]. Therefore, atherosclerosis is often a benign chronic disease until a sudden plaque disruption creates the conditions for harmful events. Plaque disruptions may not always lead to a cardiovascular event: autopsies have found an average of two disrupted plaques per patient dying from coronary artery disease [Falk et al., 1995]. Fewer than half of these plaques had thrombosis sufficient to critically obstruct flow.

Plaque disruptions are highly mechanical in nature, with the failure presumed to being analogous to fracture or fatigue seen in engineering materials [Akyildiz et al., 2014; Richardson et al., 1989; Versluis et al., 2006]. A number of mechanical loading mechanisms may be responsible for plaque failure: tension, compression, circumferential bending, longitudinal flexing, and shear [Falk et al., 1995].

Given the potential consequence of plaque disruption, clinicians seek to prevent cardiovascular events through medical or surgical intervention. Risk of cardiovascular events must be balanced against risks and costs of the intervention. Currently, the degree of stenosis of the vessel (or narrowing relative to the original lumen diameter) and the presence of any symptoms are the main determinants for surgical intervention. Risk is reasonably well predicted for severe (>70%, high risk) and mild (<30%, low risk) stenosis [ECSTGC Authors, 1991; Falk et al., 1995; Ferguson et al., 1999]. However, the majority of cardiovascular events are linked to plaques with moderate stenosis, for which stenosis is a poorer predictor of risk.

Therefore, improved criteria and tools are required to evaluate risk of cardiovascular events. Given the mechanical nature of plaque disruption, biomechanical criteria and models to assess risk have been an active field of research [Gijsen and Migliavacca, 2014; Holzapfel et al., 2014; Richardson, 2002; Sadat et al., 2010; Teng, 2011]. These and other studies will be further reviewed in Section 1.4.

While artery is a fibrous material, changes to the fibre structure caused by atherosclerosis have yet to be characterised. Therefore, the impact of fibre structure changes on plaque mechanics has also not previously been studied. Changes to fibre structure is hypothesised to affect both stiffness and toughness of artery tissue. The failure mechanisms leading to plaque disruption are not well understood, but are critical in assessing tissue failure.

The main objectives of these studies are therefore to:

- Characterise changes to the microstructure from atherosclerosis
- Determine effects of fibre structure on stresses in plaques
- Identify links between fibre structure, geometry, and stress
- Understand the role of fibre structure in artery material properties
- Consider microstructure-based mechanisms in plaque disruption

Microscopy, image processing, computational modelling, and experiments will be used to understand the role of fibre structure in plaque mechanics. Findings will be compared to previous studies and clinical reports of plaque disruption.

1.2 Anatomy and Physiology in Atherosclerosis

This section will review the general anatomy of atherosclerotic plaques, plaque disruption and vulnerability, clinical assessment of plaques, and cellular processes in atherosclerosis. The intention is to provide a broad overview of atherosclerosis, giving context for the role of fibre structure in plaque mechanics.

1.2.1 General Anatomy of Atherosclerotic Plaques

Coronary and carotid plaques have similar features to one another. A carotid plaque is shown in Figure 1.1.

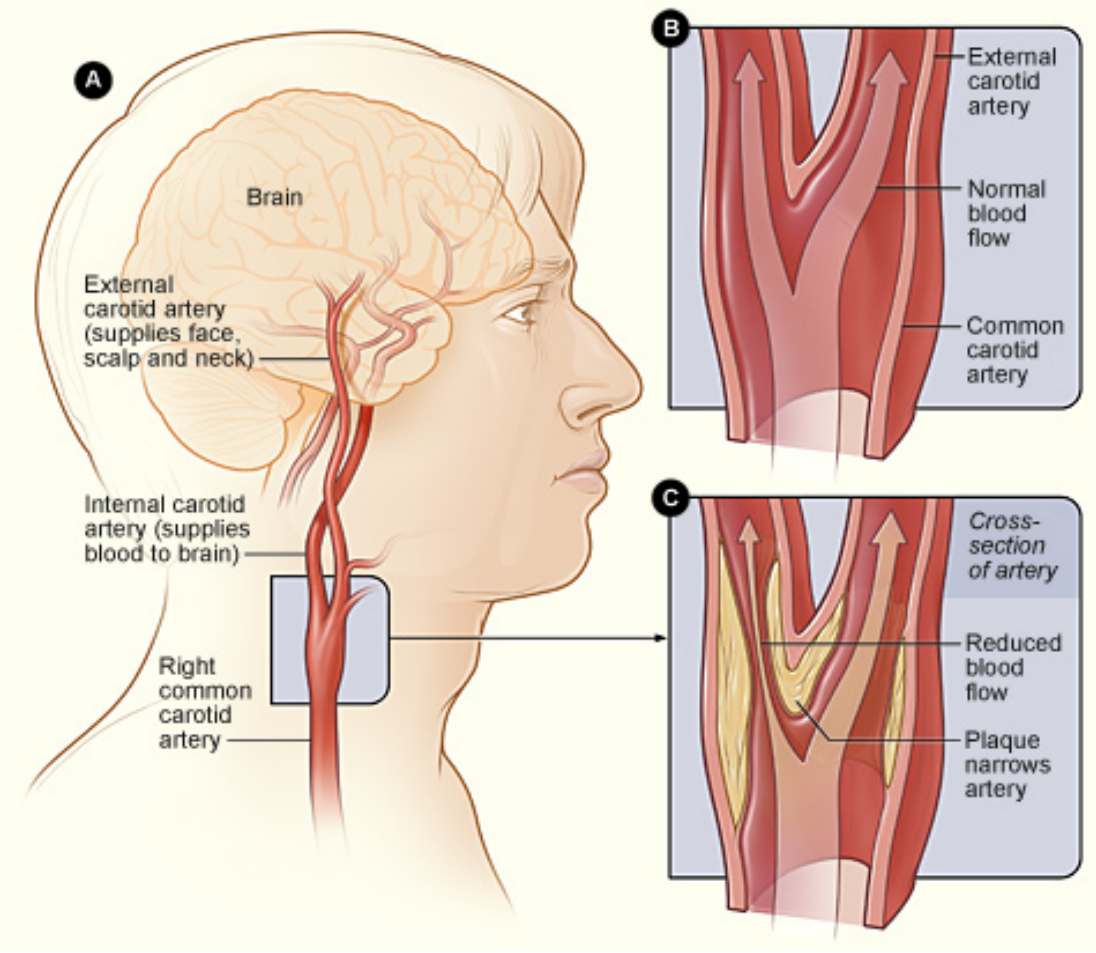

Figure 1.1: Illustration of a carotid atherosclerotic plaque (from the NIH National Heart, Lung, and Blood Institute, www.nhlbi.nih.gov).

Plaques develop and grow at several common locations such as the carotid bifurcation. A lipid pool becomes incorporated into the artery wall, causing the lumen to narrow and interfering with blood flow. Disruption of the plaque can occlude the vessel at the rupture, or downstream where the vessel narrows.

Atherosclerosis is notable for lipid accumulation and the chronic inflammation of the plaque, and processes involved in these features are thought to determine disease progression [Halvorsen et al., 2008]. A histological cross-section of a coronary plaque is shown in Figure 1.2, with key regions of the plaque labelled.

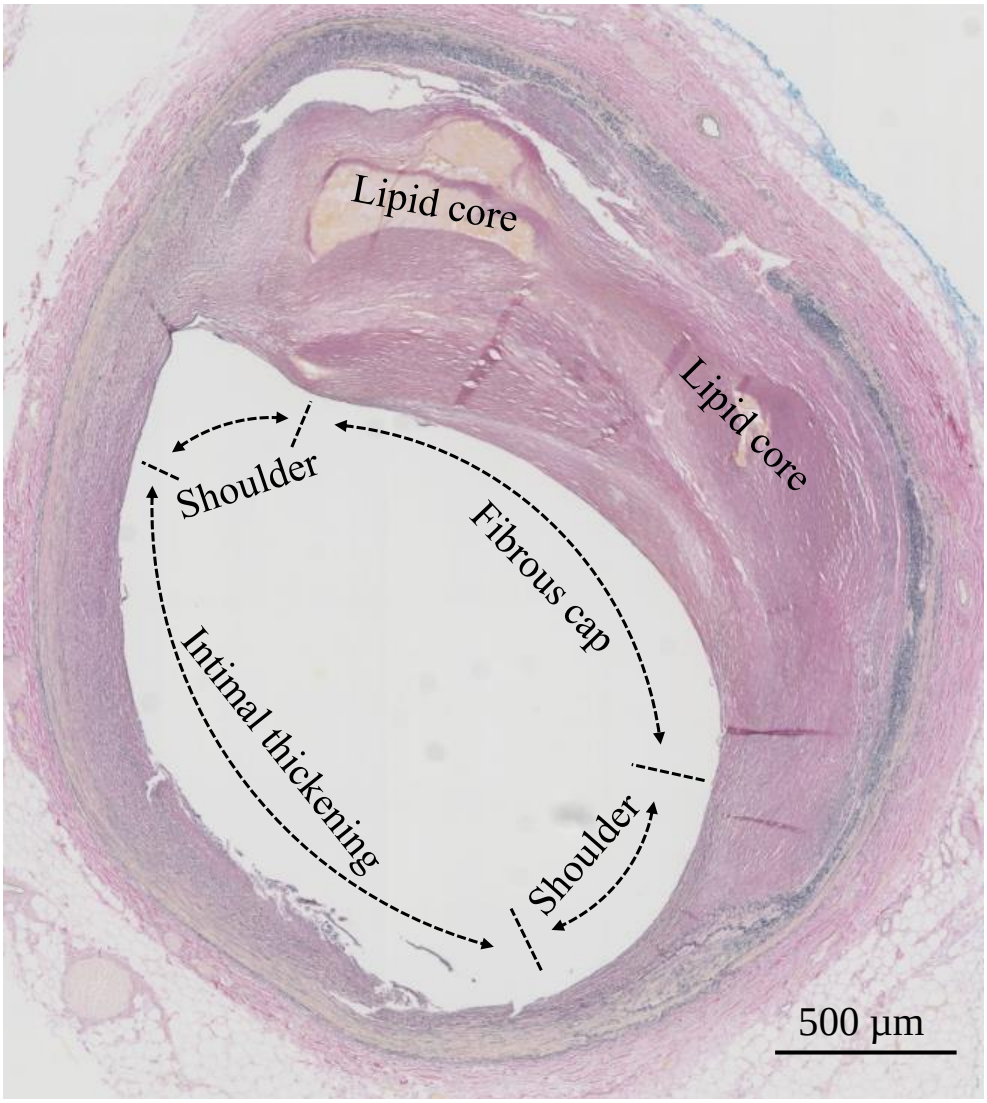

Figure 1.2: A histology section of a carotid plaque, with key regions labelled.

The development of the lipid core (stained yellow in Figure 1.2) causes thickening of the artery wall and narrowing of the lumen. Often, plaque development is asymmetric, while healthy vessels have circular cross-sections. The non-lipid tissue in the plaque is primarily collagen (pink), with some elastin (purple). The lipid core is covered by a fibrous cap, which connects to fibrous tissue beside the lipid core at the shoulder regions. The shoulder region is a frequent site of plaque rupture, especially in coronary plaques [Redgrave et al., 2006; Richardson et al., 1989]. Other ruptures occur in middle of the fibrous cap. The intimal thickening (IT) region is across from the lipid core, and is typically less affected by atherosclerosis but still thicker than healthy intima. Calcification is often present in plaques (diffuse light pink; the lighter bands in the fibrous cap in Figure 3.4), and luminal thrombus and intra-plaque haemorrhage are sometimes present (neither are present in Figure 3.4).

1.2.2 Plaque Disruption and Vulnerability

Atherosclerotic plaque disruption includes rupture and erosion of the fibrous cap. Rupture is from fracture of the fibrous cap, while erosion is from thinning of the cap [Falk et al., 1995; Halvorsen et al., 2008]. This allows the lipid core to contact the blood or even escape from the plaque. Since the lipid is highly thrombogenic, plaque disruption can lead to thombosis, which can restrict blood flow [Falk et al., 1995; Halvorsen et al., 2008].

Research has sought to identify features of vulnerable plaques and vulnerable patients, or plaques and patients with higher risk of acute events [Halvorsen et al., 2008]. For example, patients with unstable angina have a higher incidence of new coronary events, but almost half of these new events are caused by a different plaque from the one originally causing symptoms [Halvorsen et al., 2008]. Additionally, chronic inflammation and cytokines are found with atherosclerosis, suggesting that systemic mechanisms may be implicated in risk of acute cardiovascular events [Halvorsen et al., 2008].

Vulnerable plaques are thought to have large lipid-rich necrotic cores, thin fibrous caps, and more inflammation [Falk et al., 2013, 1995; Halvorsen et al., 2008]. Intra-plaque haemorrhage, which is the infiltration of erythrocytes (red

blood cells) into plaques, has been linked to atherosclerotic progression and fate. Plaques having intra-plaque haemorrhage are more likely to cause cardiovascular events through their rupture than by erosion or severe stenosis [Kolodgie et al., 2003]. Intra-plaque haemorrhage is found in plaques with larger necrotic cores, more inflammation, and plaque instability [Kolodgie et al., 2003].

Several reports have proposed a link between intra-plaque haemorrhages and the angiogenesis of neovessels within the plaque [Depre, 1996; Kolodgie et al., 2003; McCarthy et al., 1999; Moreno et al., 2006; Sluimer et al., 2009; Yu et al., 2011]. Neovessels are likely extensions of the vasa vasorum, although neovessels lack a smooth muscle layer and have disrupted endothelial layers [Depre, 1996; Kolodgie et al., 2003; Moreno et al., 2006; Sluimer et al., 2009]. These vessels then allow lipid material, likely from haemorrhage, into the plaque. Macrophages infiltrate the plaque in response to haemorrhage, possibly becoming trapped and apoptotic [Kolodgie et al., 2003]. Compounds in the intra-plaque haemorrhage and dead macrophages may damage the collagen fibre structure. Plaque progression, symptoms, rupture risk, and lipid content are linked with neovessel density [McCarthy et al., 1999; Moreno et al., 2006; Sluimer et al., 2009].

1.2.3 Role of Imaging in Clinical Assessment

Imaging techniques are important tools in the clinical assessment of atherosclerotic plaques [Sadat et al., 2009], and have been used to make patient-specific biomechanical models (reviewed in Section 1.4.3). In the past, X-ray angiography was the major technique used to identify geometry of the blood conduit, but does not capture soft tissues of the artery [Sadat et al., 2009]. Magnetic resonance imaging (MRI) is currently the most promising technique, and can measure the lipid core, fibrous cap, and intraplaque haemorrhage. Contrast-enhanced MRI can improve the visualization of the fibrous cap, and give indications of neovessels and macrophage infiltration of the plaque [Sadat et al., 2009]. Computed Tomograhy (CT) has been used, but it has less ability to differentiate soft tissue components and requires relatively large doses of ionizing radiation [Sadat et al., 2009]. Ultrasound can give reasonable geometry of the plaque and vessel, but has a lower spatial resolution [Teng et al., 2013a]. Radionucleotide imaging, such as

through ^{18}F-fluorodeoxyglucose-Positron Emission Tomography (FDG-PET), is an emerging technique for imaging macrophage infiltration [Sadat et al., 2009].

A major consideration in the clinical assessment of plaques is the degree of stenosis or narrowing caused by the plaque. Several studies have demonstrated that for severe stenosis (defined in different studies as >50%, >60%, or >70% reduction in diameter), surgical risk from pre-emptive carotid endarterectomy is significantly lower than risk from cardiovascular events [ECSTGC Authors, 1991; Ferguson et al., 1999; Hobson and Weiss, 1993; Rothwell and Goldstein, 2004; Taylor, 1991]. One major stroke is prevented for every six severe lesions operated on [Taylor, 1991]. For mild carotid stenosis (<30%), benefit of surgery is not seen and few strokes are from these plaques [ECSTGC Authors, 1991]. However, recommendations for plaques with moderate stenosis are less clear, with less reduction in risk from surgery compared with severely stenotic plaques. Plaques with moderate stenosis are more numerous than with severe stenosis, and therefore most strokes are caused by plaques with moderate stenosis [ECSTGC Authors, 1991; Falk et al., 1995; Ferguson et al., 1999].

Research Efforts in Plaque Imaging

Research efforts have been considering ways to identify components or geometric parameters that can assess risk of plaque disruption better than stenosis alone [Davies et al., 2010; Sadat et al., 2009; Teng, 2011]. These approaches often consider biomechanics and computational modelling [Holzapfel et al., 2014; Richardson, 2002; Taylor and Humphrey, 2009; Teng et al., 2013a]. MRI and intravascular ultrasound (IVUS) are the major modalities being investigated due to their ability to image soft tissues. MRI is already used clinically to identify plaque components, but has limited spatial resolution [Sadat et al., 2009].

IVUS with elastography techniques has compared stiffness between plaque types [de Korte et al., 2000] and has been used to estimate local Young's Moduli [Baldewsing et al., 2005]. Virtual histology using IVUS found significant predictors of major coronary events: classification as a non-calcified thin cap atheroma, minimum lumen area under 4 mm^2, plaque burden over 70%, higher remodelling index, and higher plaque volume [Calvert et al., 2011]. However, a

study using a porcine atherosclerotic model was unable to correlate necrotic core geometries from IVUS with those from histology [Thim et al., 2010].

FDG-PET is a promising technique for estimating macrophage infiltration in plaques, and therefore degree of inflammation [Davies et al., 2010]. Optical coherence tomography (OCT) is an emerging technique but has potential to indicate fibre structure. Fibre detection has been demonstrated *in vitro* with bovine tendon (primarily Type I collagen), with a resolution of 1-15 μm to a depth of 700 μm [de Boer et al., 1997]. OCT has also been combined with computational models to estimate local material properties in arteries [Karimi et al., 2008].

1.2.4 Cellular Processes in Vulnerable Plaques

Within a plaque, the balance between the synthesis and degradation of the fibre structure is thought to be a key determinant of atherosclerosis progression. Collagen fibres are primarily synthesised by vascular smooth muscle cells (VSMC) and degraded by matrix metalloproteinases (MMP), which is produced by macrophages and less commonly by VSMC [Deguchi et al., 2005; Halvorsen et al., 2008; Libby, 2013]. Tissue structure is remodelled through these processes, with structural changes occurring in as little as one month [Yu et al., 2011]. Many biological processes have been suggested to regulate the activity, proliferation, and fate of VSMC and macrophages in plaques [Halvorsen et al., 2008].

Atherosclerotic progression is modulated by inhibition and apoptosis of the VSMC [Yu et al., 2011]. VSMC apoptosis occurs in both growth and reduction remodelling, and up to 70% of local VSMC have been observed to die within 90 minutes [Yu et al., 2011]. Apoptotic regions are repopulated by VSMC from adjacent tissue over several days or weeks. The process of mass apoptosis and repopulation occurs in vascular injury, atherosclerosis, and aneurysm formation [Yu et al., 2011]. It seems to be productive in injury repair, but it promotes features of vulnerable plaques in atherosclerosis [Bennett et al., 2012; Yu et al., 2011]. VSMC death has been linked to inflammation, but the causal direction is unclear; clearing dead VSMC seems to also progress atherosclerosis [Bennett et al., 2012]. VSMC apoptosis is a complicated process, and may be the result of several different mechanical, growth factor, and extracellular matrix based signalling

pathways. Further, apoptosis produces signalling factors to surrounding tissues, which may cause secondary cellular responses [Bennett et al., 2012].

Biological factors that affect collagen structure therefore affect the material properties and geometry of the tissue. Conversely, the cells are stimulated in part by mechanical pathways. Tissue is always undergoing remodelling, so cellular activity, geometry, fibre structure, and mechanics are coupled and can change on the order of days or weeks.

1.3 The Microstructure in Atherosclerosis

This section will review features of the fibrous microstructure, changes to the microstructure from disease, and current microscopy techniques being used to characterise fibrous microstructures.

1.3.1 General Microstructure of Arteries

The material properties of an artery are determined by the fibrous network of collagen and, to a lesser degree, elastin and vascular smooth muscle cells (VSMC) [Gasser et al., 2006]. The artery is made of three main layers, which from the lumen outwards are the intima, media, and adventitia (See Figure 1.3).

Each of the three tissue layers have different fibre structures. The fibre orientation and alignment of fibres is different in the different layers. The intima is thin and cellular. The media has sheets where fibres are well aligned within the sheet, but alternating sheets have opposite primary fibre orientations. The adventitia has more scattered fibres.

Artery biomechanics often consider an artery coordinate system, which is a cylindrical system. In considering 2D sections of the 3D geometry, planes are often used that are formed by two axes of this coordinate system (axial, circumferential, and radial; see Section 5.3.2 for details and sketches of these planes relative to fibre structures.)

As collagen is the primary mechanical component in both atherosclerotic and healthy tissue, discussion will focus on collagen fibre structures and types. Collagen fibres orient themselves along the principal direction of tensile stress, in

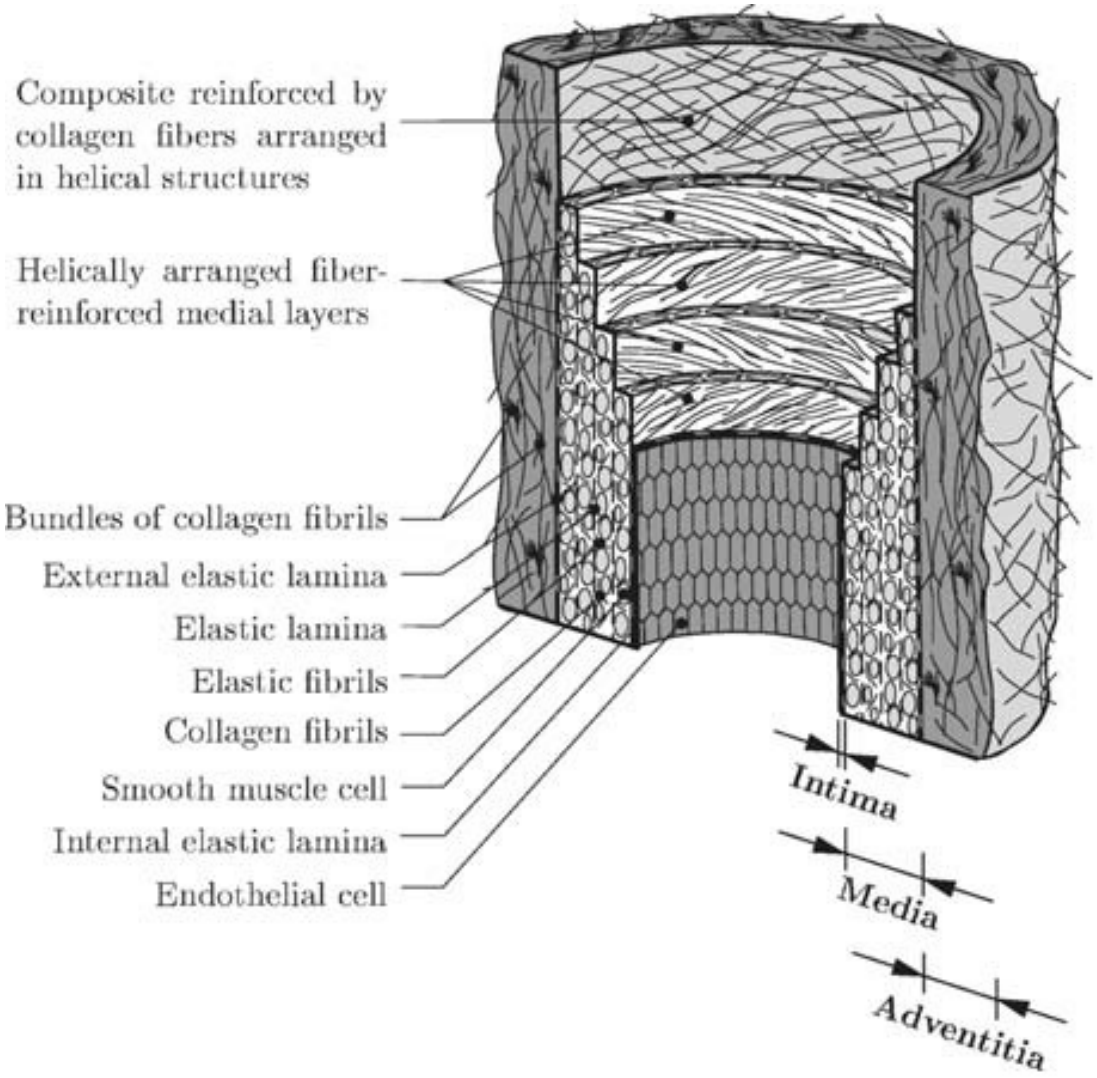

Figure 1.3: The layers of artery tissue, showing concentric sheets of predominately collagen fibres being the major component in the walls of the artery (from [Holzapfel, 2008]).

sheets similar to flakes in a pastry [Clark and Glagov, 1985]. Most collagen fibres are taut at diastolic pressures, so elastin, being less stiff, gives the artery its extensibility [Clark and Glagov, 1985]. Characterizing the distribution, size, and composition of fibres in healthy and atherosclerotic tissue could suggest factors involved in atherosclerotic progression and fate [Clark and Glagov, 1985].

It is known that, in all three artery layers, Type I and III collagen are the primary components of the extracellular matrix [Shekhonin et al., 1985]. Type IV and V collagen are found in the basement membranes around endothelial cells and VSMC in healthy intima and media. Type V collagen is spread diffusely within the intima.

1.3.2 Changes to Microstructure from Disease

Atherosclerosis is characterized by the accumulation of collagen and changes to its organization. While the studies in this thesis did not make distinctions between collagen types, the changes to relative composition of collagen types will be briefly reviewed. In fibrous plaques, the intima thickens with accumulation of Type I and III collagen, but little or no Type IV or V collagen is present [Shekhonin et al., 1985]. However, some Type IV collagen does form thick structures around VSMC. While healthy artery tissue has finely assembled structures, atherosclerotic tissue has rougher collagen fibres that are arranged in altered structures [Plenz et al., 1999; Shekhonin et al., 1985]. Type VIII collagen is highly expressed in the later stages of the disease and is proposed to be involved in angiogenesis (development of neovessels) [Plenz et al., 1999].

Collagen-based tissues are dynamic materials; mechanical and biological factors cause structural remodelling at rates measured in weeks. For instance, immobilization of a rabbit knee joint for nine weeks changed the rate of collagen turnover, tissue composition, and material properties of the tissue [Amiel et al., 1982]. The half-life of collagen in healthy arteries is 60-70 days, but diseased can increase the turnover rate ten-fold [Martufi and Gasser, 2012]. Considering the potential for rapid growth and remodelling, assessment of atherosclerotic plaques should ideally account for changes to the microstucture [Wilson et al., 2013].

1.3.3 Microstructure Imaging

A number of microscopy techniques have characterised the microstructure of arterial tissue. Immunoflourescence was used in early studies to identify types of collagen and their relative densities in healthy and atherosclerotic tissue [Shekhonin et al., 1985]. Histological staining with picoserius red and polarised light microscopy have been used to image collagen fibres and calculate 3D fibre orientation [Finlay et al., 1998]. Mason's Trichrome staining and image processing were used to evaluate fibre structure in coronary plaques, and compared with theoretical fibre structures optimised from fluid-structure interaction models that used the plaque geometry [Pagiatakis et al., 2015].

Fibre structure was characterised in the three layers of healthy human thoracic aorta, abdominal aorta, and common iliac arteries by polarised light microscopy [Schriefl et al., 2012b]. Collagen fibre structures were assessed using a Fourier transform-based method [Schriefl et al., 2012a]. Most layers had two families of fibres, each wound helically about the axis of the vessel in opposing primary orientations. Fibres within each family were dispersed around the primary orientation [Schriefl et al., 2012a,b]. The exception was the medial layer of common iliac arteries, which had a one fibre family that was oriented in the circumferential plane. The two-family helical systems in other samples had angles of approximately 45°, and were more axial in the adventitia but more circumferential in the media. The fibres were most aligned with one another in the adventitia, and most dispersed in the intima. In all layers, the fibres were relatively tangential to the luminal surface, and their orientation had little or no radial component [Schriefl et al., 2012a,b]. Polarised light microscopy has also been used to characterise 3D waviness and orientation in the common carotid adventitia of rabbit arteries [Rezakhaniha et al., 2012].

While scanning electron microscopy (SEM) was a popular technique in the past to image artery microstructure, its use declined with improvements to light microscopy [Tranfield and Walker, 2013]. However, SEM can image at higher magnifications and resolutions, especially with recent improvements to SEM machines and sample preparation techniques [Tranfield and Walker, 2013].

Multiphoton microscopy is a relatively new technique, which is able to produce 3D images to a depth of about 100 μm [Chow et al., 2014; Tsamis et al., 2013; Zoumi et al., 2004, 2002]. A key advantage of this technique is the ability to identify and discriminate between collagen and elastin, without any modification to the tissue such as stains or surface coatings [Zoumi et al., 2004]. Both collagen and elastin provide an image signal from two photon fluorescence, but only collagen produces second harmonic generation photons (reviewed in more detail in Chapter 6). Therefore, multiphoton microscopy can be used during material tests to compare fibre structure at varying strains and stresses [Zoumi et al., 2004].

Optical coherence tomography (OCT) is a developing technique that could allow for *in vivo* characterisation of fibre structure [de Boer et al., 1997]. MRI has been used *in vitro* to calculate fibre orientation in porcine artery tissue [Flamini et al., 2013]. Both techniques show potential for eventual clinical use.

1.4 Biomechanics and Computational Analysis

Artery is a complex material, exhibiting viscoelasticity, hysteresis, anisotropy, growth, remodelling, and non-linearity [Holzapfel and Ogden, 2010; Sadat et al., 2010; Taylor and Humphrey, 2009]. Changes from disease further alter the composition, geometry, microstructure, and material properties of the tissues.

In particular, the biomechanics of plaque rupture are not well understood, but biomechanical approaches have potential to improve the clinical management of atherosclerosis [Taylor and Humphrey, 2009]. Biomechanical models have been shown to be more predictive than plaque stenosis in assessing plaque vulnerability, but improvements and extensive validation studies are needed before such models are ready for routine clinical use [Sadat et al., 2010].

Several approaches that have been used to assess the biomechanics of atherosclerosis will be reviewed. Although artery is a fibrous tissue, it has been more popular to model it using continuum mechanics (see Section 1.4.1), typically with phenomenologically derived parameters that are fitted to material test data. Section 1.4.2 will review structurally-driven biomechanical models. Patient-specific biomechanical models use imaging to construct geometries based on the anatomy of an individual plaque (see Section 1.4.3). While this dissertation considers the

solid biomechanics of arteries, biomechanical models of blood flow and blood-wall interaction have also been developed [Tang et al., 2009; Yang et al., 2008]. Biomechanical models and techniques have been co-developed with material characterisation experiments, which will be reviewed in Section 1.5, and informed by tissue microstructure (see Section 1.3).

1.4.1 Continuum Material Models

Arterial tissue is most often modelled using continuum mechanics, where material testing data is fitted to find parameters of the constitutive material model [Cacho et al., 2007; Gasser et al., 2006; Holzapfel, 2008; Holzapfel and Ogden, 2010; Kroon and Holzapfel, 2008]. Both isotropic and anisotropic material models have been established, with anisotropic parameters derived from material test data or microscopy of fibre structure.

A variety of material models have been used to describe the response of artery, including neo-Hookean, Yeoh, Mooney-Rivlin, and Ogden [Teng et al., 2015b]. An invariant-based material model with a neo-Hookean component to represent the ground matrix and an exponential component that accounts for anisotropy from fibre structure has been developed [Gasser et al., 2006; Holzapfel and Ogden, 2010]. An invariant is used to consider fibre orientation (the local mean fibre direction) and a constant parameter is used to describe fibre dispersion (which accounts for directional variance about the mean). Therefore, fibre structure is represented statistically in the continuum solid, rather than considering discrete, individual fibres [Gasser et al., 2006; Holzapfel and Ogden, 2010].

Such constitutive laws are usually assumed to be incompressible for artery tissue [Holzapfel and Ogden, 2010]. 2D models, with a plane strain assumption, and 3D models are both commonly used [Holzapfel et al., 2014]. The plane strain models are accepted for investigating the independent role of various factors in mechanics, but 3D models are preferred in assessing the mechanical state of a particular plaque.

Most biomechanical models report stresses [Holzapfel et al., 2014], although stretches (or strains) have also been reported from models or directly from imaging [Teng et al., 2013b]. However, physiological blood pressure is typically be-

tween two and ten times lower than would be needed in such models to produce stresses that exceed the tensile strength of the tissue [Huang, 2012].

A Paris Law-like material model has been proposed for fatigue-like behaviour, serving as a mechanism leading to failure of a plaque at lower stresses due to high cycle loading [Huang, 2012].

1.4.2 Structure-based Material Models

Biomechanics have also considered structure-based approaches, where constitutive models are based on physical quantities of the tissue [Chen and Kassab, 2016; Lanir, 1983; Thunes et al., 2016]. In contrast, material parameters in continuum or phenomenological models do not have physical meanings; they are simply fitted from experimental data [Lanir, 1983]. Fibres are modelled individually in structure-based models [Chen and Kassab, 2016; Lanir, 1983]. Fibre structure modifies anisotropic stiffness in continuum models [Gasser et al., 2006]. Structure-based models can therefore better account for fibre waviness, cross-linking, size, defects, density, and type [Chen and Kassab, 2016; Chen et al., 2011; deBotton and Oren, 2013; deBotton and Shmuel, 2009; Lanir, 1983; Sáez et al., 2014; Thunes et al., 2016]. Structure-based models may predict local mechanics and represent material test data better than continuum-based models [Chen and Kassab, 2016; Chen et al., 2011; Maceri et al., 2010; Sáez et al., 2014].

Micromechanical structure-based models have been developed for fibres to lock (become infinitely stiff) at a maximum strain [deBotton and Shmuel, 2009], separate deformation of the fibres and ground matrix [Chen et al., 2011], and for multiple families of fibres [deBotton and Oren, 2013]. Microstructural models have considered the interaction of elastin and proteoglycans in the extracellular matrix [Ritter et al., 2009]. A multi-scale structure-based model representing the hierarchical nature of soft, collagen-rich tissues from nano, micro, and macro scales has been proposed [Maceri et al., 2010].

Microstructural models assume that the critical scale for mechanics and failure is at the size of fibres, or about 0.1-10 μm [Chen and Kassab, 2016; Lanir, 1983]. In contrast, structurally-modified continuum models assume a larger critical scale, so can use a statistics-based fibre structure [Gasser et al., 2006].

A finite element micromechanical model has been used to understand the mechanics, failure, and defect tolerance of biomimetic fibrous scaffolds [Koh et al., 2013]. Fibre geometries for the model were built from scanning electron microscopy (SEM) images, in unloaded and loaded samples. Experiments with standard and notched samples were used to set model properties, and results were compared with those from the model [Koh et al., 2013].

1.4.3 Patient Specific Modelling of Plaques

Patient-specific computational models, where biomechanical material models are applied to geometry from medical imaging or microscopy, are well established in research [Holzapfel et al., 2014]. The eventual objective is use in clinical evaluation of atherosclerosis, particularly for plaque rupture risk [Sadat et al., 2009].

Histology was used to construct geometries in the first patient-specific finite element (FE) studies, one of which compared twelve plaques that had caused fatal myocardial infractions with twelve stable plaques [Cheng et al., 1993]. Ruptured plaques had significantly higher peak stresses, and seven of the twelve ruptures had occurred at the location of peak stress. In another FE-based study, histology was used to evaluate the geometry near neovessels, since these features were too small to be imaged clinically [Teng et al., 2012]. Histology has also been used to evaluate fibre structure of an iliac artery used in a FE study of angioplasty balloon expansion [Gasser and Holzapfel, 2007].

However, recent patient-specific models of athersclerotic plaques mostly extract geometries from medical imaging techniques [Holzapfel et al., 2014]. Medical imaging techniques have the advantage of being non-destructive and closer to the eventual goal of clinical use [Holzapfel et al., 2014; Sadat et al., 2009].

Magnetic resonance imaging (MRI) is probably the leading clinical imaging modality to obtain plaque geometries for evaluating biomechanics due to its good soft tissue contrast, lack of ionizing radiation, and non-invasiveness [Teng et al., 2013a]. In addition to geometry, MRI is able to segment the plaque by tissue type and identify histological features like intraplaque haemorrhage, calcification, and the presence of a lipid-rich necrotic core [Teng et al., 2013a].

A 3D finite strain constitutive model using a stochastic fibre structure and modelling structural damage [Rodríguez et al., 2006] was implemented as a finite element model using MRI generated geometry [Rodriguez et al., 2008]. Additional MRI-based FE studies have considered changes to the lipid core and calcification [Kiousis et al., 2009], lumen curvature [Li et al., 2008], and stiffness estimation through elastography [Taviani et al., 2008].

While many studies have used patient-specific biomechanical modelling to answer various questions, relatively few have evaluated larger groups of patients or compared biomechanical results to clinical outcomes [Holzapfel et al., 2014]. One such study evaluated 70 carotid plaques through MRI and finite element analysis, finding that higher stresses were linked to symptomatic, unstable, and vulnerable plaques had higher stress [Sadat et al., 2011].

A complication in computational modelling of atherosclerosis is that material properties are highly location- and component-dependant [Sadat et al., 2010]. Fibrous cap stiffness can change by a factor of five depending on cell and calcium content and a factor of twenty for different loading directions [Sadat et al., 2010].

Currently, no imaging modality is able to image fibre structure *in vivo*. MRI is limited by image resolution, which prevents detecting small structures in the tissue. Resolution can be somewhat improved with longer scanning times, but requires patients to be still in the machine for longer [Auer et al., 2006]. Statistical algorithms have been proposed to estimate geometry of features that are about half the edge length of a MRI voxel, but would still have a resolution which is an order of magnitude too low to detect fibres [Auer et al., 2006]. Research-use MRI have been able to estimate collagen orientation *in vitro*, but the tissues were partially dissected and research MRI machines are considerably different from those used clinically [Flamini et al., 2013; Pierce et al., 2010].

IVUS [Baldewsing et al., 2005; de Korte et al., 2000] and OCT [Azinfar et al., 2015; de Boer et al., 1997; Karimi et al., 2008] have been used with computational modelling to estimate local material properties of tissue, and show potential for imaging fibre structures. A downside of these techniques is they require vascular access, so are more invasive than MRI.

1.5 Material Testing of Arteries

Material tests have been developed in parallel with biomechanical models. Model parameters are fitted from stiffness test data and model failure criteria are proposed from experiments testing strength and toughness. For both stiffness and failure, there remains a relative lack of material testing data due to differences between vessels, variable components with samples, disease states, and protocols used by different researchers [Richardson, 2002; Walsh et al., 2014]. Data for failure is particularly sparse and variable, and the mechanical mechanisms involved in plaque disruption remain unknown [Holzapfel et al., 2014; Walsh et al., 2014].

1.5.1 Characterising Stiffness

Several types of tests have been used to characterise stiffness in plaque tissue, often with the results used to fit parameters in biomechanical models [Barrett et al., 2009; Holzapfel et al., 2014, 2004; Loree et al., 1994; Maher et al., 2009; Sommer and Regitnig, 2009; Walsh et al., 2014].

Uniaxial Tests

At least nine studies have used uniaxial tensile tests to characterise atherosclerotic plaques, often with strips cut in different directions to evaluate anisotropy [Walsh et al., 2014]. However, considerably different material properties were found, possibly due to differences protocols. Studies had differences in vessel types, sample storage protocol, sample length-to-width ratios, sample clamping, whole versus layer-dissected samples, loading protocols, and reporting metrics [Walsh et al., 2014]. While most protocol differences can be justified by the particular objectives of a study, the lack of standardisation makes it difficult to compare studies and use data in different biomechanical models from the one used by the study [Walsh et al., 2014].

Artery becomes stiffer at higher strains and full-thickness artery (as opposed to any individual layer) is stiffer in the circumferential direction than the axial [Walsh et al., 2014]. The relative stiffness of different tissues (intima, media, and fibrous cap) depends on direction of loading, with the media stiffer circum-

ferentially and the intima stiffer axially [Holzapfel et al., 2004]. The stiffnesses of the media and fibrous cap have been found to be similar in the circumferential direction, but both are significantly stiffer than the lipid or intra-plaque haemorrhage [Teng et al., 2014]. Uniaxial tests have found no difference in stiffness between cellular, hypo-cellular, and calcified plaques at physiological loading levels but significant differences were found at higher loads [Loree et al., 1994]. As an order of magnitude, the tangent modulus of arterial tissue at physiological stretches is about 100-1000 kPa.

Other Stiffness Tests

One study has considered biaxial tensile tests on human carotid arteries, which found lower stiffnesses than are usually reported from uniaxial tensile tests [Kural et al., 2012]. *In vivo*, the artery has a near constant axial stretch ratio of about 1.05-1.1 throughout the blood pressure cycle, while the circumferential direction has a similar pre-stretch but distends with increasing blood pressure [Holzapfel et al., 2014; Kural et al., 2012].

Biaxial properties have been evaluated by applying axial pre-stretch and lumen pressurisation to intact and layer-dissected carotid arteries [Sommer and Regitnig, 2009]. Axial stretch was found to be constant with pressure for a stretch ratio of about 1.15 for intact samples, but axial stress changed with pressure for layer-dissected samples irrespective of the stretch ratio.

Indentation of carotid plaques has been studied, finding a shear modulus of 7-100 kPa [Barrett et al., 2009]. Characterising stiffness through non-invasive medical imaging has been attempted using MRI [Nederveen et al., 2014; Taviani et al., 2008], ultrasound [Hansen et al., 2014], IVUS [Baldewsing et al., 2005; de Korte et al., 2000], and OCT [Karimi et al., 2008]. Such elastography-based efforts have been able to provide different stiffness values for different material components of the tissue, but are generally limited by the spatial and temporal resolution of the imaging method.

It is becoming common to combine microscopic imaging with material tests to evaluate the influence of components and structure on anisotropic stiffness [Kural et al., 2012; Teng et al., 2014; Walsh et al., 2014]. Macrophage density has been

correlated to lower strength in fibrous caps [Lendon et al., 1991]. Microscopy of collagen networks have been used with mechanical extension tests to find structurally motivated parameters for biomechanical stiffness [Holzapfel, 2006] and damage models [Weisbecker et al., 2012]. Micro-calcification has been linked to rupture locations in SEM images, and Fourier transform infrared spectroscopy (FTIR) proposed as a clinical tool to evaluate calcification [Mulvihill et al., 2013]. The response of collagen fibre orientation has been considered in cyclical tension of bovine pericardium [Sellaro and Hildebrand, 2006]. Loaded perpendicular to the fibre orientation caused fibres to reorientate toward the loading direction, while loading parallel to the fibre orientation decreased fibre waviness [Sellaro and Hildebrand, 2006].

1.5.2 Characterising Properties of Material Failure

The mechanics of failure in artery tissue are not well characterised or understood, limiting the ability of biomechanical models to predict plaque disruption [Holzapfel et al., 2014; Richardson, 2002].

Along with stiffness, uniaxial [Teng et al., 2015a; Walsh et al., 2014] and pressurisation tests [Sommer and Regitnig, 2009] have been used to assess the strength of plaques. Variability within and between uniaxial studies is at least as high for strength values as for stiffness, and strength measurements are further complicated by test strips often failing near or slipping out of their clamps [Teng et al., 2015a; Walsh et al., 2014]. Uniaxial tensile tests do not replicate *in vivo* loading, so the failure location in an test strip may not represent the failure location, and therefore stress, in a plaque [Walsh et al., 2014]. Pressurisation tests are more representative of physiological loading, but require a more complex apparatus. Test samples in these tests are also more difficult to image fracture development and propagation [Sommer and Regitnig, 2009].

Plaques are anisotropic: the media is stronger circumferentially but the intima and fibrous cap are stronger axially [Holzapfel et al., 2004]. However, plaque tissue fractures at a similar stretch ratio (about 1.5) in either direction [Teng et al., 2015a; Walsh et al., 2014]. Compared to healthy tissue, strength of atherosclerotic tissue is decreased in the intima but increased in the media [Holzapfel et al., 2004].

Failure properties at the microscale have been relatively unstudied. Fibril-level material tests of Type I collagen from tendon tissue have been done using atomic force microscopy [Svensson et al., 2013]. Tensile material properties of the Type I collagen were: modulus (2-3 GPa), ultimate stress (200-400 MPa), ultimate strain (16-20%) [Svensson et al., 2013]. Differences in cross-linking and fibril length (1-450 μm) were proposed as reasons for differences in properties [Svensson et al., 2013]. It is worth noting that this modulus for Type I collagen is approximately 1000 times that of bulk artery tissue [Walsh et al., 2014], which suggests artery should be considered as a composite fibrous or cellular material.

Fracture and Toughness

While plaque rupture is assumed to result from the fibrous cap fracturing, only two studies have been found that attempted to mechanically characterise fractures in plaques. One study compared the geometry of a crack against stress in the tissue adjacent to the crack in uniaxially stretched carotid strips with lateral notches [Davis et al., 2016]. Cracks widened as they extended, but stress ahead of the crack tip was relatively constant after the crack began extending [Davis et al., 2016]. The magnitude of the constant propagating stress increased with collagen content but decreased with macrophage density, with this stress ranging from about 0.2-1 MPa in different samples [Davis et al., 2016].

Fracture toughness has been compared to tissue composition and location in human femoral atherosclerotic plaques [Cunnane et al., 2016]. A lubricated guillotine test measured toughness, which increased with calcification and varied by location in the plaque and by patient, but was lower than the toughness of healthy pig tissue [Cunnane et al., 2016].

Due to lack of fracture-based tests in atherosclerotic tissue, studies using other arterial tissue and similar fibrous soft materials will be reviewed. Arterial dissection was modelled by *in vitro* tests of peeling between the concentric layers of the artery, with test results compared to histological findings for components in the tissue and damage to the extracellular matrix in human aorta [Sommer et al., 2008] and carotid arteries [Tong et al., 2011].

Failure mechanisms in notched electrospun biomimetic scaffolds were tested under tension, and combined with SEM imaging of the microstructure to develop a micromechanics model and a fracture toughness model [Koh, 2013; Koh et al., 2013]. Failure was brittle for gelatin scaffolds, but ductile for polycaprolactone (PCL) scaffolds, suggesting differences at the fibre-level from links between fibres and the ability for fibres to rearrange themselves [Koh, 2013].

Trouser tear tests have been used to quantify fracture toughness of porcine adipose tissue [Comley and Fleck, 2010] and descending aorta [Purslow, 1983]. These tests found a relatively constant tearing strength in a specimen, with small oscillations from individual fibres being loaded and failing [Comley and Fleck, 2010; Purslow, 1983]. These studies developed analytical models to describe material behaviour [Comley and Fleck, 2010; Purslow, 1983], and damage to the collagen fibres and rearrangement near the crack tip was observed in the adipose tissue using SEM [Comley and Fleck, 2010].

The Comley and Fleck analysis and toughness model for soft tissue tearing will be briefly summarized [2010]. A simple model for material toughness, J_c, is in Equation 1.1:

$$J_c = \frac{2\bar{F}}{B} \tag{1.1}$$

where $\bar{F}$ is the average tearing force and B is the specimen thickness.

Failure from High Cycle Loading

Cyclic loading and its effect on material properties have been considered for porcine coronary arteries [Gilpin, 2005], porcine aorta [Chu et al., 2013], and atherosclerotic and healthy human arteries [McCord, 1992]. In general, these *in vitro* studies are limited by having few samples, tissue degradation over long tests, and lack of *in vivo* processes that might reverse or accelerate damage.

After cyclic tensile loading, porcine coronary strips had lower tensile strength and evidence of tearing, delamination, and increased collagen disorder [Gilpin, 2005]. High-cycle (>10,000) tensile loading decreases fracture toughness and tensile stiffness in porcine aorta [Chu et al., 2013].

Bending tests to 500,000 cycles in human arteries caused intima fracture in $\frac{12}{14}$ plaque samples versus $\frac{3}{13}$ healthy samples (p=0.03) and elastin damage was noted in $\frac{7}{7}$ of the outer media of fatigue-tested samples compared to $\frac{1}{7}$ of the untested control samples (p=0.002) [McCord, 1992]. Fractures were most frequent at the plaque shoulders and the location of peak bending. However, tensile stiffness and ultimate tensile strength did not significantly change with number of bending cycles [McCord, 1992].

1.6 Dissertation Outline

This dissertation contains the following chapters:

Chapter 2 presents a study using scanning electron microscope (SEM) imaging to observe the microstructure of atherosclerotic plaques. The study identified differences in microstructure between plaque regions at different magnifications, which guided the design of other studies in this dissertation.

Chapter 3 describes image processing of histologically prepared atherosclerotic arteries, which quantified fibre structure in different plaque regions. In the SEM study reported in Chapter 2, the highest scale in the hierarchy of fibre structures appeared to be different between plaque regions, so this scale was considered as a first step in characterising fibre structure in atherosclerosis.

Chapter 4 describes finite element (FE) models that were used to study the role of fibre structure on stresses in atherosclerotic plaques. The FE models used a previously developed constitutive law [Gasser et al., 2006] and, for the first time, included patient-specific fibre structures in the models (found in Chapter 3). Isotropic FE models, without fibre structure, and anisotropic FE models, with fibre structure, were built and compared. Components of stress relative to fibre orientation were calculated for the anisotropic FE models to suggest loading modes that are more likely to cause failure.

Chapter 5 details experiments used to characterise tearing toughness in healthy porcine arterial tissue, and link tearing properties to material stiffness and fibre structure. Trouser tear tests were used to test tearing toughness, as has been done previously. Here, tearing was considered in more artery coordinate system planes relative to the fibre structure than has been done previously in a single study,

allowing the failure modes proposed in Chapter 4 to be compared. Also, the role of fibre structure on tearing toughness has not previously been considered.

Chapter 6 reports uniaxial tensile tests in unnotched and notched strips of healthy porcine artery under multiphoton microscope imaging. Using image processing, fibre structure was compared between different layers of the tissue and at different stretches. In the notched strips, behaviours of the microstructure near the crack tip were observed and compared for notches in different tissue planes.

A brief summary and key findings of these studies are highlighted in Chapter 7.

Chapter 2

SEM Observations of Carotid Atherosclerotic Plaques

2.1 Abstract

A short study of atherosclerotic plaque microstructure was completed using scanning electron microscope (SEM) imaging. Fibre structures were imaged and compared between different regions of the plaques, and at different magnifications. Different plaque regions (fibrous cap, shoulders, IT, and lipid core) had distinct features to their fibre structures. Images at different magnification revealed three levels of fibre structure hierarchy, where bundles of fibres from a smaller level formed the fibres of a larger level. Several fractures and fissures were observed in the fibre structures, with different degrees of healing or repair. Fractures and fissures were mainly in the same direction as fibres. Similar fibre structures were observed in sections of the artery cross-section as for the axial-radial plane of the artery. The observations from this SEM study were used to guide and motivate the studies that will be described in the following chapters of this dissertation.

2.2 Introduction

Scanning electron microscopy (SEM) was a common technique for imaging artery tissue in the past, although it has largely been replaced by light microscopy-based techniques [Tranfield and Walker, 2013]. The primary advantage of SEM is a greater resolving power, allowing smaller structures to be imaged.

In this chapter, SEM imaging was used in an observational study of the fibrous microstructure in human carotid atherosclerotic plaques. The role of fibre structure in atherosclerosis has been relatively under-studied, so the critical scale in the hierarchy of fibre structure in plaque mechanics is not known. SEM imaging was used to determine if fibre structure changed with atherosclerosis, and suggest which scale of fibre structure is most important for plaque mechanics.

Section 2.3 outlines the methods used in this observational study. Section 2.4 presents the findings from SEM imaging through discussion of representative micrographs. Section 2.5 summarises the observations and motivates the studies presented in the following chapters of this dissertation.

2.3 SEM Methods

Twelve human carotid plaques were collected from carotid endarterectomies and prepared for SEM imaging (under Cambridgeshire Research and Ethics Committee Ref. 07/H0306/123, consent obtained from the patient or relatives as appropriate). Preparation was done by Dr. Jeremy Skepper at CAIC. The carotid plaques were demineralized for two months in a 5% ethylene diamine tetra-acetic acid (EDTA) and 0.1M PIPES buffer (piperazine-N,N'-bis(2-ethanesulfonic acid)), with the solution changed weekly. Following this, the samples were dehydrated in solutions of increasingly concentrated ethanol (50%, 70%, and 95% to 100%). To remove lipid in the plaques, they were put in a solution of 50% chloroform and 50% methanol for one week, with the solution changed daily. Following this, plaques were washed in ethanol and critical point dried in a Polaron E5000 machine (Quorum Technologies, Laughton, UK).

Plaques were cut through the wall thickness: axially and in the cross-section, to expose structures inside the plaque (see Section 5.3.2 for details of sectioning

planes). These sections were mounted on 13 mm aluminium stubs and sputter coated with 15 nm of iridium to make the sample surface conductive. They were viewed in a Verios 460 scanning electron microscope (FEI, Oregon, USA), operated at 3 keV and with a probe current of approximately 25 pA. The probe current was changed for each scan to maintain contrast in regions of the sample with higher or lower conductivity.

Samples were first imaged at minimum magnification to identify key regions (shoulders, lipid deposits, suspected fissures, thrombus, etc). Low magnification images were taken across the entire plaque, excepts for areas with similar fibres in a few of the large plaques. Images of increasing magnification were taken at representative regions of each plaque as well as at any fractures, fissures, or luminal thrombus. SEM micrographs showing key findings from the wider set of images are presented and discussed in this chapter.

2.4 SEM Results

This section summarises observations from the SEM imaging of carotid plaques. Section 2.4.1 introduces the different plaque regions and differences in their fibre structures. Section 2.4.2 considers the role of scale and hierarchy in fibre structure. Section 2.4.3 describes fractures, fissures, and evidence of healing that were observed in this SEM study. While the other sub-sections use images in the cross-sectional plane of the artery, Section 2.4.4 shows plaque regions, structures, and failure mechanisms are similar in the axial-radial plane of the tissue.

2.4.1 Comparison of Different Plaque Regions

Figure 2.1 shows a composite SEM image of a carotid plaque (A) with details of the lipid core (B), shoulder region (C), and intimal thickening (IT) region (D).

The composite image (Figure 2.1A) shows a typical carotid plaque. The lipid core (top left of the composite image) has a shoulder to either side. A fissure or partial fracture can be seen near the upper-left shoulder. The lipid core was split in this sample from the carotid endarterectomy procedure used to retrieve the sample. The fibrous cap is between the lumen and the lipid core, and is

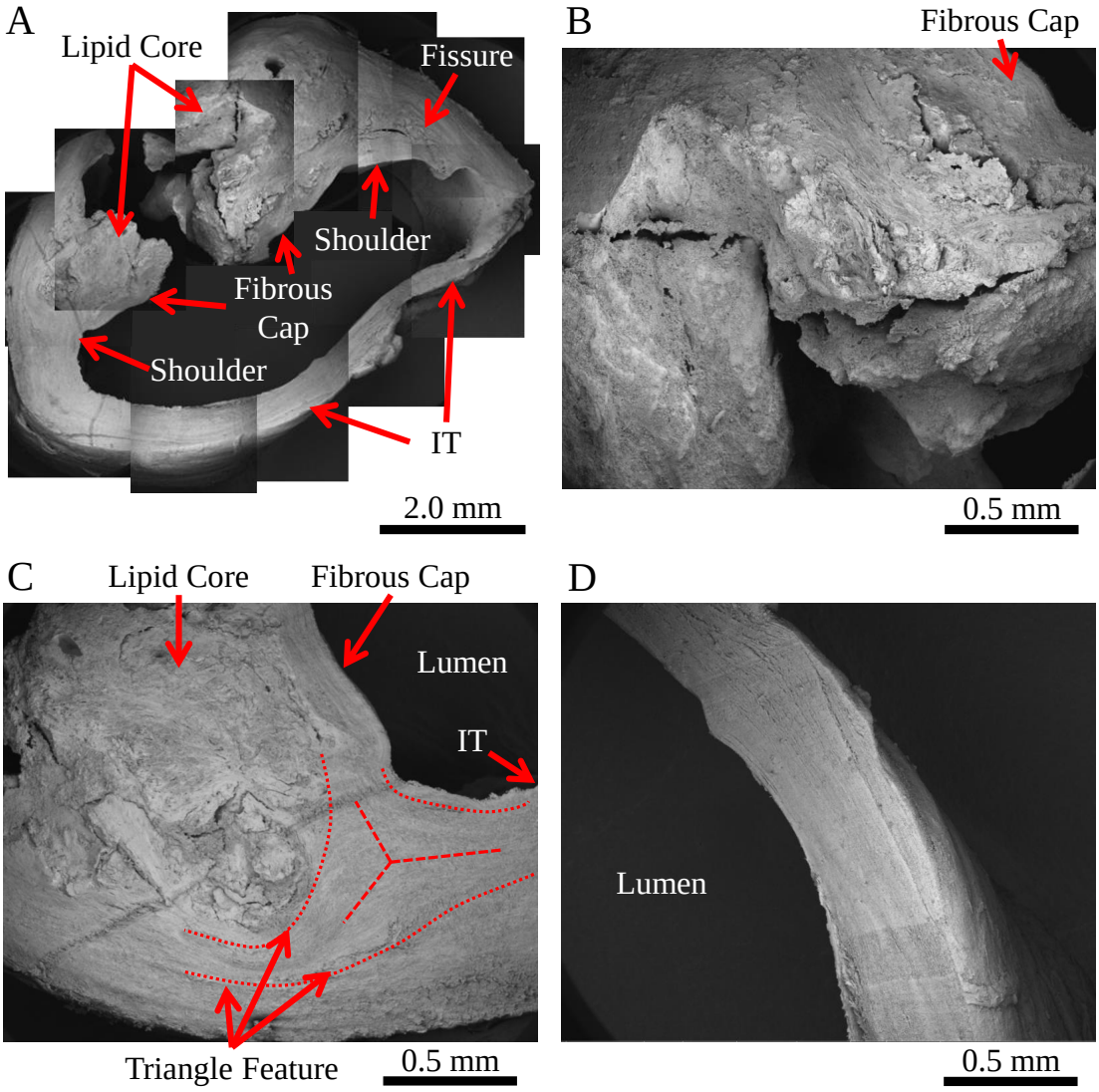

Figure 2.1: A.) Composite SEM image of a carotid plaque, with key regions labelled, B.) A more detailed SEM image of the lipid core, C.) SEM image of a shoulder region, and D.) SEM image of an IT region.

continuous with the shoulders. The IT region is opposite the lipid core (across the lumen) and is a relatively healthy region of the plaque.

The lipid microstructure (see Figure 2.1B) shows more thrombus (spongy texture) than collagen fibres, and was highly disorganised compared to other plaque regions. Fissures, voids, cells, and thrombus were commonly seen. The voids (dark pores surrounded by bright tissue) may have been lipid or calcium deposits, which were removed in the tissue's preparation.

The fibrous cap region can be seen in the upper left of Figure 2.1B and C. The fibrous cap is about 200 μm thick, and its fibres are parallel, dense, and well aligned with the luminal surface. While the fibres had similar characteristics to the IT (see Figure 2.1D), there was considerably more cell infiltration in the fibrous cap. Fissures were observed near boundary between the lumen and lipid, likely from having different material properties.

Shoulder regions (see Figure 2.1C) are a frequent site of fracture and rupture [Daemen et al., 2016; Falk et al., 2013]. Geometrically, they are often the sharpest corner of the lumen and they are often a thinner region of the fibrous cap. Fibres near the lumen wrap smoothly from the fibrous cap to the IT. Deeper fibre groups in the shoulder travel from the IT region to behind the lipid core. Fibres groups also wrap the lipid core, from the fibrous cap to the tissue deep to the lipid core. These three sides of fibre groups form a triangle-like feature at the shoulder. Each of these edges look to be coherent family-groups, but there is limited blending between the groups. Fibres within the triangular region appeared to be more dispersed, which could indicate a weaker fibre structure.

This triangle-shaped fibre structure feature was hypothesised to be a vulnerability. Delamination could occur at boundaries between the fibre groups. In some samples, the boundary between fibre groups from the IT region was close to the lumen near the shoulder. Stresses are often highest at the shoulder lumen, and a weakness from this boundary could allow fractures to propagate more easily from the lumen to the lipid core, causing plaque rupture.

The IT is a thinner and more organised region of the plaque (Figure 2.1D). The collagen fibres were well aligned with the luminal surface and were parallel to one another. Few voids, cells, or fissures were observed in the IT region. The microstructure of the IT region closely resembled that of healthy artery tissue.

2.4.2 Fibre Structure at Different Magnifications

A study of the IT at different magnifications is shown in Figure 2.2.

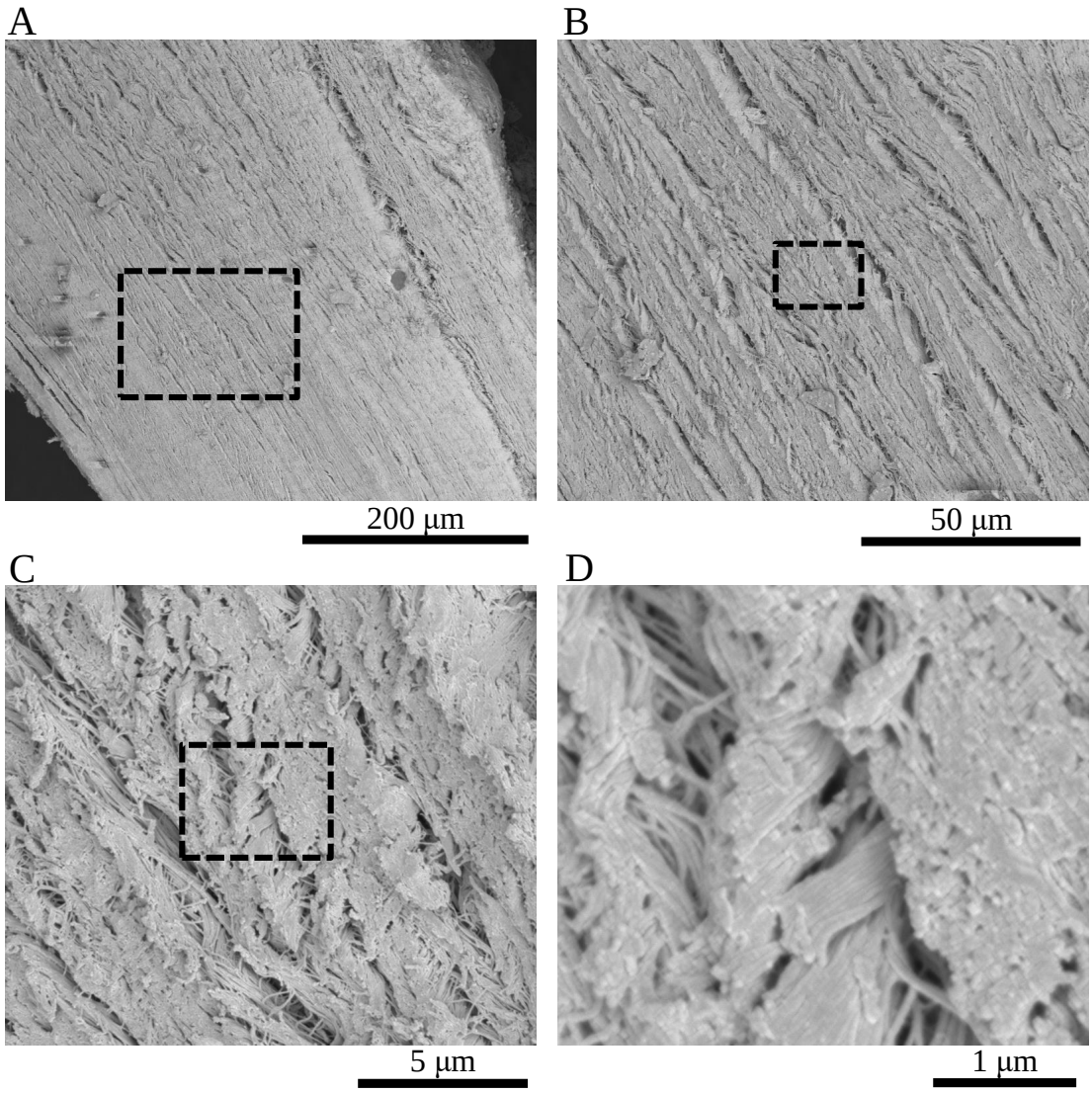

Figure 2.2: Multiscale SEM study of fibre structure in an IT region, with the dashed box indicating the region magnified in the next image. Magnification is indicated by the scale bars: A.) 200 μm, B.) 50 μm, C.) 5 μm, and D.) 1 μm.

The full thickness of the IT region (about 400 μm) is shown in Figure 2.2A. Fibres were relatively dense and nominally parallel with one another and the luminal surface. Some narrow gaps (darker) can be seen parallel to the fibres, suggesting intermittent breaks between concentric sheets of fibres.

Figure 2.2B is magnified about 4× compared to Figure 2.2A. The fibre structure is generally similar to that in the less magnified image. The gaps between fibres are likely due to the imaged plane being though the concentric sheets of fibres making the tissue. Relatively few fibres bridge across these gaps, so they may be vulnerable to tearing. A few cells can be seen (rounded structures, diameter around 5 μm), but fewer than were seen at this magnification in the fibrous cap, shoulder regions, and lipid core.

Figure 2.2C is magnified about 40× compared to Figure 2.2A. The hierarchical nature of the fibre structure can now be seen, with Figure 2.2B and C showing the larger fibres to be bundles of smaller fibres. The larger fibres (bundles of smaller fibres) had a diameter of approximately 5-20 μm, and the smaller fibres making the bundle had a diameter of about 0.5-1 μm. The smaller fibres were more disordered and wavy. They appeared to wrap around the other small fibres in a bundle, but individual small fibres sometimes switched between bundles. Smaller fibres in the fibrous cap and shoulder regions appeared to be narrower, suggesting they were newer. In the shoulder regions, fibres seemed to be more scattered and the structure seemed to have higher porosity.

Figure 2.2D is magnified about 200× compared to Figure 2.2A. Another step in the hierarchical fibre structure is revealed, with the smaller fibres found in bundles of even smaller fibres, having diameters of approximately 50 nm. These fibres are locally parallel to one another, but have waviness over the length of the small bundles. Like the 0.5-1 μm diameter fibres, 50 nm diameter fibres also sometimes switched between the larger units they formed. While each respective layer of hierarchy of the fibres-units is relatively coherent locally, cumulative shifts through the layers means some of the individual fibres are highly misaligned with the large bundle orientation.

2.4.3 Observations of Fissures, Fractures, and Healing

Figure 2.3 shows examples of fissures, fractures, and healing that were observed in the SEM study.

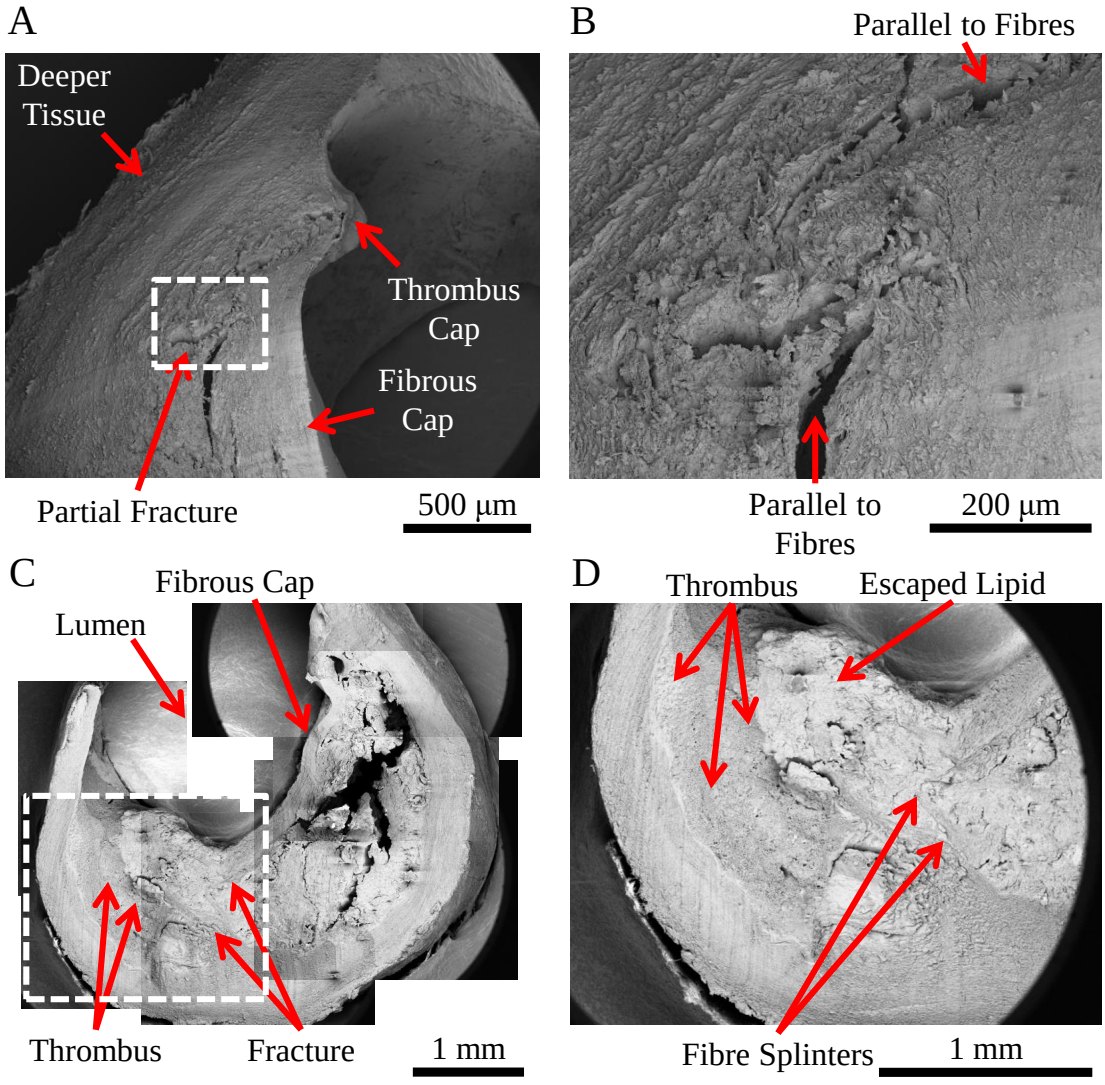

Figure 2.3: A.) Fissure or partial fracture with healing (rotated from upper left of Figure 2.1A), B.) Magnification of (A), indicated by white box, showing the fracture was mainly parallel to fibres, C.) Composite SEM image of another plaque with a recent rupture near the left shoulder, and D.) Magnification of (C), showing fractured splinters of the fibrous cap in thrombus and escaped lipid.

Figure 2.3A shows a fissure or partial fracture, which was labelled near the right shoulder in Figure 2.1A. Healing is evidenced by a thrombus-filled cap that protrudes into the lumen (thrombus can be seen in higher magnification images, not visible here). The partial fracture is mainly parallel to fibres, suggesting the fracture propagated by delamination between the concentric sheets of fibres. The fracture occurred in region of the triangle fibre feature that was described in Section 2.4.1. Here, the boundary between fibre groups going to either side of the lipid core passed within about 100 μm of the lumen, where the fracture crossed a narrowed part of the fibrous cap to the lumen.

A portion of the partial fracture is magnified in Figure 2.3B. The fracture was more parallel to fibres, but changed planes where fibres were more disorganised in the triangle fibre feature. Secondary fractures appear to break off from the primary fracture.

The fracture not being connected to the lipid core also suggests the fracture started at the lumen. An important question is why the fracture did not fully propagate to the lipid core, which would presumably rupture the plaque. Sufficient energy may have been absorbed by the tearing material to prevent complete fracture. Partial fracture may have provided relief from locally-concentrated stresses, with the load being shared more evenly by surrounding tissues after fracture. Alternatively, the material properties may have changed deeper into the tissue perhaps with the disorganised tissue in the triangle feature having increased fracture toughness.

Another suspected fracture is examined in Figure 2.3C, which is a composite image of another carotid plaque. A relatively thin fibrous cap has fractured near the shoulder in the lower left of the image, with partial escape of the lipid core and thrombosis on the luminal wall. The escaped lipid and thrombus has considerably narrowed the patent cross-section of the lumen.

The ruptured region is magnified in Figure 2.3D. Slender fragments of the fibrous cap are embedded in the escaping lipid and thrombus, suggesting fracture was caused by tearing between fibre sheets and the sheets sliding over one another. Different regions of the thrombus had different textures, cell densities, and degrees of incorporation into surrounding tissues. This suggests dynamic events were involved in the rupture, perhaps with the current structures being the result

of several smaller ruptures. These observations match clinical experiences that ruptures can be transient events and lead to plaque growth resulting in lumen narrowing [Falk et al., 2013].

2.4.4 Fibre Structure in the Axial Direction

Whereas the previous images in this chapter have been from the cross-sectional plane of the artery, Figure 2.4 shows SEM micrographs of sections in the axial direction, but still through the wall thickness of the artery (axial-radial plane).

Figure 2.4A shows a small lipid core deposit, sectioned in the axial-radial plane. Similar to plaque regions in the artery cross-section (for example, in Figure 2.1), a fibrous cap enclosed the lipid core from the lumen of the vessel. Fibres from the fibrous cap, deeper tissue behind the lipid core, and healthier tissue adjacent to the lipid core intersected in a triangle-shaped feature. Fibres in the triangle feature smoothly wrapped the lumen and lipid core boundaries, similar to a lap joint in a lay-up composite material.

A fracture in the axial-radial section is shown in Figure 2.4B. Similar to the fracture described in Figure 2.3, the fissure was mainly parallel to the direction of fibres, suggesting the tissue fractured between fibres. The fracture was lined with fresh thrombus (including circular red blood cells).

Figures 2.4C and D show two magnifications of fibres in the axial-radial section of the fibrous cap, where (D) is at the dashed box indicated in (C). The multi-scale fibre structure has similar features as were reported for the circumferential plane in Figure 2.2. At the highest level of the hierarchy, fibres were dense and relatively parallel to one another. With magnification, at least three levels of hierarchy were apparent in the fibre structure, where bundles of smaller fibres jointly formed larger fibres.

2.5 Discussion and Conclusions

Fibre structure was found to be different by plaque region, and quantitative differences are tested in Chapter 3. Fibre structures unique to particular plaque regions could explain the relative frequency of ruptures in the different regions.

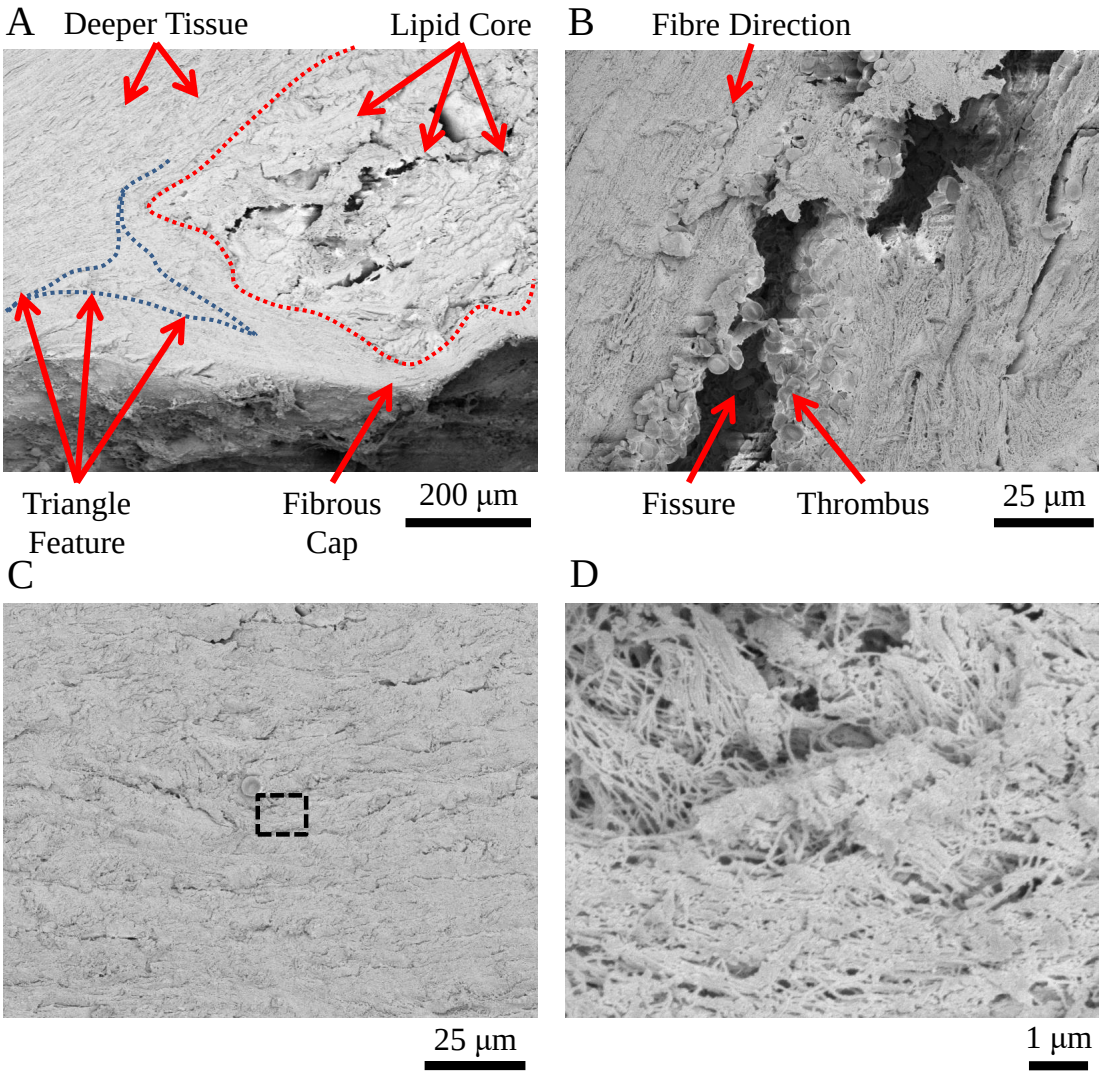

Figure 2.4: A.) Shoulder region of an atherosclerotic plaque, sectioned in the axial-radial plane of the artery, B.) A fracture with fresh thrombus from the sample in (A), C.) SEM image of an axial-radial section of the fibrous cap of the plaque from (A), and D.) Magnified section from (C), showing the finer levels of fibre structure hierarchy in the axial-radial section.

Three levels of hierarchy were identified in the fibre structure. As a first step in considering the role of fibre structure in mechanics, further studies in this dissertation only considered the largest fibre structures (diameters near 5-20 μm).

Fractures observed in the SEM images suggested that failure occurs between fibres rather than the fibres themselves fracturing, which was further considered in experiments described in Chapters 5 and 6. Observations of the partial fractures suggested that failure involves the interplay of geometry, fibre structure, and mechanics. These interactions were further considered in studies detailed in Chapters 3 and 4. Fibre structure was hypothesised to affect both the stress environment and strength of the tissue. Coupling between geometry, fibre structure, and mechanics will be considered throughout this dissertation.

Chapter 3

Characterisation of the Fibrous Microstructure of Atherosclerotic Plaques

3.1 Abstract

Fibre structure (primary orientation and dispersion) was calculated from histology images of human coronary and carotid atherosclerotic plaques. The shoulder regions, which are frequently the location of plaque rupture, had fibres that were less aligned with the luminal tangent and had higher fibre dispersion. Coronary and carotid plaques generally had similar fibre structures to one another. Linear regression models were used to determine if fibre structure could be predicted from plaque geometry. Fibre structure was found to have weak coupling with some geometry parameters. Different geometry parameters were statistically significant predictors for the coronary plaques and the carotid plaques.

3.2 Introduction

In healthy arteries, the tissue forms concentric layers of fibres that are dispersed about a primary orientation or pitch angle, with alternating layers having opposed primary orientation or pitch angle [Clark and Glagov, 1985] (see Figure 1.3 and

Section 5.3.2). Atherosclerosis causes disruptions in this orderly arrangement, and the concentric condition is violated due to differences in thickness and composition through an artery cross-section [Creane et al., 2011; Gasser et al., 2006; Shekhonin et al., 1985].

Being a fibrous material, the mechanics of plaques are presumably governed by fibre structures, but the precise role of fibre structure has been relatively unstudied (as reviewed in Section 1.3). In Chapter 2, different regions of atherosclerotic plaques were observed in SEM images to have different fibre structures. This chapter details a quantitative study of fibre structures in atherosclerotic plaques.

Human carotid and coronary atherosclerotic plaques were studied using image processing techniques on histologically prepared artery cross-sections. The major goal was to quantify and compare the fibre microstructures in different plaque regions. As a first step, the local primary fibre orientation and dispersion about this orientation were used to describe fibre structure. Thus, fibre dispersion is analogous to the variance in fibre orientation.

Atherosclerotic progression is thought to result in increased dispersion in the fibre network [Creane et al., 2011; Shekhonin et al., 1985]. Fibre dispersion here will follow the definition used in the Gasser et al. [2006] constitutive material model for fibrous tissues.

Figure 3.1 outlines the work-flow of the image processing methodology that will be described in this chapter. Section 3.3 describes the selection, preparation, and geometries of the atherosclerotic plaques used in this study. The methodology for detecting fibres and for calculating fibre orientation and dispersion are presented, along with validation of these methods, in Section 3.4. Fibre orientation and dispersion results are provided in Section 3.5. To identify any dependence or coupling, linear regressions modelled the fibre microstructure results against plaque geometry, with results in Section 3.6. These results are discussed in Section 3.7, with a summary and conclusions of the study stated in Section 3.8. The geometry and fibre structure of these plaques were used to build finite element (FE) models, described in Chapter 4, and these statistical techniques were also used in Chapters 5 and 6.

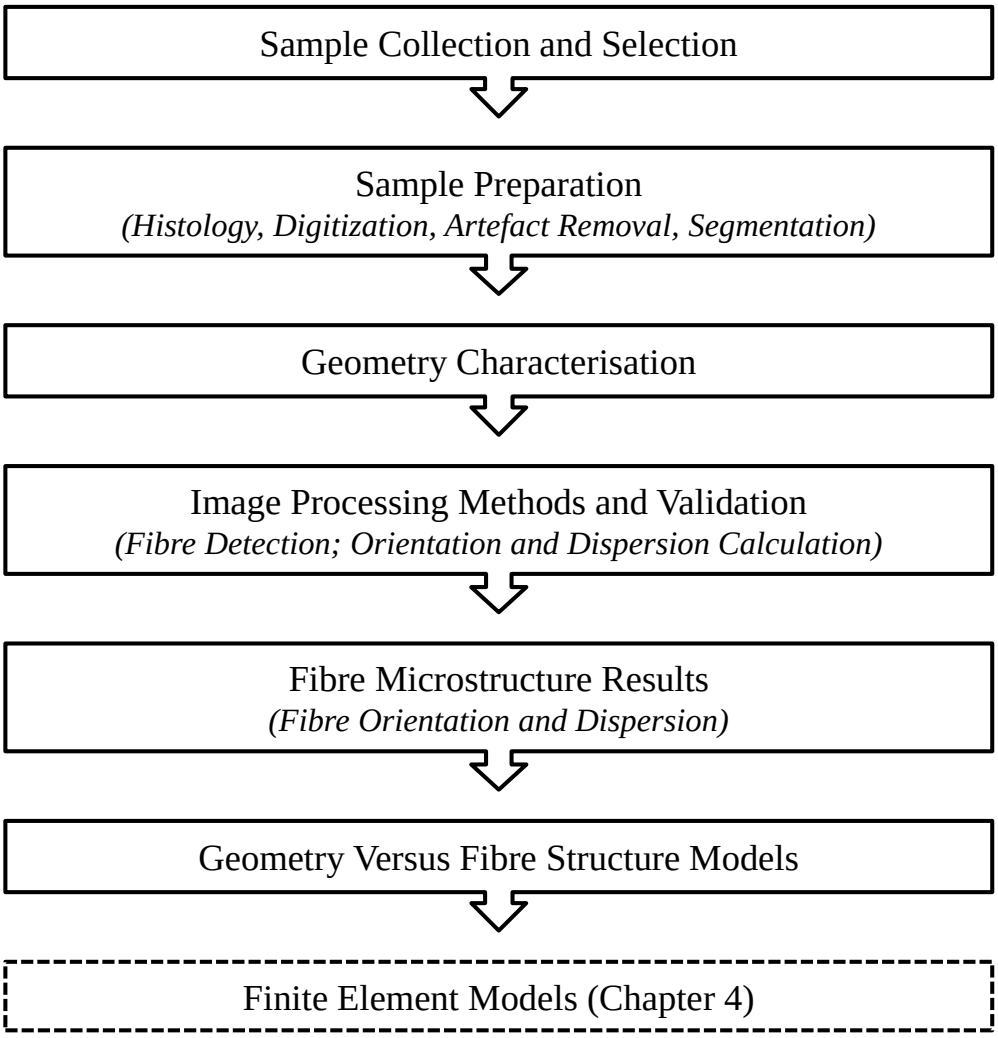

Figure 3.1: Chapter structure outline: main processes for characterising fibre microstructure in histologically prepared atherosclerotic plaques.

3.3 Preparation of Plaque Images

The selection and histological preparation of histology samples is detailed in Section 3.3.1. Digitised histology images were pre-processed and have artefacts repaired, as described in Section 3.3.2. Contours for boundary edges of the plaque were determined as detailed in Section 3.3.3. Section 3.3.4 explains the plaque regions and their segmentation. Key geometry parameters, as defined in Section 3.3.5, were calculated for each plaque.

3.3.1 Histological Sample Selection and Preparation

Sixteen coronary [Brown et al., 2015] and fifteen carotid histological samples were selected from larger sample sets prepared for previous studies. Ethics approval (Cambridgeshire Research and Ethics Committee Ref. 07/H0306/123) and consent from the patient or relatives was obtained as appropriate. Histological images with severe artefacts, such as large missing sections, severe geometry distortions, and large sections of folded tissue, were excluded. Refer to [Brown et al., 2015] for the detailed methodology used in preparing the histological samples. For convenience, a summary is included below.

Sample collection and histology staining was prepared by various colleagues in the Radiology and Cardiovascular Medicine Departments at Addenbrookes Hospital. Human left anterior descending coronary arteries were harvested during autopsy within 48 hours of non-coronary death, in consultation with a pathologist. The arteries, including about 40 mm of surrounding tissue, were dissected and placed immediately in a 4°C phosphate-buffered saline. Formalin (10%, buffered) was used to fix the arteries for at least 24 hours. Arteries were de-calcified with EDTA (ethylene diamine tetra-acetic acid) in preparation for histology. The samples were cut into 5 μm sections and stained with hematoxylineosin (H&E) and/ or Verhoeff's Van Gieson (EVG).

Human carotid atheromas were collected from tissue removed in carotid endarterectomy procedures. Being removed from the inside of patent vessels, these samples typically do not include the adventitia and deeper media of the original artery. They also have an artefact of at least one incision through the ring of the tissue into the lumen, created from the surgical removal of the atheroma.

The carotid samples were similarly stored in a formalin solution, sectioned, and stained with EVG or H&E. The differences between the samples should be highlighted. The coronary samples were from deceased donors who did not have symptomatic coronary artery disease. In contrast, the carotid samples were taken from carotid endarterectomy patients, the majority of whom would likely be have symptoms. None of the plaques of either type had ruptured, but all were considered by experienced pathologists to be plaques at risk of rupture.

While neither EVG nor H&E is specific to collagen, EVG better labels components of the tissue (red: collagen, black: elastin and cell nuclei, yellow: lipid). H&E is a general stain which has less specificity than EVG (pink: collagen, pale pink: elastin, cell nuclei: blue). To increase the number of samples, six carotid H&E stained slides were included in the image processing analysis, while all other samples used EVG. A study validated H&E for detect collagen fibres in atherosclerotic tissue (Section 3.4.8).

The resulting histology slides were digitised at 40× magnification with a Nanozoomer machine (Hamamatsu Photonics KK, Hamamatsu, Japan). Images were exported at a 1920×1200 pixel resolution.

3.3.2 Geometry Tracing and Damage Repair

A sample digitized image is shown in Figure 3.2A. Each digitised image was imported into GIMP (GIMP 2.8.14, GNU Image Manipulation Program, GIMP Development Team) to repair damage from the surgical extraction and artefacts from histological preparation (examples labelled in Figure 3.2B). While the majority of potential samples available for this study were rejected due to major artefacts, nearly all still had minor artefacts.

These artefacts were removed or reduced using functions in GIMP, with close attention limit modifications and to avoid modifying tissue without artefacts. The impact on subsequent image processing would have been greater from leaving artefacts than from these repairs. Repairs were done by deletion, local blending using the *Smudge Tool*, local deformation using GIMP's *Cage Transform Tool*, and/ or copying of adjacent regions.

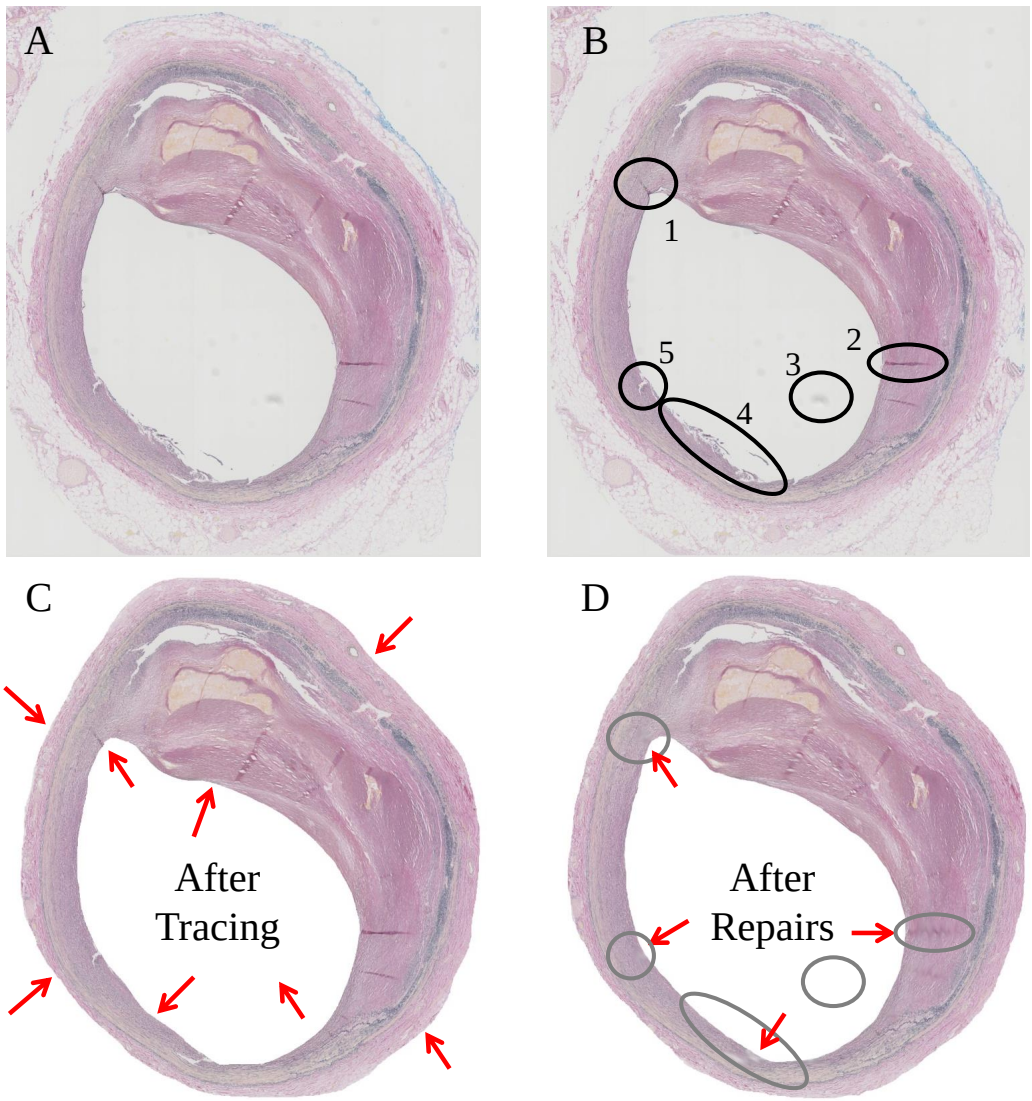

Figure 3.2: A.) A digitised EVG preparation of an atherosclerotic coronary artery, B.) Plaque from (A) with artefacts labelled (1: Distorted geometry and over-recoiled fibres, 2: Dark bands from folding, 3: Matter in the lumen, 4: Separation of tissue at an edge, and 5: Gaps or tears in tissue), C.) Plaque with lumen and outer edge contours traced to define plaque from background (emphasised by red arrows), and D.) Sample image after repair of artefacts from (B) (changes emphasised by red arrows).

In general, the artefacts were less frequent in critical regions like the fibrous cap or shoulders, and increased attention was paid to any modifications made in these zones (see Figure 3.2C and D).

Lumen and Outer Edge Tracing

The background of the image of the plaque was removed by manually tracing the lumen and outer edge of the specimen. Edges were traced to be smooth and locally parallel to fibres, as the lumen and boundaries between artery layers would have been *in vivo*. Chopped fibres could result in unrealistic fibre geometry and sharp corners could be stress concentrations in subsequent FE analysis (Chapter 4). The trace of the lumen removed tissue fully or mostly torn from the main plaque (see the lower lumen in Figure 3.2A and B). Pieces that were less torn were usually preserved to avoid excessive thinning of the plaque. Small folds or waves in the tissue, as shown in Figure 3.2B-1, were traced parallel to fibres deep to the fold, which were probably due to recoil without lumen pressure.

Coronary plaques were surrounded by differing amounts of connective and cardiac tissue, so were traced around the adventitia for consistency (i.e. material removed outside the plaque between Figure 3.2B and C). Carotid plaques were traced around the media. For the FE analysis (Chapter 4), a section was added to the carotid plaques to represent the adventitia.

Specific Image Repair Techniques

In general, fold and similar artefacts, such as the dark lines perpendicular to the lumen in Figure 3.2B-1 and -2, were mended by local blending. These dark lines would be detected as fibres in subsequent operations and would lead to errors in fibre structure calculations. Care was taken to minimise distortions caused by blending, and the results would be more affected if the artefacts were not repaired. The resulting image of the illustrative plaque is shown in Figure 3.2D.

Larger artefacts were mended where possible by local deformation. For this, the region to deform was selected. The boundary of the region can then be deformed to the desired shape, and the region was deformed (while minimizing local enlargements) to match the new edge positions. Figure 3.3A shows a plaque

with the adventitia delaminating from the media. A repair by local deformation (Figure 3.3B) returned the tissue thickness and fibre structure to their *in vivo* states. Similarly, the lower region of the plaque in Figure 3.3C was distorted inwards, causing an unrealistically tight luminal surface at the shoulders. Local deformation corrected local convexity from lack of lumen pressure (Figure 3.3D).

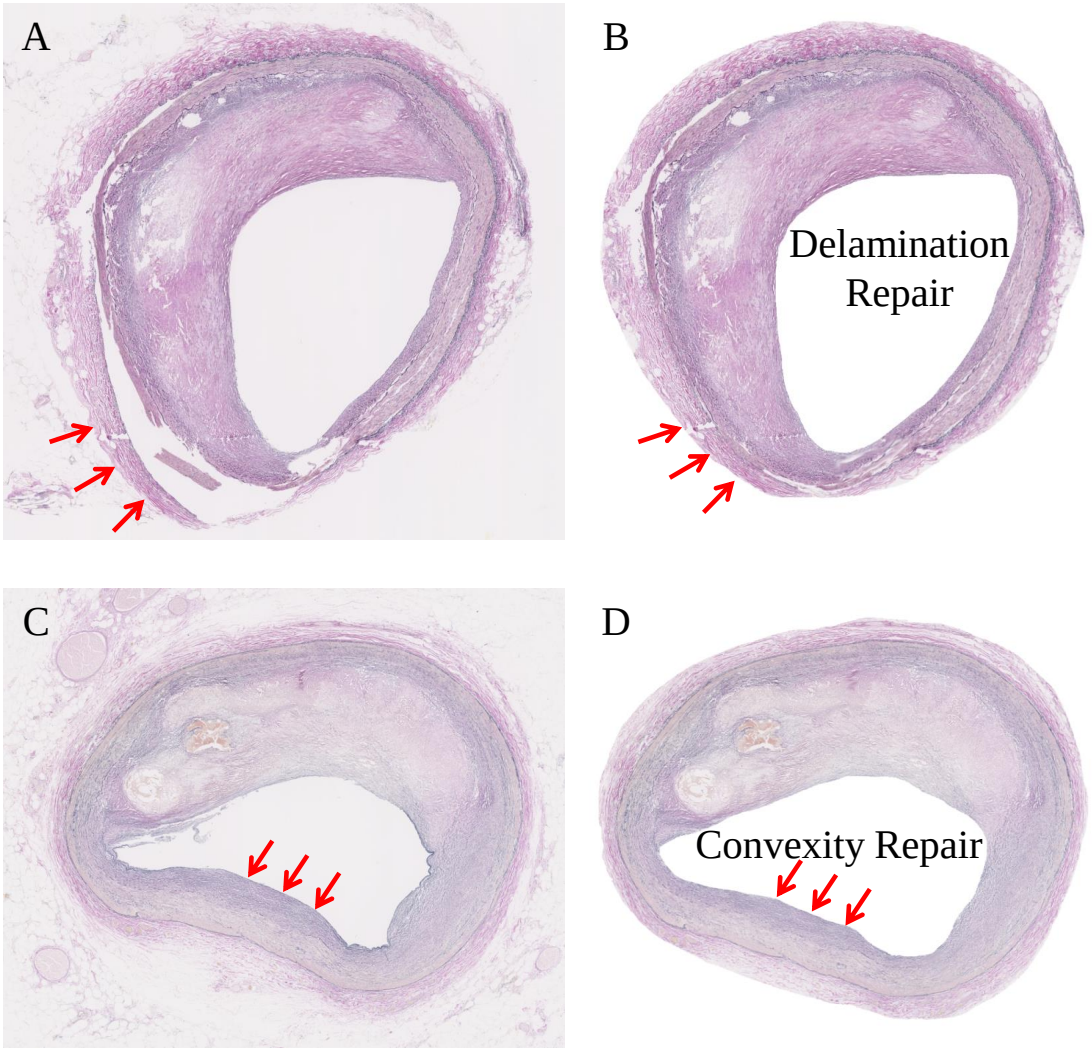

Figure 3.3: A.) A coronary plaque with a delaminating adventitia (emphasised by red arrows), B.) Repair of this adventitia, C.) Convexity in lower half of a coronary plaque (emphasised by red arrows), and D.) Repair of convexity.

Artefacts that could not be repaired by other methods were repaired by copying adjacent tissues into the affected zones. Repair by copying adjacent tissues was most frequently used when a portion of the lipid core missing.

Often, repairs by local deformation or copying adjacent regions caused an artefact at the repair boundary, which were reduced by local blending. Images were inspected at repair sites for irregularities at subsequent processing steps.

3.3.3 Extracting Plaque Boundaries

After background removal and any artefact repairs, the image was imported to Matlab (MATLAB 2016a, The MathWorks, Inc, Nantick, MA, USA) for subsequent analysis of geometry and fibre properties. A mask was made to separate the plaque region from the image background, using the manual traces of the lumen and outer edges.

For each plaque, height (vessel diameter within the external elastic lamella (EEL) in the vertical dimension of image) was measured in pixels (Matlab) and in millimetres (Nanozoomer). The conversion factor between the unit systems was calculated. Here, height refers to the diameter in this direction, as the vessel were often not perfectly circular.

Pixels were spaced at approximately 4 μm for coronary and 8 μm for carotid plaques. Geometry parameters (see Section 3.3.5) and FE models (in Chapter 4) were defined in millimeters. Image processing used pixel coordinates.

Pixels on the outer and luminal edges of the plaque $p(x, y)$ were obtained from the manual geometry trace (see Section 3.3.2) and ordered into a contour for each edge. Thus, each pixel on an edge became a point in a contour. To remove sharp corners in the plaque geometry, Matlab's *lowess* smoothing filter (weighted linear regression) [Cleveland, 1979] with a span of 25 points ($-12<i<12$) was applied to each contour. Span length was selected based on the length of true features on the plaque (about 100 μm or larger) and the spacing between pixels. Equation 3.1 calculates the regression weights for each point in the span of the filter, w_i. Dummy points were duplicated from the end of the contour vector to

its start (and the reverse), to allow for the span of the filter to wrap the contour.

$$w_i = \left(1 - \left|\frac{p(x,y) - p(x,y)_i}{d(p(x,y))}\right|^3\right)^3 \tag{3.1}$$

These regression weights were used to preform a weighted, linear least-squares regression using a first degree polynomial. The weighting favours points nearer to the point being filtered. Sample plaque contours are shown in Figure 3.4C.

For carotid plaque samples, the outer contours were dilated 20% to account for the adventitia and media remaining in the body after CEA. This dilation was chosen as the adventitia made about 20% of the radii of coronary plaques. The dilated region was not considered for fibre structure analysis, but was used for FE models (Chapter 4).

The geometry contours were down-sampled to every 20^{th} point to allow faster pre-processing in the FE models. The geometry contours of a sample plaque are shown in Figure 3.4C: blue is the lumen, black is lipid, and red is the outer edge.

3.3.4 Segmented Plaque Regions

Regions of fibrous cap (FC), intimal thickening (IT), shoulders, and lipid core were manually segmented by selecting points along the regions' boundary (see Figure 3.4A), guided by the advice of a histologist. While some plaques had complex geometry, they were assumed for region segmentation to have one FC, one IT, two shoulders, and one lipid core to allow easier comparison between plaques. A global region (all tissue in Figure 3.4B) and a global excluding lipid core region (GEX; media and adventitia in Figure 3.4B) were also considered. Segmented regions were used as masks to calculate fibre properties and mechanical characteristics within a region and for comparison between regions. The boundary of the lipid core was extracted as a contour to be used with the outer and lumen contours in making FE models (Chapter 4).

3.3.5 Geometry Characterisation of Plaques

Mechanics are known to be affected by geometry in atherosclerotic plaques [Calvert et al., 2011; Cheng et al., 1993; Loree et al., 1992; Richardson et al., 1989; Stone

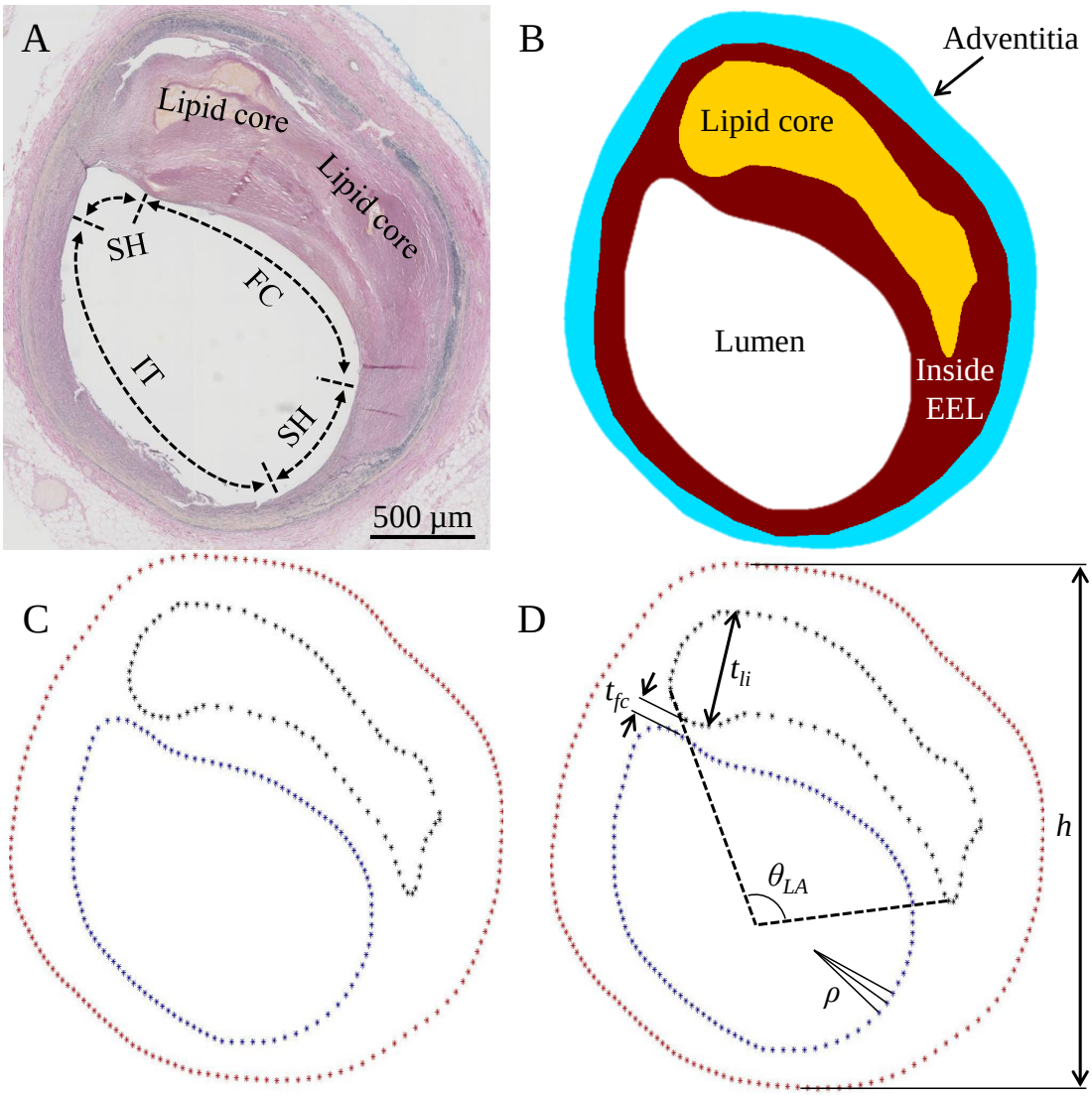

Figure 3.4: A.) Illustrative coronary atheroma with segmented regions labelled, B.) Labelled areas for geometry characterisation (EEL: external elastic lamella), C.) Geometry contours for the lumen, lipid, and outer edge, and D.) Key geometry parameters and how they were calculated.

et al., 2011; Teng, 2011]. Plaques with thin fibrous caps, large lipid cores, tighter shoulder curvature, and more narrowing are thought to be at higher risk of rupture and clinical events. This section defines and characterises the geometry of the plaques studied by image processing (this chapter) and FE analysis (Chapter 4).

Geometrical parameters were selected due to clinical findings of risk associated with the geometry type, expected changes to fibre properties, or expected changes to mechanics from the parameter [Calvert et al., 2011; Cheng et al., 1993; Loree et al., 1992; Richardson et al., 1989; Stone et al., 2011; Teng, 2011]. Parameters are reported for each plaque in the study, with summaries by plaque type. Geometry of coronary and carotid plaques was compared to identify features that had similar sizes for both plaque types or that scaled with plaque size. Since carotid arteries are considerably larger than the coronary, measurements that are scaled or normalised to vessel size may give better comparisons. If features are found to be similar between the coronary and carotid plaques, it would be justified to combine the two into a larger sample set for statistical analysis.

The following parameters were considered:

- Plaque area (A_{pl}, [mm^2])
- Lumen area (A_{lu}, [mm^2])
- Plaque burden ($\%_{pb}$, [%])
- Lipid area (A_{li}, [mm^2])
- Lipid fraction ($\%_{li}$, [%])
- Lipid thickness (t_{li}, [mm])
- Lipid arc (θ_{li}, [°])
- Fibrous cap thickness (t_{fc}, [mm])
- Shoulder radius of curvature (ρ, [mm])
- Normalised shoulder radius of curvature (ρ_{norm}, unitless)

Geometry parameters of the plaques are provided in Table 3.1, detailing the mean values for the carotid, coronary, and combined sets of plaques. The coronary and carotid plaques were compared using a two-sample t-test for each geometric parameter. There was considerable variability between plaques of the same type (carotid or coronary); the highest value of a geometry parameter was often several times the lowest value.

Parameter	All Plaques	Carotid	Coronary	p-value
A_{pl} (mm^2)	15.4	25.9	5.57	$<$ **0.001**
A_{lu} (mm^2)	9.43	16.1	3.19	$<$ **0.001**
$\%_{pb}$ (%)	63.7	64.6	62.8	0.714
A_{li} (mm^2)	4.63	7.75	1.70	$<$ **0.001**
$\%_{li}$ (%)	28.5	29.6	27.5	0.598
t_{li} (mm)	1.07	1.45	0.710	$<$ **0.001**
θ_{li} (°)	151	164	139	0.381
t_{fc} (mm)	0.242	0.316	0.173	**0.001**
ρ (mm)	1.15	1.83	0.508	$<$ **0.001**
ρ_{norm}	0.237	0.339	0.141	**0.031**

Table 3.1: Summary of geometry measurements for the plaque samples. The All Plaques column is for a combined set of carotid and coronary plaques together. The p-value is from a two-sample t-test comparing carotid against coronary.

Plaque Area

The plaque area (A_{pl}) was the tissue within the external elastic lamella (EEL), which is the purple ring between the media and adventitia in Figure 3.4A. It is the combined area of the intima, media, and lipid core (red, yellow, and lumen in Figure 3.4B). To calculate A_{pl}, the number of pixels in the image of the region were counted, then converted to mm^2. Carotid plaques had a considerably larger A_{pl} than the coronary plaques (mean of 25.9 mm^2 vs 5.57 mm^2, p<0.001).

Lumen Area

Like A_{pl}, the lumen area (A_{lu}) was calculated from each plaque's image and converted to mm^2 (see Figure 3.4B). Carotid plaques had a larger A_{lu} than coronary (mean of 16.1 mm^2 vs 3.19 mm^2, p<0.001).

Plaque Burden

Plaque burden ($\%_{pb}$) is a non-dimensional measure describing the ratio of A_{pl} to the combined area within the EEL (A_{pl} and A_{lu}; see Equation 3.2).

$$\%_{pb} = \frac{A_{pl}}{A_{pl} + A_{lu}}(100\%) \tag{3.2}$$

Higher values suggest further progression of the disease. Plaque burden is an important clinical metric, with higher $\%_{pb}$ being implicated in rupture and clinical events [Calvert et al., 2011; Störk et al., 2004]. Clinically, $\%_{pb}$ is typically measured by imaging as a percentage of remaining lumen relative to expected lumen if the tissue was healthy. In clinical and research, $\%_{pb}$ is usually presented into banded categories (example: low 0-30%, moderate 31-69%, high >70%). Here, the lumen was not pressurised, which will result in a smaller A_{lu} and over-estimating the $\%_{pb}$.

Plaque burden was not significantly different for carotid and coronary plaques (mean of 64.6% vs 62.8%, p=0.714). The set of plaques studied here would mostly be classified as having moderate or high $\%_{pb}$ (relative to the clinical bands listed above). While higher $\%_{pb}$ is known to be a greater clinical risk, moderately occluded plaques are far more frequent and therefore result in the majority of cardiovascular events [Alderman et al., 1993]. All plaques in this study had a $\%_{pb}$ of at least 35%, so are representative of plaques that may be at risk of rupture. At present, risk stratification between plaques with moderate narrowing is limited, and is a key goal of this research. The A_{pl} and A_{lu} were different for each plaque type, but $\%_{pb}$ was similar, suggesting scalability to vessel size.

Lipid Area

The lipid area (A_{li}) was measured from the segmented lipid region of each plaque image, and converted to mm^2 (yellow area in Figure 3.4B). Carotid plaques also had a larger A_{li} compared to coronary (mean of 7.75 mm^2 vs 1.70 mm^2, p<0.001).

Lipid Fraction

Lipid fraction ($\%_{li}$) was the proportion of A_{li} relative to the combined area within the EEL (A_{pl} and A_{lu}; see Equation 3.3).

$$\%_{li} = \frac{A_{li}}{A_{pl} + A_{lu}}(100\%) \tag{3.3}$$

Like plaque burden, $\%_{li}$ was similar for the carotid and coronary plaques (mean of 29.6% vs 27.5%, p=0.598), so suggested geometric scalability between the two plaque types. The mean $\%_{li}$ was less than half the mean $\%_{pb}$; fibrous tissue contributed more to narrowing than lipid volume. Clinical reports have noted that >70% of plaque volume is fibrous tissue [Falk et al., 1995].

Lipid Thickness

Lipid thickness (t_{li}) was measured in each image as the maximum distance across the lipid in a direction away from the lumen (see Figure 3.4D). Lipid thickness is related to $\%_{li}$ and A_{li}, but further describes a lipid core's shape. The t_{li} was thicker in carotid plaques compared to coronary (mean of 1.45 mm vs 0.710 mm, p<0.001).

Lipid Arc

Lipid arc (θ_{li}) was the angle the lipid core occupies relative to the centre of the lumen (see Figure 3.4D). The widest points of the lipid core were selected manually and the centre of the lumen was calculated as the area centroid of the lumen. Lipid arc is also a measure of fibrous cap length. The θ_{li} is found through Equation 3.4, where a and b are the vectors from the lumen centre to the two widest points of the lipid.

$$\theta_{li} = \text{atan}\left(\frac{|a \times b|}{a \cdot b}\right) \tag{3.4}$$

The mean θ_{li} was similar for carotid and coronary plaques (mean of 164° vs 139°, p=0.381). Few lipid regions extended beyond half the circumference.

Fibrous Cap Thickness

Minimum fibrous cap (FC) thickness (t_{fc}) was manually measured for each plaque (see Figure 3.4D). Thin FC, particularly in conjunction with larger lipid deposits, are known to be higher risk plaques [Falk et al., 1995].

The minimum t_{fc} was significantly thinner for coronary plaques than carotid (mean of 0.173 mm vs 0.316 mm, p=0.001). In some plaques, fibrous cap thickness varied by location, which may play a role in fibre distribution and mechanics. In particular, a thin FC near the shoulders may be subjected to higher stresses, while a thin centre of the FC may be vulnerable to erosion.

Shoulder Radius of Curvature

The radius of curvature (ρ) is reported for the lumen for both shoulder regions (see Figure 3.4D). As three adjacent points define a circle, ρ was calculated for each point on the lumen contour using that point and one point to either side. The radius of the circle is ρ, solved using the coordinates of the three points.

For each shoulder, points on the lumen contour closest to the segmented shoulder were selected, and their corresponding ρ was used to calculate the median ρ for the shoulder. The median was chosen as it is a general description of the region, reducing influence of localised values and convex curvature.

The coronary plaques had a tighter ρ than carotid (0.508 mm vs 1.83 mm, p<0.001). The tightness of ρ could change fibre architecture. Assuming fibres are tangent to the lumen, lipid core, and external elastic lamella, fibre geometry would be defined by ρ, t_{fc} and the shape of the lipid core. Sharp changes to geometry, as measured at the shoulders by ρ, are also known stress concentrations.

Normalised Shoulder Radius of Curvature

To investigate if ρ was coupled to overall vessel size, it was normalised against the external elastic lamella diameter of the respective plaques (ρ_{norm}) measured vertically in a plaque image. In particular, this parameter would be useful in determining if ρ was dependent on difference in size between the coronary and the carotid plaques.

For ρ_{norm}, there was still a significant difference in curvature between the coronary and carotid plaques (0.141 vs 0.339, p=0.031). While the coronary plaques had a lower ρ_{norm} compared to carotid, the difference between the plaque types was less than for ρ, which was not scaled for plaque size.

3.4 Image Processing Methodology

Several methods of quantifying local fibre direction were considered. Many existing methods involve calculating directional gradients, using a fast Fourier transform, or similar techniques to find directional rates of change in an image [Püspöki et al., 2016; Rezakhaniha et al., 2012; Schriefl, 2013; Schriefl et al., 2012b]. Images of arterial atherosclerosis have spatially-varying fibre arrangements as well as multiple types of material comprising the tissue.

The strategy used in this study was to first identify fibres through edge detection, which acts similar to a gradient-based orientation calculation. Orientation of identified fibres was then calculated as the major axis of an identified fibre's second moment of area. By isolating a fibre before calculating its orientation, texture in the image that is adjacent to but not connected with the fibre does not affect its calculated orientation. Since fibres in the histology images are as viewed in the 2D cross-sectional slice of tissue, orientation is only considered in this plane. These fibres refer to the sheet-like arrangements sketched in Figures 1.3 and 5.3.

3.4.1 Identifying Fibres by Edge Detection

To identify fibres, several edge detection filters were compared. Detected fibre-edges should have features similar to fibres in the histology images (example: Figure 3.3D). For example, a well performing edge detection filter should find a relatively high density of fibres in the fibrous region, with fewer fibres in the lipid core and as few fibres as possible in the background of the image. Detected fibres should be relatively long and slender, with a similar size and spacing in histology images. Fibres should be nominally aligned with the luminal tangent.

The following edge detection filters were considered: Canny, Sobel, Prewitt, Roberts, and Laplacian of Gaussian. The Canny method finds edges by searching

the gradient of the input image for local maxima. It applies a threshold for each set of 'strong' edges and 'weak' edges; the weak edges are only accepted if adjacent to a strong edge. The Sobel, Prewitt, and Roberts methods use their respective approximations of the derivative of the image to calculate the gradient of the image. Edges are pixels above a single gradient threshold. The Laplacian method applies a Laplacian transform to a Gaussian filtered image. Edges are zero-crossings in the Laplacian filtered image.

The default input parameters were tried first for each filter. The input parameters of promising filters were then adjusted to try to improve precision in detecting fibres. Generally, changing input parameters made only small changes to the performance of a given filter.

Results of Different Edge Detectors

Plots of fibres detected in the illustrative plaque (Figure 3.2D) by each of the edge detection filters are shown in Figure 3.5. To better display edge features, plots are magnified and centred at the upper left of the plaque (see Figure 3.5A).

The Canny filter had a high density of edges detected in the fibrous region, but less difference in edge density for the lipid core compared to some other methods (Figure 3.5B). Edges detected by the Canny filter were more connected, slender, and evenly spaced than any of the other methods.

The Sobel and Prewitt filters (Figure 3.5C and D) had a lower density of edges detected, but a greater difference in edge density between the fibrous regions and the lipid core. However, these filters produced edges that were not connected to one another and were inconsistently spaced.

The lowest density of edges was detected using the Roberts filter, but it showed stronger differences between fibrous and lipid regions (Figure 3.5D). This filter produced edges that were short, disconnected, and unevenly spaced.

Similar to the Canny filter, the Laplacian method detected a high density of fibres in both the fibrous region and the lipid core (Figure 3.5F). However, the edges it detected were less evenly spaced and were interconnected laterally, which would cause challenges in calculating fibre orientation.

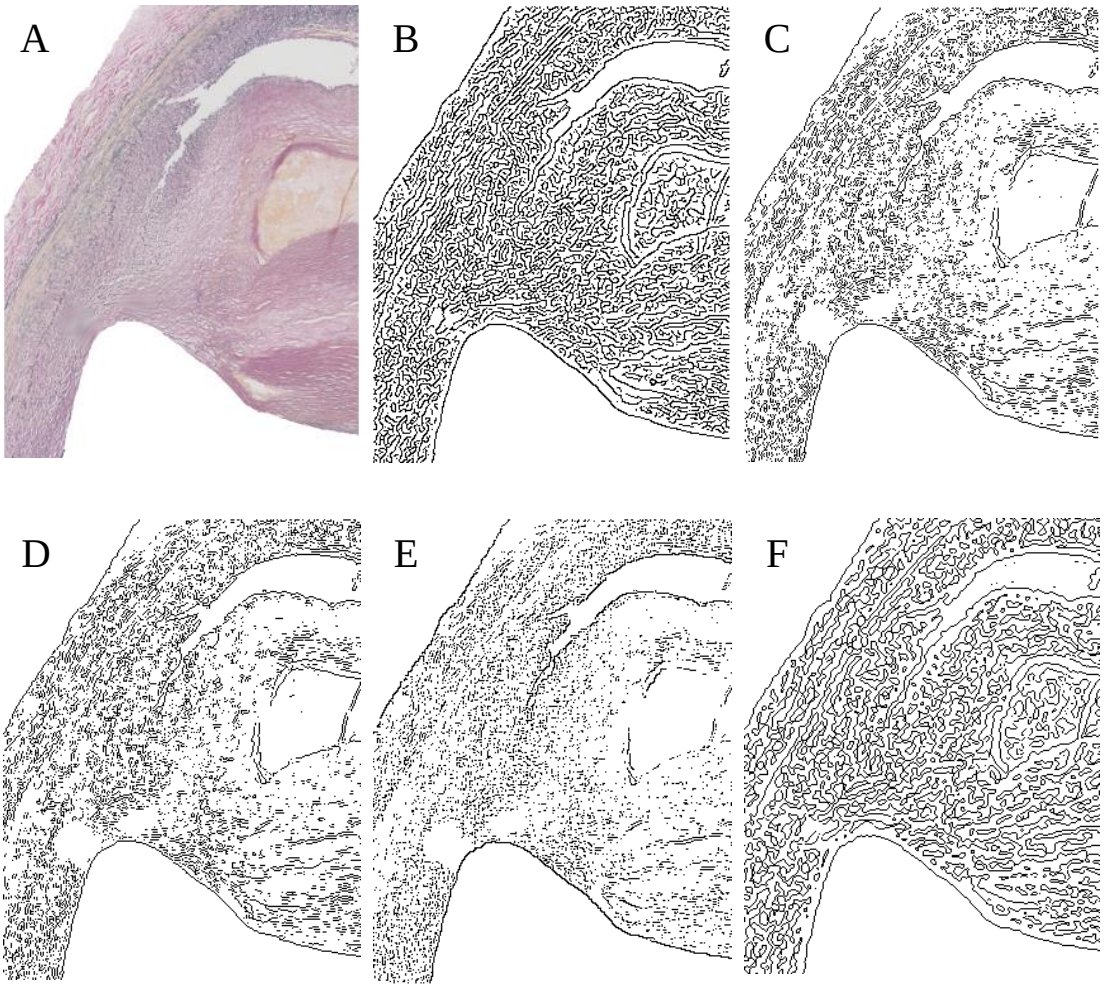

Figure 3.5: Detected edge-fibres for different edge detection methods available in Matlab, shown at magnification at A.) The upper-left of the illustrative plaque. The results of each filter are shown for: B.) Canny, C.) Sobel, D.) Prewitt, E.) Roberts, and F.) Laplacian of Gaussian. A better performing edge detector should have a high density of fibres in the fibrous regions, a lower density of fibres in the lipid core, and slender well-connected fibres.

Therefore, the Canny edge detection filter was selected as the best method to identify fibres, and will be further described and validated later in this chapter. The major shortcoming of this filter was over-detection of fibres in the lipid core. While there are true fibres in the lipid core, fibre structure results will be reported for a global region and a global excluding lipid core (GEX) region.

3.4.2 Fibre Detection by the Canny Method

Collagen fibres, having strong contrast against the background, were assumed to be indicated by edges in the image. The Canny edge-detect method [Canny, 1983] was used to identify these fibres, according to the Matlab *p* implementation of the algorithm. Key details of this method will be outlined.

Gaussian Blurring

As the Canny edge detector identifies edges as high gradients in the image, noise must be filtered to prevent it being predicted as an edge. A 1-D Gaussian kernel, H, was applied independently in both directions of the image to create a smoothed image (see Equation 3.5).

$$H = \frac{1}{\sqrt{2\pi}\sigma_G^2} \exp\left(-\frac{k^2}{2\sigma_G^2}\right) \tag{3.5}$$

The smoothed image was then convoluted with a kernel of the gradient of H.

The values used in this function were informed by the diameter of fibres in the image (approximately 10-25 μm), pixel size (approximately 4 μm for coronary and 8 μm for carotid), and representative pixel values (approximate RGB pixel values for fibres: [200, 180, 190], and between fibres: [175, 140, 170]). A Gaussian filter is a bell-shaped weighting function, where standard deviation (here, σ_G=$\sqrt{2}$ pixels) defines the width of the bell. This is a typical value for a Canny filter, and preserves features of the fibres. The bell shape is limited to the span of the filter (k, here: -5 to $+5$ pixels). Different values of σ_G and k were tried, with the reported values giving the best results.

Edges From Image Gradients

The gradient of the filtered image were calculated in both directions (G_x and G_y). The magnitude of gradient (G) at each pixel was calculated by Equation 3.6:

$$G = \sqrt{{G_x}^2 + {G_y}^2} \tag{3.6}$$

Two thresholds were used to set values of intensity gradient to be edges: high (strong edges) and low (weak edges). The high-threshold was selected as the gradient value such that 30% of pixels in the image were strong-edges. This is a relatively high number, but necessary because most of the tissue is thin fibres. The low-threshold was set at 40% of the high-threshold value. Pixels above the low-threshold and adjacent to a high-threshold edge were also considered edges. This method acted to connect edge segments detected by the first threshold. These longer, connected edges were more representative of the true fibres.

Connected pixels of these edges (assumed to each indicate an individual fibre) were found using the *regionprops* algorithm in Matlab, grouping adjacently and diagonally connected pixels (8-connectivity). Connected edges larger than 500 pixels were partitioned into several smaller features by overlaying a 75×75 grid, which removed the pixels from the fibres/ edges intersecting with the grid. Since a large connected edge was assumed to indicate only one fibre, partitioning allowed fibre structure to be calculated more locally. Fibre-features containing fewer than ten connected pixels were removed, as they were too small to give reliable indication of fibre structure.

Validation of Detected Fibres

Fibres detected by the Canny method in the illustrative plaque (Figure 3.6A) are shown in Figure 3.6B. The coloured squares in the illustrative plaque correspond to the magnified (10×) images and corresponding detected edges with the same colour (Figure 3.6C-F). The magnified images were re-acquired at a higher resolution in Nanozoomer, as this study was intended to study the largest scale features in the hierarchy of fibre structure. However, the Canny algorithm uses Gaussian blurring, so the processed results are much less affected by the image resolution than these pixelated images would imply.

Figure 3.6C shows a shoulder region with high dispersion (spread of fibre orientation), both in the magnified histology and detected fibre images. The selected region is at the boundary between fibres running behind the lipid core and to the fibrous cap. Detected fibres in this IT region have slightly less dispersion, and are primarily oriented vertically (Figure 3.6D). In the enlarged images with dispersed fibres, the texture is not coherent and it is difficult to match structures in the paired images. These fibrous cap regions (Figure 3.6E and F) had lower dispersion and a more apparent primary fibre fibre orientation.

These magnified zones were selected to provide a wide range of fibre dispersion and orientation values, but are not necessarily representative of their plaque region type. The same magnified images will also be used in validation of the methods to calculate fibre orientation and dispersion later in this chapter. Most fibres had a lower dispersion and texture similar to the magnified regions in Figure 3.6E and F. Therefore, the fibre detection methods were validated as being able to identify fibre structures in the histology images used in this project.

3.4.3 Cartesian Fibre Orientation

Orientation of each fibre was calculated by the *regionprops orientation* algorithm in Matlab [Haralick and Shapiro, 1992]. This method calculates the second moments of area for each fibre-feature (I_{xx}, I_{yy}, and I_{xy}) and θ_{fibre}, the Cartesian angle of the major axis relative to the horizontal. If I_{xx} is less than I_{yy}, the orientation angle can be calculated as in Equation 3.7. For the opposite case, the numerator and denominator of the arctangent are reversed.

$$\theta_{fibre} = \text{atan}\left(\frac{|I_{xx} - I_{yy}| + \sqrt{|I_{xx} - I_{yy}|^2 + 4I_{xy}^2}}{2I_{xy}}\right); \theta_{fibre} \in [-90°, 90°] \quad (3.7)$$

To avoid ambiguity in describing a fibre's orientation, orientation values were checked to ensure they remain in the range $[-90°, 90°]$. If a fibre's orientation fell outside the range, it was replaced by the equivalent orientation in the opposite direction (example: $100° \equiv -80\,°$). Avoiding directional ambiguity was important for subsequent steps in evaluating the fibre structure.

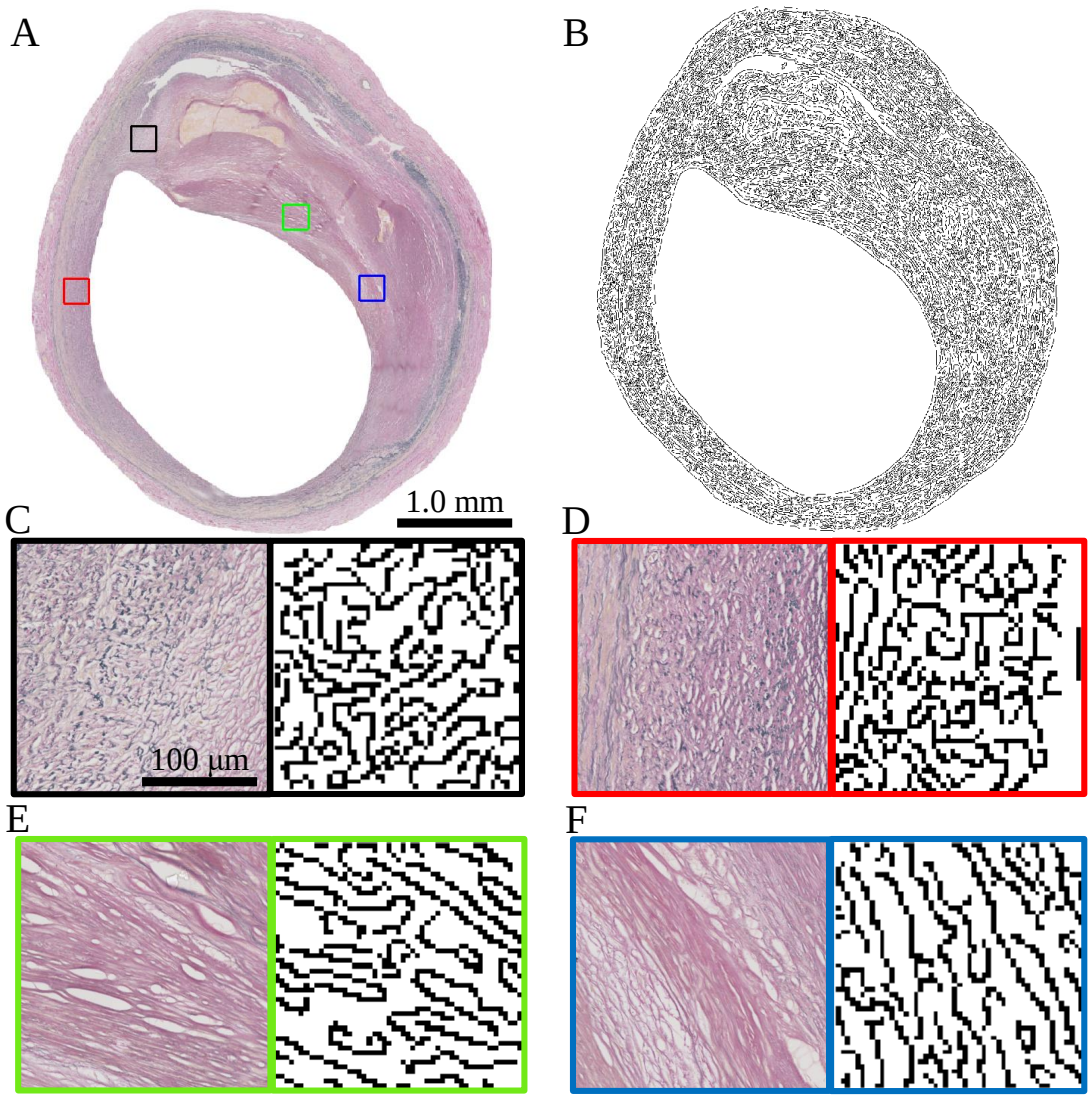

Figure 3.6: A.) Histology image of illustrative plaque indicating colour-coded regions of enlargement, B.) Fibres detected in illustrative plaque using the Canny method, C.) Enlargement of shoulder region of histology image and detected fibres, D.) Enlargement of IT region of histology image and detected fibres, E.) Enlargement of fibrous cap region of histology image and detected fibres, and F.) Enlargement of another fibrous cap region and detected fibres.

A fibre's orientation was assigned to each pixel constituting that fibre. For the illustrative plaque (see Figure 3.7A), the pixel orientations relative to the horizontal are indicated by colour in Figure 3.7B. In general, the orientation of fibres are nominally tangent to the lumen in both the histology image and calculated orientations.

For further validation, regions selected by coloured squares in Figure 3.7A are magnified approximately 10× and plotted alongside orientation for detected fibres in Figure 3.7C-F. The lines representing fibre orientation are centred on their corresponding fibre that was detected in the histology image (see Figure 3.6 for the detected fibres). Calculated fibre orientation is indicated by the angle of the plotted line. To emphasise larger fibres, plotted line lengths correspond to the square root of the number of pixels detected for the fibre.

The shoulder region (in Figure 3.7C) had a very high dispersion (also see Figure 3.10C). Therefore, neither the magnified histology image nor the synthetic plots had a primary fibre orientation.

The IT region (Figure 3.7D) had high dispersion, but fibres were coherent enough to show a primarily vertical orientation in the paired images. Fibres were less dispersed in the fibrous cap region (Figure 3.7E and F), where a match between fibre orientation in the paired images can be seen. Therefore, the orientation of detected fibres was successfully determined. Since the synthetic fibres are generated from the detected fibres, the synthetic plots also suggest the degree of fibre dispersion.

3.4.4 Local Mean Fibre Orientation

Local mean fibre orientation (θ_μ) was calculated for each pixel in the sample's mask, and describes the orientation of the local material rather than of individual fibres. The primary purpose was to fill small gaps between detected fibres, such as those from fibre waviness or recoil without lumen pressure, with an assumed orientation. Secondly, the local mean serves to filter or smooth the orientation calculated for individual fibres.

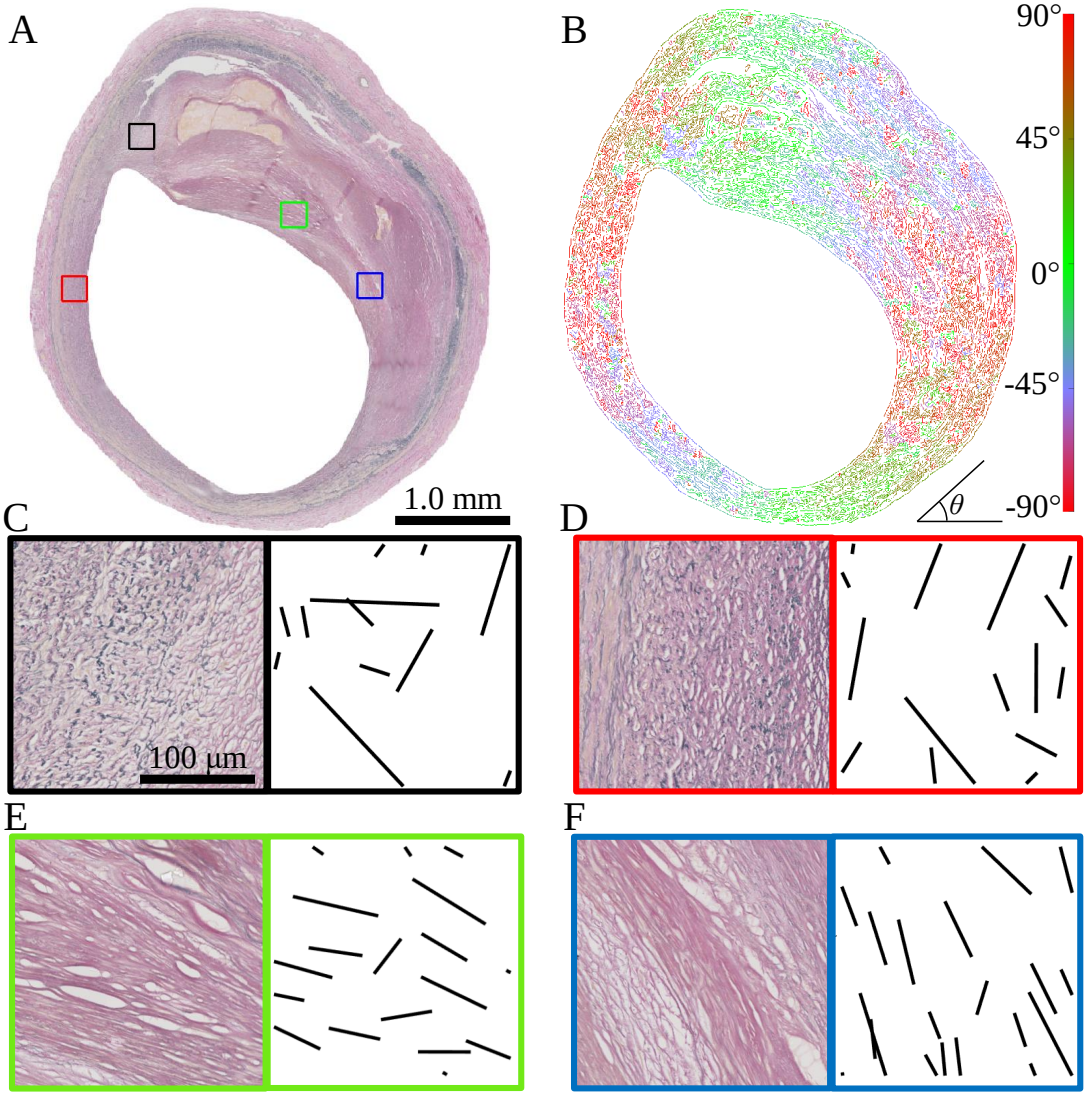

Figure 3.7: A.) Histological image of illustrative plaque indicating enlargements (C)-(F), B.) Detected fibres in illustrative plaque, coloured by calculated orientation relative to horizontal, C.) Enlargement of shoulder region of (A), paired with a plot of synthetic fibres each have the orientation of a detected fibre at the same location in the histological image, D.) Enlargement of IT region of (A), paired with a plot of similar synthetic fibres, E.) Enlargement of fibrous cap region of (A), paired with a plot of similar synthetic fibres, and F.) Enlargement of another fibrous cap region of (A), paired with a plot of similar synthetic fibres.

For each pixel in a plaque, the circular mean was calculated for the orientation of detected fibres within a 51×51 pixel ROI, as in Equation 3.8. A circular mean, rather than a standard mean, is required because fibre orientation is π-periodic or bi-directional (for example: 0°≡180° and +90°≡ −90°).

$$\theta_\mu = \frac{1}{2}\text{atan}\left(\frac{\langle\sin(2\theta_{fibre})\rangle}{\langle\cos(2\theta_{fibre})\rangle}\right); \theta_\mu \in [-90, 90] \tag{3.8}$$

The local mean fibre orientation of the illustrative plaque is shown in Figure 3.8A. Here, fibres running horizontally had an orientation of 0°, and +90° and −90° are equivalent and vertical.

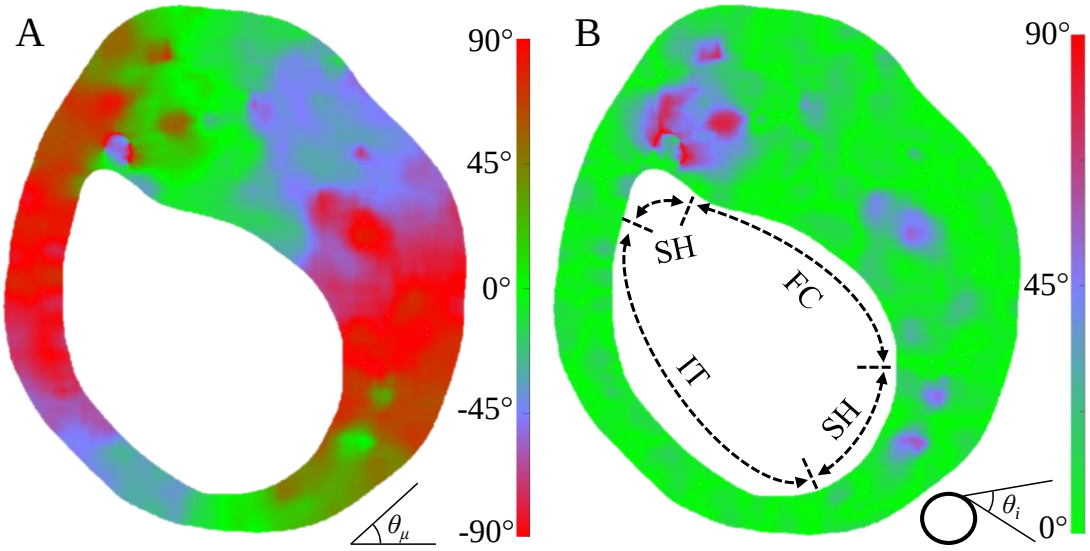

Figure 3.8: A.) Local mean fibre orientation (relative to horizontal) for the illustrative coronary plaque and B.) Fibre orientation referenced to the contour of the lumen and outer edge of the plaque, or local fibre misalignment from its expected orientation of being tangent to the lumen.

Validation Against Generated Fibre Structures

To validate the complete method of detecting fibres and calculating the orientation of these fibres, synthetic fibres were generated at known angles on the illustrative plaque's geometry mask. The synthetic fibres were made by assigning pixel intensities (I) according to the 2D periodic function in Equation 3.9:

$$I = I_{fibres} + \sin(\omega[i\cos(\theta_{target}) + j\sin(\theta_{target})](I_{fibres} - I_{base}) \tag{3.9}$$

where the periodicity of fibres (ω) was $\frac{2\pi}{6}$, so the wavelength of fibres was six pixels (about 30 μm, similar to the diameter and spacing of true fibres). Synthetic pixel intensity values were set to be similar to those in the histology images for fibres (I_{fibres}: [200, 180, 190]) and between fibres (I_{base}: [175, 140, 170]).

Fibres were generated at target angles (θ_{target}) of 0°, 45°, 90°, −30°, −45°, and −60°. These angles were selected to be representative of a range of possible values, and distinguish between positive and negative.

Magnified images of the upper-left shoulder regions of the plaques with generated fibres are shown in Figure 3.9. The generated plaques had fibre orientation calculated by the same process as the histological images.

Table 3.2 shows the results of the validation, comparing the expected orientation with the mean calculated fibre orientation for each generated plaque image.

Expected	Calculated
0°	0.11°
45°	45.0°
90°	89.9°
−30°	−30.1°
−45°	−45.1°
−60°	−60.0°

Table 3.2: The mean calculated fibre orientation compared to the generated fibre angle plaque images with parallel generated fibres.

While the generated plaques have no image artefacts or fibre dispersion, the image processing method was able to calculate orientation to a high precision (within about 0.1°).

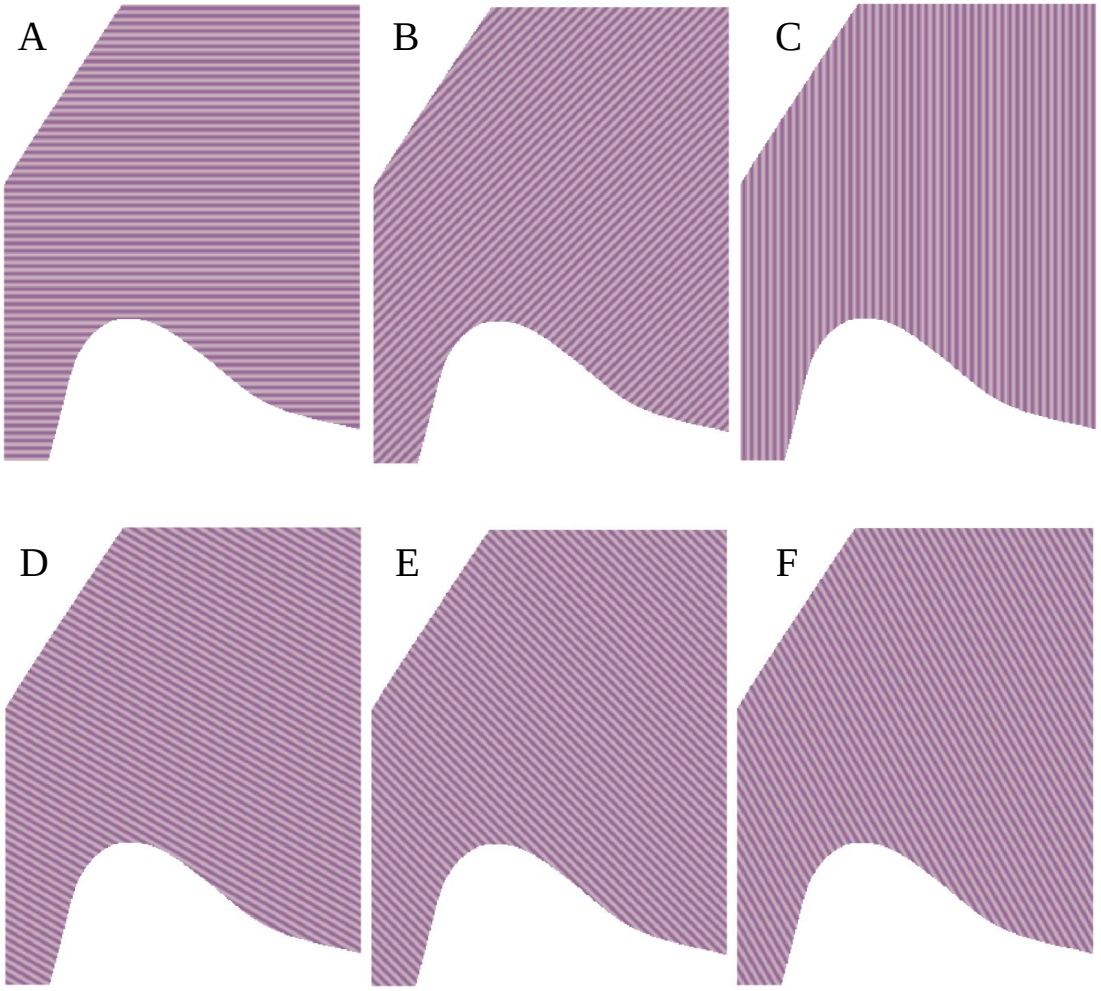

Figure 3.9: The upper-left shoulder region of the six generated fibre plaques used to validate fibre detection and orientation calculation: A.) 0°, B.) 45°, C.) 90°, D.) −30°, E.) −45°, and F.) −60°

3.4.5 Referenced Fibre Orientation or Fibre Misalignment

For local assessment of fibre orientation, it is convenient to describe fibre orientation relative to an artery coordinate system or an expected local orientation (see Figures 1.3 and 5.3).

In healthy arteries, collagen is organised in circumferential layers and the lumen is approximately circular [Clark and Glagov, 1985]. The largest stress in the plaque is the circumferential stress, so it is thought that the fibres are deposited circumferentially to bear the load efficiently [Clark and Glagov, 1985]. Therefore, healthy arteries are well described using a cylindrical (3D: axial, circumferential, and radial) or a circular (2D: circumferential and radial) coordinate system.

However, atherosclerotic plaques do not typically develop evenly or symmetrically. The lumen is rarely circular and the thickness of the vessel varies around the circumference. Therefore, a circular coordinate system would not represent the geometry and would be a poor local reference for fibre orientation. A modification to the circular coordinate system was therefore developed.

Fibres along the lumen and outer edge of the plaque were observed to be tangent to those edges, as they would be in a healthy artery. Points on edge contours ($p_{x,y}$) were calculated earlier in this chapter (see Figure 3.4B). Fibre orientations at the lumen and outer edges of the geometry ($\theta_p(x_i, y_i)$) were expected to be tangent to the edges (see Equation 3.10).

$$\theta_p(x_i, y_i) = \text{atan}\left(\frac{p(y_{i+1}) - p(y_i)}{p(x_{i+1}) - p(x_i)}\right); \theta_p \in [-90°, 90°] \tag{3.10}$$

Orientation at the lumen and outer edges of the plaque ($\theta_p(x_i, y_i)$) was interpolated through the plaque geometry using the *griddata* function in Matlab, using linear triangulation. The grid to be interpolated was the same size and resolution as the plaque mask, so interpolated values each correspond to a pixel of the original plaque mask. Therefore, an artery coordinate system was created, where each pixel had an expected fibre orientation (θ_{ref}).

The fibre orientation that had been calculated relative to horizontal (θ_μ) was then referenced to the artery coordinate system by the expected fibre fibre orientation (θ_{ref}), as in Equation 3.11:

$$\theta_i = |\theta_\mu - \theta_{ref}|; \theta_i \in [-90°, 90°] \tag{3.11}$$

where θ_i is the calculated fibre orientation in the artery coordinate system. In other words, θ_i is the angle of fibre misalignment relative to the expected orientation. For simplicity, the direction of misalignment or sign of θ_i was ignored.

Figure 3.8B shows the fibre orientation of the illustrative plaque relative to the artery coordinate system. Fibres in the IT region (left and bottom) are well aligned with their expected orientation. Fibres in the shoulder regions (upper left and lower right) are more misaligned with their expected orientation. These quantitative findings match gross observations of fibre orientation in the histology image of the illustrative plaque.

3.4.6 Methods to Calculate Fibre Dispersion

The local fibre dispersion, a measure of fibre orientation variance, described fibre structure alongside fibre misalignment. This analysis assumed one fibre family in the 2D artery cross-section. A fibre family is a group of fibres having a similar primary orientation.

Dispersion (κ) was calculated pixel-by-pixel for all plaques by the same method as Gasser et al. [2006]. A 51×51 ROI of orientation from detected fibres only (θ_{fibre}) were used around each pixel to calculate κ. The primary fibre direction was taken as the local mean fibre orientation (θ_μ) at the respective pixel. Therefore, orientations from detected fibres (θ_{fibre}) within the ROI were referenced to the local mean fibre orientation (i.e. the maximum of the distribution is at θ_μ). Since the distribution was π-periodic, it was transformed to be within [0°, 180°] for the dispersion calculation (see [Gasser et al., 2006] for further details and explanation).

The frequency of orientation ($\hat{P}(\theta)$) from detected fibres in the ROI (relative to local primary direction) was calculated for twenty evenly-spaced bins. A low number of bins were used because there were relatively few independent fibres in

each ROI. The frequency distribution of fibre orientation was normalised to an orientation density function ($P(\theta)$) according to Equation 3.12:

$$P(\theta) = \eta \hat{P}(\theta) \tag{3.12}$$

where the normalisation parameter (η) is calculated in Equation 3.13:

$$\eta = \frac{2}{\int_0^\pi \hat{P}(\theta)\sin\theta \mathrm{d}\theta} \tag{3.13}$$

This normalisation function is a conversion that reduces a 3D spherical fibre orientation distribution to a 1D orientation density function. The reduction assumes that fibres are isotropically distributed about a central preferred orientation. The sine component adjusts for the spherical integration mesh having smaller elements at the poles compared to the equator (see [Gasser et al., 2006]).

The dispersion (κ) is calculated for each pixel according to Equation 3.14:

$$\kappa = \frac{1}{4}\int_0^\pi P(\theta)\sin^3\theta \mathrm{d}\theta \tag{3.14}$$

The integrations in Equations 3.13 and 3.14 were solved numerically by the trapezoidal rule, using the edges of the bins (θ) as integration points.

3.4.7 Fibre Dispersion Properties

Dispersion is an analogue to standard deviation for circular statistics, with values from κ=0 (perfect local alignment of the fibres) to κ=$\frac{1}{3}$ (even distribution or isotropic). Values of κ>$\frac{1}{3}$ are possible and were observed. This can occur when the distribution of fibre orientation about their mean or primary direction is not bell-shaped. As an example, two families of fibres would result in a double-hump distribution, which could have κ>$\frac{1}{3}$.

Figure 3.10A shows the κ calculated for each pixel of the illustrative plaque. The shoulders and lipid region had higher κ, as was expected. The fibrous cap and IT regions had relatively low dispersion. In this figure, green corresponds to lower and red is for higher dispersion. Differences between regions for κ were not as clear as they were for fibre orientation (such as in Figure 3.8B).

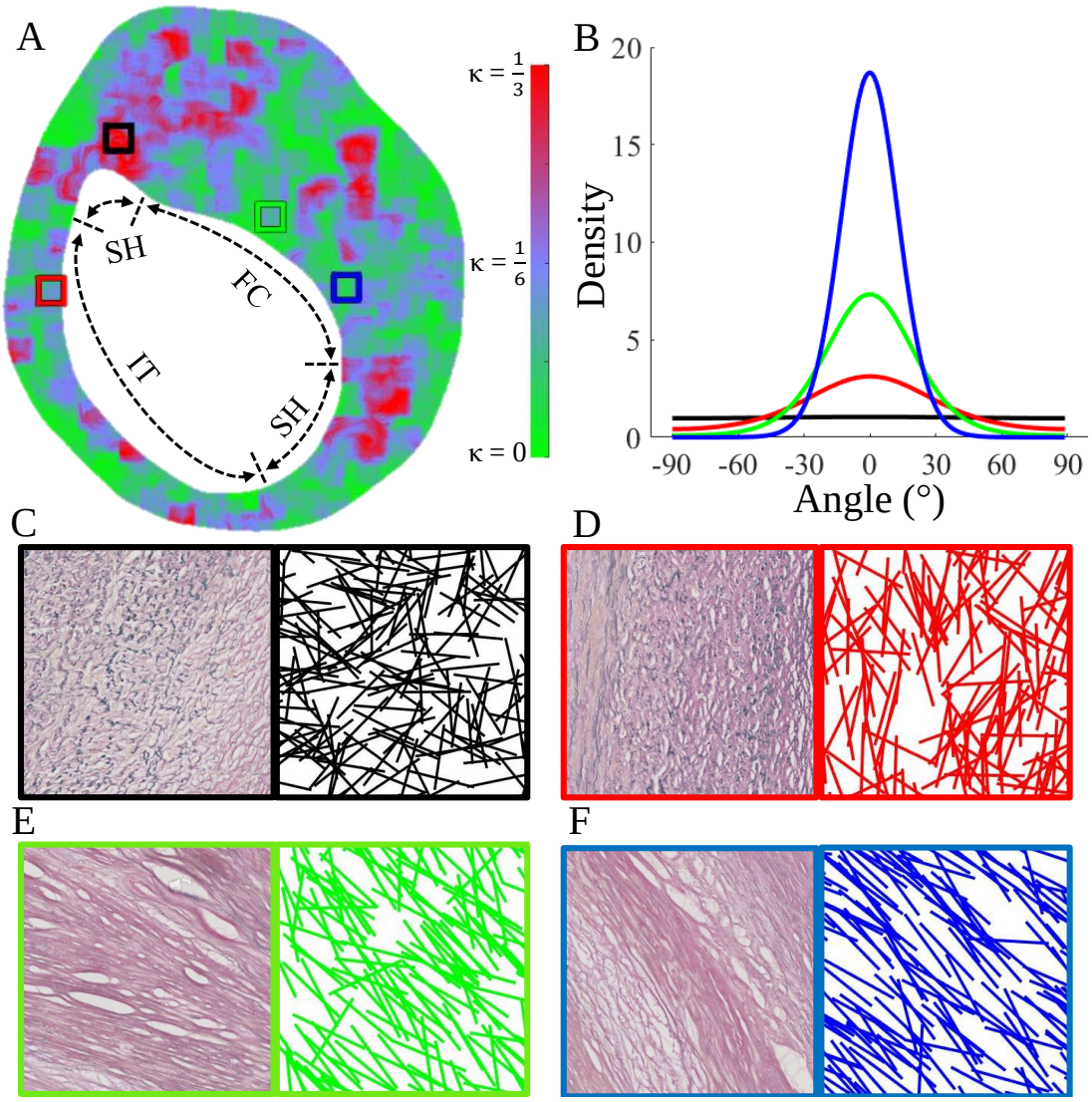

Figure 3.10: A.) Fibre dispersion for the illustrative coronary plaque with enlargements for (C)-(F) indicated by box colour, B.) Fibre orientation density distributions for κ values equivalent to (C)-(F), C.) Enlargement and generated fibres for κ=0.330, D.) For κ=0.234, E.) For κ=0.136, and F.) For κ=0.054.

A von Mises distribution is the analogue to a normal distribution for circular statistics, and has the density function (Equation 3.15):

$$P_m(\theta) = 4\sqrt{\frac{b}{2\pi}}\frac{\exp[b(\cos(2\theta)+1)]}{\mathrm{erfi}(\sqrt{2b})} \tag{3.15}$$

where b is the concentration parameter of the distribution (similar to standard deviation in a normal distribution), erfi is the imaginary error function [Gasser et al., 2006], and θ here is fibre orientation relative to the local primary orientation. Values of b were found iteratively to produce the κ for each of the four selected regions (see Table 3.3).

Region	Colour	b	κ
Shoulder	Black	0.035	0.330
IT	Red	1.00	0.234
FC A	Green	2.18	0.136
FC B	Blue	4.96	0.054

Table 3.3: Region type, colour used to indicate location, concentration parameter, and dispersion of the four illustrative sites of fibre dispersion. The colour column references the location in Figure 3.10A labelled with the same colour.

The synthetic fibre density distributions are shown in Figure 3.10B, where colour is used to match the curve with the locating box in Figure 3.10A. Isotropic distribution of fibres (κ=$\frac{1}{3}$) has a constant distribution of fibre orientation, similar to the shoulder (κ=0.330, black region). Increasing values of κ result in a narrower distribution about the prime orientation of the fibres.

For further explanation of κ and to provide method validation, synthetic fibres were generated at the same fibre orientation and dispersion as calculated at four locations of the illustrative plaque (see Figure 3.10A). Figure 3.10C-F shows enlargements of the representative zones (left), paired with plots of synthetic fibres that were generated with the same local mean fibre orientation and dispersion (left). Colour of the paired image boarders and of the synthetic fibres matches these to their location in Figure 3.10A. Paired images show good match in both fibre orientation and dispersion. There are clear differences in dispersion for each of the four paired images, with κ decreasing from Figure 3.10C to F. Therefore, the methodology is validated to identify and describe different values of κ.

The sample locations in Figure 3.10 were selected to provide a range of values, rather than being representative of the particular plaque region. Finite element models in Chapter 4 used the same dispersion as the fibrous cap zone highlighted by green in Figure 3.10A and E (κ=0.136).

Another method for calculating dispersion was used on the illustrative plaque to validate the methods (see Appendix A.1). Good correlation was found between the dispersion value from the two methods (R^2=0.690). Therefore, κ was validated as a repeatable measure of fibre structure.

3.4.8 Validation of Histology Stain

The image processing described here used EVG or H&E stains, which stains collagen pink. However, other components can be stained similar colours. H&E is a relatively non-specific stain, where a variety of components could produce a pink-purple colour assumed in this project to be collagen. While collagen comprises 40-60% of protein content in atherosclerotic plaques [Shekhonin et al., 1985], a short study confirmed that H&E stained images could be used to calculate fibre structure. EVG stains collagen and elastin more specifically than H&E, so the use of EVG would also be validated in proving H&E.

Two adjacent slices of a cerebral atherosclerotic artery (separated by about 5 μm) were histologically prepared and analysed. One was stained with H&E (Figure 3.11A) and the other with Masson's Trichrome (Figure 3.11B). Masson's Trichrome stain is more specific for collagen, which is indicated by a blue colour. Unfortunately, no paired slices with these stains were available from the coronary or carotid sample set. The paired slices were prepared by the methods detailed earlier in this chapter. The resulting images are shown in Figure 3.11.

There were some geometry differences between the slices, such as near the left side of the lumen and at the delamination between the media and adventitia. To align the images and correct geometry differences, the Masson's Trichrome image was registered onto the H&E image as a deformable body, using the Matlab *imregister* function (with an affine transform and mono-modal configuration). Fibre orientation, misalignment, and dispersion were calculated for the H&E and the Masson's Trichrome images.

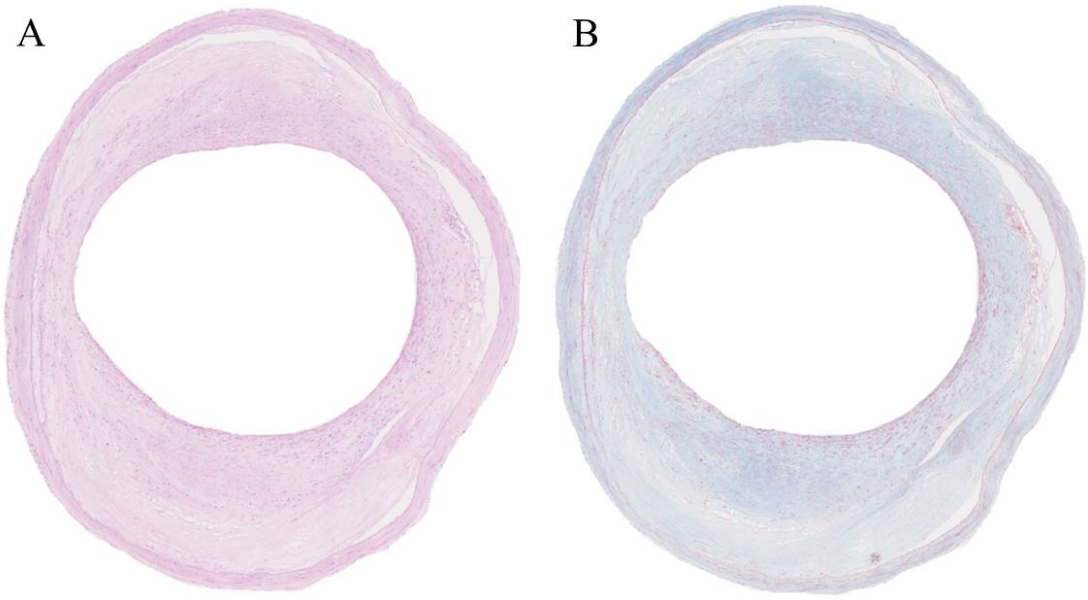

Figure 3.11: Digitised and artefact-corrected atherosclerotic cerebral artery histology slides with: A.) H&E and B.) Masson's Trichrome.

There was a strong correlation (R^2=0.970) between the local mean fibre orientation (θ_μ) by pixel from the H&E and Masson's Trichrome images. Fibre misalignment for the H&E and Masson's Trichrome images is shown for the fibre orientation referenced to the artery coordinate system (Figure 3.12A and B).

Since the lipid was present around all but a short section at the left side of the artery, the shoulder and IT regions were quite small. Differences between the fibre misalignment in these regions could be from segmentation or true differences in fibre structures.

Fibre dispersion for the two images was calculated and is shown in Figure 3.13A (H&E) and B (Masson's Trichrome). Broadly, dispersion is lower at the lumen and outer edge of the plaque and higher in the lipid-rich crescent around the right side of the plaque.

Fibre dispersion for each pixel had a moderate correlation (R^2=0.539) between the H&E and Masson's Trichrome stained images. As dispersion is derived from fibre orientation and assumes a bell-shaped distribution, differences in fibre orientation are magnified when calculating fibre dispersion. General patterns between the two fibre dispersion plots were similar. Differences can be seen at the left

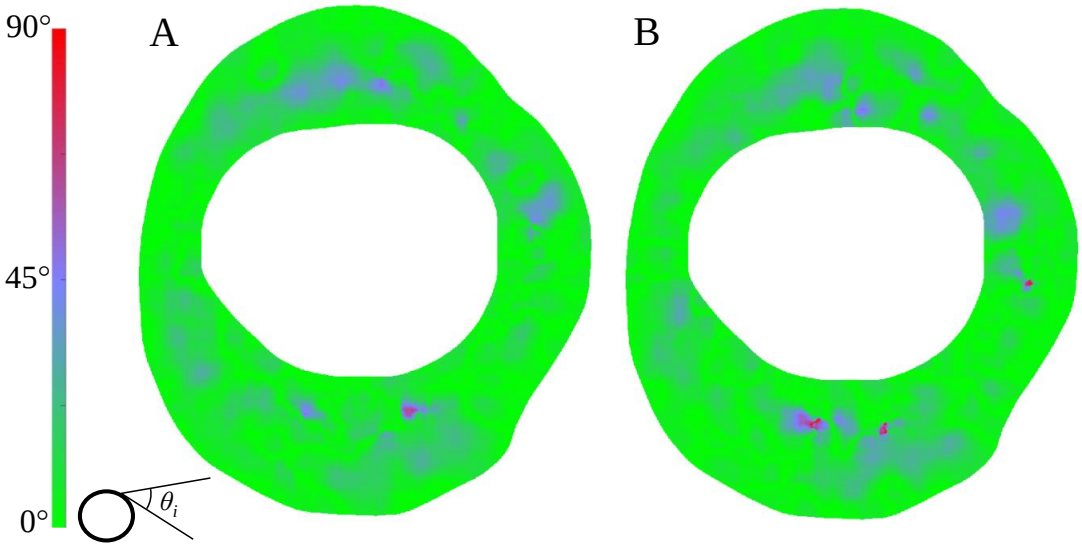

Figure 3.12: Misalignment of fibres or fibre orientation relative to the artery coordinate system for atherosclerotic cerebral artery histological images with: A.) H&E stain and B.) Masson's Trichrome stain.

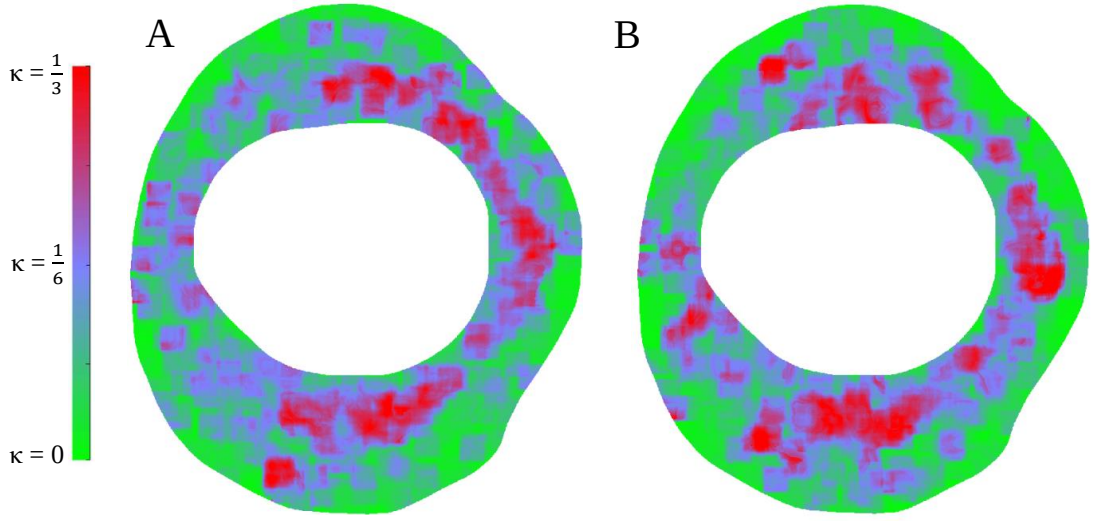

Figure 3.13: Fibre dispersion compared between two atherosclerotic cerebral artery histology slides with: A.) H&E stain and B.) Masson's Trichrome stain.

side of the lumen and near the delamination between the media and adventitia, where the fibre structures in the original images are different.

In general, there was a good match between the fibre orientation, misalignment, and dispersion calculated using the H&E and Masson's Trichrome stain. The small differences could be attributed to localised differences in geometry and fibre structure in adjacent histology slices. Therefore, using H&E stain to detect collagen fibres has been validated for this study. Furthermore, these results indicate strong repeatability in calculating fibre orientation and moderate repeatability in calculating fibre dispersion from histology images.

3.5 Fibre Structure Results

Fibre orientation and dispersion were calculated for all 16 coronary and 15 carotid plaques used in this project. This section reports the fibre orientation results first (Section 3.5.1), followed by those for fibre dispersion (Section 3.5.1).

For each fibre orientation and dispersion, histograms will show the distributions of fibre structure in each segmented region of the illustrative plaque. Summary values of orientation and dispersion will be presented for each plaque type and segmented region. Statistical tests will be used to determine if different segmented regions have different fibre structures, and if the two plaque types have different structures. A value of $p<0.05$ was considered statistically significant.

3.5.1 Fibre Misalignment Results

Fibre misalignment was calculated for all regions within the plaque sample masks (see Figure 3.4 for region definitions). Fibre misalignment was the fibre orientation referenced to the artery coordinate system, or the misalignment of fibres' orientation with their expected orientation (see Section 3.4.5).

Variation in Values

Fibre misalignment had considerable variance between samples, regions, and even within a single region. Figure 3.14 shows relative density distributions for fibre misalignment in each segmented region of the illustrative plaque. The histogram

bars represent the number of pixels within that range of fibre misalignment values, relative to the total number of pixels.

While the histograms in Figure 3.14 are for only one plaque, representative features can be discussed. In general, fibres were nominally oriented in the reference direction, but there was a long tail of highly-misaligned fibres. The shoulder regions (Figure 3.14A) had some highly misaligned fibres, while the fibrous cap (Figure 3.14B) and IT (Figure 3.14C) did not. The global region (all tissue in the plaque, Figure 3.14D) had some highly misaligned fibres, but many of these were in the lipid core or shoulder regions.

Summary Fibre Orientation Results

The median and intra-quartile range of fibre misalignment was calculated for each region in each plaque. Summary fibre misalignment values are presented in Table 3.4, segmented by region and plaque type (coronary, carotid, or all plaques). Summary values are reported as the mean of the median and intra-quartile ranges for the respective region and plaque type. A two-sample t-test was used to identify significant differences in fibre misalignment between the coronary and carotid plaques for each region.

Region	All Plaques	Carotid	Coronary	p
Fibrous Cap	6.18 [5.49, 9.24]	6.18 [5.57, 10.3]	6.10 [5.46, 8.97]	0.680
Shoulder	13.0 [6.74, 17.3]	13.4 [7.05, 16.3]	12.9 [6.56, 18.0]	0.450
IT	6.55 [5.06, 8.96]	6.54 [5.21, 11.3]	6.66 [5.06, 8.63]	0.474
Global	9.22 [8.15, 11.6]	9.85 [8.83, 13.1]	8.63 [7.63, 9.27]	0.057
GEX	7.50 [6.67, 8.82]	8.72 [7.57, 10.0]	7.33 [6.05, 7.68]	**0.015**

Table 3.4: Summary results of fibre misalignment (in degrees): median and intra-quartile range for fibre misalignment in key regions. Values for the carotid and coronary plaques were compared by a t-test to calculate the p-value.

For the regions around the lumen (fibrous cap, shoulders and IT), coronary and carotid plaques had similar fibre misalignment. Fibre misalignment within the GEX (global excluding lipid) region was statistically higher for the carotid plaques than the coronary, although the difference in fibre misalignment was small. This difference could be from the carotid plaques not having adventitia, which had relatively low fibre misalignment in the coronary plaques.

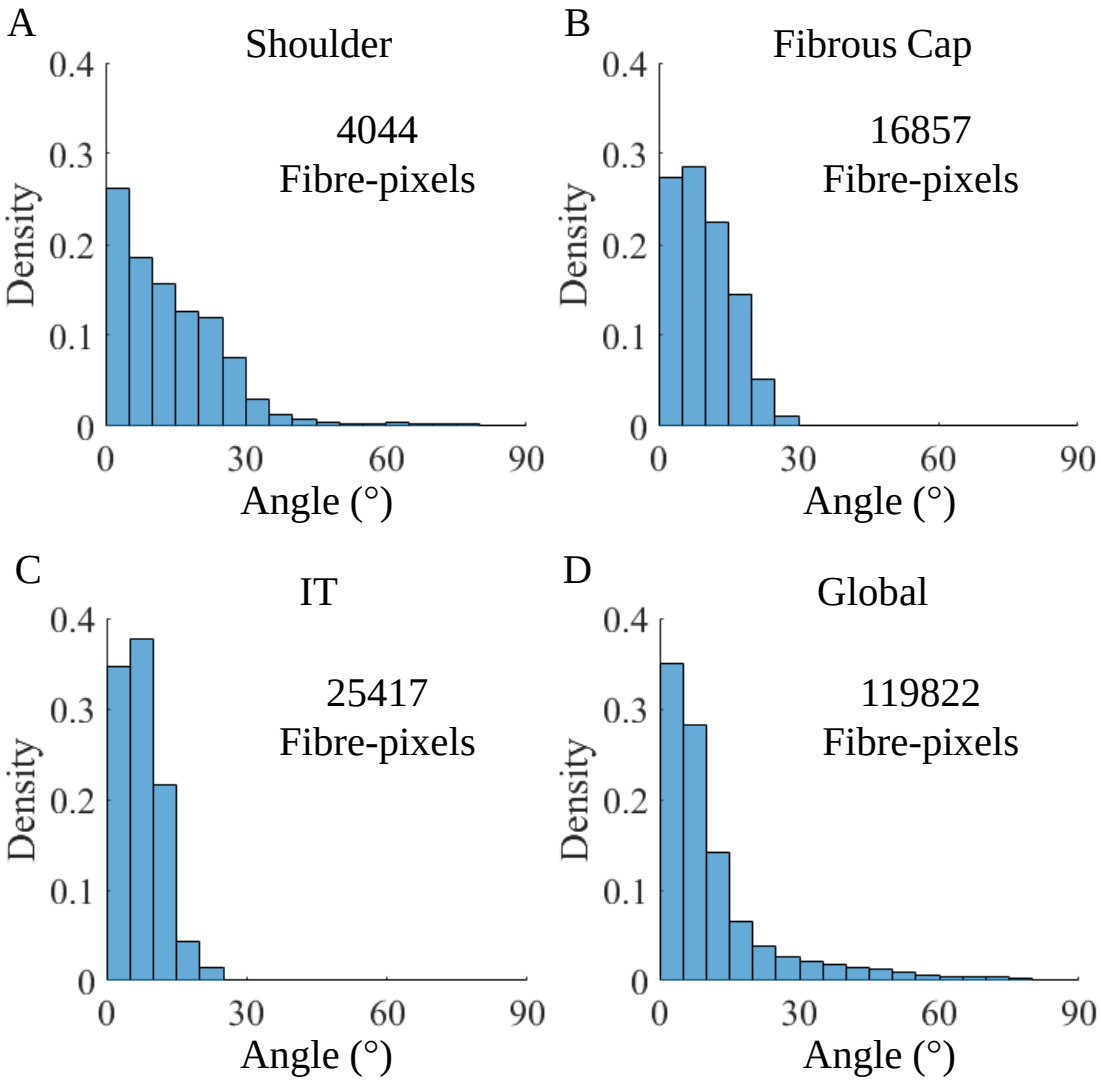

Figure 3.14: Fibre misalignment density distributions by region for a sample plaque, in degrees, for regions: A.) Shoulder, B.) Fibrous cap, C.) IT, and D.) Global.

Comparisons Between Regions

Two-tailed, paired t-tests compared median fibre misalignment between the segmented plaque regions. The global region was not considered since it was similar to the GEX region, but was influenced by fibres detected in the lipid core. Comparisons were made for carotid, coronary, and all plaques (see Table 3.5).

Region 1	Region 2	All Plaques	Carotid	Coronary
Shoulder	Fibrous Cap	$<$ **0.001**	$<$ **0.001**	$<$ **0.001**
Shoulder	IT	$<$ **0.001**	$<$ **0.001**	$<$ **0.001**
Shoulder	GEX	$<$ **0.001**	$<$ **0.001**	$<$ **0.001**
Fibrous Cap	IT	1.000	0.921	0.906
Fibrous Cap	GEX	0.453	0.278	0.795
IT	GEX	0.498	0.369	0.990

Table 3.5: p-values of paired t-tests of fibre misalignment between the two plaque regions specified in the left columns, by set of plaque type.

The shoulder region had higher fibre misalignment than the fibrous cap, IT, or GEX region for all plaque types (p<0.001). It had almost twice the misalignment of other regions (see Table 3.4), which had no significant difference in fibre misalignment between one another.

Discussion of Section

Since the IT region was most similar to healthy media, it could be used as a reference to identify changes to the fibre structure in other regions from atherosclerosis. The shoulder region is a common location for plaque rupture, so the role of shoulder fibre misalignment in rupture mechanics must be further investigated.

3.5.2 Fibre Dispersion Results

Fibre dispersion (κ) was calculated by pixel for each plaque used in this study. Results will be presented as they were for fibre misalignment. First, histograms will show the relative density of κ values in the illustrative plaque. Second, summary κ results will be presented, by region type and plaque type. This summary table includes the results of a t-test comparing κ between the carotid

and coronary plaques for each region type. Third, κ will be compared by a paired t-test between the different plaque regions.

Variation in Values

The relative density of κ in each segmented region of the illustrative plaque is shown in Figure 3.15.

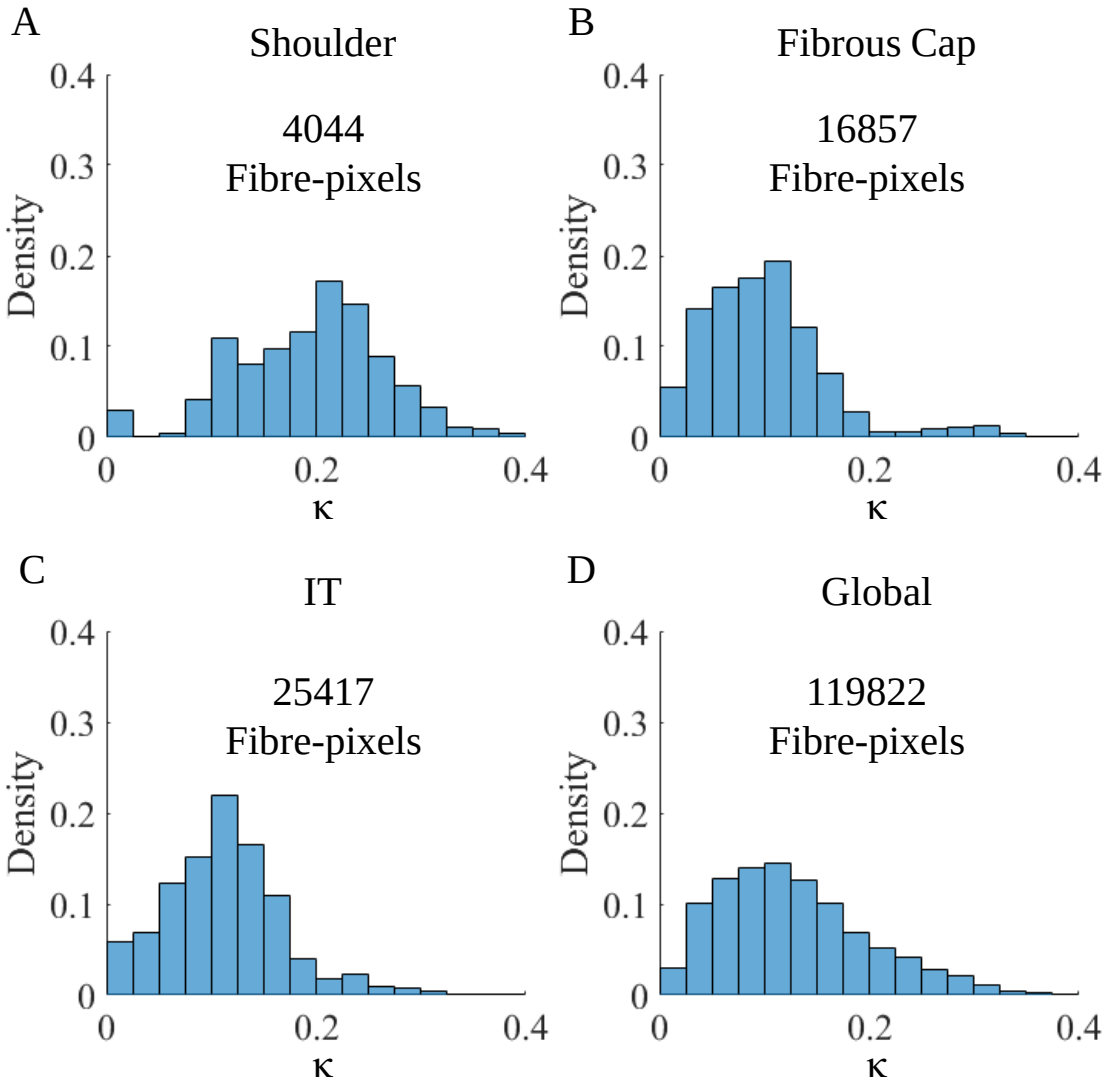

Figure 3.15: Density distributions of fibre dispersion by region for a sample plaque for regions: A.) Shoulder, B.) Fibrous cap, C.) IT, and D.) Global.

The distribution of κ in the shoulder regions (Figure 3.15A) was wider and centred about a higher value than the other regions. The relative density of dispersion values for the fibrous cap (FC) and IT regions had a similar width and central value (Figure 3.15B and C). The distribution for the fibrous cap region had a slight skew to the left, favouring lower κ. For the global region (Figure 3.15D), the distribution of κ values was centred similar to those for the fibrous cap and IT, but had a wider distribution and more higher values of κ.

Summary Fibre Dispersion Results

The median and intra-quartile range for κ was calculated for each region type and plaque type. The mean values for the median and intra-quartile range of each respective sample-region was calculated for each set of plaques (see Table 3.6). The fibre dispersion in the coronary and carotid plaques were compared by region using a two sample t-test.

Region	All Plaques	Carotid	Coronary	p
FC	0.094[0.081,0.110]	0.102[0.081,0.128]	0.093[0.081,0.105]	0.207
Shoulder	0.150[0.120,0.184]	0.150[0.120,0.182]	0.150[0.121,0.192]	0.662
IT	0.121[0.103,0.141]	0.129[0.103,0.137]	0.119[0.103,0.144]	0.971
Global	0.128[0.110,0.156]	0.146[0.130,0.170]	0.119[0.105,0.128]	**0.001**
GEX	0.112[0.101,0.128]	0.122[0.113,0.160]	0.105[0.096,0.112]	**0.002**

Table 3.6: Summary results of κ: median and intra-quartile range for fibre misalignment in key regions. Values for the carotid and coronary plaques were compared by a t-test to calculate the p-value.

For the regions around the lumen (fibrous cap, shoulders and IT), coronary and carotid plaques had similar κ within each respective region. Fibre dispersion within the global (p=0.001) and GEX (p=0.002) regions was statistically higher for the carotid plaques than the coronary. The carotid plaques did not have adventitia, which had relatively low fibre dispersion for the global and GEX regions of the coronary plaques.

Comparisons Between Regions

Two-tailed, paired t-tests compared dispersion properties between regions for carotid, coronary, and all plaques (see Table 3.7).

Region 1	Region 2	All Plaques	Carotid	Coronary
Shoulder	Fibrous Cap	$< \mathbf{0.001}$	$< \mathbf{0.001}$	$< \mathbf{0.001}$
Shoulder	IT	$< \mathbf{0.001}$	**0.005**	$< \mathbf{0.001}$
Shoulder	GEX	$< \mathbf{0.001}$	**0.029**	$< \mathbf{0.001}$
Fibrous Cap	IT	**0.009**	0.295	**0.008**
Fibrous Cap	GEX	$< \mathbf{0.001}$	**0.013**	**0.022**
IT	GEX	0.307	0.239	**0.012**

Table 3.7: p-values of paired t-tests of κ between the two plaque regions specified in the left columns, by set of plaque type.

The shoulder region had higher κ than the fibrous cap, IT, or GEX regions. Dispersion was also higher in the GEX region than the fibrous cap for coronary, carotid, and the combined set of plaques. The IT region had higher dispersion than the fibrous cap for the coronary and combined sets of plaques.

Discussion of Section

The shoulder region, which was found to have a uniquely high fibre misalignment, had a higher κ compared to other regions. Dispersion was higher for the shoulder and lower for the fibrous cap compared to the IT region, which is assumed to be more similar to healthy tissue.

3.6 Linear Regression Modelling

Linear regression models (*fitlm* in Matlab) were used to identify coupling between plaque geometry (see Section 3.3.5) and fibre structure within a segmented region (median fibre misalignment or median fibre dispersion). Since the size of a plaque is coupled to plaque type, models will be reported for the carotid only, coronary only, and combined set of all plaques (see Equation 3.16):

$$y_i = Ax_i + B + \epsilon_i \tag{3.16}$$

where x_i was the value of a plaque's geometry parameter, y_i was the value of a plaque-region's fibre structure parameter, and ϵ_i was the error between the fitted model and the data for each plaque. The regressions provide estimates for the slope (A) and intercept (B) of the linear model, which will be reported below for each combination of fibre property and geometry.

A p-value will be reported for each regression, which is the result of a t-test of the null hypothesis that the slope (A) is zero. If the slope is zero, the fibre property (y_i) does not depend on the geometry property (x_i). A value of $p<0.05$ was considered as showing y_i had a significant relationship with x_i. Additionally, a coefficient of determination (R^2) will be reported for each regression. The R^2 value is a measure of how tightly coupled the geometry and fibre structure parameters are, with higher values indicate tighter coupling. Conversely, a low R^2 value indicates weaker coupling and suggests the modelled x_i parameter is one of several factors affecting y_i. As fibre structures are complex, it is expected they are dependant on multiple factors and R^2 will be relatively low for linear regressions against only one geometry parameter.

Interpreting Linear Regression Models

In deciding if the coronary and carotid plaques can be combined into set of all plaques, the slope (A) and confidence (p) should be considered for each the carotid and coronary sets. If the A and p-values of each the coronary and carotid sets of plaques were similar, the linear regression for a given geometry parameter using the set of all plaques was accepted. However, the linear regressions for a given geometry parameter using all plaques should be treated as suspect if the A and p-values for the individual sets were different from one another.

If the regression for a given geometry parameter was significant for at least one of the carotid, coronary, or combined set of plaques, all three sets were included in the table to allow comparison. If the regression was only significant for combined set and both variables in the regression were significantly different for each plaque type, then the finding was rejected. Instead, it was assumed that the variables in the significant regression were acting as proxies for plaque type. For example, the regression between GEX fibre misalignment and lipid thickness (t_{li}) had a $p<0.05$

for the combined plaque set only, but both variables were significantly different between the plaque types (see Tables 3.1 and 3.6).

It is worth remembering that a significance threshold of $p<0.05$ implies a rate of 1/20 regressions falsely reporting a link. Since 120 regressions were done (ten geometry parameters; four segmented regions; three sets of plaque type) for each fibre misalignment and dispersion, about six regressions for each fibre misalignment and dispersion should be expected to incorrectly find a significant link between fibre structure to geometry.

For linear regressions of fibre structure within shoulder regions, the radius of curvature (ρ) and the normalised shoulder radius of curvature (ρ_{norm}) geometry parameters were those of the same shoulder. For other segmented regions, the higher value of the two shoulders in a plaque was used.

3.6.1 Fibre Misalignment and Geometry Regressions

The median fibre misalignment in each segmented plaque-region was fitted by a linear regression to each geometry parameter considered in this project (see Section 3.3.5). These regressions were done and will be reported for the carotid only, coronary only, and a combined set of both plaques.

In Section 3.3.5, some geometry parameters were found to be significantly different between the carotid and coronary sets of plaques. Fibre misalignment was found to be similar between the carotid and coronary plaques within the fibrous cap, shoulder region, and IT. However, fibre misalignment was significantly different for the GEX region, and the difference between the regions was nearly significant for the global region (p=0.057). Since there were relatively few samples in either set of plaques, it would be convenient to combine them to raise the statistical power. Results for statistically significant ($p<0.05$) linear regressions of fibre misalignment from geometry parameters are shown in Table 3.8.

For the fibrous cap (FC) region, a thicker FC (t_{fc}) was a statistically significant predictor of higher fibre misalignment in the coronary plaques. However, the t_{fc} of one coronary plaque was over twice that of the other coronary plaques (but still thinner than some carotid plaques). With the outlying sample ignored, the regression between t_{fc} and fibre misalignment was not significant (p=0.844).

	All Plaques			Carotid			Coronary		
	A	p	R^2	A	p	R^2	A	p	R^2
Fibrous Cap									
t_{fc}	5.52	0.255	0.05	-5.03	0.601	0.02	**18.5**	**0.006**	**0.42**
Shoulder									
$\%_{pb}$	**14.7**	**0.041**	**0.07**	7.72	0.378	0.03	**30.0**	**0.023**	**0.16**
t_{fc}	**18.0**	**0.012**	**0.10**	18.8	0.118	0.09	**31.0**	**0.014**	**0.19**
ρ_{norm}	-0.24	0.852	0.00	-2.37	0.384	0.00	**-30.2**	**0.022**	**0.16**
IT									
$\%_{pb}$	**12.3**	**0.002**	**0.28**	**15.8**	**0.003**	**0.50**	3.87	0.555	0.03
$\%_{li}$	**10.3**	**0.013**	**0.15**	**18.3**	**0.011**	**0.40**	-0.40	0.951	0.00
t_{li}	**1.77**	**0.035**	**0.14**	**2.90**	**0.040**	**0.29**	0.18	0.915	0.00
A_{lu}	-0.07	0.226	0.05	**-0.18**	**0.039**	**0.29**	-0.12	0.790	0.01
GEX									
$\%_{pb}$	**7.57**	**0.002**	**0.29**	**6.17**	**0.040**	**0.29**	**9.44**	**0.009**	**0.40**
t_{fc}	**7.45**	**0.002**	**0.28**	1.37	0.763	0.01	**10.6**	**0.001**	**0.53**
A_{lu}	0.01	0.852	0.00	**-0.92**	**0.046**	**0.27**	-0.11	0.681	0.01

Table 3.8: Slope (A), p-value, and coefficient of determination (R^2) for linear regressions between fibre misalignment and geometry parameters. Statistically significant regressions ($p<0.05$) are in bold. Regressions were done for the carotid and coronary sets of plaques separately, then for a combined set of all plaques. Regressions are only shown here if a significant regression was found for a given geometry parameter in at least one of the plaque sets.

Higher fibre misalignment in the shoulder region was predicted by increased plaque burden ($\%_{pb}$) for coronary and the combined set of plaques, supported by a weak trend in carotid plaques. Shoulder region fibre misalignment was also linked to thicker t_{fc} for the coronary and combined sets of plaques, and showed a weak trend for carotid plaques. When the coronary plaque with the thickest t_{fc} was removed from the regression model, the links weakened to trends for the coronary (p=0.061) and combined set of plaques (p=0.067). Fibre misalignment in the shoulders of the coronary plaques was predicted by smaller values for normalised radius of lumen curvature at the shoulders (ρ_{norm}).

For the IT region, higher $\%_{pb}$, lipid fraction ($\%_{li}$), and lipid thickness (t_{li}) were statistically significant predictors of fibre misalignment for the carotid and combined set of plaques. For the carotid plaques only, decreases in lumen area (A_{lu}) was found to be linked to increased fibre misalignment in the IT region.

Only higher plaque burden ($\%_{pb}$) in the GEX regions was coupled with fibre misalignment for all three sets of plaques. Lower A_{lu} predicted fibre misalignment for the carotid plaques only. Higher t_{fc} was linked to GEX fibre misalignment for the coronary and combined sets of plaques. With the coronary plaque having the highest t_{fc} ignored, the regression was not a significant for coronary plaques (p=0.806), but significantly predicted the combined set of plaques (p=0.015).

Discussion of Section

Fibre misalignment was relatively low for all regions except the shoulders, so it was not surprising that only limited coupling was found between fibre misalignment and geometry. To increase the sample size and provide a wider range of geometries, regressions were done for a combined set of carotid and coronary plaques. However, regressions often found conflicting results for the independent coronary and carotid plaque sets. This suggests it is not appropriate to combine the sets for the parameters used in those regressions.

In summary, several geometric factors were statistically correlated with fibre misalignment (low p-value), but these correlations were relatively weak (low R^2). Since fibre misalignment was not strongly coupled to plaque geometry, it may be an independent factor of plaque mechanics.

3.6.2 Fibre Dispersion and Geometry Regressions

Using the same approach as for fibre misalignment, the median fibre dispersion in each segmented plaque-region was fitted by a linear regression to each geometry parameter. Again, regressions were preformed for the carotid only, coronary only, and combined set of both plaques.

Results for statistically significant linear regressions ($p<0.05$) of fibre dispersion from geometry parameters are shown in Table 3.9.

	All Plaques			Carotid			Coronary		
	A	p	R^2	A	p	R^2	A	p	R^2
Fibrous Cap									
$\%_{li}$	-0.10	0.082	0.10	-0.10	0.332	0.07	**-0.12**	**0.021**	**0.33**
Shoulder									
t_{fc}	-0.04	0.365	0.01	0.07	0.438	0.02	**-0.16**	**0.020**	**0.17**
ρ_{norm}	0.01	0.646	0.00	0.02	0.361	0.03	**-0.16**	**0.029**	**0.15**

Table 3.9: Slope (A), p-value, and coefficient of determination (R^2) for linear regressions between fibre dispersion and geometry parameters. Statistically significant regressions ($p<0.05$) are in bold.

For the fibrous cap region, a higher $\%_{li}$ was linked to higher dispersion for coronary plaques. The shoulders of the coronary plaques had a significant link between fibre dispersion and lower t_{fc} and ρ_{norm}. Recall that one coronary plaque had a t_{fc} that was considerably higher than the other values in the coronary set. However, the links for lower t_{fc} and ρ_{norm} were still statistically significant even with that coronary plaque removed from the regression. No geometry parameter was linked to fibre dispersion in the IT or GEX regions.

Discussion of Section

In summary, fibre dispersion was weakly coupled to plaque geometry, so should be considered as an independent parameter to describe atherosclerotic plaques. Further study on the role of fibre dispersion in plaque mechanics is justified, and was considered in the studies that are reported in following chapters.

3.7 Discussion, Limitations, and Future Work

3.7.1 Differences between Plaque Regions and Types

The fibre structures and geometries of coronary and carotid atheromas were analysed from histological images. After pre-processing to remove artefacts in the histological images, plaque geometry was examined, with a focus on parameters known or suspected to predict clinical events in plaques. Carotid plaques were larger than the coronary plaques, but several size-independent geometry parameters were not significantly different between the plaque types (such as $\%_{pb}$, $\%_{li}$, and θ_{li}, see Section 3.3.5). Where the two plaque types are found to be similar, they can be analysed as a combined set to give a larger sample size. Further study with additional samples may provide more conclusive results.

For the fibrous cap, shoulder, and IT regions, neither fibre misalignment nor dispersion were significantly different between the coronary and carotid plaques (see Section 3.5). The shoulder region had significantly higher fibre misalignment and dispersion than the fibrous cap, IT, or GEX regions. The IT region was considered here as healthier tissue, with lower fibre misalignment and moderate fibre dispersion. The shoulder region of a plaque has increased risk of plaque rupture, which has been explained as a consequence of sharper lumen curvature at the shoulders [Li et al., 2008]. However, the role of fibre structure should also be investigated.

Linear regression models identified coupling between fibre misalignment or fibre dispersion and geometry parameters (see Section 3.6). Plaque burden ($\%_{pb}$), fibrous cap thickness (t_{fc}), and the luminal curvature at the shoulder regions normalised to plaque height (ρ_{norm}) were identified as geometry parameters that may predict fibre structure in the shoulder regions. For the fibrous cap, lipid fraction ($\%_{li}$) and t_{fc} were identified as possible predictors of fibre structure. However, these relationships were relatively weak (low R^2) and were found for only one of the carotid or coronary sets of plaques, so fibre misalignment and dispersion are independent or weakly coupled to geometry. If coupling had been strong, fibre structure may have been able to be inferred from geometry using current clinical imaging techniques.

3.7.2 Mechanically-Important Fibre Structures

Qualitative discussion of the fibre organisation is merited. Fibre families often bifurcated around the lipid core, as was observed in the SEM analysis in Chapter 2. Seam-like features were observed from the ends of the lipid core, typically extending towards the lumen at the shoulder regions and forming a 'triangle' with the third edge being fibres wrapping the lipid core. These features often corresponded with regions of fibres quantitatively misaligned with the lumen, for example in the shoulder region of Figures 3.8B, 3.10A, and 3.10C.

Fibre dispersion was a more complex metric than fibre misalignment. Because fibre dispersion is calculated from the fibre orientation within a local region, errors and anomalies in fibre orientation are propagated to fibre dispersion. Fibre dispersion assumes a bell-shaped distribution about a primary fibre orientation. Therefore, it is sensitive to errors in the assumed primary fibre orientation and to fibres that are very misaligned with this primary orientation.

An evenly scattered 'background' of fibre distribution would not affect the primary fibre orientation, but could considerably increase fibre dispersion (see the density functions in Figure 3.10B). If multiple families of fibres were present, a region may be calculated having relatively high fibre dispersion, even if the fibres were coherent with their respective families. At the shoulder regions, two fibre families were present at the 'seam' or 'triangle' fibre feature, where fibres groups split from one another (see Section 2.4.1).

Dispersion may play a role as a secondary parameter, modifying the action of fibre orientation. Since fibres are stiffest in their length or axis, fibre orientation determines the direction of principal stress. Fibre dispersion may determine how loads are spread laterally across the fibre network by recruiting adjacent fibres.

3.7.3 Limitations and Future Directions

Limitations from Sample Preparation

Regions were manually segmented based on the advice of a histologist. These anatomical regions are qualitatively defined, so some variability in the results can be attributed to the segmentation. To allow comparison between plaques,

each plaque was segmented into one lipid core, one fibrous cap, one IT, and two shoulders. The lipid core is often blended with fibrous tissue and many plaques had additional smaller lipid regions that were either ignored or segmented to be included with the single lipid region. Some plaques had lipid deposits and severe intimal thickening nearly the whole circumference of the plaque, making it difficult to segment between the shoulders and IT (see Figure 3.11).

The vessel lumen were not pressurised, which likely altered geometry and fibre structures compared to the *in vivo* states.

The 'triangle' feature seen between the shoulders and lipid core could be independently segmented in future studies. This feature does not appear to be previously defined, so there was no guidance on how it should be segmented. These 'triangle' regions had fibre structures resembling a lap joint; fibre families appeared to split to either side of the lipid core. In engineered structures, a common failure mode of fibrous materials is delamination of at a lap joint, so mechanical investigation of this region is warranted. A recent report on carotid plaques reported 92% of fissures occurred between fibre layers, and suggested shear as a likely failure mode [Daemen et al., 2016].

Carotid samples in this study were harvested from carotid endarterectomies, so had artefacts from the surgery. In spite of rejecting severely distorted samples, both coronary and carotid plaque images had artefacts from their histological preparation, which would have impacted the fibre structures. Therefore, artefacts were repaired to be more representative of the original anatomy.

Role of Timing, Scale, and Technique of Imaging

The developmental history of these fibre structures requires further investigation. In some cases, the fibrous cap and shoulders resemble a hastily built sarcophagus to enclose the lipid core. Perhaps rapidly progressing atherosclerosis requires remodelling with insufficient time to optimise biomechanics. With more understanding of the progression of fibre architecture, pharmacological interventions may be able to target pathways promoting more stable remodelling.

Fibre properties may vary at different magnifications, but this study only considered the largest microscale fibres, as a first step in understanding the

microstructure. Other fibre parameters (such as collagen density and waviness [Rezakhaniha et al., 2012; Schrauwen et al., 2012]) and other components (such as elastin, proteoglycans, calcifications, and lipid deposits) likely contribute to mechanics, and could be considered in a follow on to this study. Filtering the histology image by colour could be used to segment different components such as lipid, cell nuclei, muscle fibres, elastin, and collagen.

Presently, collagen fibres cannot be visualised *in vivo*. Developing technologies may one day allow for these observations directly, perhaps through intravascular optical coherence tomography [Nadkarni et al., 2007] or texture analysis through MRI [Flamini et al., 2013]. Continued work on developing these technologies is required. Before then, it may be possible to infer fibre parameters from imaged plaque geometry. Some links were found here between geometry and fibre structure, but these links were generally weak. New geometry parameters that describe the shape of the shoulder lumen and lipid core may be more predictive of disruptions to fibre structure in the shoulders and 'triangle' regions.

3.8 Conclusions

Histological images of coronary and carotid plaques were studied through image processing to quantify geometry and fibre structure in different regions of the plaques. The carotid plaques were found to be significantly larger than the coronary plaques, but there was no significant difference in plaque burden, lipid fraction, or lipid arc between the two plaque types.

Fibre structure was characterised by fibre misalignment and fibre dispersion. The shoulder regions had higher fibre misalignment than the fibrous cap or IT regions. For the shoulders, fibrous cap, or IT regions, there was no significant difference in fibre misalignment between the carotid and coronary plaques.

Fibre dispersion was also calculated for the carotid and coronary plaques. The shoulder regions had higher fibre dispersion than the fibrous cap or IT regions. Fibre dispersion within the shoulders, fibrous cap, or IT was not significantly different between the carotid and coronary plaques.

The shoulder region is a frequent site of plaque rupture. Since it was found to have higher fibre misalignment and dispersion than other regions, the role of

fibre structure in plaque mechanics and vulnerability should be considered.

Linear regression analysis was performed for geometry parameters against fibre misalignment and dispersion. In general, fibre misalignment and dispersion had weak correlation to geometry, so should be considered as independent factors in plaque mechanics.

Chapter 4

Finite Element Modelling of Atherosclerosis with Patient-Specific Geometry and Fibre Structure

4.1 Abstract

Using the geometry and fibre architecture of the atherosclerotic plaques studied in Chapter 3, patient-specific finite element (FE) models were built. To understand the influence of fibre structure, FE analysis considered isotropic (without fibre structure) and anisotropic FE models (with fibres about the local fibre orientations calculated in Chapter 3). Different maximum principal stresses were found for the isotropic and anisotropic FE models. The two model types often predicted different plaque-regions to have the highest stress, and therefore the highest rupture risk.

Stresses in the anisotropic FE models were mostly along fibres, but there were considerable shear stresses. Since tissue is strongest in the direction of fibres, failure analysis should consider stresses directed along and shearing between fibres. A recent study of carotid plaque fissures suggested most fissures are caused by delamination from shear loading [Daemen et al., 2016].

The carotid and coronary plaques were found to have differences in their mechanics, with stresses being relatively higher in the fibrous caps of carotid plaques and the shoulders of coronary plaques. Univariate linear regression models found significant relationships for plaque geometry, fibre structure, and isotropic stresses with anisotropic stresses. These regression models suggested that multiple factors contribute to stresses. Multivariate regressions improved predictive quality compared to the univariate regressions.

In summary, fibre structure was found to have a considerable role in the mechanics of atherosclerotic plaques, and should be considered in assessing stresses and rupture risk.

4.2 Introduction

Finite element (FE) analysis is frequently used in research to evaluate the mechanics of atherosclerosis and has been proposed as a tool for clinical evaluation of rupture risk [Holzapfel et al., 2014; Sadat et al., 2010]. Relationships have been established between FE stress and plaque geometry, composition, and rupture location [Cheng et al., 1993; Kiousis et al., 2009; Li et al., 2008; Teng, 2011; Teng et al., 2012]. However, the role of fibre structure in plaque mechanics has been mostly overlooked in previous FE studies.

Most previous FE models of plaques have used an isotropic material model [Sadat et al., 2010; Teng et al., 2012; Versluis et al., 2006; Wenk et al., 2010] or an anisotropic material model with an assumed, rather than calculated, fibre orientation [Chai et al., 2014; Gasser and Holzapfel, 2007; Holzapfel et al., 2014; Kiousis et al., 2009; Rodríguez et al., 2008].

Using fluid-structure interaction models, the direction of maximum principal stress vectors in a plaque (modelled isotropically, ignoring fibres) have been found to be well aligned with the fibre structure (from histology and image processing) [Pagiatakis et al., 2015]. An anisotropic FE model of the carotid bifurcation has been built, in which fibres are iteratively remodelled to optimise fibre orientation and dispersion to the principal strains [Creane et al., 2011]. The *in silico* remodelled fibre structures were compared qualitatively to fibre structures that had been previously described in healthy and atherosclerotic arteries.

An anisotropic constitutive model for arterial tissue has been developed by Gasser et al. [2006]. The model separates the tissue into an isotropic component (for the ground matrix) and an anisotropic component (for the collagen fibres in the tissue). Tissue fibres are assumed to have a primary fibre orientation about which individual fibres are dispersed. The degree of anisotropy is determined by the degree of fibre dispersion.

This material model was used for the fibrous tissues in the plaques in this study, and will be more thoroughly reviewed in Section 4.3.4. For each carotid and coronary plaque analysed in Chapter 3, two comparative FE models were made: isotropic (fibre structure ignored) and anisotropic (fibre structure included). For the anisotropic FE models, components of stress relative to the fibre direction (σ_{11}, σ_{22}, and σ_{12}; see Section 4.3.5) were calculated.

The FE models were created in the Abaqus FE package (Abaqus 6.13-2, Dassault Systèmes, France; see Section 4.3). Plaque geometry was reconstructed from histology images as a 2D FE models in Section 4.3.1. Section 4.3.3 describes the boundary conditions and loading used in the FE models. The constitutive models and material parameters used in the FE models are described in Section 4.3.4. Section 4.3.5 describes parameters used in the FE solver and output variables from the FE analysis. Validation, verification, and sensitivity analysis of the FE models are detailed in Section 4.4.

Results of the FE models are presented in Section 4.5. Section 4.5.1 details summary results by region and plaque type, and compares stresses found for the carotid plaques with those from coronary. Results from the isotropic and anisotropic FE models are compared in Section 4.5.2. Components of anisotropic stress relative to the fibre direction are compared in Section 4.5.3. Stresses within different plaque regions are compared in Section 4.5.4. Section 4.5.6 reports results for the stress transformation angle, which is the angle between maximum principal stress and fibre direction.

Section 4.6 presents linear regression models between FE stress results and plaque geometry (Section 4.6.1), fibre structure (Section 4.6.2), and isotropic maximum principal stress (Section 4.6.3). Multivariate regressions were also used to predict FE stress results (Section 4.6.4).

Section 4.7 discusses these results and their broader implications. The risk of rupture suggested by the FE results is considered in Section 4.7.1. Advantages of these FE models are discussed in Section 4.7.2. Differences in mechanics between plaque types and plaque regions are described in Section 4.7.3. Limitations of this study and suggested further directions are discussed in Section 4.7.4. Key findings and conclusions of this chapter are presented in Section 4.8.

4.3 Finite Element Analysis Methodology

To build the FE models, plaque geometries were imported to Abaqus, consisting of contours for the lumen, lipid core, and fibrous tissue (itself including the intima, media, and adventitia, see Section 4.3.1). Local mean fibre orientation, calculated for each plaque in Chapter 3, was assigned to each element in FE mesh of the fibrous tissue (see Section 4.3.2). A static, physiological pressure (16 kPa; approximately 120 mmHg) was applied to the luminal wall, and models were constrained to their 2D plane (see Section 4.3.3).

Section 4.3.4 details the material models used for the fibrous and lipid tissues. To assess the importance of fibre structure, two FE models were created and compared for each plaque: an isotropic FE model (with fibre dispersion of κ=0.333) and an anisotropic FE model (κ=0.136). The FE solver parameters and output variables are detailed in Section 4.3.5. The coronary plaque that was used in Chapter 3 will also be used throughout this section to illustrate the models.

4.3.1 Finite Element Model Geometry

Contours for the external and lipid boundaries of the plaques were used to make the 2D FE geometry for each plaque (see Section 3.3.3). Recall that the outer contour of carotid plaques was dilated by 20% to account for the adventitia, which was left in the carotid endarterectomy patient.

Points defining the contours of the lumen, outer, and lipid core edges (see Figure 4.1A) were imported to the Abaqus FE analysis package as splines.

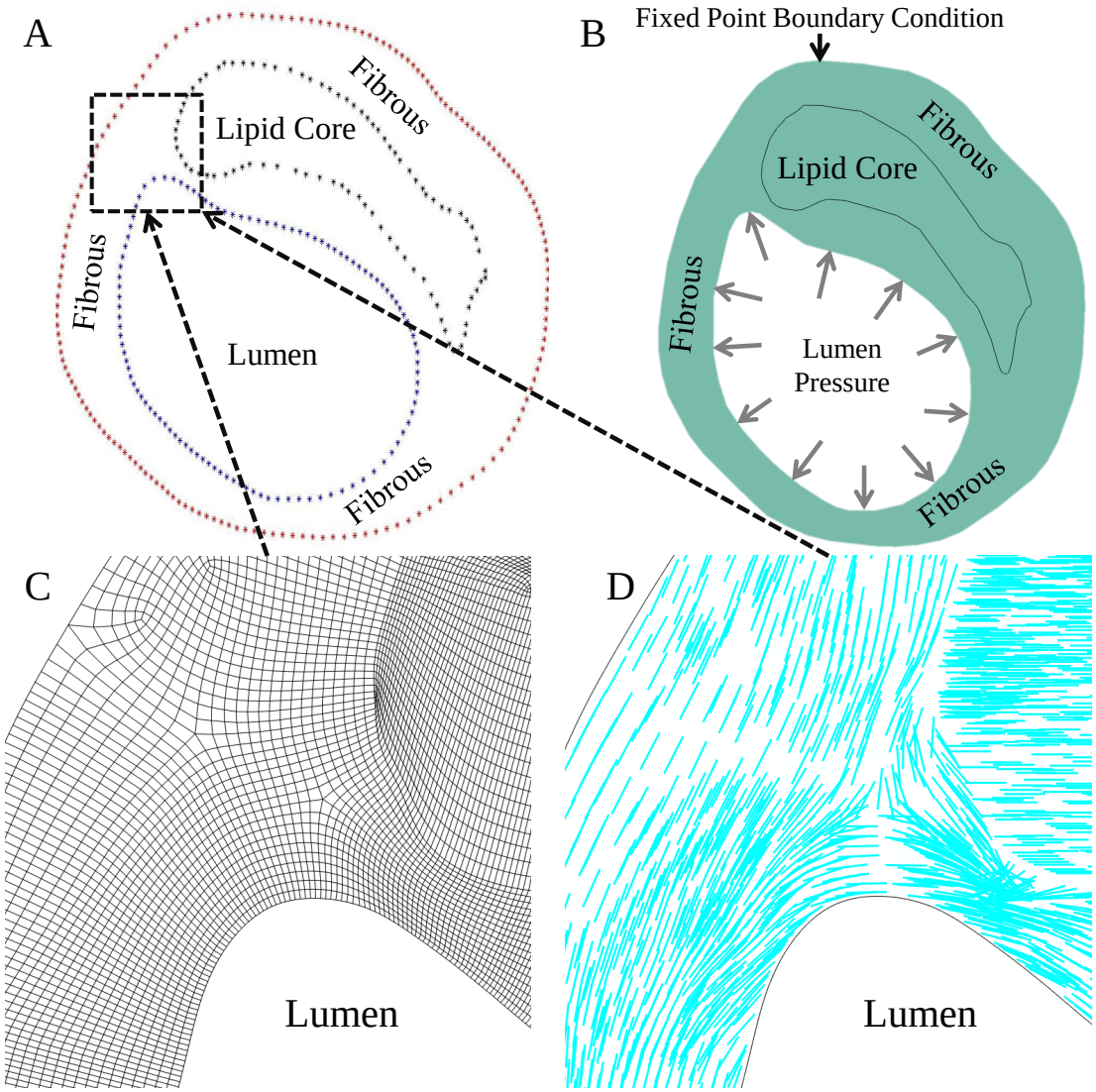

Figure 4.1: A.) Geometry contours for the illustrative coronary plaque, B.) Part in Abaqus, showing the fibrous section, lipid core section, loading by lumen pressure, and fixed point used as a boundary condition, C.) FE mesh density transitioning from the lumen to outer edge of the shoulder region, and D.) Local fibre orientation assigned to the shoulder of the FE model.

The imported contours resulted in three regions of the model: lipid core, fibrous tissue, and lumen. Fibrous tissue included the adventitia, media, intima, fibrous cap, shoulders, and IT. The lipid core and fibrous tissue were each assigned to sections (see Figure 4.1B).

4.3.2 Elements, Meshing, and Orientation Assignment

The FE meshing used S4R elements, which are 4-node, 3D quadrilateral stress/ displacement shell elements with a reduced integration and large-strain formulation. While the models are rendered 2D by imposing a boundary condition on the shell surface (see Section 4.3.3), 3D elements are required for Abaqus's built-in material model for modelling tissue with fibres dispersed around a primary orientation. Thus, the shell elements were assigned a thickness of 1.0 mm. Mesh seed spacing was informed by a mesh convergence study (see Section 4.4.3).

Mesh Seeding

For an efficient mesh, the lumen, lipid, and outer edge were independently assigned mesh seed densities. The lumen edge used 5 μm seeds, to increase the mesh density where stresses were expected to be highest. For computational efficiency, the outer edge had 50 μm seeds, because stresses were expected to be lower. The lipid contour was seeded with 10 μm edge seeds, to promote a smooth transition in mesh density between the lumen, lipid, and outer edge. For comparison, collagen bundles in the histology images were about 10-25 μm wide.

Meshes were created from the seeds using Abaqus's *medial axis* algorithm. Coronary FE models had about 30,000 elements (Figure 4.1C shows a representative mesh of a shoulder region) and carotid models had about 100,000 elements.

Orientation Assignment

After meshing, the nodes (index and coordinates) and elements (index and nodes) of the model were exported to Matlab. Elements were mapped to pixels in the plaque image. The local mean fibre orientation (see Section 3.4.4) was assigned to each element as an Abaqus *orientation field* (Figure 4.1D). The orientation of the fibrous tissue is generally tangential to the lumen and lipid, as was observed in

previous chapters. Since the lipid sections were isotropic, they do not have fibre orientation and Figure 4.1D shows horizontal orientation (the default element orientation is the first unit vector of the global coordinate system).

4.3.3 Boundary Conditions and Loading

A fully constrained boundary condition was applied to the first point of the outer geometry contour (indicated Figure 4.1B). The surface of the shell geometry was constrained to its plane, making the analysis 2D in spite of using 3D shell elements. A radially-outward static pressure of 16 kPa (approximately 120 mmHg, representing systolic blood pressure) was applied to the luminal surface.

4.3.4 Material Model

To isolate the role of fibre structure in mechanics, the FE models were simplified by assuming material in the plaque was either fibrous tissue or lipid core. In reality, different fibrous tissues (intima, media, and adventitia) have differences in their composition and material properties, and tissues often have a mixture of lipid and fibres. There are also other components in plaques such as calcium and intra-plaque haemorrhage that were considered as being either fibrous or lipid tissue in these FE models.

The fibrous tissue in the plaque was modelled as a Gasser-Ogden-Holzapfel anisotropic, incompressible, hyperelastic solid. For the full description and development of this material model, please refer to the original paper describing it [Gasser et al., 2006]. A brief summary will be presented here, starting with the material's strain energy density ($\overline{\psi}_f$) function in Equation 4.1:

$$\overline{\psi}_f = C_{10}(\overline{I}_1 - 3) + \frac{k_1}{2k_2}(\exp\{k_2[\kappa\overline{I}_1 + (1-3\kappa)\overline{I}_4 - 1]^2\} - 1) \qquad (4.1)$$

where C_{10} represents the neo-Hookean, isotropic contribution of the matrix of the material. Constants k_1 and k_2 are parameters describing the response of the fibrous portion of the material, and contribute to considerable strain stiffening. The FE models used previously reported material parameters for carotid plaque tissue (C_{10}=0.056 MPa, k_1=41.08 MPa, k_2=1749.6) [Heiland et al., 2013].

Fibre dispersion (κ) is the same as was defined in Section 3.4.6. Here, κ was used to differentiate isotropic FE models (κ=0.333; ignores fibre structure) from anisotropic FE models (κ=0.136; considers fibre structure).

Invariant $\overline{I}_1$ in Equation 4.1 is the first invariant of $\overline{\mathbf{C}}$, which is the distortion component of the right Cauchy-Green deformation tensor ($\mathbf{C}$), as in Equation 4.2:

$$\overline{I}_1 = \mathrm{tr}(\overline{\mathbf{C}}); \quad \overline{\mathbf{C}} = J^{-\frac{2}{3}}\mathbf{C} = J^{-\frac{2}{3}}(\lambda_r^2 + \lambda_c^2); \quad J = \det(\mathbf{F}); \tag{4.2}$$

where λ_c and λ_r are the respective stretch ratios in the circumferential and radial directions. The deformation gradient is $\mathbf{F}$, and J describes the change in the material volume (assumed to be incompressible; J=1). Since the FE model was constrained to be 2D and arteries have limited axial deformation with blood pressure, the model assumed there was no axial strain in the artery (λ_a=0).

The fibre orientation is described by the invariant $\overline{I}_4$, which assumed fibres in the 2D cross-section belonged to a single family of fibres (see Equation 4.3):

$$\overline{I}_4 = (\lambda_c \cos\theta_\mu)^2 + (\lambda_r \sin\theta_\mu)^2 \tag{4.3}$$

where θ_μ is the local mean fibre orientation (see Section 3.4.4), assigned element-by-element. As analysis was restricted to the 2D cross-section, fibre orientation was only considered in this plane. Typically, this constitutive model is used for modelling the circumferential-axial fibre structure, with two opposing families of fibres wound helically along the artery [Gasser et al., 2006].

The lipid core was modelled as an incompressible, isotropic, hyperelastic solid with a reduced polynomial formulation, as in Equation 4.4:

$$\overline{\psi}_l = K_{10}(\overline{I}_1 - 3) + K_{20}(\overline{I}_1 - 3)^2 \tag{4.4}$$

Parameters were found by fitting uniaxial strain data for plaque lipid to this strain energy density function ($\overline{\psi}_l$). The material parameters were K_{10}=22.5 kPa and K_{20}=215 kPa (data and fitting method from segmented lipid tissue of human carotid plaques [Teng et al., 2014]).

4.3.5 Finite Element Solver Parameters and Outputs

Non-linear geometry controls (*nlgeom* in Abaqus) and a stabilisation *damping factor* of 2×10^4 were used in the FE analyses. The initial step size was 0.001 and the maximum allowed step increment was 0.25, expressed as a proportion of the applied load. The analysis was run using 95% of eight 2 GB processors. Each FE model took approximate two hours to simulate.

Analysis was run for the isotropic model first. The dispersion value of the fibrous tissue was changed, and the analysis was run as the anisotropic model. Stress and element area were extracted from completed analysis. The following stresses were extracted, and will be further referred to by the listed terms:

- Isotropic maximum principal stress ($\sigma_{1,i}$)
- Anisotropic maximum principal stress ($\sigma_{1,a}$)
- Axial stress (σ_{11}): anisotropic stress directed along fibres
- Transverse stress (σ_{22}): anisotropic stress normal to fibres
- Shear stress (σ_{12}): anisotropic stress for sliding between fibres
- Anisotropic stresses: a collective reference to the σ_{11}, σ_{22}, and σ_{12}
- Stress transformation angle (θ_σ): the orientation of $\sigma_{1,a}$ relative to fibres

Anisotropic maximum principal stress ($\sigma_{1,a}$) is related to the anisotropic stresses by Equation 4.5:

$$\sigma_{1,a} = \frac{\sigma_{11}+\sigma_{22}}{2} + \sqrt{\left(\frac{\sigma_{11}-\sigma_{22}}{2}\right)^2 + (\sigma_{12})^2} \tag{4.5}$$

In a previous FE study, maximum principal stress in the fibrous cap was found to be aligned with fibre orientation calculated from histological images [Pagiatakis et al., 2015]. In the present study, the stress transformation angle (θ_σ) was calculated for the angle between the local primary fibre orientation, or axial direction of the fibres, and anisotropic maximum principal stress (see Equation 4.6):

$$\theta_\sigma = \frac{1}{2}\text{atan}\left(\frac{2\sigma_{12}}{\sigma_{11}-\sigma_{22}}\right) \tag{4.6}$$

The stress transformation angle is equivalent to the stress transformation between the coordinate system of a fibre and the plane stress condition. Similar to fibre misalignment and shear stress, θ_σ will be reported as an absolute value.

Plaque Regions

Stresses were calculated for each segmented region of each plaque: fibrous cap, shoulders, intimal thickening (IT), global, and global excluding lipid (GEX; see Section 3.3.4). Elements in the FE models were mapped to the plaque regions that had been segmented in images of the plaques in Section 3.3.4.

The fibrous cap and shoulder regions are nearer to the lipid core and along the lumen. Plaque rupture occurs in these regions. The IT region is along the lumen, but contains tissue that is less affected by atherosclerosis. Therefore, the fibrous cap and the shoulder regions can be compared with the IT region to identify changes to mechanics from atherosclerosis. The global region is for all tissues in the plaque, including the fibrous cap, shoulders, IT, and lipid core. The GEX (global excluding lipid) region is all the fibrous tissues.

Criteria for Reporting Stresses

FE models attempting to quantify risk of plaque rupture often compare stress results to experimentally-derived failure strength [Holzapfel et al., 2014]. Thus, it is desirable to be able to compare some characteristic stress state for a plaque or plaque region. However, peak elemental stress could be unrealistically high due to poor mesh sizing, poor mesh quality, or discontinuities in fibre orientation (see Section 4.4.2). Previously, FE analysis of abdominal aortic aneurysms found that the 95^{th} or 99^{th} percentile of wall stress was more reproducible than the peak stress [Speelman et al., 2008].

Furthermore, the FE elements were smaller than fibres, so a stress for fibre failure should be present in several elements. There can be considerable differences in stress between the highest-stress elements, as will be shown in Section 4.4.2. Therefore, the peak stress in a FE model may be much higher than the stress that could actually cause failure.

For comparison between FE models and with experimental failure stresses, two metrics were developed for reporting maximum stress in a plaque region: an area-based criterion and a 95% criterion. Results are presented in Section 4.5 for the area-based criterion and Appendix A.3 for the 95% criterion. The criteria were designed to provide an objective characteristic stress for each plaque region, while avoiding the limitations of the peak elemental stress. Both criterion gave similar results (compared in Section 4.5.5).

Area Stress Criterion

First, stress was calculated as the stress exceeded by 2500 μm^2 of a segmented region (will be referred to as the area criterion). Elements in each plaque region were ordered by stress. The cumulative area of the highest-stress elements was calculated until 2500 μm^2 of the region was found. The stress of the last element required to reach this sum was determined to be the characteristic stress for that plaque region. This was done for each plaque region and each stress type.

An area of 2500 μm^2 is equivalent to a 50$\times$50 μm zone, which was large enough to contain several collagen fibre bundles (10-25 μm wide). Therefore, the stress reported by the area criterion covers an estimated minimum area for fracture. The area criterion assumed relatively few artefacts from modelling and avoided bias from large areas with low stress.

The area criterion ignores around 15-30 of the highest-stress elements in each region and reports the next highest stress. The highest-stress elements in a region were usually adjacent to one another, although larger regions sometimes had several high-stress zones. Because they included the elements in other regions, the global and GEX regions reported similar stresses that were at least as high as those in the sub-regions.

95% Stress Criterion

Second, stress was calculated as the 95^{th} percentile of stress for the area of a segmented region (will be referred to as the 95% criterion). Similar to the area criterion, elements were ordered by descending stress and the cumulative area of the highest stress was found. For the 95% criteria, the summation threshold was

the stress exceeded by 5% of the area of the region. Therefore, the number of elements making up the 95% criterion varied with region size. For the illustrative plaque, the approximate number of elements with stress exceeding the reported stress were: 40 for each shoulder; 180 for the fibrous cap; 250 for the IT; and 2100 for the global region. For comparison, elements had about 5-10 μm edges, and each element had an area of about 70 μm^2 (see Section 4.3.2).

The 95% criterion of stress assumed that errors from modelling were equally distributed between regions, justifying larger regions having more elements above the reported stress. A downside of this metric was that it is decreased if a region has large areas of low stress. The highest stresses were usually found in relatively small zones near the lumen (see Figure 4.2).

Stress Transformation Angle Reporting

Unlike other FE results, the stress transformation angle was reported as the median and intra-quartile range within a region. The mechanical relevance of the stress transformation angle also depends on the magnitude of stress. An element could have a high stress transformation angle, but is not relevant if the magnitude of stress is low. Therefore, stress transformation angle was used to generally characterise a region, in a similar manner as fibre misalignment was reported in Chapter 3.

Batch Analysis

As a batch process, isotropic and anisotropic FE models were created and run for each of the 16 coronary and 15 carotid histological plaque samples.

4.4 Model Verification and Validation

Having outlined the FE model construction and parameters, a series of short studies providing verification and validation of the FE models will be detailed. Except where otherwise noted, the representative coronary plaque that demonstrated the fibre structure methods in Chapter 3 will be used in the FE verification and validation studies.

First, stress band plots will illustrate the morphology of the various stresses in Section 4.4.1. Next, a mesh density convergence study will be described in Section 4.4.3, justifying the seed spacing for the lumen, lipid, and outer edges of the plaque. Thirdly, a study of FE sensitivity to the added adventitia thickness in a representative carotid plaque will be described in Section 4.4.4. Fourthly, Section 4.4.5 will report a sensitivity study of FE results to local fibre orientation. Lastly, the sensitivity of FE results to fibre dispersion will be considered in Section 4.4.6.

4.4.1 Representative Stress Band Plots

FE visualisation plots are shown for the isotropic (Figure 4.2A) and anisotropic FE models (Figure 4.2B-E) of the coronary plaque that was used for figures in Chapter 3. Discussion of these stress plots will be made to reflect general observations for all coronary and carotid plaques that were studied.

For any stress type, stresses were generally higher near the lumen, particularly in the shoulder regions. There were often increased stresses at the interface between the lipid and fibrous tissues. These features have been noted in previous FE models of atherosclerosis, and the magnitude of stresses are comparable [Holzapfel et al., 2014; Teng et al., 2013b].

For the isotropic models (Figure 4.2A), isotropic maximum principal stress was usually highest in the shoulder regions, especially when these regions had tighter radii of curvature. Stresses were low deeper into the tissue.

For the anisotropic FE model, slender bands of higher anisotropic maximum principal stress and axial stress reached deeper into the tissue (bands indicated by red arrows in Figure 4.2B and C). Axial stress was the largest component of anisotropic stress and was nearly as large as anisotropic maximum principal stress. Fibre orientation, which is also the direction of axial stress, is therefore linked to mechanics. Shear and particularly transverse stresses were about an order of magnitude lower than axial stress. While tensile transverse stresses could lead to Mode II fracture, transverse stress was mainly compressive and tensile stresses were low. Delamination from shear is another proposed failure mode, resulting in a Mode I or III fracture [Daemen et al., 2016]. While the axial

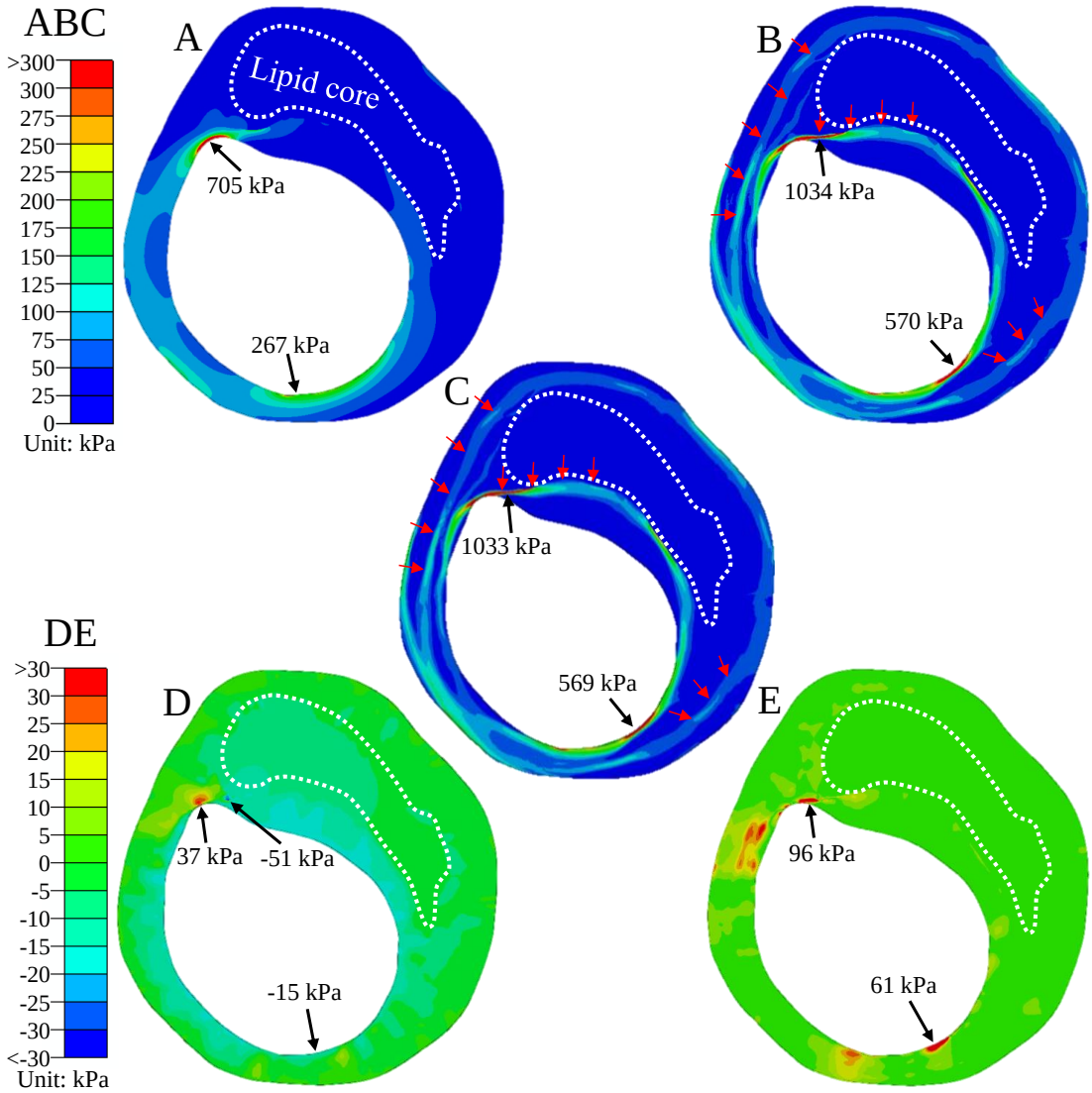

Figure 4.2: FE stress results for the illustrative plaque for A.) Isotropic maximum principal stress, B.) Anisotropic maximum principal stress, C.) Axial stress (nearly identical to anisotropic maximum principal stress), D.) Transverse stress, and E.) Magnitude of shear stress, in kPa. Local peak stresses are indicated. Red arrows in B and C indicate deep bands of higher stress compared to the deeper tissues in the isotropic model. Note different scales for ABC and DE.

stresses were the highest of the anisotropic stresses, the tissue is weaker in other loading modes. Transverse and shear stresses, while lower than axial stress, could still be responsible for failure.

4.4.2 Probability Density Distributions of Stresses

Like fibre orientation and dispersion in Chapter 3, stresses within a plaque varied considerably by location. Probability distribution plots were used to understand the variability within each segmented region of the representative coronary plaque. The bars of the probability distribution plots in this section indicate the density of stress within the indicated range for the region being plotted. Probability density is used rather than frequency to allow easier comparison between regions of different sizes.

Probability density plots of anisotropic maximum principal stress are shown by plaque region in Figure 4.3. The value calculated by each stress criterion (peak stress, 95% criterion, and area criterion) are labelled.

For all regions, most elements had low stress, with the highest levels of stress being found in only a few elements in the region. The shoulder region (Figure 4.3A) and fibrous cap (Figure 4.3B) had more elements with high stress than the IT region (Figure 4.3C). The global region (Figure 4.3D), which includes all elements in the FE model, had a small number of elements with high stresses but most had low stress.

The three stress criteria (peak, area, and 95%) would report considerably different stresses for each region (criteria are labelled by vertical lines in Figure 4.3). The area criterion (green) seems to be the most realistic assessment, and is more consistently placed in the distribution plots in the different regions. The peak stress (blue) is often much higher than the next most stressed elements, so is vulnerable to singularities, mesh distortion, and discontinuities between fibres. Conversely, the 95% criterion is clearly influenced by the number of elements in a region, and severely under-reports stress in the fibrous cap and global regions.

Probability density plots for other stress types show similar patterns, and are included in Appendix A.2.1.

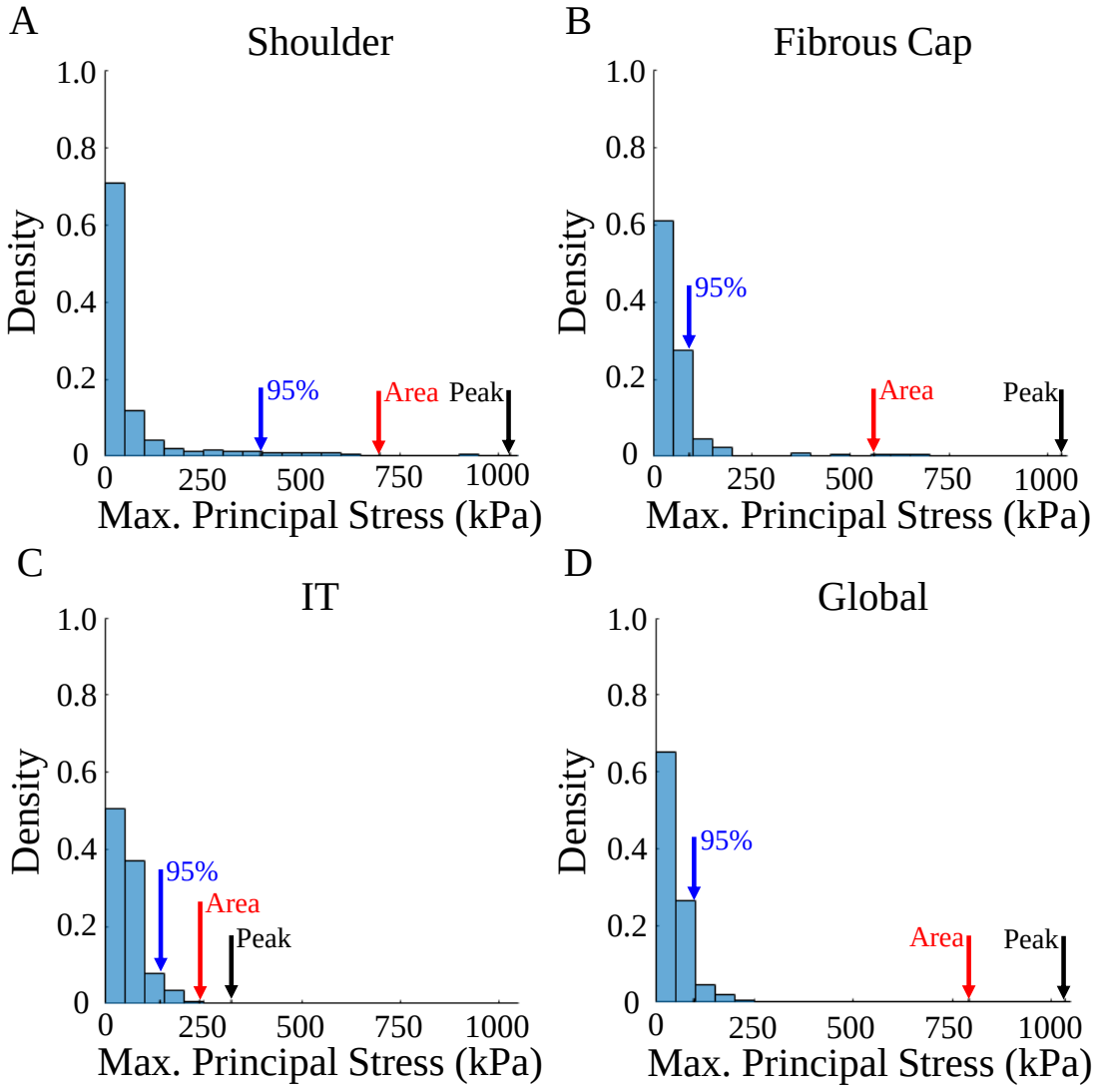

Figure 4.3: Probability density plots for anisotropic maximum principal stress by region: A.) Shoulder, B.) Fibrous cap, C.) IT, and D.) GEX. Peak, area criterion, and 95% criterion stresses (kPa) are labelled.

4.4.3 Mesh Convergence Study

Generally for FE models, increasing mesh density improves accuracy (assuming the mesh is of good quality), but increases simulation time. Improvements to accuracy diminish as the mesh becomes more fine, so a mesh density is said to have converged when changes to the results become negligible.

A mesh density study was performed on the anisotropic model of a representative coronary plaque. The outer edge seed density was kept consistent for all of the models (50 μm). The edge seed spacing for the lipid contour and the lumen edge were changed, with FE analysis using the combinations shown in the first two columns of Table 4.1. The table also lists the number of elements in the resulting mesh, maximum displacement in the model, 95% criterion stress, and area criterion stress.

Lipid Seeding (μm)	Lumen Seeding (μm)	Number of Elements	Maximum Displacement (μm)	95% Criterion (kPa)	Area Criterion (kPa)
50	50	3664	111.3	118	465
30	30	7245	112.6	116	634
20	20	11983	113.0	116	710
10	10	29889	112.7	112	705
10	7.5	33349	113.0	117	772
10	5	42778	113.0	122	791
10	3	55429	113.1	122	745

Table 4.1: Mesh sensitivity study parameters and results: element seed spacing for the lipid and lumen edges, number of elements in the generated mesh, the model's maximum displacement, and the anisotropic maximum principal stress by the 95% and area criteria.

The maximum displacement in the model is almost constant for element seeds of 20 μm and smaller. This would suggest the overall stiffness of the model has converged for these mesh densities.

Stress by the 95% criterion changed by less than 10% across the range of mesh spacings that were considered. When lumen seed spacing was decreased from 5 μm to 3 μm, the 95% criterion stress did not change.

For the area criterion, stress increased considerably between the mesh with 50 μm seed spacings and that with 20 μm. For mesh seed spacings of 20 μm or less, area criterion stresses were within about 10% of one another.

Section Discussion

Based on this mesh convergence study, FE models in this chapter used the element seed spacing of 10 μm for the lipid contour and 5 μm for the lumen contour. At this mesh density, variability from mesh size is considerably less than variability of soft tissue material properties. These sizes are also structurally justified, as they are a similar or smaller size than the fibres in the tissue (diameter of about 10-25 μm).

Several factors that contribute to stress variability in these models will not improve with a finer mesh, especially in elements with the highest stresses. A finer mesh could even increase stresses calculated at singularities in the model, such as at sharp corners in the geometry or discontinuities in the fibre structure. With re-meshing, stresses could vary from changes to element shapes and re-sampling of the fibre structure. Considering this, the area criterion stress would likely have variability regardless of mesh density.

4.4.4 Thickness of Added Adventitia Layer

As the carotid samples were obtained from endarterectomy, the entire adventitia and potentially some of the media were absent from their histology images. To account for the missing material, FE models of carotid plaques were dilated outward by 20%, which was approximately the ratio of adventitia thickness to plaque radius for coronary plaques.

Using a representative carotid plaque, a range of material was added by outward dilation of the geometry to account for the adventitia were assessed through FE analysis, to determine the sensitivity of FE results to the proportion of outward dilation. Outward dilations were considered in 10% increments, as a proportion of the plaque radius.

The outward dilations and FE results for the models built for this sensitivity study are shown in Table 4.2.

Outward Dilation (%)	Maximum Displacement (μm)	95% Criterion (kPa)	Area Criterion (kPa)
0	194	167	683
10	142	149	600
20	128	142	580
30	119	147	566
40	112	141	559
50	106	143	543

Table 4.2: Outward dilations of FE models of a carotid plaque to account for the adventitia, with FE results for each dilation. FE results were for maximum displacement, the 95% stress criterion, and the area stress criterion.

With greater dilation and therefore wall thickness, maximum displacements decreased. The 95% and area criteria of maximum principal stress also decreased as the added thickness increased. However, the largest changes to FE results were between the models with 0% and 10% added thickness. Therefore, adding thickness to carotid FE models to account for the adventitia was an important improvement to these models.

Section Discussion

Differences were relatively small between FE results of models with outward dilations between 10-30%. Therefore, the assumed dilation of 20% that was used for carotid plaques in this study is relatively insensitive to variabilities in the true thickness of their adventitia. Changes to the output parameters were relatively small for added thickness's of $\geq$20%. They can be attributed to random re-sampling variations from the slightly different meshes for each FE model.

4.4.5 Sensitivity Test: Local Fibre Misalignment

A sensitivity test of local fibre orientation or misalignment on anisotropic stresses was performed using the illustrative coronary plaque.

The fibre misalignment sensitivity study had several purposes. First, it will help define accuracy requirements for measurements of fibre misalignment, including from future *in vivo* imaging. Second, the sensitivity study will explicitly

consider the effect of fibre misalignment on stress magnitudes (links are also considered by linear regression models in Section 4.6.2). Thirdly, the sensitivity study can assess the role of fibre misalignment on the stress transformation angle between fibres and maximum principal stress. Lastly, this study considers the degree to which fibre structure affects the FE results of adjacent regions, because only one shoulder region's fibres were changed.

Description of Models

FE analysis calculated stresses in the illustrative coronary plaque for rotations of fibre orientation in the top left shoulder of the plaque (SH1) of: $-10°$, $-5°$, $0°$, $+5°$, $+10°$, and $+20°$. A positive rotation angle is defined as counter-clockwise. The SH1 region originally had median fibre misalignment of $+12.7°$, rotated counter-clockwise from the lumen tangent direction. Therefore, the effective median fibre misalignment of the SH1 in each model was the sum of the original fibre misalignment and the rotation angle (for a range of $2.7°$ to $32.7°$). No other parameters of the FE models were changed.

Stresses Versus Fibre Rotation Angle

The area criterion of stress (for each segmented plaque region and for each stress type) is plotted against the angle of rotation for fibres in the SH1 (see Figure 4.4).

For different fibre rotations, stresses changed in the left shoulder (SH1) region, the fibrous cap (FC) region, and the global excluding lipid (GEX) region. The fibrous cap is next to the SH1, and the GEX region included both the SH1 and fibrous cap. Therefore, the GEX stresses were always at least as high as those in other regions. The right shoulder (SH2) and intimal thickening (IT) regions were further from the rotated fibres, and their predicted stresses changed little with SH1 fibre rotation angle. This suggests that fibre structure is a local parameter, affecting the stress state of nearby tissues but not the entire plaque.

Maximum principal and axial stress were nearly identical (Figure 4.4A and B); stresses were mainly along fibres. In the SH1, fibrous cap, and GEX regions, these stresses were highest for the original SH1 fibre structure (no rotation), and decreased with increasing SH1 fibre rotation.

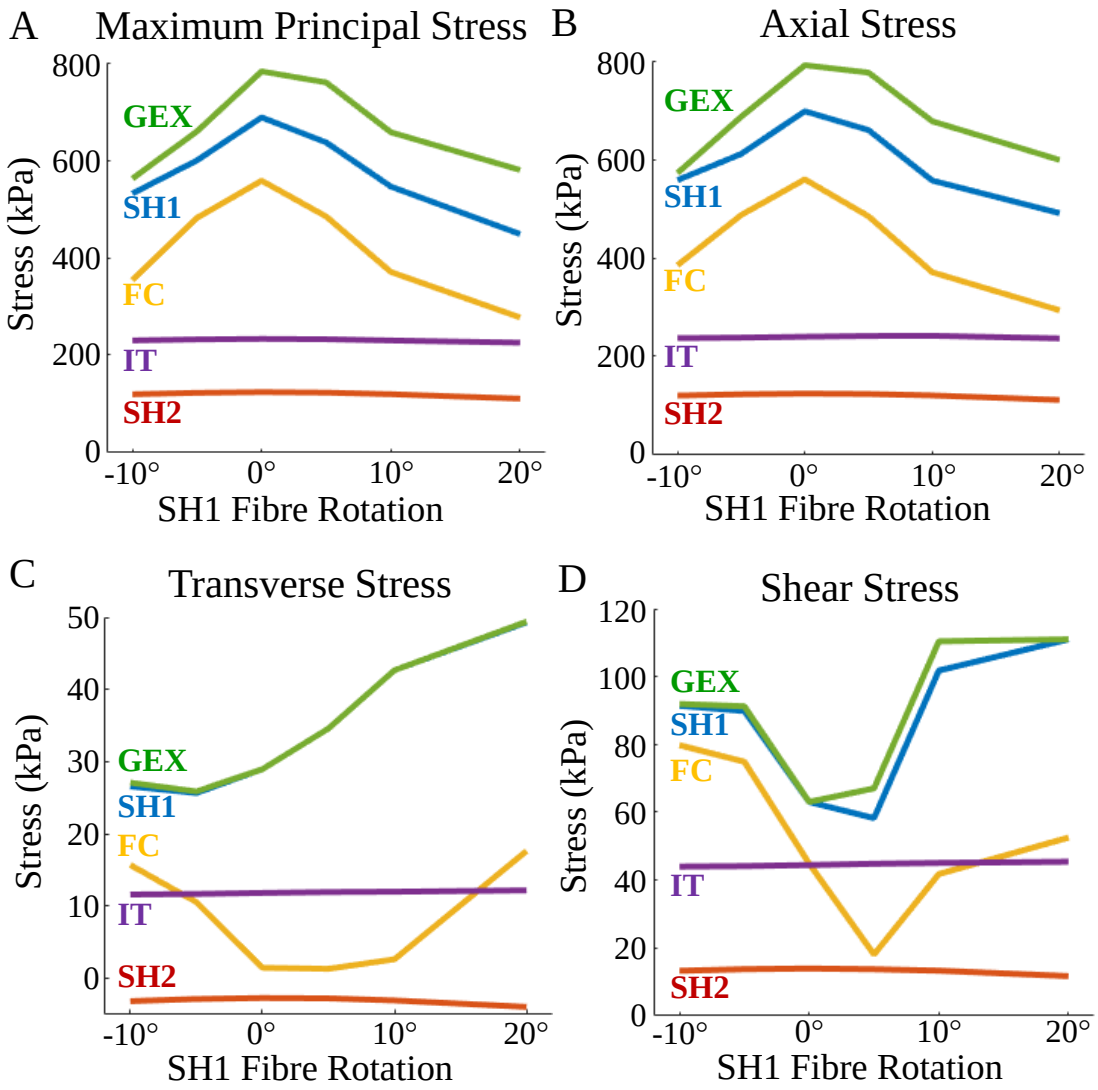

Figure 4.4: Stresses in different plaque regions versus rotation of fibre orientation in the left shoulder (SH1), for: A.) Anisotropic maximum principal, B.) Axial, C.) Transverse, and D.) Shear stresses (kPa). FC is the fibrous cap, SH1 and SH2 are the left and right shoulders, IT is the intimal thickening region, and the GEX is global excluding lipid region (all fibrous tissues).

Transverse stresses (Figure 4.4C) increased with clockwise SH1 fibre rotations, which directed fibres to be even more misaligned with the luminal surface in the SH1 region. Transverse stresses were low compared to other stress types.

Shear stresses (Figure 4.4D) in the SH1, fibrous cap, and GEX regions were lower with smaller SH1 fibre rotations, and higher for larger rotations. Recall that maximum principal stress and axial stress were highest in these regions for lower SH1 fibre rotations, so shear stress had an opposite trend.

FE Band Plots

FE band plots of maximum principal stress for the six FE models with different fibre rotations in SH1 are shown in Figure 4.5.

The models shown in Figures 4.5A and B have less fibre misalignment than the FE model with no SH1 fibre rotation (Figure 4.5C). Figures 4.5D-F have increasingly more fibre misalignment in the SH1 than the non-rotated FE model. The key features of these plots are the relative changes to the bands of higher stress near the shoulder that fibres were rotated in (indicated by red arrows).

With increasing fibre misalignment, the band of higher stress that crosses the shoulder to the fibrous cap is deflected in the same direction as fibres are rotated. Magnitudes of stress in a deeper band of higher stress, which goes from the IT to behind the lipid core, also seem to be affected by fibre rotations. This suggests fibre misalignment angle at the shoulder influences the load sharing between the fibrous cap and tissues behind the lipid core. Stress patterns away from the rotated shoulder did not change with fibre rotations.

The six FE band plots for axial stress were nearly identical to those for anisotropic maximum principal stress, so are not shown. FE band plots for transverse and shear stresses are shown and discussed in Appendix A.2.2.

Stress Transformation Angles

The stress transformation angle (between the fibre direction and direction of anisotropic maximum principal stress) was calculated for the SH1 for the FE model corresponding to each fibre rotation angle. Table 4.3 compares the fibre rotation angle in the SH1 with the median stress transformation angle.

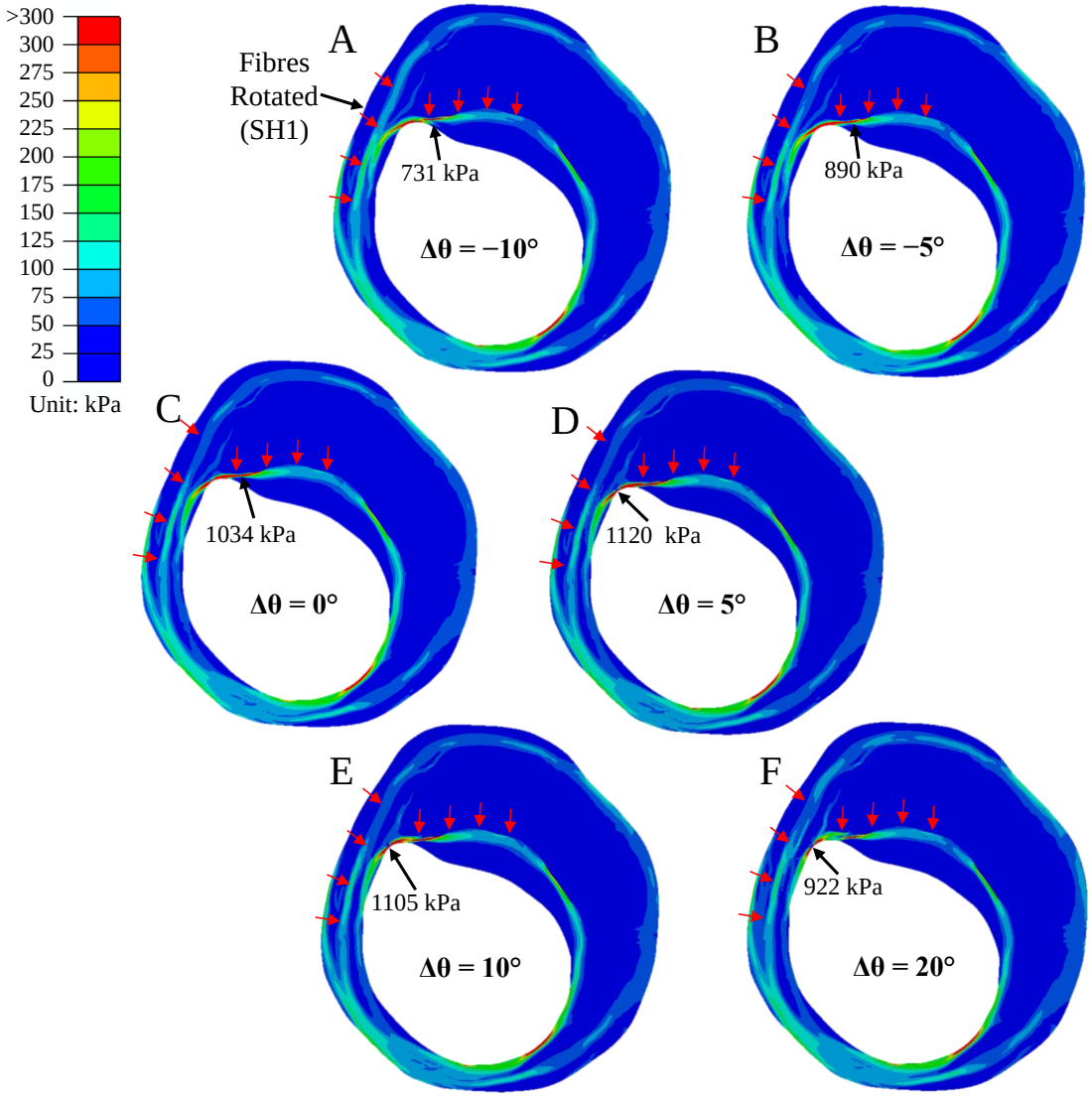

Figure 4.5: Maximum principal stress (kPa) for a study of FE sensitivity to fibre misalignment, by rotating fibres in the left shoulder (SH1) counter-clockwise: A.) −10°, B.) −5°, C.) 0° (non-rotated model), D.) +5°, E.) +10°, and F.) +20°. Key changes to stress profiles are highlighted by red arrows, peak stress in SH1 is labelled.

Fibre Rotation	Stress Angle
−10°	20.5°
−5°	17.9°
0°	17.1°
+5°	19.1°
+10°	22.7°
+20°	44.8°

Table 4.3: The fibre rotation angle in the SH1 compared to the SH1 median stress transformation angle for the orientation sensitivity test.

Recall that the stress transformation angles were calculated for each element in the region, and the angles were magnitudes (no negative angles; see Section 4.3.5). The reported (or characteristic) stress transformation angle for a plaque region was the median of these elemental values. The stress transformation angle is higher when the shear and transverse stresses are higher, relative to the axial stress. In Table 4.3, the stress transformation angle increased with fibre rotations in SH1, suggesting fibre misalignment affects the relative magnitude of stress components.

Discussion of Orientation Sensitivity Study

Stresses were found to be highly sensitive to fibre rotations (see Figure 4.4), especially for fibre rotations in the SH1 of $>\pm5°$. Even with only a $\pm5°$ change in fibre misalignment, anisotropic maximum principal stress decreased by 13% and shear stress increased by 44% for the SH1. In Chapter 3, the mean shoulder fibre misalignment for all plaques was found to be 13.0°, with an intra-quartile range of [6.74°, 17.3°] (see Table 3.4). Therefore, calculating fibre orientation from histology image and using element-specific fibre orientation is justified and required for accurate results. Future technologies attempting to characterise fibre architecture *in vivo* should aim to measure fibre orientation to within $\pm5°$.

For small SH1 fibre rotations, maximum principal and axial stresses were higher, but shear stresses were lower. This suggests the natural fibre structure is optimised for higher stresses along fibres or for lower shear. Fibre structures are thought to be created and modelled in response to local stresses and delamination

by shear has recently been proposed as a major contributor to fissures in plaque tissue [Creane et al., 2011; Daemen et al., 2016]. These observations suggest that fibre structures undergo remodelling to minimise local shear stress.

4.4.6 Sensitivity Test: Global Dispersion

While fibre orientation was calculated locally for each element in the FE models, fibre dispersion was accounted for by a constant material parameter (κ=0.136 in the anisotropic FE models, see Section 4.3.4). This was partly due to how easily each fibre structure parameter could be modified in the FE package.

To assess the model sensitivity to fibre dispersion (κ), six different κ values were tested in a representative coronary plaque FE model. By comparing the sensitivity results to the range of κ values found in Chapter 3 (see Table 3.6), the effect of approximating κ as a constant can be estimated.

Description of Models

The models used κ=0.333 (isotropic model), 0.234, 0.185, 0.136, 0.095, and 0.054. Two of these (κ=0.234 and 0.054) were used to illustrate representative values for κ in Figure 3.10. For comparison, results in Chapter 3 showed fibrous caps had the lowest dispersion (with a 25^{th} percentile of κ=0.081) and the shoulder regions had the highest (with a 75^{th} percentile of κ=0.184). No other FE parameters were changed.

Stresses Versus Fibre Dispersion

The FE model's fibre dispersion (κ) is plotted against the area criterion of stress for each segmented plaque region, plotted by stress type (see Figure 4.6).

The results for anisotropic maximum principal stress and axial stress were nearly identical (Figure 4.6A and B). The maximum principal stress and axial stress decreased with increasing κ in all regions. However, stresses only changed by about 15% or less within the range of fibre dispersion found in Chapter 3 ($0.095<\kappa<0.185$) compared to the fibre dispersion used in this chapter (κ=0.136).

Transverse stresses (Figure 4.6C) were very small compared to other stresses, and mostly compressive (see Figure A.4).

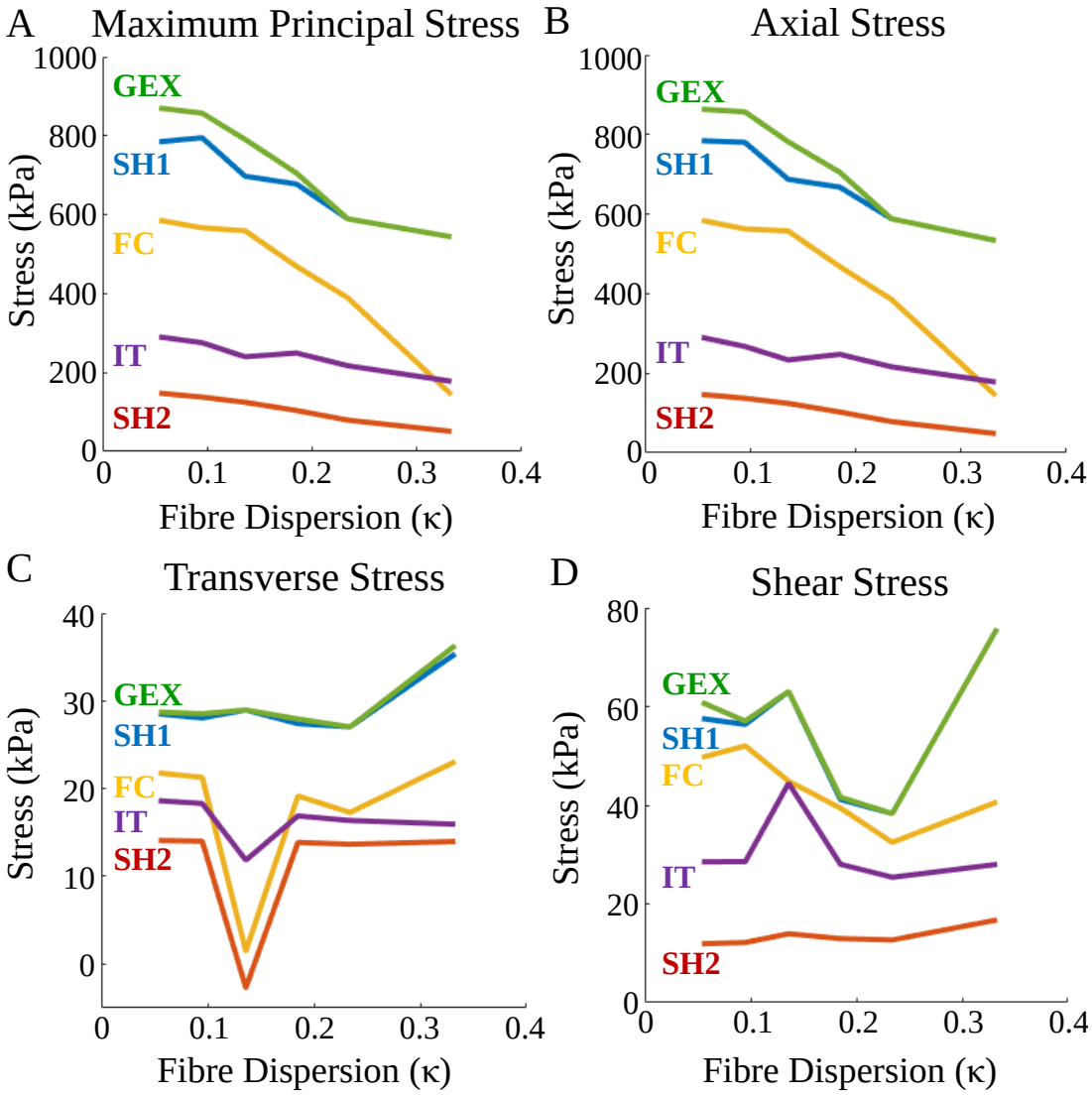

Figure 4.6: Stresses in different plaque regions compared to the FE model's κ, for: A.) Maximum principal stress, B.) Axial stress, C.) Transverse stress, and D.) Shear stress.

Shear stresses (Figure 4.6D) were higher than transverse stresses, but lower than maximum principal or axial stresses. Shear stresses changed with κ in the various regions, but these changes had no clear patterns and were relatively small in magnitude.

FE Band Plots

Maximum principal stresses for the six models are shown in Figure 4.7. With increasing κ, the slender bands of stress (indicated by red arrows in Figure 4.7) became more pronounced and peak stresses at the lumen increased. However, the biggest differences was between the isotropic model (κ=0.333, Figure 4.7A) and any of the other FE models.

Axial stresses were nearly identical to the maximum principal stresses and transverse stresses were very low; their FE band plots are not shown. FE band plots for shear stresses are shown and discussed in Appendix A.2.3.

Discussion of Fibre Dispersion Sensitivity Study

Within the range of fibre dispersion values found in Chapter 3 (see Table 3.6), stresses had relatively small changes. Therefore, the anisotropic FE models were relatively insensitive to κ, so were not limited by using an approximate global value for κ. In the future, improvements to the FE models could be made by assigning region- or element-specific dispersion values, but these improvements are expected to be relatively minor.

4.5 Finite Element Analysis Results

This section will present summary stress results for the finite element (FE) models, for the area criterion of stress. Recall that the area criterion of stress was the stress exceeded by 2500 μm^2 of a segmented plaque region (see Section 4.3.5).

Section 4.5.1 details summary FE results for each plaque type, plaque region, and stress type. The maximum principal stresses calculated by the isotropic and anisotropic FE models are compared in Section 4.5.2. Section 4.5.3 reports the components of stress relative to fibre directions in the anisotropic FE models.

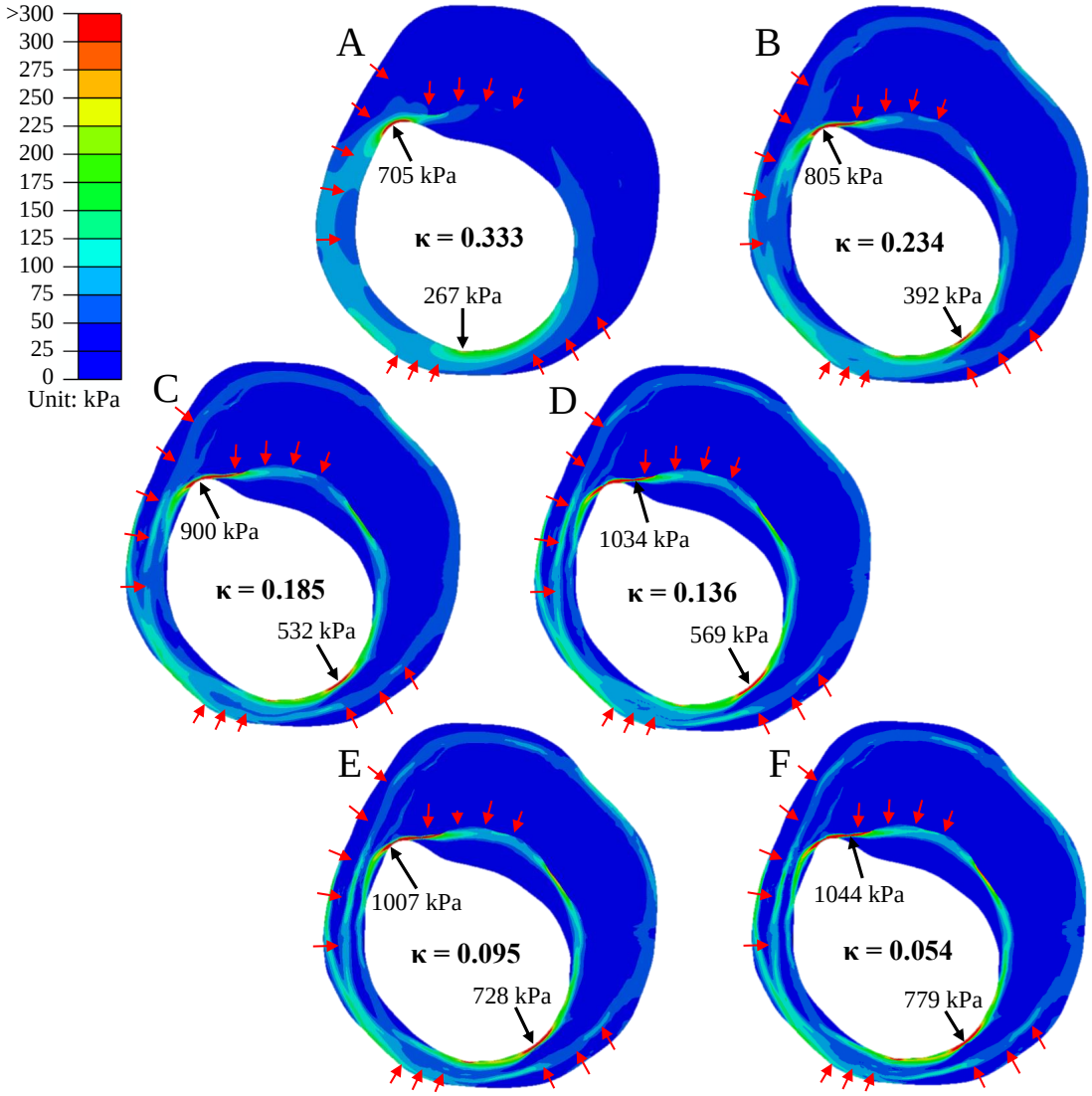

Figure 4.7: Maximum principal stress for a study of FE sensitivity to κ, using these global values for κ: A.) 0.333 (isotropic), B.) 0.234, C.) 0.185, D.) 0.136 (anisotropic FE model), E.) 0.095, and F.) 0.054; in kPa. Key changes to stress profiles are highlighted by red arrows, and the peak stresses in the SH1 and across the lumen from the SH1 are labelled.

The stresses calculated for different plaque regions are compared in Section 4.5.4. Section 4.5.5 considers stress results from the area criterion with those using the 95% criterion (see Appendix A.3 for 95% criterion stress results). Lastly, Section 4.5.6 reports the stress transformation angles (between fibres and maximum principal stress) for each plaque region.

4.5.1 Summary Stress Results

For each stress type and plaque type, the median and intra-quartile range of the area criterion of stress for each plaque-region are shown in Table 4.4. The middle three columns separate results by plaque type (all plaques, carotid, and coronary). A two-sample t-test compared the results between the coronary and carotid plaques for each combination of stress and region type, with $p<0.05$ considered significant.

The main purpose of Table 4.4 is to compare the coronary, carotid, and combined sets of plaques in the columns of the table. A secondary purpose is to provide a general sense of differences between stress types and plaque regions, which will be further detailed in Sections 4.5.3, 4.5.3, and 4.5.4.

For isotropic maximum principal stress, carotid plaques had significantly higher stress than coronary in the fibrous caps. However, stress was higher for coronary plaques in the shoulders, global, and GEX regions (see Table 4.4). For anisotropic maximum principal and axial stress, carotid plaques had significantly higher stress than coronary plaques in the fibrous cap.

Discussion of Section

Stresses in the global (whole plaque) and GEX (only fibrous tissue) regions were higher than other regions because they included all high stress zones from other regions. The GEX and global stresses were nearly identical because stresses were rarely highest in the lipid core. Therefore, analysis will focus on the regions around the lumen (fibrous cap, shoulders, and IT) and the global region will not be reported in subsequent sections.

A wide range of area criterion stresses were reported in different FE models for a given region type and plaque type. The 75^{th} percentile for a given region

Region	All Plaques	Carotid	Coronary	p
Isotropic Maximum Principal Stress (kPa)				
Fibrous Cap	95.7 [47.2, 143]	140 [82.5, 196]	55.1 [28.6, 123]	**0.015**
Shoulder	127 [77.5, 211]	91.5 [61.3, 177]	161 [120, 299]	**0.004**
IT	142 [103, 212]	121 [79.2, 158]	170 [124, 253]	0.447
Global	298 [231, 479]	243 [209, 325]	426 [279, 586]	**0.020**
GEX	298 [231, 479]	243 [209, 325]	426 [279, 586]	**0.020**
Anisotropic Maximum Principal Stress (kPa)				
Fibrous Cap	179 [86.0, 358]	319 [153, 380]	101 [21.3, 206]	**0.021**
Shoulder	223 [125, 297]	241 [134, 341]	210 [118, 275]	0.491
IT	229 [137, 315]	216 [131, 302]	234 [177, 319]	0.378
Global	496 [409, 642]	584 [447, 688]	462 [400, 542]	0.125
GEX	496 [409, 642]	584 [447, 688]	462 [400, 542]	0.125
Axial Stress (kPa)				
Fibrous Cap	173 [85.3, 356]	318 [151, 379]	94.5 [19.9, 204]	**0.021**
Shoulder	220 [124, 295]	238 [133, 331]	204 [117, 271]	0.494
IT	227 [135, 312]	215 [130, 296]	230 [176, 318]	0.387
Global	495 [407, 638]	584 [445, 669]	461 [398, 541]	0.153
GEX	495 [407, 638]	584 [445, 669]	461 [398, 541]	0.153
Transverse Stress (kPa)				
Fibrous Cap	-0.5 [-9.3, 4.9]	1.7 [-4.5, 6.8]	-4.0 [-11, 4.1]	0.059
Shoulder	7.2 [1.3, 14]	4.4 [1.3, 12.8]	8.9 [1.3, 16.4]	0.877
IT	5.0 [-0.1, 12.9]	3.4 [-1.0, 9.8]	11.1 [2.0, 14.9]	0.437
Global	21.0 [15.2, 33.6]	21.0 [14.2, 36.4]	21.0 [16.1, 32.4]	0.553
GEX	21.0 [15.2, 33.6]	21.0 [14.1, 36.4]	21.0 [16.1, 32.4]	0.554
Shear Stress (kPa)				
Fibrous Cap	19.8 [9.7, 35.0]	22.1 [18.9, 46.5]	14.5 [5.7, 31.7]	0.081
Shoulder	29.2 [17.3, 42.3]	29.8 [17.3, 42.9]	27.4 [17.3, 40.4]	0.607
IT	29.7 [21.1, 48.3]	24.8 [17.7, 46.0]	34.1 [24.8, 48.4]	0.305
Global	60.7 [49.9, 101]	71.2 [48.5, 144]	57.6 [52.1, 80.8]	0.114
GEX	60.7 [49.9, 101]	71.2 [48.5, 144]	57.6 [52.1, 80.8]	0.114

Table 4.4: Median and intra-quartile range for FE stress within each combination of plaque region (rows), plaque type (columns), and stress type (groups of rows); in kPa. p-values are for the comparison between carotid and coronary plaques.

and stress type was often twice that for the 25^{th} percentile. Since rupture is assumed to occur when stress exceeds strength and the majority of plaques do not rupture, plaques with the highest stress should be considered most closely.

4.5.2 Maximum Principal Stresses Compared

This section compares the maximum principal stresses calculated by the isotropic models with those calculated by the anisotropic models. Results for the coronary plaques will be presented first, followed by those for the carotid plaques.

Coronary Plaques

For the coronary plaques, a pair-wise comparison of maximum principal stress between the isotropic and anisotropic models is shown in Figure 4.8. A two-tailed, paired t-test was used to determine if maximum principal stress was significantly different between the two model types.

In Figure 4.8, the dashed lines indicate results for the same individual plaque and region. Results from the anisotropic model were significantly higher ($p<0.05$) than those for the isotropic model for the fibrous cap and IT region.

Carotid Plaques

For the carotid plaques, a pair-wise comparison of maximum principal stress between the isotropic and anisotropic models is shown in Figure 4.9. A two-tailed, paired t-test was used to test significant differences between the two model types.

Maximum principal stresses in carotid plaques (Figure 4.9) were significantly higher ($p<0.05$) for the anisotropic FE model than the isotropic model for the fibrous cap, shoulders, and GEX regions.

Discussion of Section

For both carotid (Figure 4.8) and coronary (Figure 4.9) plaques, maximum principal stress changed considerably between the two model types for some individual plaque-regions. Maximum principal stress could be higher or lower in either the isotropic or anisotropic FE models. Often, the individual plaque-regions with the

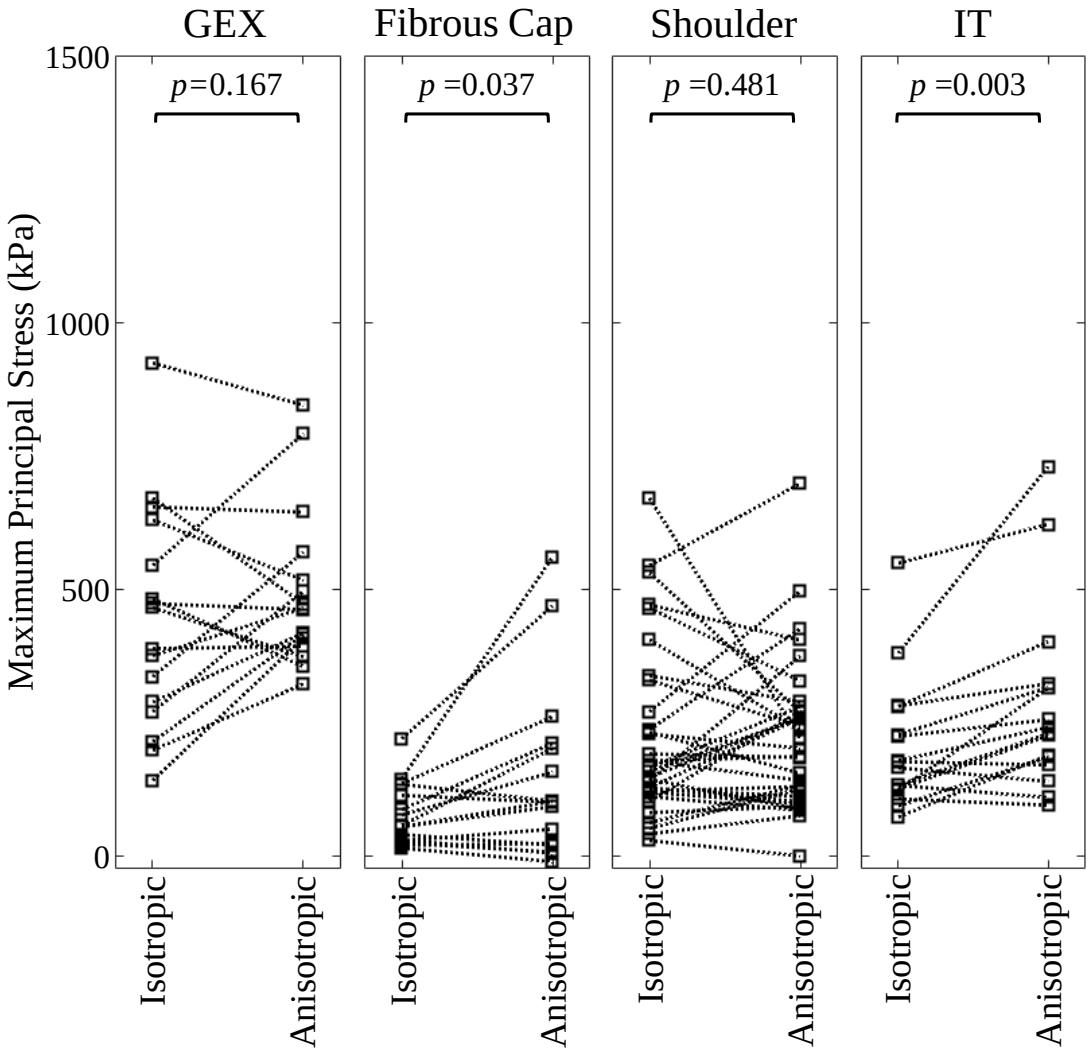

Figure 4.8: Coronary plaques: maximum principal stress pairwise comparison between isotropic and anisotropic FE models, by plaque region.

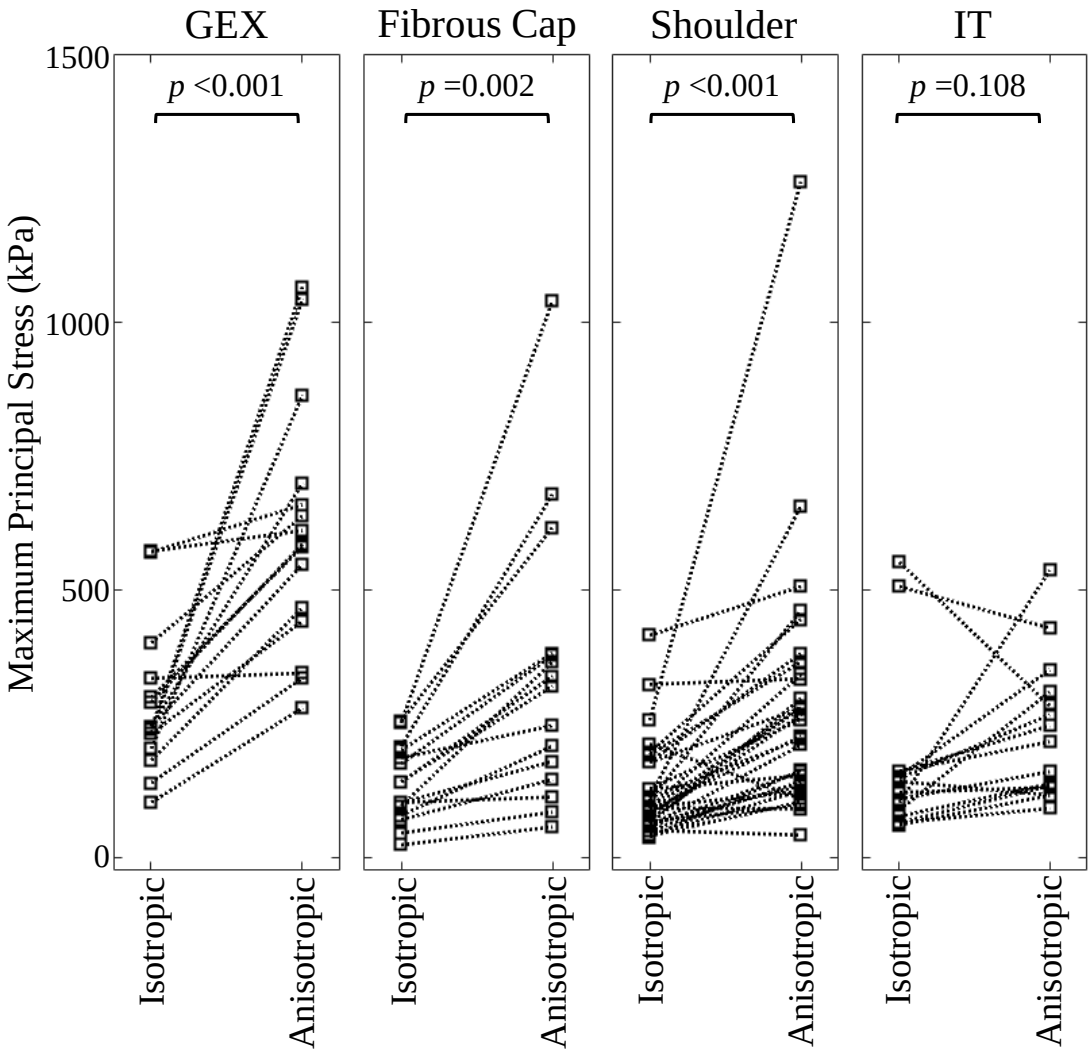

Figure 4.9: Carotid plaques: maximum principal stress pairwise comparison between isotropic and anisotropic FE models, by plaque region.

highest maximum principal stresses were different for each model type. Since the plaque-regions with the highest stresses are assumed to have the highest rupture risk, these differences imply that the isotropic and anisotropic models would each select different plaques to be high-risk.

4.5.3 Comparison of Anisotropic Stress Components

For the anisotropic FE models, components of stress were calculated relative to the fibres: axial, transverse, and shear (see Section 4.3.5). In this section, the components of stress are compared through box plots.

The box plots indicate the median (horizontal red line), intra-quartile range (blue box), expected data range (dashed whiskers), and outliers (red '+'). The expected data range (w) is found by Equation 4.7:

$$w = [q_1 - 1.5(q_3 - q_1), q_3 + 1.5(q_3 - q_1)] \tag{4.7}$$

where q_1 is the 25^{th} percentile of data and q_3 is the 75^{th} percentile of data. Outliers are points outside w, and are individually plotted.

Coronary Plaques

Figure 4.10 compares axial, transverse, and shear stress for the different regions of coronary plaques. Axial stress was higher than the shear or transverse stress. Shear stresses were higher than transverse stresses, which were compressive in most elements. Since transverse compression is not an expected failure mode and was also small in magnitude, maximum transverse compression is not reported.

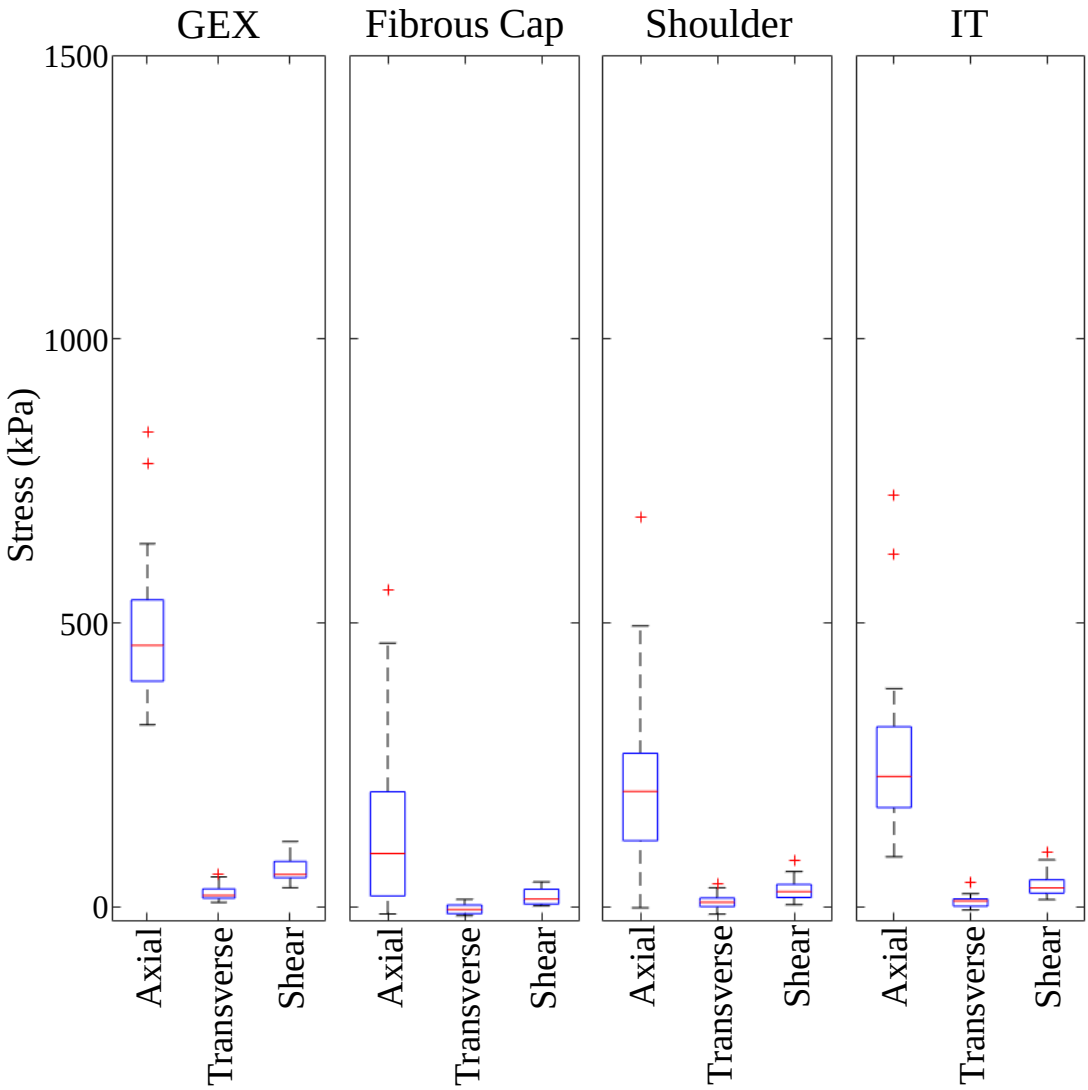

Figure 4.10: For coronary plaques: box plots comparing axial, transverse, and shear stresses for each plaque region.

Carotid Plaques

Figure 4.11 compares axial, transverse, and shear stress for the different regions of carotid plaques. Similar to the coronary plaques, axial stress was highest, followed by shear stress, and transverse stress was lowest in carotid plaques.

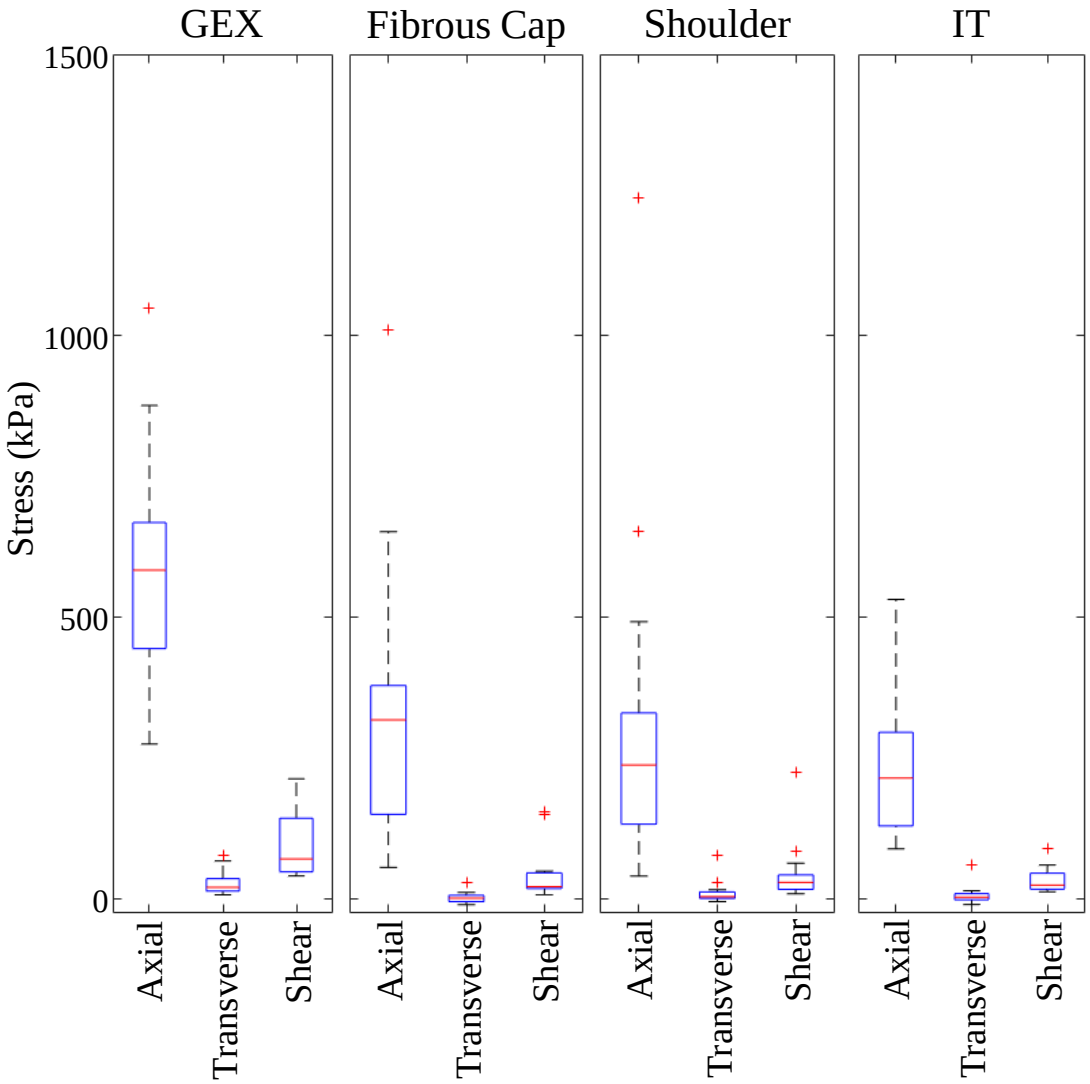

Figure 4.11: For carotid plaques: box plots comparing axial, transverse, and shear stresses for each plaque region.

Discussion of Section

For either plaque type, axial stress was considerably higher than transverse or shear. Therefore, the majority of load was carried by the fibres, and the direction of anisotropic maximum principal stress was similar to the fibre direction. Local fibre orientation therefore influences the stress state of a plaque.

Transverse stresses were smaller than shear stresses, so not likely to be responsible for failure. While shear stresses were smaller than axial stresses, artery material is also strongest in the direction of fibres. Shear and axial stress should be further investigated for their roles in tissue fracture and plaque rupture.

4.5.4 Stresses Compared between Regions

Table 4.5 provides the results of two-tailed, paired t-tests comparing the stress in two regions of the same sample. The two leftmost columns of the table indicate the regions being compared. The other two columns separate comparisons by plaque type (carotid or coronary). Rows of the table are used to group comparisons for different stress types. Since the global and GEX regions also contained the other plaque regions (fibrous cap, shoulders, and IT regions), their stresses were always significantly higher.

For the coronary plaques (left column of Table 4.5), stresses were significantly higher in the shoulders than the fibrous caps for all stress types. Isotropic maximum principal, transverse, and shear stresses were significantly higher in the IT regions than the fibrous caps in coronary plaques. Shear stress was significantly higher in the IT regions than the shoulders in coronary plaques. For the carotid plaques, no two regions were found to have significantly different stresses.

Discussion of Section

A number of significant differences were found for stresses between two different regions in the coronary plaques. Stresses in the IT regions were highest, followed by the shoulders, and fibrous cap stresses were lowest.

Stresses in the carotid plaques showed a different (but not statistically significant) trend of stresses being higher in the fibrous caps, followed by the shoulders, and the IT regions had lower stresses.

Region 1	Region 2	Carotid	Coronary
Isotropic Maximum Principal Stress			
Fibrous Cap	Shoulder	0.482	**0.000**
Fibrous Cap	IT	0.554	**0.004**
Shoulder	IT	0.175	0.562
Anisotropic Maximum Principal Stress			
Fibrous Cap	Shoulder	0.338	**0.031**
Fibrous Cap	IT	0.206	0.059
Shoulder	IT	0.257	0.126
Axial Stress			
Fibrous Cap	Shoulder	0.335	**0.033**
Fibrous Cap	IT	0.204	0.063
Shoulder	IT	0.263	0.124
Transverse Stress			
Fibrous Cap	Shoulder	0.190	**0.000**
Fibrous Cap	IT	0.627	**0.004**
Shoulder	IT	0.588	0.956
Shear Stress			
Fibrous Cap	Shoulder	0.732	**0.002**
Fibrous Cap	IT	0.549	**0.004**
Shoulder	IT	0.536	**0.041**

Table 4.5: p-values from paired t-tests of stress between the plaque regions specified in the two leftmost columns, by plaque type (columns) and stress type (grouped rows).

The relative differences in stress by region may explain differences in rupture location between plaque types that have been found in previous histological analysis. Coronary plaques had 63% of ruptures occur in the shoulders versus 37% in the fibrous caps [Richardson et al., 1989]. For carotid plaques, 40% of ruptures occur in the shoulders versus 60% in the fibrous caps [Redgrave et al., 2006]. For example, comparing the relative stress in the fibrous cap and shoulder regions between Figures 4.8 and 4.9 or Figures 4.10 and 4.11. Stresses in the shoulder regions are generally higher than the fibrous caps for the coronary plaques, but the stresses in each region are more similar for carotid plaques.

4.5.5 Evaluation of the Two Stress Criteria

In addition to the area criterion of stress, stresses were calculated for the 95% criterion (see Section 4.3.5 for criterion definition and Appendix A.3 for results).

Generally, the area and 95% criterion had similar findings. For either, maximum principal stress in a plaque-region could be considerably different between the isotropic and anisotropic FE models (see Section 4.5.2 and Appendix A.3.2). Axial stresses were highest, followed by shear stresses, and transverse stresses were low for either criterion (see Section 4.5.3 and Appendix A.3.3). The relative stress magnitudes for respective combinations of region, plaque, and stress type were similar for either criteria (see Sections 4.5.1 and 4.5.4; and Appendix A.3.1 and A.3.4).

Reported stresses were higher with the area criterion, and are closer to values reported for plaque strength [Walsh et al., 2014]. The area criteria had the advantage of having a more physical basis, by matching the estimated size of a damage process zone. Presumably, the critical size of a process zone is relatively independent of region type or size, whereas the 95% criterion reports a lower stress for regions with large areas of low stress.

Plaque rupture occurs in the fibrous cap as opposed to the shoulder region for about 60% of carotid plaques [Redgrave et al., 2006] and 33% of coronary plaques [Richardson et al., 1989]. The area criterion found stress to be higher in the fibrous cap than the shoulder regions for more plaques than the 95% criterion, but still fewer plaques than would be expected.

Discussion of Section

While the two criteria had similar findings, the area criterion seemed more representative of stresses that could cause failure. In the future, the area criterion could be further refined to ensure the 2500 μm^2 region is continuous and has some minimum dimensions. This would avoid reporting the stress from separate or very narrow zones (like the high stresses for the global and GEX regions) and would be more even representative of a critical failure size.

4.5.6 Stress Transformation Angle

Axial stresses were the largest component of stress in the anisotropic FE models (see Section 4.5.3), implying that stresses were mainly directed along fibres. The stress transformation angle, here defined as the angle between the anisotropic maximum principal stress and fibre direction, is a measure of how aligned stress was with fibres (see Section 4.3.5 for full definition). Stress transformation angle is reported as the median and intra-quartile range of values within a plaque region.

Summary Results

Summary results for the stress transformation angles for each plaque region and plaque type are reported in Table 4.6.

Region	All Plaques	Carotid	Coronary	p
Fibrous Cap	6.45 [5.08, 10.7]	5.80 [4.14, 9.20]	7.38 [5.63, 12.5]	0.076
Shoulder	10.8 [5.83, 19.3]	12.8 [5.99, 19.3]	10.0 [5.35, 18.3]	0.501
IT	7.18 [5.23, 15.1]	5.63 [4.20, 7.17]	12.5 [6.27, 17.5]	**0.008**
GEX	7.34 [6.62, 10.4]	7.34 [5.79, 10.2]	7.45 [6.69, 10.9]	0.220

Table 4.6: Stress transformation angle summary results for each plaque region and type, in degrees. The p-value is for a two-sample t-test comparing the region's stress transformation angle between the coronary and carotid plaque types.

Since the axial stresses were higher than the shear or transverse stresses, stress transformation angles were low. Stress transformation angle had considerable variability within and between individual plaque-regions. For the IT region, the

coronary plaques had significantly higher stress transformation angles than the carotid plaques, but other regions had no significant differences.

Comparison between Regions

Paired t-tests compared the stress transformation angle between different segmented regions of the same plaque (see Table 4.7).

Region 1	Region 2	Carotid	Coronary
Shoulder	Fibrous Cap	**0.001**	0.131
Shoulder	IT	**0.001**	0.573
Fibrous Cap	IT	0.926	0.327
Shoulder	GEX	**0.001**	**0.008**
Fibrous Cap	GEX	0.224	0.106
IT	GEX	0.330	**0.040**

Table 4.7: p-values from paired t-tests of stress transformation angle between the two plaque regions specified in the left columns, by plaque type (right columns).

For both plaque types, the shoulder region had a significantly higher stress transformation angle than the GEX region. For carotid plaques, the stress transformation angle was significantly higher in the shoulder region than the fibrous cap or IT regions. For coronary plaques, the stress transformation angle was higher in the IT than the GEX region.

Discussion of Section

Stress transformation angles were small, so maximum principal stresses were mostly (but not completely) in the direction of fibres. The shoulder regions, which had unique fibre structure (see Chapter 3) and higher stresses (this chapter), generally had a higher stress transformation angle than other regions.

The magnitudes of stress transformation angles were similar to the magnitudes of fibre misalignment found in Table 3.4. However, the particular values for stress transformation angle and fibre misalignment were different, so stress transformation angle was not simply a proxy for fibre misalignment. In other words, there is an angular misalignment between maximum principal stress and fibres, as well as a misalignment between fibre orientation and the luminal surface.

4.6 Linear Regression Modelling

Linear regression models were used to identify relationships between FE stress results, geometry, and fibre structure. The linear regressions followed the same methodology as described in Section 3.6.

Since anisotropic maximum principal stress was nearly identical to the axial stresses, only regressions for anisotropic maximum principal stress will be reported. Stress transformation angle was also considered by these regressions.

Linear regressions were modelled for the regions around the lumen (fibrous cap, shoulder, and IT regions), using the coronary, carotid, and combined sets of plaques. Rupture involves the fibrous cap or shoulder regions, so regressions were expected to identify predictors of higher stress in these regions. Stresses in the IT region, assumed to be healthier tissue, were expected to have fewer relationships with fibre or geometry parameters.

Section 4.6.1 reports linear regressions to compare stresses with geometry parameters. Section 4.6.2 models stresses with fibre misalignment and dispersion. Section 4.6.2 compares anisotropic stresses with isotropic maximum principal stress. Section 4.6.4 models stresses with fibre misalignment and dispersion in multivariate regressions.

4.6.1 Stress Results and Geometry Regressions

Finite element stress results were modelled against geometry (see Tables 4.8 and 4.9). The geometric properties used here were defined in Section 3.3.5 and used for linear regressions between fibre structure and geometry in Section 3.6.

Isotropic Maximum Principal Stress

For the fibrous cap, higher radius of curvature at the shoulder (ρ) predicted higher isotropic maximum principal stress. Higher normalised shoulder radius of curvature (ρ_{norm}) predicted higher isotropic maximum principal stresses in fibrous caps of the coronary and combined sets of plaques. Tighter corners at the shoulder resulted in higher isotropic maximum principal stress in the fibrous cap.

	All Plaques			Carotid			Coronary		
	A	p	R^2	A	p	R^2	A	p	R^2
Isotropic Maximum Principal Stress									
Fibrous Cap									
ρ	**24.3**	**0.000**	**0.39**	**18.8**	**0.020**	**0.35**	**95.2**	**0.011**	**0.38**
ρ_{norm}	**74.6**	**0.003**	**0.26**	52.2	0.066	0.24	**356**	**0.003**	**0.48**
θ_{li}	**0.37**	**0.027**	**0.16**	0.13	0.596	0.02	**0.60**	**0.003**	**0.47**
Shoulder									
ρ	**-36.4**	**0.004**	**0.13**	-16.0	0.090	0.10	**-238**	**0.003**	**0.25**
ρ_{norm}	**-110**	**0.026**	**0.08**	-48.4	0.148	0.07	**-757**	**0.008**	**0.21**
θ_{li}	**-0.50**	**0.035**	**0.07**	**-0.41**	**0.034**	**0.15**	-0.39	0.389	0.03
IT									
θ_{li}	**-0.66**	**0.042**	**0.14**	0.42	0.320	0.07	-0.75	0.121	0.16
Anisotropic Maximum Principal Stress									
Fibrous Cap									
ρ	**76.4**	**0.001**	**0.35**	59.4	0.052	0.26	**269**	**0.012**	**0.37**
ρ_{norm}	**207**	**0.017**	**0.18**	140	0.192	0.13	**856**	**0.017**	**0.34**
θ_{li}	0.69	0.232	0.05	-0.06	0.950	0.00	**1.31**	**0.035**	**0.28**
Shoulder									
t_{fc}	**583**	**0.002**	**0.15**	**826**	**0.033**	**0.15**	**497**	**0.043**	**0.13**

Table 4.8: Slope (A), p-value, and coefficient of determination (R^2) for linear regressions of maximum principal stress against geometry parameters. Statistically significant regressions ($p<0.05$) are in bold.

	All Plaques			Carotid			Coronary		
	A	p	R^2	A	p	R^2	A	p	R^2
Transverse Stress									
Fibrous Cap									
ρ	**2.35**	**0.030**	**0.15**	1.34	0.356	0.07	**15.4**	**0.008**	**0.41**
ρ_{norm}	6.28	0.128	0.08	3.16	0.520	0.03	**44.5**	**0.025**	**0.31**
θ_{li}	**0.05**	**0.049**	**0.13**	0.02	0.632	0.02	**0.08**	**0.010**	**0.39**
A_{pl}	**0.34**	**0.030**	**0.15**	0.24	0.463	0.04	0.91	0.333	0.07
A_{li}	**0.96**	**0.017**	**0.18**	0.69	0.249	0.10	2.14	0.255	0.09
Shoulder									
ρ	-2.27	0.090	0.05	-1.90	0.260	0.05	**-16.9**	**0.014**	**0.18**
ρ_{norm}	-7.19	0.165	0.03	-4.48	0.457	0.02	**-64.8**	**0.006**	**0.22**
t_{fc}	9.89	0.503	0.01	**56.6**	**0.030**	**0.16**	-17.4	0.473	0.02
Shear Stress									
Fibrous Cap									
ρ	6.64	0.062	0.12	3.75	0.517	0.03	**28.7**	**0.001**	**0.53**
ρ_{norm}	13.7	0.315	0.04	5.18	0.792	0.01	**71.4**	**0.029**	**0.30**
θ_{li}	0.02	0.782	0.00	-0.08	0.599	0.02	**0.12**	**0.030**	**0.29**
A_{pl}	**1.26**	**0.012**	**0.20**	1.45	0.248	0.10	2.04	0.178	0.13
A_{li}	**3.15**	**0.016**	**0.19**	2.52	0.294	0.08	5.09	0.088	0.19
t_{li}	**21.0**	**0.035**	**0.14**	19.7	0.327	0.07	4.90	0.631	0.02
Shoulder									
t_{fc}	**66.9**	**0.025**	**0.08**	**149**	**0.022**	**0.18**	-3.87	0.903	0.00
A_{li}	0.48	0.555	0.01	-0.288	0.84	0.00	**5.01**	**0.047**	**0.13**
$\%_{li}$	15.1	0.672	0.00	-34.4	0.59	0.01	**71.1**	**0.021**	**0.17**
Stress Transformation Angle									
IT									
$\%_{li}$	6.43	0.581	0.01	**14.8**	**0.049**	**0.27**	2.60	0.901	0.00

Table 4.9: Slope (A), p-value, and coefficient of determination (R^2) for linear regressions of transverse stress, shear stress, and stress transformation angle against geometry parameters. Statistically significant regressions (p<0.05) are in bold.

Wider lipid arc angles (θ_{li}) predicted higher isotropic maximum principal stress within the fibrous caps of the coronary and combined sets of plaques. The lipid arc angle also measures the length of the fibrous cap, so a wider θ_{li} would have more high-stress area around the lumen within the fibrous cap.

For the shoulder region, a smaller radius of curvature at the shoulder (both ρ and ρ_{norm}; tighter corners) predicted higher isotropic maximum principal stress for the coronary and combined sets of plaques. A narrower θ_{li} was linked to higher isotropic maximum principal stress within the shoulders of the carotid and combined sets of plaques.

Higher isotropic maximum principal stress in the IT region was only predicted by a narrower θ_{li}, using the combined sets of plaques. A narrower θ_{li} would indicate a shorter fibrous cap, and therefore a larger IT with more high-stress elements around the lumen.

Anisotropic Maximum Principal Stress

For the fibrous cap, higher shoulder radius of curvature (both ρ and ρ_{norm}; less tight corners) was linked to higher anisotropic maximum principal stress for the coronary and combined sets of plaques. A wider θ_{li} was linked to higher anisotropic maximum principal stress for the coronary plaques.

For anisotropic maximum principal stress in the shoulder region, thicker fibrous caps (t_{fc}) predicted higher stress. This was an interesting result, because thick fibrous caps are typically thought to be protective and reduce risk of rupture [Falk et al., 2013].

Transverse Stress

Transverse stress in the fibrous cap was predicted by higher shoulder radius of curvature (ρ) for the coronary and combined sets of plaques. Higher normalised shoulder radius of curvature (ρ_{norm}) predicted higher transverse stress for fibrous caps in coronary plaques. A wider θ_{li} indicated higher transverse stress within the fibrous caps of the coronary and combined plaques. Higher A_{pl} and A_{li} predicted higher transverse stress in the fibrous cap, but only for the combined set of plaques.

For transverse stresses in the shoulders, a smaller radius of curvature in the shoulder (both ρ and ρ_{norm}; tighter corners) predicted higher stress for the coronary plaques. Higher transverse stress in the shoulders of the carotid plaques was predicted by a thicker t_{fc}.

Shear Stress

Shear stress in the fibrous cap increased with shoulder radius of curvature (both ρ and ρ_{norm}) for the coronary plaques. A wider θ_{li} predicted higher shear stresses for the coronary plaques. Higher values for A_{pl}, A_{li}, and t_{li} predicted higher fibrous cap shear stresses for the combined set of plaques.

Shear stress in the shoulder region increased with t_{fc} for the combined and carotid sets of plaques. For the coronary plaque set, shoulder shear stress increased with A_{li} and $\%_{li}$.

Stress Transformation Angle

No geometry parameter was linked to the stress transformation angle in the fibrous cap or shoulder regions. Higher $\%_{li}$ predicted higher stress transformation angles in the IT for the carotid plaques. For the carotid plaques, higher $\%_{li}$ predicted higher stress transformation angles.

Discussion of Section

Linear regressions identified a number of significant relationships between stresses and geometry parameters. The fibrous cap had a greater number and stronger relationships for stress versus geometry (lower p-values, higher R^2 values) compared to the shoulder region. More and stronger relationships were also found for the coronary plaques compared to carotid.

In the coronary plaques, more and stronger relationships were found for geometry parameters with stresses in the fibrous cap compared to the shoulders. For carotid plaques, more relationships were found for stresses in the shoulders. This suggests differences in the mechanics of each plaque type.

There were fewer significant links with stress in the IT region, which is assumed to be healthier tissue, compared to the fibrous cap or shoulder regions.

Therefore, the IT region regressions have acted as controls, giving more confidence that regressions identified true links for the fibrous cap and shoulder regions.

4.6.2 Stress Results and Fibre Structure Regressions

Linear regression models were used to determine relationships for fibre misalignment or fibre dispersion with stresses, with significant regressions ($p<0.05$) shown in Table 4.10). The fibre misalignment and dispersion for each plaque-region were the median values found in Section 3.5.

	All Plaques			Carotid			Coronary		
	A	p	R^2	A	p	R^2	A	p	R^2
Transverse Stress									
Shoulder									
θ_i	**0.82**	**0.001**	**0.16**	**1.28**	**0.001**	**0.33**	0.44	0.191	0.06
κ	**114**	**0.005**	**0.12**	80.3	0.182	0.06	**156.3**	**0.006**	**0.22**
Shear Stress									
Shoulder									
θ_i	**1.15**	**0.030**	**0.08**	**2.30**	**0.022**	**0.17**	0.14	0.752	0.00
Stress Transformation Angle									
Fibrous Cap									
θ_i	0.28	0.820	0.00	**0.71**	**0.001**	**0.60**	0.060	0.983	0.00
κ	45.7	0.697	0.01	**41.6**	**0.040**	**0.29**	318	0.369	0.06
Shoulder									
κ	**91.3**	**0.003**	**0.13**	**81.9**	**0.019**	**0.18**	104	0.149	0.07
IT									
θ_i	**0.87**	**0.038**	**0.14**	0.38	0.155	0.15	**2.25**	**0.002**	**0.49**

Table 4.10: Slope (A), p-value, and coefficient of determination (R^2) for linear regressions between anisotropic stress results and fibre parameters. Statistically significant regressions ($p<0.05$) are in bold.

Anisotropic Maximum Principal Stress

Isotropic models ignored fibre structure, and linear regression models using fibre structure found no significant relationships. Neither fibre misalignment nor dispersion predicted maximum principal stresses in the regions around the lumen.

Transverse Stress

For transverse stress in the shoulders, higher fibre misalignment (θ_i) predicted higher stress for the carotid and combined sets of plaques. Increasing fibre dispersion (κ) predicted higher shoulder transverse stress for the coronary and combined sets. For the fibrous cap and IT regions, fibre structure did not significantly predict transverse stresses.

Shear Stress

Shoulder shear stress increased with θ_i for the carotid and combined sets of plaques. For the fibrous cap and IT regions, fibre structure did not significantly predict shear stresses.

Stress Transformation Angle

Fibrous cap stress transformation angle increased with θ_i and κ for the carotid plaques. The stress transformation angle in the shoulder region increased with κ for the carotid and combined sets of plaques. For the IT region, stress transformation angle increased with θ_i for the coronary and combined sets of plaques.

Discussion of Section

Fibre structure predicted transverse and shear stresses in the shoulders, with fibre misalignment a stronger predictor in the carotid plaques and fibre dispersion stronger in the coronary. In contrast, regressions between geometry and stress values (Section 4.6.1) were stronger in the fibrous cap and in the coronary plaques. This may be explained by fibrous cap and IT regions having a lower and narrower range of values for fibre misalignment and dispersion, compared to the shoulders

(see Tables 3.4 and 3.6). The IT region had few significant links for geometry or fibre structure with stresses, so acted as a control for both sets of regressions.

Fibre misalignment and dispersion were stronger predictors of the stress transformation angle than for the individual components of stress. Therefore, fibre structure is more of a factor in how closely principle stress aligns with the axial direction of fibres than in the specific magnitudes of stresses. This also explains why fibre structure predicted transverse and shear stresses, but not maximum principal stress. In other words, higher fibre misalignment or dispersion transferred stress from being more aligned with fibres to loading modes the tissue is weaker in.

4.6.3 Isotropic Maximum Principal Stress Regressions

Linear regression models were used to determine relationships between isotropic maximum principal stress and stresses in the anisotropic FE models, with results shown in Table 4.11).

Anisotropic Maximum Principal Stress

Higher isotropic maximum principal stress was a significant predictor of higher anisotropic maximum principal stress for all regions, except the IT region in carotid plaques.

Transverse Stress

Higher isotropic maximum principal stress predicted higher transverse stress for all regions, except the IT region in coronary plaques.

Shear Stress

Higher isotropic maximum principal stress predicted higher shear stress for all regions, except the IT region in coronary plaques.

	All Plaques			Carotid			Coronary		
Region	A	p	R^2	A	p	R^2	A	p	R^2
				Anisotropic Maximum Principal Stress					
FC	**2.86**	**0.000**	**0.74**	**3.08**	**0.000**	**0.72**	**2.35**	**0.000**	**0.68**
SH	**0.54**	**0.001**	**0.16**	**1.38**	**0.003**	**0.28**	**0.52**	**0.000**	**0.35**
IT	**0.73**	**0.000**	**0.41**	0.36	0.120	0.18	**1.22**	**0.000**	**0.74**
				Transverse Stress					
FC	**0.12**	**0.000**	**0.59**	**0.11**	**0.006**	**0.45**	**0.13**	**0.000**	**0.69**
SH	**0.07**	**0.000**	**0.39**	**0.11**	**0.000**	**0.41**	**0.06**	**0.000**	**0.52**
IT	**0.07**	**0.000**	**0.41**	**0.09**	**0.000**	**0.65**	0.05	0.069	0.22
				Shear Stress					
FC	**0.32**	**0.000**	**0.42**	**0.39**	**0.020**	**0.35**	**0.20**	**0.000**	**0.60**
SH	**0.09**	**0.001**	**0.17**	**0.22**	**0.002**	**0.30**	**0.08**	**0.000**	**0.50**
IT	**0.11**	**0.000**	**0.41**	**0.11**	**0.001**	**0.62**	0.09	0.068	0.22
				Stress Transformation Angle					
FC	**-0.13**	**0.026**	**0.16**	-0.00	0.770	0.01	-0.24	0.069	0.22

Table 4.11: Slope (A), p-value, and coefficient of determination (R^2) for linear regressions between anisotropic stress results and the isotropic maximum principal stress in the same region. Fibrous cap (FC) and shoulder (SH) regions are abbreviated. Statistically significant regressions ($p<0.05$) are in bold.

Stress Transformation Angle

Fibrous cap stress transformation angle decreased with higher isotropic maximum principal stress for the combined set of plaques.

Discussion of Section

For the fibrous cap in particular, isotropic maximum principal stress was a stronger predictor of anisotropic stresses than geometry or fibre structure (lower p-value and higher R^2, see Sections 4.6.1 and 4.6.2). However, most correlations were still only moderate ($0.3 \leq R^2 \leq 0.7$), indicating fibre structure affected stresses in ways that the isotropic FE models could not fully predict.

Most relationships between isotropic maximum principal stress and anisotropic stresses were stronger for the fibrous cap than for the shoulder region (higher R^2, lower p-value for the fibrous cap), and for the coronary plaques compared to carotid. This suggests there were subtle but important differences between the mechanics of coronary and carotid plaques.

Compared to the regressions for anisotropic stresses, relationships between isotropic maximum principal stress and the stress transformation angle were fewer and weaker. Therefore, higher isotropic maximum principal stress predicted increases to anisotropic stresses, but was mostly unable to anticipate the relative magnitudes of each stress component (axial, transverse, and shear).

4.6.4 Multivariate Regressions

Multivariate regressions were used to identify stronger but more complex predictions of stresses compared to the single variable linear regressions.

Multivariate Regression Methods

Starting from a regression model with no predictor variables, predictor variables were added by a stepwise iterative strategy (*stepwiselm* in Matlab). Predictor variables were added to or removed from the regression model if doing so increased the adjusted-R^2 (R^2_{adj}) by at least 0.05.

Adjusted-R^2 was 'adjusted' by the number of parameters in the model, by Equation 4.8:

$$R^2_{adj} = 1 - \left(\frac{n-1}{n-p}\right)\frac{SSE}{SST} \tag{4.8}$$

where n was the number of plaque-regions in the regression, p was the number of terms in the model (including the intercept), SSE was the sum of squared error, and SST was the sum of squared total.

Adjusted-R^2 is more suitable in evaluating the quality of a multivariate model, because R^2 will always increase with additional predictor variables. A threshold of $\Delta R^2_{adj} \geq 0.05$ was used to avoid including variables in a model that had only marginal impact on model precision. If more than one parameter met the threshold in a given iteration, the parameter giving the largest ΔR^2_{adj} was added.

Interaction terms (such as $x_1 x_2$) were considered only if all parameters making these terms were already included in the model. Higher-order terms (such as x_1^2) were only considered if all their lower-order terms were in the model.

The predictor variables that were considered were: geometry parameters, fibre misalignment, fibre dispersion, isotropic maximum principal stress, and plaque type. Multivariate regressions were only done for the combined sets of plaques, but plaque type was included a possible predictor variable.

Multivariate Models by Region and Stress Type

Multivariate regression models found by this strategy are shown in Table 4.12.

Anisotropic Maximum Principal Stress

Anisotropic maximum principal stress prediction in the fibrous cap was improved by a model using isotropic maximum principal stress ($\sigma_{1,i}$) with lipid thickness (t_{li}). The strongest multivariate model for the shoulder region used isotropic maximum principal stress ($\sigma_{1,i}$) with fibrous cap thickness (t_{fc}). Anisotropic maximum principal stress in the IT region was best predicted by a model using $\sigma_{1,i}$ only.

	Multivariate Model Equation	R^2_{adj}
Anisotropic Maximum Principal Stress		
FC	$2.69\sigma_{1,i}$ + $90.6t_{li}$ - 141	0.79
SH	$0.63\sigma_{1,i}$ + $690t_{fc}$ - 23.7	0.34
IT	$0.73\sigma_{1,i}$ + 125	0.40
Transverse Stress		
FC	$0.12\sigma_{1,i}$ - 12.6	0.58
SH	$0.06\sigma_{1,i}$ + $0.67\theta_i$ - 9.51	0.48
IT	$0.07\sigma_{1,i}$ - 4.03	0.44
Shear Stress		
FC	-$0.29\sigma_{1,i}$ - $1.44\theta_i$ - $13.6t_{li}$ + $0.06\sigma_{1,i}\theta_i$ + $0.19\sigma_{1,i}t_{li}$ + 20.4	0.73
SH	$0.10\sigma_{1,i}$ + $83.7t_{fc}$ - 3.28	0.27
IT	-$0.10\sigma_{1,i}$ - $26.9\%_{li}$ - $11.3t_{li}$ + $1.01\sigma_{1,i}\%_{li}$ + 27.4	0.60
Stress Transformation Angle		
FC	-$0.12\sigma_{1,i}$ - $55.3t_{fc}$ + 40.4	0.21
SH	$3.16\theta_i$ + $11.1\%_{li}$ - $0.35\theta_{li}$ - $265t_{fc}$ - $8.22\theta_i\%_{li}$ + $1.31\theta_{li}t_{fc}$ + 68.3	0.43
IT	-$59.2t_{fc}$ + 28.6	0.09

Table 4.12: The multivariate models found for each combination of plaque region (left column) and stress type (grouped rows). The equation of each multivariate model in middle column, including predictor variables, their slopes, and a constant term. The R^2_{adj} for the regression model is in the rightmost column, with higher values indicating a stronger prediction.

Transverse Stress

Transverse stress in the shoulder region was best predicted by $\sigma_{1,i}$ combined with fibre misalignment (θ_i). Transverse stresses in the fibrous cap and IT regions were best predicted by a univariate model using $\sigma_{1,i}$.

Shear Stress

Fibrous cap shear stress was best predicted by a multivariate model using $\sigma_{1,i}$, fibre misalignment (θ_i), t_{li}, $\sigma_{1,i}$-θ_i interaction, and $\sigma_{1,i}$-t_{li} interaction. Shoulder shear stress was best predicted by a model of $\sigma_{1,i}$ and t_{fc}, but was relatively weak (R^2=0.27). Shear stress in the IT was best modelled against $\sigma_{1,i}$, $\%_{li}$, t_{li}, and $\sigma_{1,i}$-$\%_{li}$ interaction.

Stress Transformation Angle

Stress transformation angle in the fibrous cap was predicted best by a model using $\sigma_{1,i}$ and t_{fc}, but the model was comparatively weak (R^2=0.21). Shoulder stress transformation angle was best predicted by a model using θ_i, $\%_{li}$, lipid arc (θ_{li}), t_{fc}, θ_i-$\%_{li}$ interaction , and θ_{li}-t_{fc} interaction. The best prediction for IT stress transformation angle was from t_{fc} alone, but was very weak (R^2=0.09).

Discussion of Section

Multivariate regressions were able to produce stronger links than univariate models for nearly all stress parameters and plaque regions.

Multivariate models for stresses all included $\sigma_{1,i}$ as a predictor variable. Only multivariate models for the shoulder and IT stress transformation angles did not include $\sigma_{1,i}$. Of the ten possible geometry parameters, only t_{li}, t_{fc}, θ_{li} and $\%_{li}$ were selected to be used in any multivariate model. For fibre structure, only θ_i was used; κ was not used in any multivariate regression model. Plaque type (carotid or coronary) was also not selected for any model.

Two multivariate models had two interaction terms and a third had a single interaction term. The slope for each interaction term variable should be considered along with the interaction term's slope. For example, if the interaction's

slope was positive but slopes of the individual variables were negative, the model suggested that stress was higher only when both variables have higher values. If the interaction's slope was negative but each individual parameter coefficient was positive, higher stress was predicted when only one of the individual variables was higher.

4.7 Discussion

Sixteen coronary and fifteen carotid plaques had their fibre structure analysed (see Chapter 3) and were used to create 2D FE models. For each plaque, an isotropic FE model, without fibre structure, and an anisotropic FE model, which included fibre structure, were made.

Stress results were compared between the isotropic and anisotropic models, with significant and sometimes large differences in principal stress found between the two models. Anisotropic models also had their components of stress relative to fibre direction (axial, transverse, and shear) reported. Axial stresses were highest, followed by shear, but transverse stresses were low. Statistics were used to identify regions having higher stress, and regressions identified relationships between stress, plaque geometry, and fibre structures.

4.7.1 Interpreting Rupture Risk from Stress Results

Heart attacks and strokes are often caused by the rupture of an atherosclerotic plaque [Falk et al., 1995; Halvorsen et al., 2008]. Rupture is presumed to occur from physiological loading exceeding the material strength of the tissue. Patient-specific computational models have been proposed as a way to predict rupture and clinical events, many of which have been compared and summarised by Holzapfel et al. [Holzapfel et al., 2014]. The stresses predicted in this study were comparable to those in previous reports. Rupture risk is assumed to be related to stress in the tissue, and a threshold value is often used to divide lower- and higher-risk plaques [Holzapfel et al., 2014]. Since rupture is a relatively rare event compared to the number of plaques, few plaques should be indicated as higher-risk.

Review of Plaque Failure Criteria

A major limitation of this approach in assessing rupture risk is a lack of experimental studies characterising tissue strength. Results from studies that have been done show high variability in strength values both across and between their samples [Walsh et al., 2014]. Circumferential strips of carotid plaque tested under uniaxial tension have reported rupture at Cauchy stresses across an approximate range of 100 kPa to 4000 kPa, with different studies having a mean rupture stress from about 300 kPa to about 3000 kPa [Walsh et al., 2014]. Failure stretch ratios have been found to be between about 1.2 and 1.9, with the mean values for any one study being between about 1.4 and 1.7. Some of the variability between studies can be explained by differences in methodology.

Studies finding lower values of stress at failure often tested whole plaque samples, while higher failure stress was found for plaques separated into layers. A whole-plaque sample would be a composite material, containing more compliant components such as the lipid core as well as stiffer fibrous tissues. Therefore, the whole-plaque sample would have a lower effective stiffness, and report a lower stress for failure than the actual stress in the stiffer fibrous cap. In contrast, the reported stretch ratio is the same in the fibrous cap whether it is tested alone or as part of a whole-plaque sample. Failure stretch ratios have less variability between previous experimental studies than reported failure stresses.

A further limitation of these tests is that uniaxial tensile tests are not representative of *in vivo* mechanics and will fail at the weakest point of the material. Since stresses vary considerably by location in the tissue, the weakest point of the tissue may not correspond with the highest stresses.

Failure Criteria Applied to Finite Element Results

To avoid these complexities, many computational studies have used a threshold of 300 kPa (from failure stress in uniaxial tensile experiments) to indicate higher rupture risk [Holzapfel et al., 2014]. This threshold was exceeded by the anisotropic maximum principal stress in 15/62 shoulder and 10/31 fibrous cap regions (coronary: 2/16 fibrous caps and 6/32 shoulders, see Figure 4.8; carotid: 8/15 fibrous caps and 9/30 shoulders, see Figure 4.9). The differences between

plaque types match rates of rupture location, where coronary plaques have been observed to rupture at a ratio of about two shoulder ruptures for each fibrous cap rupture [Richardson et al., 1989]. For carotid plaques, the rates are reversed, with about two shoulder ruptures for every three mid-fibrous cap ruptures [Redgrave et al., 2006].

No plaque regions had maximum principal stress exceeding 3000 kPa, and only one fibrous cap and one shoulder region exceeded 1000 kPa (both in carotid plaques). None of the plaques in this study had ruptured, but they were selected as being similar to plaques at risk of rupture. Some may have eventually ruptured. Therefore, a good failure criterion should identify some, but not all, of plaques in this study as higher risk.

There is a need for further experimental measurements of tissue strength, and a better understanding of the sources of variability in strength values. Stress is used most often for assessing plaque mechanics, but strain, strain energy, and fracture toughness should also be considered. Experiments in Chapter 5 will consider the role of fibre structure on tissue material properties through uniaxial tensile, trouser tear, and notched specimen tests.

4.7.2 Advantages of Models Using Local Fibre Structures

Most previous FE models of atherosclerosis have used an isotropic material model [Sadat et al., 2010; Teng et al., 2012; Versluis et al., 2006; Wenk et al., 2010] or an anisotropic material model with an assumed (rather than imaged) fibre structure [Chai et al., 2014; Gasser and Holzapfel, 2007; Holzapfel et al., 2014; Kiousis et al., 2009].

This study considered isotropic FE models as well as anisotropic models with locally calculated and defined fibre orientation (see Section 4.3.4). Linear regression modelling found moderate correlation for maximum principal stress between the isotropic and anisotropic models (see Table 4.11). However, considerably different stresses were determined by each model type for some individual plaque-regions (see Section 4.5.2). In particular, the plaque-regions with the highest maximum principal stress were frequently different for the isotropic and anisotropic models (see Figures 4.8 and 4.9).

Multivariate regression models improved the ability to predict anisotropic maximum principal stress (see Section 4.6.4), but were still quite weak for the shoulder region (R^2=0.341). Therefore, an isotropic material model is a considerable limitation in patient-specific modelling of atherosclerotic plaques.

Fibre Orientation Precision

An anisotropic FE model with an assumed fibre orientation may be acceptable if local fibre orientation is accurate to about ±5° (see Section 4.4.5). Assuming fibres were locally tangent to the lumen did not meet this ±5° target, especially for the shoulder regions (see Table 3.4).

Patient-specific models of atherosclerotic plaques need to account for fibre structure, but there is currently no way to image fibres *in vivo*. Future study could consider interpolating local fibre orientation from the tangent directions of the lumen, plaque outer edge, and also the lipid boundary. Since fibres in the shoulder regions were observed to be also tangent to the lipid boundary (see Chapter 2), local fibre orientation from these improved geometry references may sufficiently meet the ±5° target. Alternatively, improvements to clinical imaging may allow for local fibre structure to be assessed *in vivo* to within ±5°.

Components of Stress Relative to Fibres

An advantage of the anisotropic FE models is the ability to decompose stress into components relative to the fibres (see Section 4.5.3). Axial stress was highest, indicating stress was mainly along fibres. Shear stress between fibres was lower, but was higher than transverse stress. Transverse stress was very low in magnitude and often compressive, and was therefore not expected to be a failure mode.

A recent study by Daemen et al. [2016] of carotid plaque fissure suggested shear between fibres is a major mechanism leading to fissures, which in turn were linked to intra-plaque haemorrhage. Fissures were defined as discontinuities between tissue layers that contained macrophages and red blood cells. Fissures were common, with 58% of carotid plaques having at least one fissure and 20% having multiple fissures. Fissure density was higher near the lumen, in the shoulder regions, and at interfaces between different plaque materials.

Daemen et al. [2016] speculated that fissuring is a dynamic process, and that fissures could be repaired or propagate further. A mechanism of fissure propagation from the interface of fibrous cap and lipid core to the lumen was also described, similar to the fibre seam and bands of increased stresses that have been described in this chapter.

Considering all of this, plaque rupture may depend on stresses exceeding material strength to initiate a fracture, as well as the biomechanical environment to continue propagation of the fracture completely across the fibrous cap. The high frequency of fissures noted by Daemen et al. [2016] suggested the conditions for fracture initiation may be relatively common, but rupture is rare because fractures rarely propagate completely from the lumen to the lipid core. Falk et al. [2013] defined fissures as lateral tears in eccentric coronary plaques with small necrotic cores, and suggested they are responsible for 10-15% of sudden coronary deaths. Because Falk et al. [2013] only considered fissures as complete tears from the lumen to the necrotic core, the rate of incomplete tears is probably much higher. However, Falk et al. [2013] suggested intra-plaque haemorrhage is nearly universal in coronary plaques, but there are several theories for its source.

4.7.3 Mechanics in Different Plaque Types and Regions

Throughout the image processing in Chapter 3 and the FE models in this chapter, coronary and carotid plaques were compared.

Differences Involving Geometry and Fibre Structure

Carotid plaques were larger (see Table 3.1), but they had similar fibre structures (see Tables 3.4 and 3.6). Relatively few geometry parameters were significantly linked to fibre misalignment (see Table 3.9) or fibre dispersion (see Table 3.9), but different geometry parameters were linked to each coronary and carotid plaques (see Section 4.6.1). Carotid plaques generally had higher stresses (see Table 4.4), and there were differences between the two plaque types when comparing stresses in different regions (see Table 4.5).

There were also some differences between the coronary and carotid plaque sets for which geometry and fibre parameters were significantly linked to stresses

(see Tables 4.8 and 4.10). However, multivariate regression models considered a parameter for plaque type but did not find it to improve prediction of anisotropic stresses (see Section 4.6.4).

In summary, some parameters or results used in this study were similar between the coronary and carotid plaque types but others were different. When the plaque types had similar results, using a combined set of all plaques was justified. In cases where each plaque type had different results, the results of the combined set should be considered cautiously.

Differences between the Fibrous Cap and Shoulders

Many of the differences in mechanics between the coronary and carotid plaques were related to relative differences in stress between the fibrous cap and shoulder regions for each plaque type.

For the coronary plaques, all stress types were significantly higher in the shoulders than the fibrous cap (see Section 4.5.4). In contrast, carotid plaques had no significant differences between the shoulders and fibrous cap for any stress type, and tended to have an opposite trend of higher fibrous cap stresses. Linear regression models found differences in the significant relationships between the plaque types for the two plaque regions (see Sections 4.6.1 and 4.6.2).

Clinically, the rate of plaque rupture has been found to be higher in the shoulder for coronary plaques [Richardson et al., 1989] and in the fibrous cap for carotid plaques [Redgrave et al., 2006].

The IT Region as a Healthier Control

The IT region, assumed to be healthier tissue and a zone where rupture does not occur, offers useful comparisons to results for the fibrous cap and shoulders.

Stresses in the IT region were comparable to those in the fibrous cap or shoulder regions (see Table 4.4). Fibre misalignment was similar for the IT region and the fibrous cap but the shoulders had higher fibre misalignment (see Table 3.4). Fibre dispersion in the IT was higher than the fibrous cap but lower than the shoulder regions (see Table 3.6).

The IT region had fewer significant links between fibre structure, geometry, and FE results (see Tables 3.8, 3.9, 4.8, 4.9, 4.10, and 4.11). Since the IT region had relatively few significant predictors of stress or fibre properties, there can be more confidence that significant links found between parameters for the fibrous cap and shoulder were not from random chance. Therefore, fibre structures and mechanics in the fibrous cap and shoulder can be compared to the IT region to evaluate changes caused by atherosclerosis.

4.7.4 Limitations and Future Directions

Findings and limitations from this study can be used to direct future work.

Sample Selection Considerations

Findings from this study would be strengthened with a greater sample size and comparisons to clinical case descriptions, which were not possible here due to limited access to clinical samples and data. The coronary plaques were obtained at autopsy from hearts of donors who were thought to have died from something other than coronary thrombosis. However, the carotid plaques were harvested during carotid endarterectomy, so presumably had a higher risk of rupture.

Therefore, none of the plaques considered in this study had ruptured. The different selection criteria for each plaque type may also have caused bias favouring plaques with particular geometries, fibre structures, or mechanics. Other plaque types, such as cerebral, ilaic, and aortic, could be considered in the future and compared to the results for coronary and carotid plaques.

Histology Sample Preparation

As mentioned in Chapter 3, histological samples had distortions, in spite of efforts to avoid and repair them. The histological images and resulting FE models used tissues in an unloaded stress-state, without residual stresses and strains. These limitations could be reduced by pressurising the plaque lumen when samples are histologically prepared, or by using pre-processing steps to account for changes to the geometry, fibre structure, and residual loads from the images of plaques without lumen pressure.

Region Segmentation

Plaque segmentation was simplified in this study to assume one lipid core, one fibrous cap, one IT region, and two shoulders. Regions have somewhat subjective definitions, and many plaques had several lipid cores that were grouped together or small lipid regions that were ignored. Further, tissue components exist in a continuum, with small amounts of lipid present in tissues considered fibrous and some fibres present in the lipid core. Other plaque components such as intra-plaque haemorrhage and calcium deposits were not considered at all. Fibres in this study were assumed to be collagen fibres, but future study could use additional histological stains and image processing to distinguish between elastin and each type of collagen. Plaque components also have varying densities, which could be identified by histological stain for each component and image processing, that could be considered in future FE models.

Additional Fibre Parameters

Fibre dispersion (κ) was included as a global parameter in these FE models rather than a local parameter. In future FE models, it could be defined element-by-element like fibre orientation or by region (fibrous cap, shoulder, IT, GEX) to reflect significant differences in κ between regions. Additional fibre parameters such as waviness, cross-linking, fibre diameter, and scale of fibre features could be considered in the future.

Loading Considerations and 3D Geometry

This study approximated plaque mechanics to a 2D FE model with static loading from blood pressure. While healthy arteries have only small axial strain through the blood pressure cycle, local axial strains in plaques may be significant and a 3D model should be considered. Dynamic loading and additional forces from blood flow could also be considered.

4.8 Conclusions

Finite element models were created using the geometries and fibre structures from the plaques studied in Chapter 3. For each plaque, an isotropic FE model that did not consider fibre structure and an anisotropic FE model that had element-by-element fibre orientation and a global fibre dispersion value were made. Elemental stresses were found to be distributed similar to an exponential distribution, where higher stresses had increasingly lower frequency (see Figure 4.3). Therefore, stresses were reported according to an area-based stress criterion instead of peak stress. Variation of parameter analysis found the FE models to be more sensitive to fibre orientation than fibre dispersion or the thickness of adventitia added to carotid plaques.

Significantly different maximum principal stresses were found by the isotropic and anisotropic FE models, suggesting fibre structure was needed accurately to assess plaque mechanics (see Section 4.5.2). For coronary plaques, stresses were significantly higher in the shoulders than the fibrous cap (median anisotropic maximum principal stress: 210 kPa for the shoulders and 101 kPa for the fibrous caps; see Sections 4.5.1 and 4.5.4). Carotid plaques had no significant difference in stress between the shoulder and fibrous cap, but stresses in the fibrous cap tended to be higher (median anisotropic maximum principal stress: 241 kPa for the shoulders and 319 kPa for the fibrous caps;). These findings show a similar pattern to clinical observations that rupture occurs in the shoulders about 63% of the time for coronary plaques [Richardson et al., 1989] and in the fibrous cap about 60% of the time for carotid plaques [Redgrave et al., 2006].

Anisotropic FE models considered stress in components relative to fibre direction. Axial stress was highest, indicating stress is mainly along fibres. Transverse stress was very low, suggesting transverse loading is not a likely failure mode. The magnitude of the shear stress was between the magnitudes of the axial and transverse stresses, and has recently been proposed as the main mechanism causing fissures in plaque caps [Daemen et al., 2016]. However, the mechanics involved are relatively unknown, and few studies have considered failure criteria from shear or tearing. In Chapter 5, experiment are detailed that characterised artery material properties relative to fibre structures.

Using univariate linear regression models, FE results were found to be predicted by some plaque geometry and fibre structure parameters (see Sections 4.6.1 and 4.6.2). However, most of these relationships had relatively low predictive value (low R^2). Isotropic maximum principal stress was a significant predictor of anisotropic stresses in most of the various plaque regions, but with only moderate predictive value (R^2 between about 0.3-0.7; see Section 4.6.3). Therefore, multiple factors contribute to plaque mechanics and FE models without fibre structure (isotropic models) do not full capture mechanics.

Multivariate regressions were used to predict anisotropic stresses using predictor variables from plaque geometry, fibre structure, and isotropic FE results (see Section 4.6.4). For anisotropic stresses in most regions, multivariate models improved prediction quality compared to the single variable linear regressions (indicated by a higher R^2_{adj}). Most multivariate models included isotropic maximum principal stress as a parameter.

Chapter 5

Influence of Fibre Structure on Material Toughness and Stiffness in Healthy Porcine Tissue

5.1 Abstract

A series of material tests were used alongside microscopy to consider relationships between material properties and fibre structure. In particular, anisotropy was assessed in both material properties and fibre structure in porcine carotid arteries.

Fibre structure was found to be intimately linked with material tearing toughness and stiffness. Trouser tear tests gave higher tearing toughness for tears in the axial-radial and circumferential-radial tissue planes compared to those in the axial-circumferential planes. The differences in toughness were explained by tears in the radial planes crossing tissues with higher fibre dispersion. Tissues that were more anisotropic or had lower fibre dispersion had lower tearing toughness. Fibres were oriented more in the circumferential direction than axial, and circumferential strips were stiffer than axial strips.

These experiments used healthy porcine carotid tissue to reduce variability in samples compared to diseased tissue. Since material properties were found to depend on fibre structure in healthy tissue, more variable fibre structures in atherosclerotic tissue may cause an even greater influence on material properties.

5.2 Introduction

Previous experiments of artery tissue have found considerable variability in material properties, both between studies and within individual studies [Walsh et al., 2014]. Experiments described in this chapter will consider any links between variability in fibre structure and variability in material properties.

The finite element studies in Chapter 4 found higher axial stresses (along fibres), moderate shear stresses (between fibres), and lower transverse stresses (normal to fibres; see Section 4.5.3). Since artery tissue may be weaker when loads are less aligned with fibres in the tissue, shear and axial loading were both identified as possible failure modes. Previously, the material strength of human atherosclerotic arteries has mainly been characterised by uniaxial tests [Walsh et al., 2014], which do not isolate axial or shear components of loading. Trouser tear tests [Purslow, 1983], peeling tests [Sommer et al., 2008], and fatigue tests of notched samples [Chu et al., 2013] have used pig aorta to determine fracture toughness. While each of these tests offers insights into different failure modes, the role of fibre structure in failure remains relatively unstudied.

Trouser tear and uniaxial tensile tests were used in this study to measure the toughness and stiffness of artery tissue. Image processing characterised the fibre structure in histology images of tested sample strips.

The methodology of these experiments is detailed in Section 5.3. The coordinate and plane systems used in this chapter are defined in Section 5.3.2. Section 5.3.3 details the preparation of samples used in the material tests, along with the number of samples tested and imaged by each technique. The apparatus used for material testing is described in Section 5.3.1. Details and parameters specific to each material test are given for trouser tear tests in Section 5.3.4 and for uniaxial tensile tests in Section 5.3.5. Image processing techniques to evaluate fibre structures are described for one-family fibre systems (Section 5.3.6) and for two-family fibre systems (Section 5.3.7).

Results of the experiments are provided in Section 5.4. The results section is divided into material property results (trouser tear in Section 5.4.1 and uniaxial in Section 5.4.2) and fibre structure results (in Section 5.4.3). The results are compared by graphing and linear regression models in Section 5.5.

The discussion section (Section 5.6) considers the application of these results to atherosclerotic arteries in Section 5.6.1, and lists limitations and recommended future work in Section 5.6.2. Conclusions of this chapter are summarised in Section 5.7.

5.3 Experimental Methodology

Experiments were designed to test the role of fibre structure in artery mechanics. For a more consistent sample set, healthy porcine carotid tissue was used rather than atherosclerotic human tissue. These samples still had a wide range of fibre structures, but the structure and material properties were not further complicated by disease. Atherosclerosis severely alters the geometry, material composition, and fibre structure of the tissue. Therefore, the role of fibre structure on mechanics can be considered, with less influence from other variables. It was not possible to obtain healthy human artery tissue for these experiments.

To characterise the anisotropic properties of the material, test strips were cut in pairs of circumferential and axial strips from the same artery. Tearing toughness was tested by trouser tear tests (see Section 5.3.4). Uniaxial tensile tests tested the stiffness of the tissue (see Section 5.3.5).

In addition to the three types of material tests, sample strips were divided into three categories of imaging: Verhoeff's Van Gieson (EVG) stained histology, multiphoton (see Chapter 6), and no imaging. Table 5.1 details the number of arteries used for each of the material test and imaging groups.

Imaging	Uniaxial	Trouser Tear	Notched Specimen
Histology	6	11	-
Multiphoton	4	-	4
No Imaging	3	4	-
Total	13	15	4

Table 5.1: Number of arteries used for test strips for each combination of material test type and imaging type.

A selection of the trouser tear and uniaxial test strips were histological prepared after the mechanics tests. Qualitative observations were recorded for evidence of fibre recruitment and damage in the histology images of post-test samples. Image processing was used to calculate fibre orientation and dispersion in the histological section plane (see Section 5.3.6).

Most trouser tear test strips were from arteries that also had a pair of uniaxial tensile test strips, so comparisons were made between stiffness and toughness.

Some of the uniaxial tensile and all of the notched specimen test samples were tested under a multiphoton microscope, which allows *in situ* imaging of collagen throughout the test (see Chapter 6).

Where different tests were used for the same imaging type, sample strips from the same arteries were used to allow artery-paired comparisons. For example, the histology imaging group used eleven arteries: six of these had trouser tear strips and uniaxial strips, and five arteries had trouser tear strips only. Multiple test strips were obtained from each artery: two for uniaxial tests, four for trouser tear tests, and two for notched specimen tests.

5.3.1 Materials Test Apparatus

Trouser tear (see Section 5.3.4), uniaxial tensile (see Section 5.3.5), and notched specimen tests (see Section 6.3.2) all used the same bespoke apparatus. Components of the apparatus are detailed in Figure 5.1. Photographs of the apparatus are included in Section A.4.

Peripheral components (shown in Figure 5.1) included a laptop (Sony Vaio, Sony Corporation, Tokyo, Japan), SMC100PP motor controller (Newport Corporation, Irvine, CA, USA), signal amplifier (1000 gain, bespoke to the Cambridge University Engineering Department), material micro-testing table (bespoke, designed and fabricated by various members of the Cambridge University Engineering Department, described below), light microscope (Olympus SZX16, Olympus Corporation, Tokyo, Japan), a cold lamp (KL 1600 LED, Schott AG, Mainz, Germany), and microscope camera (PL-B776F, Pixelink, Ottawa, Canada).

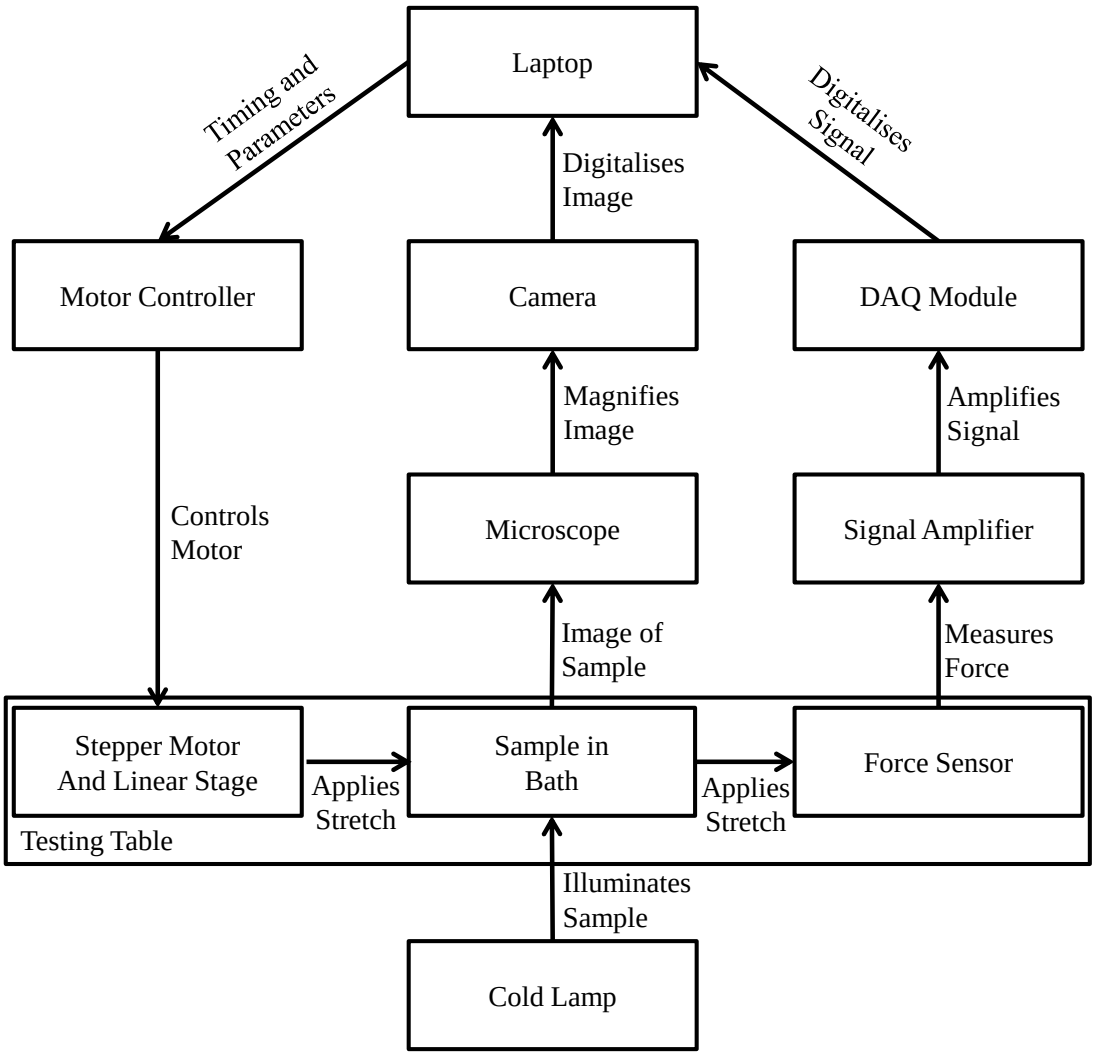

Figure 5.1: Experimental equipment and their relationship to one another.

For tests with a multiphoton microscope (LaVision BioTec TriM Scope II, Bielefeld, Germany, with an Insight Deepsee light source, Spectra-Physics, Santa Clara, CA, USA), the light microscope, cold lamp, and microscope camera were not used (see Chapter 6).

The experiments were controlled by the PC using bespoke programs in Labview (National Instruments, Austin, TX, USA). An integrated stepper motor and linear stage (MFA-PP, Newport Corporation, Irvine, CA, USA) was connected to the motor controller, which was in turn connected to the PC. Force in the sample was measured by a force sensor (bespoke to the Cambridge University Engineering Department), with the signal read by the PC through the signal amplifier and a data acquisition module (National Instruments USB-6002). Strain gauges on the force sensor were arranged in a differential configuration, such that the sensor was sensitive to displacements in the sample was being stretched, but insensitive to rotations, vertical displacements, and lateral displacements.

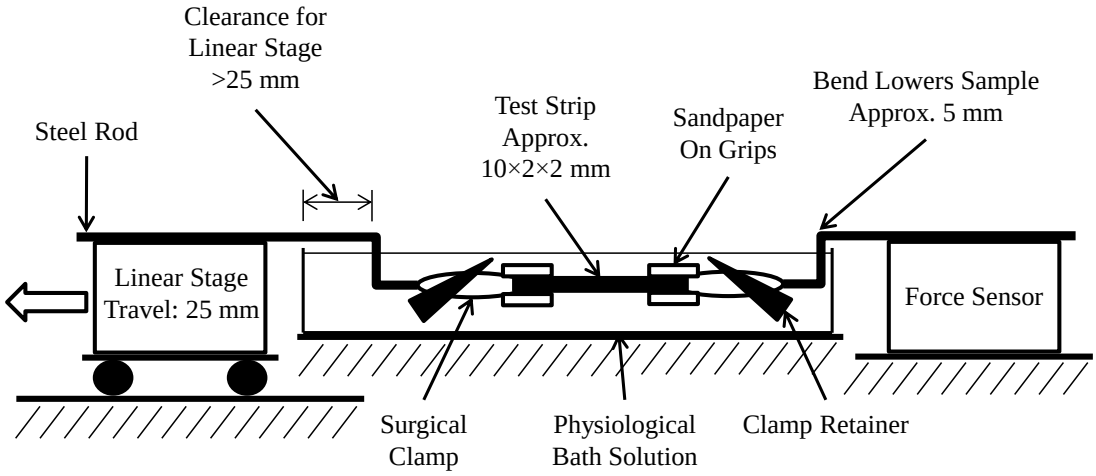

Figure 5.2: Schematic diagram of the materials micro-testing table, showing the linear stage (left), sample in bath (middle), and force sensor (right). Specific detail is given for the clamps holding the sample.

Samples were immersed in a physiological bath solution (for light microscopy or no imaging tests) or distilled water (multiphoton microscopy tests), and held by two surgical clamps (see Figure 5.2). The surgical clamps were each welded

to steel rods. Each steel rod had a right-angle bend, which was near the surgical clamps to reduce upward bending when loaded. Rods were clamped to the linear stage (left) and force sensor (right). To avoid the test strip slipping, sandpaper was glued to each surface of the surgical clamps, and a plastic clamp retainer wedge increased clamping force. The linear stage and sensor were bolted to a perspex base plate, and together comprise the material micro-testing table.

Samples were loaded so the luminal surface was towards the microscope. The clamps were adjusted to align the sample with the linear stage, and so the sample strip had neither pretension nor sag. The stepper motor and linear stage were used to finely adjust the sample to eliminate any pretension or sag.

Samples were preconditioned by five stretch cycles to a 500 μm displacement, with a five second pause at each half-cycle. During the experiments, the linear stage was moved in 50 μm steps at an average displacement rate of approximately 7 μm per second. Therefore, the loading can be considered quasi-static. For the multiphoton experiments (Chapter 6), loading was paused every 500 μm for about 90 seconds to scan the fibre structure of the sample.

5.3.2 Coordinate System Definition

Throughout this chapter (and in Chapter 6), the coordinate system and tissue planes explained in Figure 5.3 were used.

A cylindrical coordinate system is defined, where axial refers to the length direction of the artery, circumferential to the circumference, and radial to the wall thickness (see Figure 5.3A). Three planes are defined by pairs of these directions (see Figure 5.3A): circumferential-radial (Figure 5.3B), axial-radial (Figure 5.3C), and circumferential-axial (Figure 5.3D).

The planes are shown relative to a simplified sketch of fibre structure in the tissue, based on previous reports on artery microstructure [Clark and Glagov, 1985; Gasser et al., 2006; Schriefl, 2013; Schriefl et al., 2012b]. These sketches show sheets of tissue stacked in the radial direction. Fibres have high dispersion within a sheet, and less dispersed fibres between these sheets (with some fibres crossing between sheets). Within each sheet, fibres are oriented more towards the circumferential direction than axial.

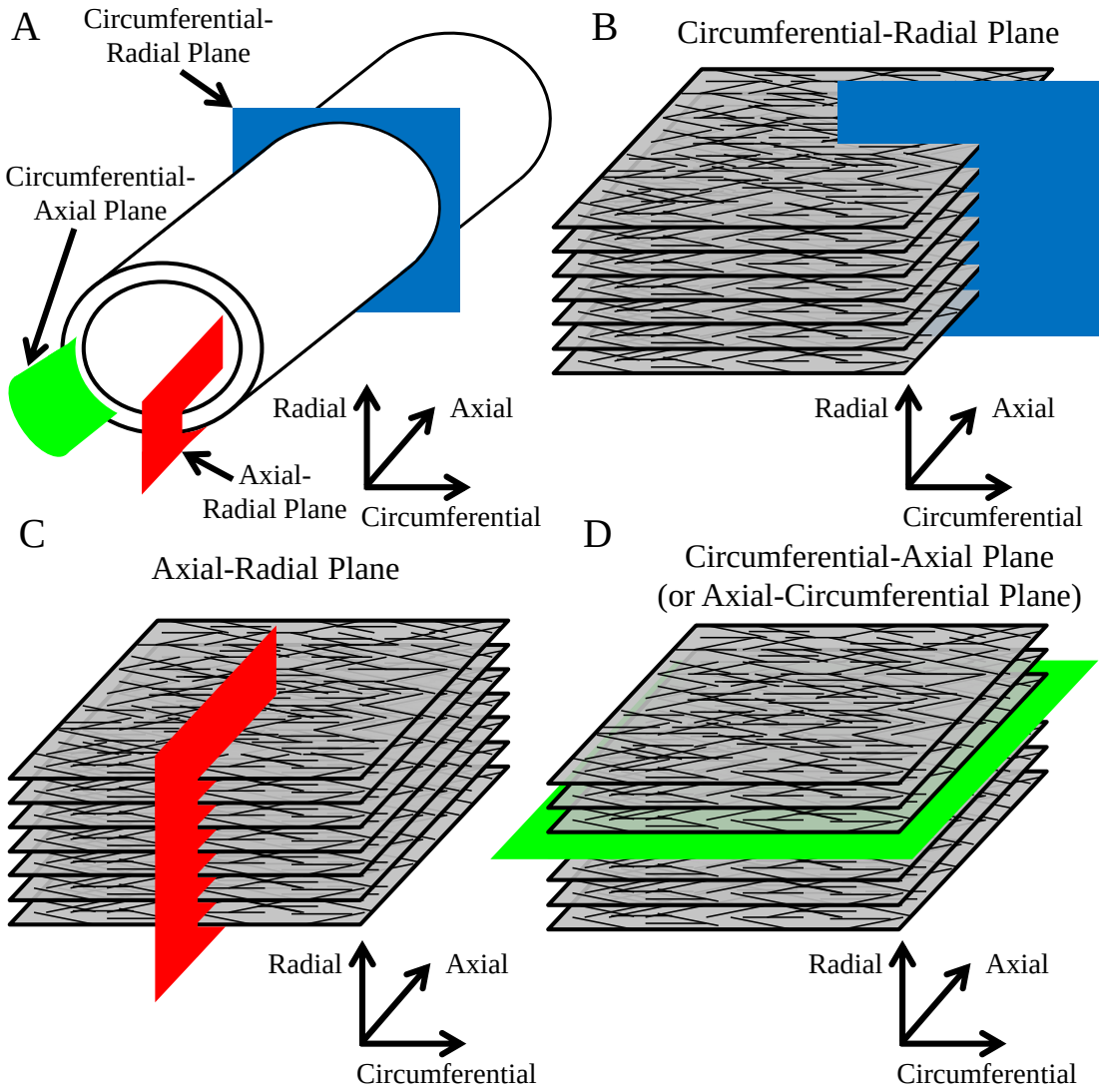

Figure 5.3: A.) Definition of the artery coordinate system (radial, axial, and circumferential) and the three tissue planes, B.) Circumferential-radial tissue plane from (A), which is through the cross-section of the artery and closest to the primary direction of fibres, C.) The axial-radial tissue plane from (A), which is through the lengthwise thickness of the artery and anti-aligned with the direction of fibres, and D.) The circumferential-axial (equivalent to axial-circumferential) plane from (A), which is between the concentric sheets of fibres.

The circumferential-radial plane (Figure 5.3B) was the cross-section of the artery. This was the plane considered in Chapter 3 for quantifying fibre structure and Chapter 4 for finite element studies of atherosclerotic plaques. The circumferential-radial plane passes through the fibre sheets of the tissue, and is nominally in the same direction as fibres within the sheets.

The axial-radial plane (Figure 5.3C) is through the thickness of the artery as well, but it is along instead of across the artery. Therefore, the axial-radial plane also passes through the fibre sheets of the tissue, but it is anti-aligned with the expected direction of fibres within the sheets.

The circumferential-axial plane (Figure 5.3D) is nominally parallel or tangential to the luminal surface of the artery. It passes between the fibre sheets, so relatively few fibres are expected to cross this plane. The circumferential-axial and axial-circumferential planes are the same plane, but rotated by 90° from one another. The first direction (axial or circumferential) denotes the lengthwise direction of the strip. For test strips used in experiments, the first word refers to the lengthwise direction the strip.

5.3.3 Tissue Source and Preparation

Porcine carotid arteries were harvested by an abattoir (Leech and Sons, Melbourne, Cambridgeshire, UK) from healthy animals that were slaughtered for butchering. The arteries were refrigerated (4°C) and used in experiments between about 24 and 72 hours after harvest.

The porcine carotid arteries (Figure 5.4A) had connective tissues, adventitia, thrombus, and minor branches removed (Figure 5.4B). Thus, the tests primarily characterise the media layer of the tissue. Circumferential strips were cut as rings (Figure 5.4C), which were opened into strips. The axial strips were cut from the remaining artery (indicated on Figure 5.4C). Strips were cut from the common carotid artery where possible. If insufficient tissue was available in the common carotid artery, axial strips were cut along the larger branching artery from the outside of the branch. The saddle forming the branch had localised thickening (indicated on Figure 5.4C), and is thought to have different fibre properties than surrounding tissue [Creane et al., 2011], so it was avoided.

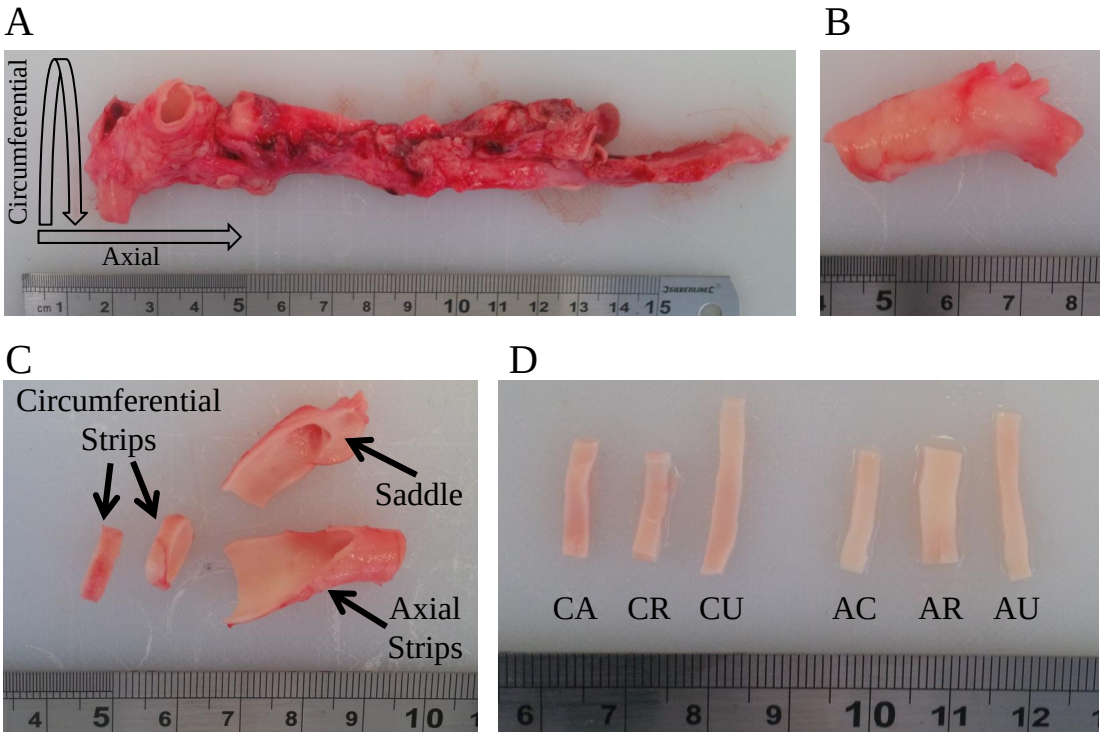

Figure 5.4: Details and preparations of experiment samples: A.) Complete porcine carotid artery as received from abattoir, B.) Porcine carotid artery with connective tissue, thrombus, and minor branches removed, C.) Partial dissection into test strips with location of circumferential and axial strips labelled, D.) Six test strips from one artery labelled by strip direction (first letter for strip direction: Circumferential or Axial, second letter for strip type: Axial, Circumferential, or Radial trouser tear; or Uniaxial).

Fully prepared test strips are shown in Figure 5.4D. Three circumferential (C) and three axial (A) strips were harvested from this artery. For each strip direction in Figure 5.4D, one uniaxial strip (U), one trouser tear test with an axial-circumferential plane cut (A or C), and one trouser tear test with a radial cut (R) were prepared. The geometries of strips were measured using images similar to Figure 5.4D, with the ruler used to calibrate pixel-based dimensions of the samples. Strips were rotated 90° to measure thickness. Further definition and details of the respective strips are provided: trouser tear in Section 5.3.4, uniaxial tensile in Section 5.3.5, and notched specimen in Section 6.3.2.

5.3.4 Trouser Tear Tests

Fifteen arteries were used for trouser tear tests, with each artery cut into four trouser tear test strips. Each of the four strips tested tearing in a different tissue plane (strip geometries defined in Figure 5.5).

Figure 5.5A defines the orientation of axial and circumferential test strips relative to the artery coordinate system. The four different types of trouser tear strips are defined in Figure 5.5B-E.

An axial-radial (AR) trouser tear strip is sketched in Figure 5.5B. In these strips, the tear was in the AR tissue plane (see Figure 5.3C), with the crack progressing in the axial direction and the crack front in the radial direction. Therefore, the tearing was primarily through the sheets of fibres that are in the axial-circumferential tissue plane (see Figure 5.3D).

Figure 5.5C shows the sketch of an axial-circumferential (AC) trouser tear strip. These tears were in the AC tissue plane (see Figure 5.3D), with the crack progressing in the axial direction and the crack front in the circumferential direction. These strips tested tearing between the fibre sheets of the tissue, and through fibre structures in the axial-radial tissue plane (see Figure 5.3C).

A circumferential-radial (CR) trouser tear strip is sketched in Figure 5.5D, where the crack progresses in the circumferential direction and the crack front is in the radial direction. Therefore, these tears were in the CR tissue plane (see Figure 5.3B), but through fibre structures in the circumferential-axial tissue plane (see Figure 5.3D).

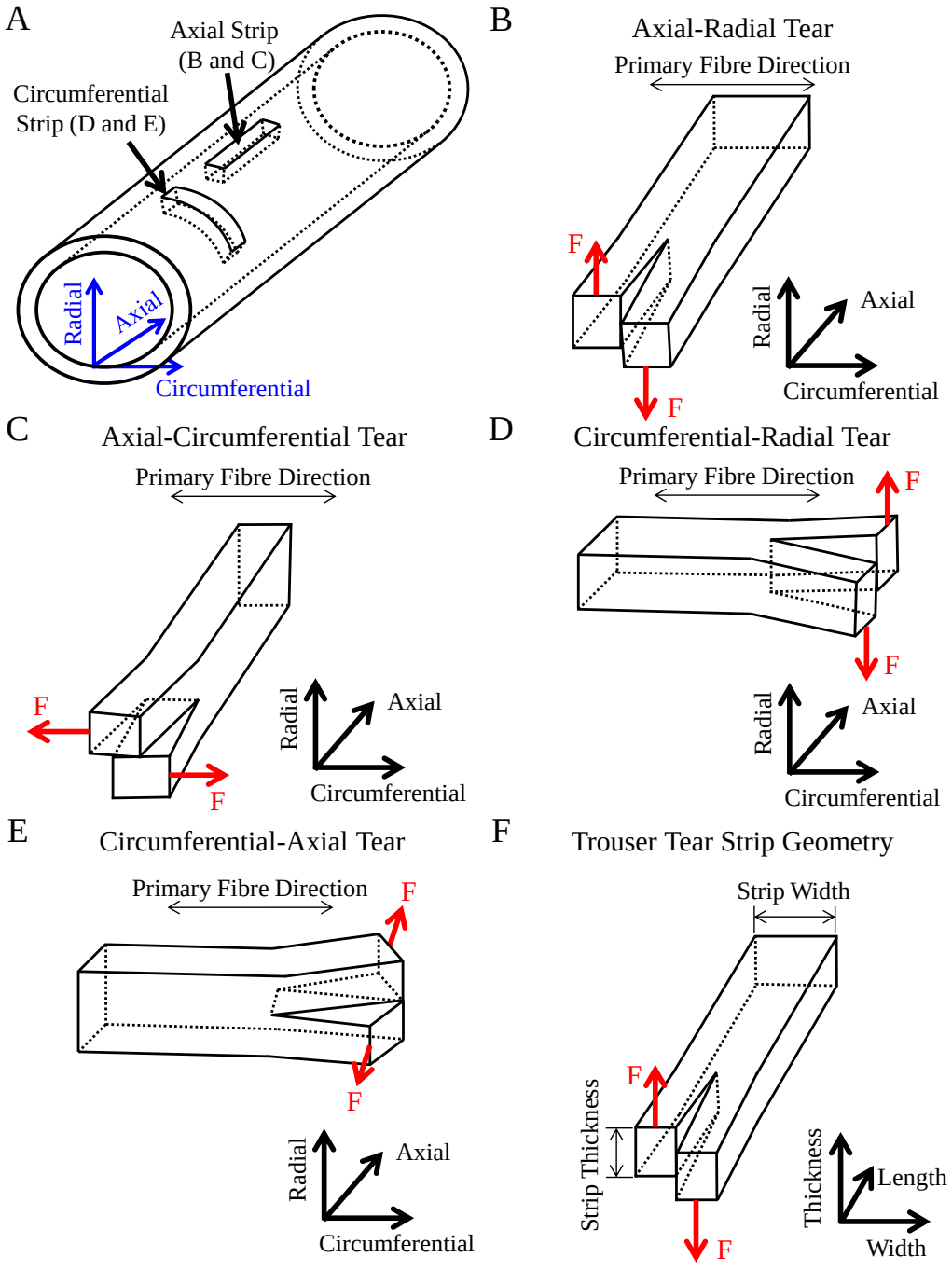

Figure 5.5: A.) Sketch of artery with coordinate system, showing relative orientations of test strips for axial (B and C) and circumferential (D and E) trouser tear samples, B.) Sketch of an axial-radial trouser tear test strip (tear is in the axial-radial plane), C.) An axial-circumferential strip, D.) A circumferential-radial strip, E.) A circumferential-axial strip, and F.) Geometry parameters labelled on a trouser tear test strip, where measurements are relative to the tearing plane coordinates, not the artery coordinate system. Note the orientation is the same for all sketches except (E) and that sketches are not to scale.

Figure 5.5E is a sketch of a circumferential-axial (CA) trouser tear strip, where the crack progressing in the circumferential direction and the crack front is in the axial direction. Therefore, these tears were in the CA tissue plane (see Figure 5.3D), but through fibre structures in the circumferential-radial tissue plane (see Figure 5.3B).

Therefore, the AR and CR test strips (Figure 5.5B and D) tore *through* fibre sheets, and were expected to have a similar and high tearing toughness. In comparison, the AC and CA test strips tore *between* fibre sheets, so were expected to have a similar tearing toughness, but lower than for the AR and CR samples.

Strip Geometries

Figure 5.5F is a sketch of key geometry measurements for the trouser tear strips. The strip thickness was in the direction of the crack front and the width was measured lateral to the crack.

Specimen geometries for the trouser tear tests are summarised in Table 5.2.

Strip Type	Strip Thickness (mm)	Strip Width (mm)
CR	1.41 [1.17, 1.61]	2.65 [2.27, 3.01]
CA	2.63 [2.32, 2.74]	1.35 [1.20, 1.84]
AR	1.15 [0.94, 1.41]	3.12 [1.87, 3.83]
AC	2.33 [2.13, 2.67]	1.38 [1.07, 1.89]

Table 5.2: Summary geometries of the trouser tear test strips, listed as the median and intra-quartile range for the strip type, for strip thickness (in tear direction) and strip width (lateral to tear).

In contrast to the geometry measurements for uniaxial tensile tests (to follow in Section 5.3.5), strip thickness was the depth the initial cut was through and the strip width was the other dimension of the cross-section for trouser tear samples. Thus, the strip thickness was the same as the artery thickness for the radial tear samples. For the AC and CA tear tests, the strip width corresponded to the thickness of the artery.

Testing and Material Parameter Methods

Trouser tear tests were reported by plotting tearing force, normalised by strip thickness (B), against displacement (see Section 5.3.1 for details on the source of these measurements from the testing apparatus).

The material tearing toughness (J_C) was calculated by Equation 5.1:

$$J_C = \frac{2\bar{F}}{B} \tag{5.1}$$

where $\bar{F}$ is the average tearing force once the crack begins propagating [Comley and Fleck, 2010; Purslow, 1989]. This tearing force was selected manually from the force-displacement plots of each test in consultation with videos of the tearing test (see sample plots with selected forces in Figure 5.10). The material toughness was calculated for each trouser tear test and compared between the four fracture planes. The J_C value was also used to investigate links with fibre structure and material stiffness.

5.3.5 Uniaxial Tensile Tests

Sketches explaining the test strips used in the uniaxial tensile tests are shown in Figure 5.6). Figure 5.6A defines the orientation of axial and circumferential test strips relative to the artery coordinate system. An axial strip, as were used in uniaxial tensile tests, is sketched in Figure 5.6B. These strips were stretched in a direction that is less aligned with most fibres in the tissue (see Figure 5.3D).

Figure 5.6C shows a circumferential uniaxial test strip, which had a stretch direction that was more aligned with the primary fibre direction.

Strip Geometries

Figure 5.6D is a sketch of key geometry measurements for the uniaxial tensile test strips. The strip thickness was the artery wall thickness, the length (between clamps) was the direction in which the strip was stretched, and the strip width was the narrower remaining dimension.

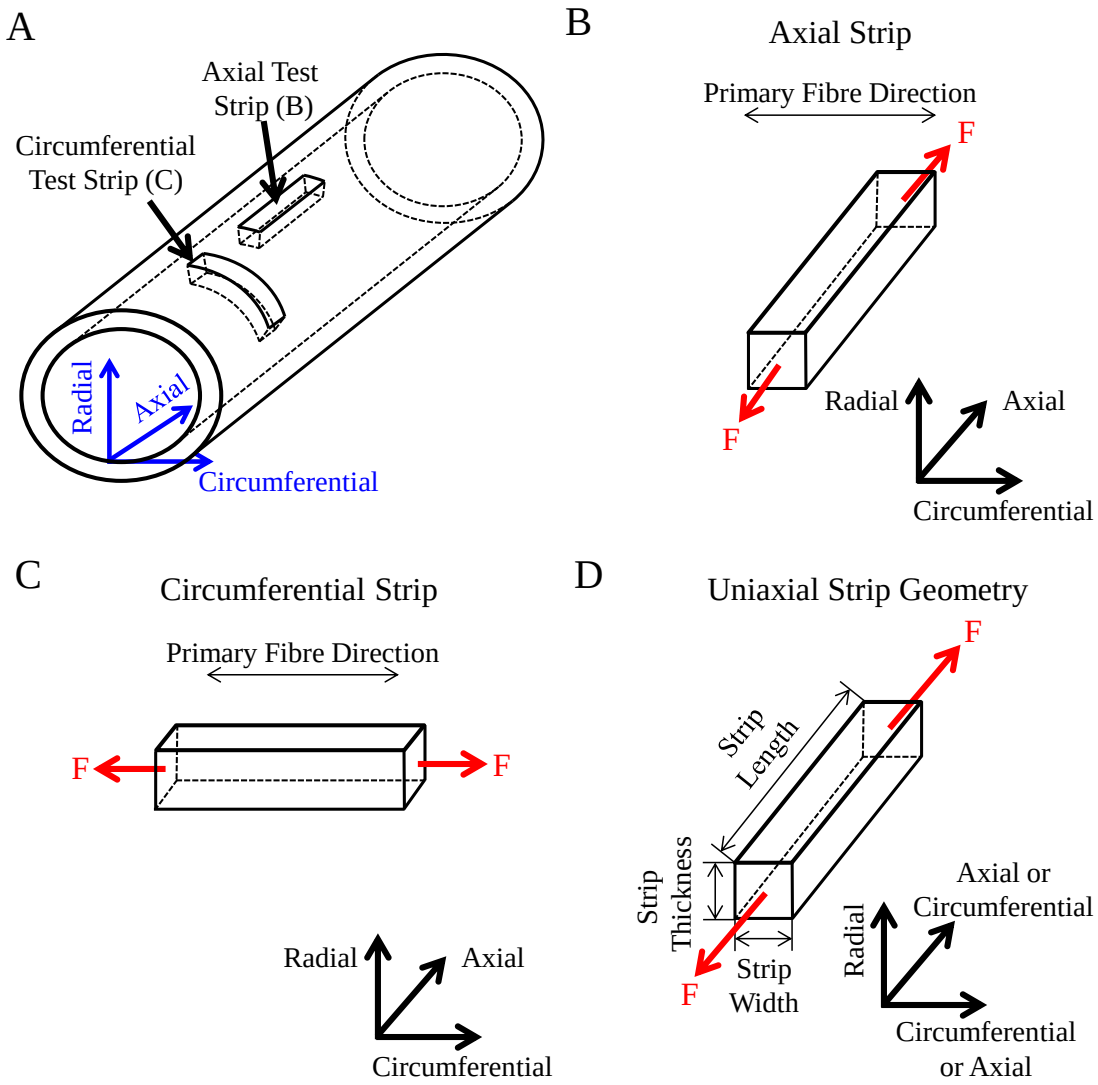

Figure 5.6: A.) Sketch of artery with coordinate system, showing relative orientations of axial and circumferential test strips, B.) Sketch of an axial test strip for uniaxial tensile tests, C.) Sketch of a circumferential test strip for uniaxial tensile tests, and D.) Geometry parameters labelled on a uniaxial tensile test strip. These sketches are not to scale.

A summary of the geometries of the uniaxial test strips is given in Table 5.3. The circumferential and axial test strips had similar average dimensions. To minimize end effects in the test results, the strips are recommended to be at least four times longer than they are thick or wide so that loading approximates pure tension [Walsh et al., 2014]. In this study, three axial and one circumferential strip were below this ratio, but their results were found to have similar material properties to other sample strips.

Geometry Parameter	Circumferential	Axial
Length (mm)	11.9 [9.59, 13.2]	11.7 [8.84, 13.2]
Thickness (mm)	0.98 [0.75, 1.12]	0.89 [0.75, 1.12]
Width (mm)	2.26 [1.29, 2.67]	2.32 [1.65, 2.50]
Length:Width	5.54 [5.16, 6.89]	5.05 [3.80, 6.91]
Length:Thickness	11.6 [9.46, 13.0]	12.0 [8.27, 16.3]

Table 5.3: Summary geometry of the uniaxial tensile test strips; the median and intra-quartile range for the circumferential and axial strips.

Testing and Material Parameter Methods

These tests used the materials test apparatus described in Section 5.3.1 to stretch the sample, while recording the applied displacement and resulting tensile force. To compare stiffness between axial and circumferential strips, Cauchy stress was plotted against stretch for each uniaxial test strip. The sample stretch (λ_1) was calculated from the sample length (l_0) and displacement (x) at each step by the motor (see Equation 5.2):

$$\lambda_1 = \frac{x + l_0}{l_0} \tag{5.2}$$

The Cauchy stress (σ_1) was calculated using the strip's unloaded width (w_0), unloaded thickness (t_0), and force (F) from the sensor (see Equation 5.3, assuming incompressibility and σ_2=σ_3=0):

$$\sigma_1 = \lambda_1 \frac{F}{w_0 t_0} \tag{5.3}$$

For a simple measurement of artery stiffness, the tangent modulus was calculated at physiological loading. For circumferential strips, physiological loading was considered as the approximate stress from systolic blood pressure, by Laplace's Law (see Equation 5.4):

$$\sigma_c = \frac{Pr}{t} \tag{5.4}$$

where P is blood pressure (assumed to be 120 mmHg or 16 kPa in pigs as well as humans [Hodgkin et al., 1982]), r is the radius of the vessel (≈6 mm for vessels in these experiments), t is the thickness of the vessel (≈1 mm), and σ_c is the circumferential stress (≈100 kPa). By Laplace's Law, the axial stress is half the circumferential stress, but the tangent modulus for axial strips was also calculated at 100 kPa to better compare stiffness between the strip directions.

To calculate the tangent modulus (E_c for circumferential or E_a for axial), the stress-stretch data was first smoothed (using Matlab's *smooth* function with *rlowess* robust weighting and a span of 5%). The tangent modulus was calculated as the slope of the stress-stretch curve at the physiological-equivalent stress, as in Equation 5.5:

$$E = \frac{d\sigma_1(\sigma_c)}{d\lambda_1(\sigma_c)} \tag{5.5}$$

5.3.6 Image Processing of Histological Samples

A sub-set (see Table 5.1) of mechanical test strips were histologically prepared, imaged, and had their fibre structure described by similar methods as were described for the plaque samples in Chapter 3. Therefore, the methodology presented in this section will reference the methods that were developed in Chapter 3, and emphasise the changes to these previous methods.

After mechanical testing, samples were preserved by formalin (10%, buffered) fixation. After at least 24 hours in the formalin solution, the tissue strips were histologically prepared with EVG staining by Nicola Figg in the Cardiovascular Medicine Department. The slides were digitised using a Nanozoomer machine at 40× magnification. Images were exported at a 7680×4800 resolution to Matlab.

These healthy tissues had consistent fibre structure throughout the sample (see Figure 5.7A). Therefore, primary fibre orientation and fibre dispersion were calculated for a manually selected region of representative tissue.

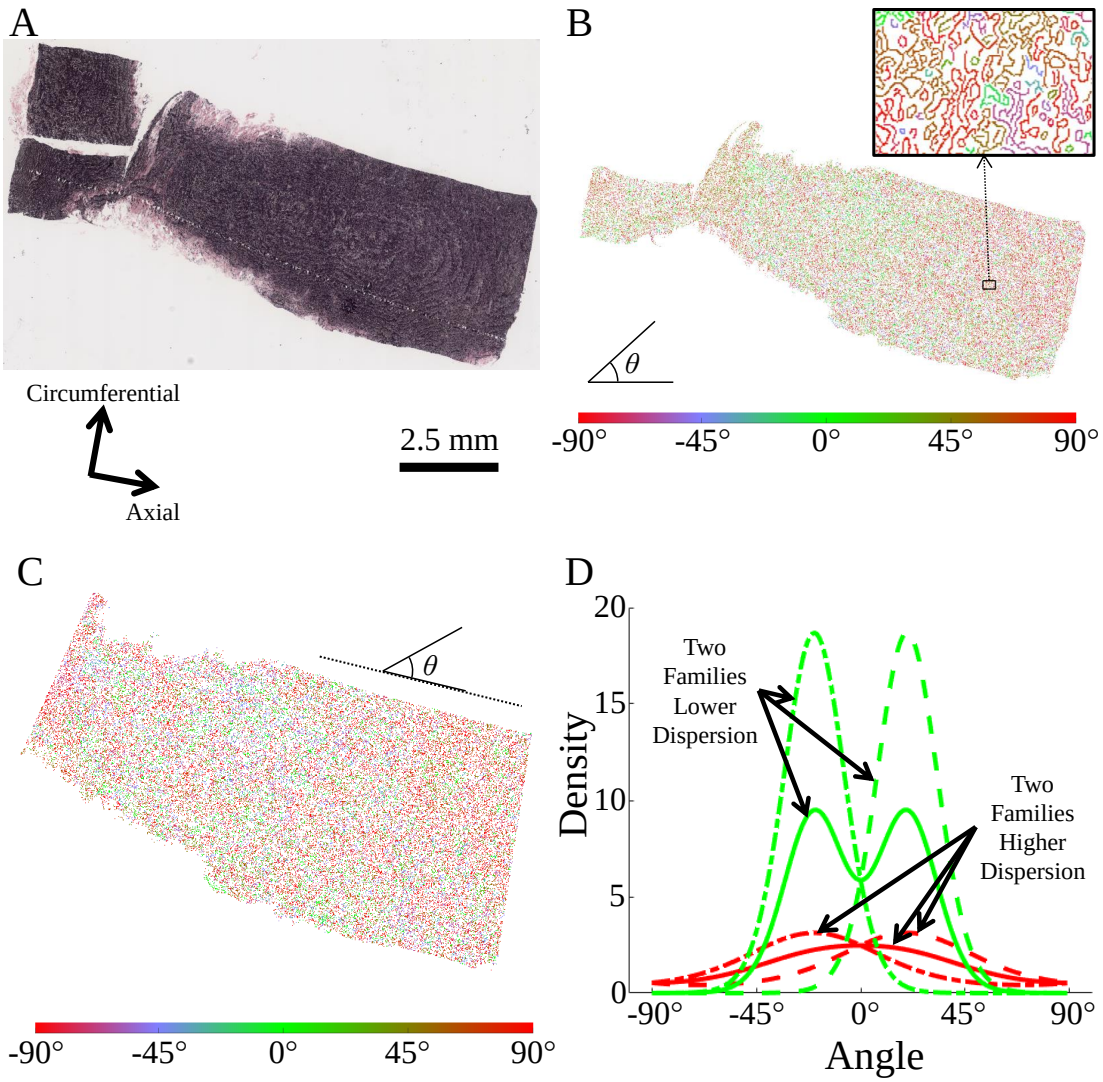

Figure 5.7: A.) Illustrative EVG histology image of a test strip, B.) Detected fibres in the test strip, with colour indicating orientation relative to the image frame (enlargement details fibres) C.) Detected fibres and orientations relative to the test strip frame. A region from (B) was manually selected to reduce artefacts, and D.) Density distributions for individual fibre families (dashed) and combined density distributions when two fibre families are present (solid).

Previous reports on microstructure in artery tissue proposed that fibres are arranged into systems of one family of fibres, two families of fibres, or an isotropic scattering of fibres [Schriefl, 2013; Schriefl et al., 2012b]. In this chapter, the axial-circumferential plane porcine arteries had fibre structures that could be similarly described. Therefore, methods were developed to characterise fibre structure as a one-family system (as in Chapter 3) and as a two-family system. These methods will be further described in the following sections.

Detection and Orientation Calculation of Individual Fibres

Fibres in the histology image were detected using the Matlab implementation of the Canny edge detection filter (see Figure 5.7B). Detected edges having more than 500 connected pixels were split into smaller connected groups by removing fibre pixels intersecting with a 75×75 grid. Edges having fewer than 10 connected pixels were removed. The orientation of each edge relative to the image frame was calculated by the *regionprops orientation* function in Matlab. Each pixel in an edge was assigned the orientation that was calculated for the whole fibre-edge.

Fibre orientations were referenced to the long axis of the test strip, which corresponded to either the circumferential or axial direction of the artery (see Figure 5.7C). To account for curves in the sample, the long axis was defined manually at each lengthwise edge of the sample. Local orientations relative to the image frame were calculated along these traced lines, and were used to calculate a local reference orientation throughout the sample using Matlab's *gridfit* function, with linear interpolation. Fibre orientations were transformed to be relative to this local reference.

Single-Family Fibre Structure

The bimodal mean fibre orientation relative to the strip's long axis (θ_i) and the fibre dispersion (κ) were calculated for each sample, using the methods similar to those described in Chapter 3. The differences were that fibre orientation and dispersion were calculated for the whole image rather than for a 50×50 ROI around each pixel, and κ was calculated using 180 discrete bins for the orientation density function ($P(\theta)$) instead of 20. The 50×50 ROI was originally needed

because the fibre structure changed with location in the atherosclerotic tissues. In the healthy porcine arteries here, fibre structure was more consistent.

5.3.7 Two-Family Fibre Structure by Curve Fitting

Analysis in Chapter 3 only considered images of the artery cross-section, which was assumed to have only one family of fibres. However, fibres in the CA plane of the artery (see Figure 5.3D) were expected to have two symmetrically opposed families of fibres that helically climb the artery [Gasser et al., 2006]. The two opposing families are assumed to otherwise be identical.

Determining the fibre dispersion of each family is not possible through the calculations used in Chapter 3, because orientation density normalisation made assumptions that required there being only one family of fibres (see Section 3.4.6).

Figure 5.7D illustrates fibre distributions (solid lines) in tissues with two fibre families (fibre distributions of individual families shown by dashed lines). If the separation of the two families is relatively small or the dispersion is relatively high, the combined distribution of fibre orientation may appear to have only one peak (red solid line) or have a double-peak distribution (green solid line). In other distributions, there were clearly two families of fibres present.

Distribution-Fitting Method to Estimate Two-Family Fibre Structure Properties

To estimate fibre structure for two families of fibres (n=2), an optimisation method was developed to fit the relative density distribution of fibre orientation ($P(\theta)_2$, equivalent to a probability density function). The two-family orientation density distribution ($P(\theta)_2$) is for the frequency of orientations calculated for pixels in the histology image, with the normalisation condition in Equation 5.6:

$$\frac{1}{2\pi}\int_0^{\pi} P(\theta)_2\, d\theta = 1 \tag{5.6}$$

where the 2π factor accounts for the distribution being in circular coordinates, but the integral is solved between [0, π] because the fibre orientation is π-periodic and had been forced to be within this range (see Section 3.4.4).

Figure 5.8 shows representative results for fibre orientation density functions ($P(\theta)_2$) found from calculated fibre orientations. The labelled parameters and fitted distribution curves will be described through this section.

All histology images in the axial-radial and circumferential-radial planes (as defined in Figure 5.3B and C) were one-family distributions similar to Figure 5.8D, but typically with a narrower density distribution (lower fibre dispersion).

Of the 22 histology images in the circumferential-axial plane (defined in Figure 5.3D), three had clearly defined two-family systems as in Figure 5.8A. Six other images had nearly isotropic fibre orientation as in Figure 5.8B, with two of these possibly having a two-family system (as shown in (B)). Two images had fibre structures similar to Figure 5.8C, where the distribution could be modelled as a one-family system or a two-family system with the families nearer to one another. The remaining 14 (of 22) images of the circumferential-axial plane, the distributions supported a one-family system as shown in Figure 5.8D.

The optimisation sought to minimize the sum of squares difference (R_{min}) between the normalised density of calculated fibre orientation ($P(\theta)_2$), and a two-family von Mises orientation density function model ($P_m(\theta)_2$), as in Equation 5.7:

$$R_{min} = \sum (P_m(\theta)_2 - P(\theta)_2)^2 \tag{5.7}$$

Both distributions are π-periodic, and considered between [0, π]. The two-family von Mises orientation density model ($P_m(\theta)_2$) is for the combination of two standard von Mises distributions. One distribution is centred at θ_1 and one at θ_2, with the combined distribution defined by Equation 5.8:

$$P_m(\theta)_2 = \frac{\exp(b\ \cos[2(\theta - \theta_1)]) + \exp(b\ \cos[2(\theta - \theta_2)])}{4\ \int_0^\pi \exp(b\ \cos\theta)\mathrm{d}\theta} \tag{5.8}$$

which is the average of two standard, π-periodic von Mises distributions. The concentration parameter (b) is equivalent to standard deviation for circular statistics, and has a direct but non-linear equivalence to fibre dispersion (κ) when a different normalisation is used (see Equations 3.15 and 3.14). Figure 5.8 shows the two individual distributions (red and green) that are combined for a two-family distribution (cyan).

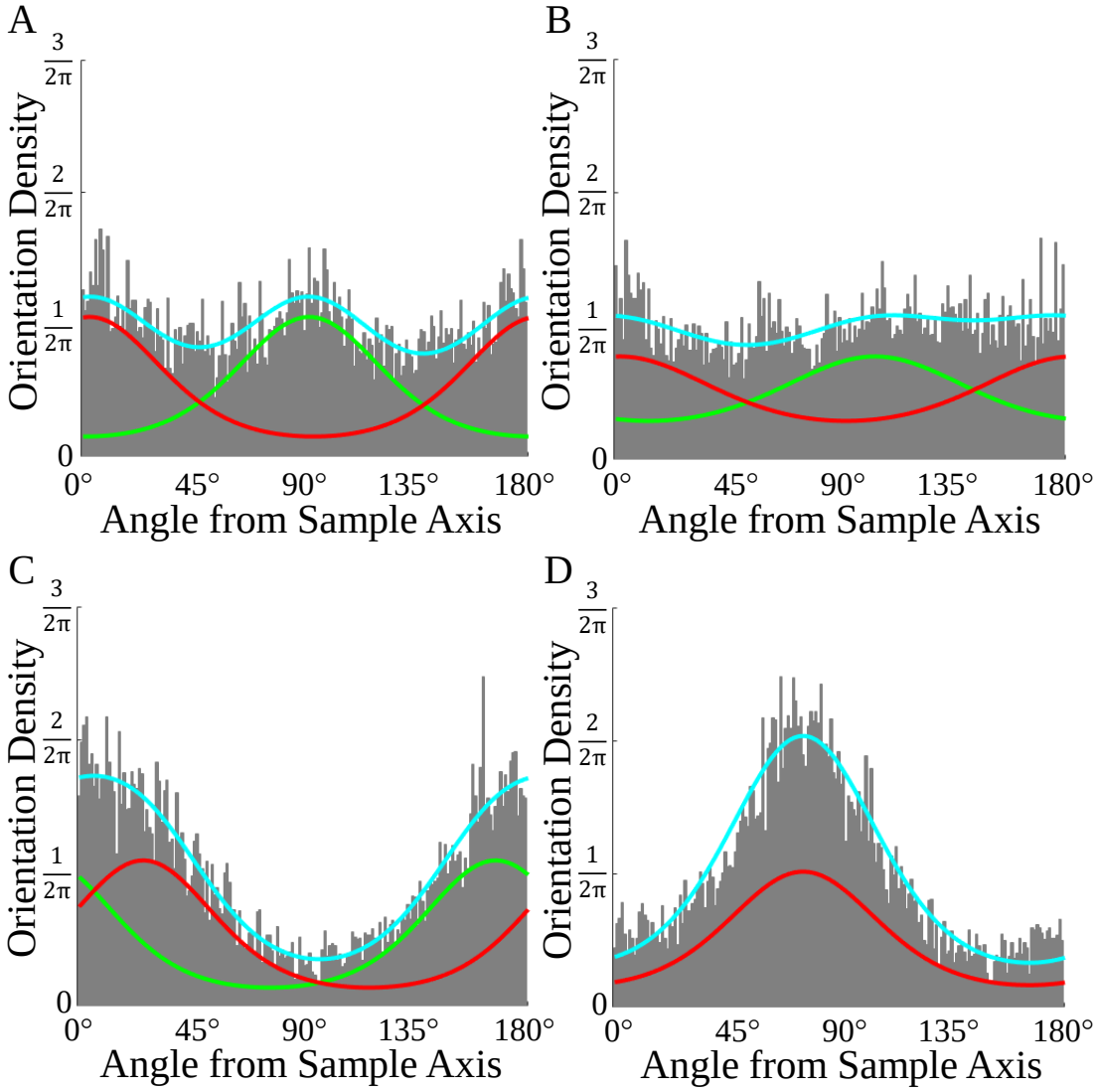

Figure 5.8: A series of representative outcomes for fibre orientation densities fitted with a two-family fibre distribution, showing: A.) Two distinct fibre families, separated by 90°, B.) A relatively isotropic fibre distribution, fitted by two fibre families with high dispersion and separated about 90°, C.) A broad, single peak distribution fitted with two fibre families separated about 45°, and D.) A moderately wide single peak distribution where the two fitted families have no separation angle, seen for the majority (14 of 22) of histology images in the circumferential-axial plane. The cyan line is for the fitted two-family orientation distribution, with the distributions of the two individual fibre families in green or red.

The peaks of the two individual von Mises distributions (θ_1 and θ_2) are related through Equation 5.9:

$$\theta_{1,2} = \theta_o \pm \theta_s \tag{5.9}$$

where the offset angle (θ_o) is the angle between the direction of the test strip and the centre of the two-family orientation density distribution ($P_m(\theta)_2$). Therefore, θ_o is expected to be similar to the mean fibre orientation (θ_i) for a one-family fibre system. The split angle (θ_s) is the angle between θ_o and the peak of each individual von Mises distribution (θ_1 and θ_2). Figure 5.8 is labelled with these various orientation parameters.

Initial Values and Solver Parameters

Values for θ_s, θ_o, and b were found by minimising Equation 5.8 using Matlab's *fminsearch* function. The initial conditions for the optimisation function were: θ_s=40°, θ_o=-30°, and b=1. These parameters were selected to avoid local minima from a one-family system (θ_s=0°) and from near-isotropic distributions where ($P_m(\theta)_2$) was approximately constant. Since the histology images also had their fibre structures evaluated assuming a one-family system, the initial values here intentionally favoured two-family systems to be found ($\theta_s \neq 0°$).

The minimisation function evaluated Equation 5.8 through 180 discrete bins, as used to make the orientation density function. Since the distribution was defined between [0°, 180°] and was bimodal (or π-periodic), the effect of θ_s and θ_o was to shift the two individual distributions. The *fminsearch* function continued iterating until the solver found a minimum of R_{min} to a tolerance of 10^{-8}, with a tolerance of 10^{-6} for the three optimised variables.

The fitted fibre dispersion for the individual von Mises distribution fibre families (κ_2) was calculated from the fitted solution's b and the von Mises distribution with spherical normalisation (see Equation 3.15). In other words, κ_2 was the dispersion of one family within a two-family system, and the two individual families had the same value for κ_2.

Histology Fibre Structure Parameters for Each Strip

For each test strip that was prepared by histology, the bimodal mean fibre orientation (θ_i), one-family κ, two-family split angle (θ_s), two-family distribution mid-point angle (θ_o), and two-family fibre dispersion (κ_2) were calculated. The values and orientation distribution plots for each sample were then reviewed to determine if the sample was best represented by a one-family, two-family, or isotropic fibre system.

5.4 Experiment Results

Results are presented for the trouser tear tests (Section 5.4.1), uniaxial tensile tests (Section 5.4.2), and fibre structure image processing (Section 5.4.3).

5.4.1 Trouser Tear Results

Trouser tear tests were used to evaluate the tearing toughness in different planes of tissue. This section starts with a summary of observations of damage to fibre structures from the trouser tear tests. Secondly, representative force-displacement plots for tearing are provided. Thirdly, summary results for tearing toughness in the four different tissue planes are reported.

Fibre Damage in Histology Images from Trouser Tear Test Samples

The trouser tear tests were used to compare mechanisms and tearing toughness in different planes of the tissue. Figure 5.9 shows EVG stained slides of tears in the axial-circumferential (A, B, and C) and axial-radial (D) planes of the artery tissue (planes defined in Figure 5.3). Recall that axial-radial (AR) tears are though fibre structures in the circumferential-axial (CA) plane, and axial-circumferential (AC) tears are through structures in the circumferential-radial (CR) plane (see Figure 5.5 for plane definitions).

Tears in the AC plane caused delamination failures (see Figure 5.9A). The tear progressed at a fairly constant depth through the sample, and travelled between rather than by breaking fibres.

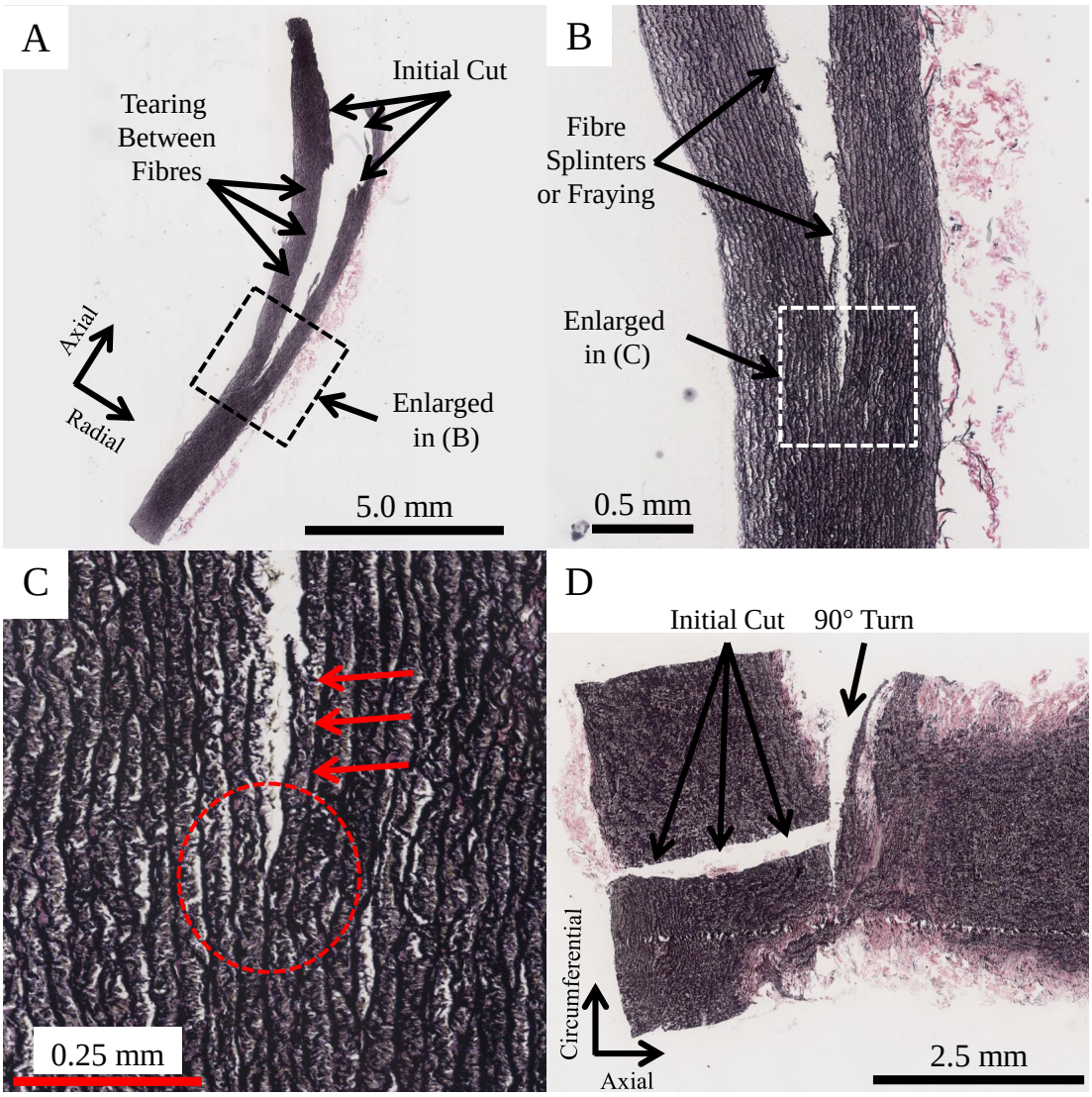

Figure 5.9: EVG-stained histology slides of tearing mechanisms in trouser tear test strips. A.) An axial-circumferential trouser tear sample (perspective shows fibre layers through thickness of artery, primary fibre orientation with layers is out of the plane), B.) 4× enlargement of (A), showing delamination between fibre layers, C.) 15× enlargement of (A), detailing the crack tip, and D.) An axial-radial trouser tear sample, where the fracture plane has turned 90° to fail in the circumferential-radial plane (imaging plane parallel to fibre layers, primary fibre orientation is vertical direction in image).

The image in Figure 5.9B was magnified about 4× to show further details of the tear. While the fracture progressed mainly between fibres, some fibres have frayed from the torn edge. The fracture sometimes changed to a parallel tearing plane at these frayed fibres. The frayed fibres appear to be ends of intact fibres, not from fibre fractures.

The tip of the fracture is shown at 15× magnification in Figure 5.9C. The region within about four fibres to each side of the crack tip appears to show damage (red dashed circle in Figure 5.9C; radius around 50-100 μm). There is evidence of fibre bridging for about 300 μm behind the crack tip (red arrows in Figure 5.9C). Similar features of damaged regions and bridging were seen in the other tearing planes.

A histology image of an axial-radial (AR) trouser tear is shown in Figure 5.9D. AR strips often failed by the tear turning perpendicular to its initial direction. Tears in other strip types rarely changed from their initial direction and did so gradually. Fibres in the AC plane are dispersed, but usually had a preferred direction towards the circumferential axis (see Section 5.4.3). Therefore, the right angle turn in the AR trouser tear samples allowed the tear to progress with less resistance by crossing fewer fibres.

In summary, tears were seen to progress around rather than through fibres. Dispersion and cross-links between fibres suggested loads and damage were spread across the network, increasing energy absorption and toughness of the material. These mechanisms will be further described in Chapter 6.

Required Force for Tearing

Figure 5.10 shows the force per unit width against displacement for a representative samples from each of the four sample types (see Figure 5.5 for sample definitions and Figure 5.3 for tearing plane definitions): axial-radial (A), axial-circumferential (B), circumferential-radial (C), and circumferential-axial (D).

The curves have an initial loading region, where the force builds from zero to a magnitude sufficient to tear the material. Most samples then tore with a relatively constant force. Once failure begins, the tearing force undulates, with force increasing as fibres are recruited around the crack tip, then dropping when

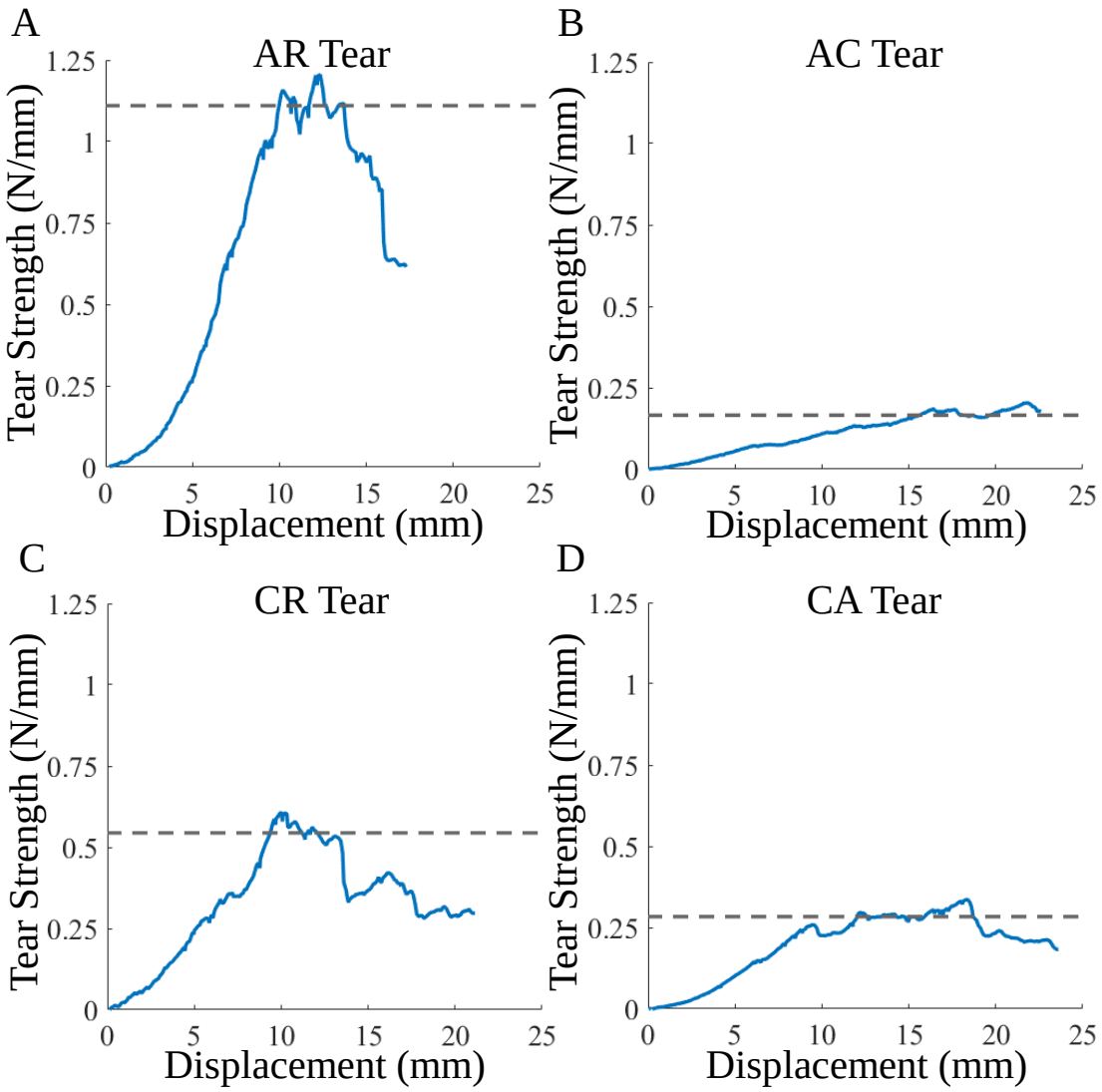

Figure 5.10: Trouser tear results from different planes of one artery (Tearing Strength is $\frac{\bar{F}}{B}$): A.) Axial-radial, B.) Axial-circumferential, C.) Circumferential-radial, and D.) Circumferential-axial. The dashed line indicates the thickness-normalised tearing force used to calculate the tearing toughness (J_C, which is the dashed line multiplied by the factor of 2).

groups of fibre bridging the crack fail. These cycles of loading, fibre recruitment, and local failure occur over about 0.5-1 mm of sample clamp displacement, with an implied crack propagation of half this distance.

Tearing Toughness

The radial plane tears (see Figure 5.10 for plane definitions) had considerably higher tear strength compared to the circumferential-axial (CA or AC) planes. The CA and AC plane tears had a similar strength to one another. The axial-radial plane (AR) had a higher tearing strength than the circumferential-radial plane (CR), but these samples often failed at a lower force by the tear turning from the AR plane to the CR plane (see Figure 5.9D).

Summary results for tearing toughness (J_C, from Equation 5.1) of all samples for tears in different planes are shown in Table 5.4.

Tear Plane	Strip Direction	Relative to Fibre Layers	J_C (kJ/m^2)
AC	Axial	Parallel	0.20 [0.15, 0.31]
AR	Axial	Through	0.99 [0.52, 1.24]
CA	Circumferential	Parallel	0.25 [0.15, 0.48]
CR	Circumferential	Through	1.04 [0.65, 1.24]

Table 5.4: Tearing toughness (J_C) for tears in each strip direction and tearing plane, reported as the median and intra-quartile range. Each tearing plane is either parallel to or through the fibre layers, which concentrically form the artery wall thickness.

Tearing toughness was significantly higher in the radial planes compared to the AC and CA planes ($p<0.001$ using a paired t-test), with the median tearing strength about four times higher in the radial planes. There were no significant differences in tearing toughness between the CR and AR planes or between the CA and AC planes. The spread of tearing toughness within a sample type was considerable, with the 75^{th}-percentile toughness value about two to three times the 25^{th}-percentile value for any sample type.

Discussion of Trouser Tear Tests

Tearing strength was considerably higher in the radial (CR and AR) planes than in the circumferential-axial (CA and AC) planes. Therefore, the CA and AC plane tears propagated with lower force, causing delamination between adjacent fibre sheets. Tears progressed more easily between fibres, evidenced by the AR samples failing by the tear turning to be in the CR plane.

While the average tearing force was used to calculate the tearing strength, the tearing force had peaks and troughs that implied fractures propagated by jumps of about 250-500 μm. This was believed to correspond with fibre recruitment and crack bridging without tear progression, followed by fracture of multiple fibres. In the histology images of trouser tear tests (see Section 5.4.1), evidence of fibre bridging was seen at a distance up to 300 μm behind the crack tip. Thus, fibre structure caused a higher peak tearing force, and short incomplete fractures through the tissue. *In vivo*, local failure may provide local strain relief, allowing high local stresses to be redistributed across a wider area of tissue.

Tearing toughness had considerable variability, with tears in the same plane having a range of about $\pm 50\%$ around the median toughness for a given tear type. In diseased tissue, even more variability would presumably be found, presenting a challenge for patient-specific computational models of plaque rupture risk. Higher stress has been proposed as a indicator of higher rupture risk, with high risk often assumed to indicated by exceeding a particular stress value. However, it is unlikely that a single value will be specific in risk prediction, since there is such variability in toughness or strength between different samples. Risk predicted by computational models should ideally be considered relative to plaque-specific toughness or strength. Section 5.5 will consider relationships between tearing toughness, stiffness, and fibre dispersion to identify determinants of toughness.

5.4.2 Uniaxial Mechanical Results

The stress-stretch relationships for the uniaxial strips are plotted in Figure 5.11. The circumferential strips (Figure 5.11A) were generally stiffer than the axial strips (Figure 5.11B). However, there was considerable range to sample stiffness, and some axial strips were stiffer than some of the circumferential strips.

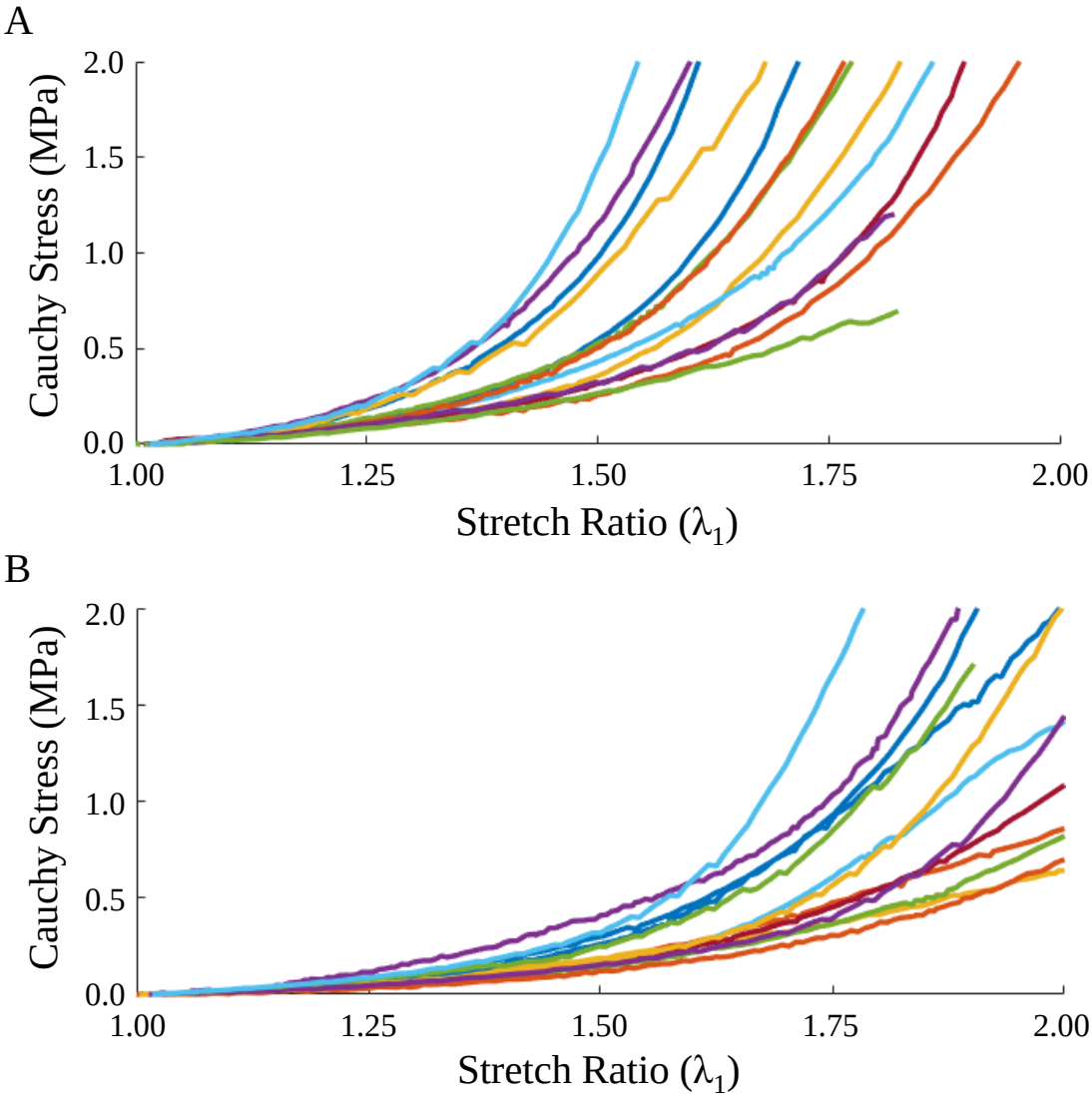

Figure 5.11: Cauchy stress versus stretch ratio for the uniaxial tests, for: A.) Circumferential and B.) Axial test strips. The plots axes are truncated to emphasise differences at physiological stiffness levels.

To compare stiffness, the tangent modulus was calculated for each sample at a stress of 100 kPa, which is approximately the circumferential stress in an artery from blood pressure (see Section 5.3.5). The median and intra-quartile range for the tangent modulus from each strip type is shown in Table 5.5.

Strip Type	Tangent Modulus (kPa)
Circumferential	825 [623, 1040]
Axial	490 [468, 545]

Table 5.5: Median and intra-quartile range for tangent modulus of circumferential and axial uniaxial test strips at 100 kPa.

The tangent modulus of the circumferential strips was significantly higher ($p<0.001$ using a paired sample t-test) than for the axial strips.

Many of the uniaxial tensile tests finished with the sample slipping from the clamps, fracturing near the clamps, or exceeding the force of the sensor. Therefore, the final values for stress and stretch of each sample in Figure 5.11 could be considered a lower-bound estimate for failure. However, these values still exceed previously reported failure stresses (about 0.3-3 MPa) and stretches (about 1.5-1.9) for human carotid plaques [Walsh et al., 2014].

5.4.3 Fibre Structure from Histological Images

Fibre structure was calculated for a total of 56 histological images of porcine arteries. These images were in four possible planes of the tissue: axial-radial (AR, 16 samples), axial-circumferential (AC, 12 samples), circumferential-radial (CR, 18 samples), and circumferential-axial (CA, 10 samples). The planes were as defined in Figure 5.3, with the AC and CA planes being the same but with the reference direction rotated 90° (from the axial direction to circumferential). The first letter in a plane's name refers to the long axis direction of the test strip, which fibre orientation was referenced to.

Representative Fibre Structure in Each of the Tissue Planes

Histology images and corresponding fibre orientation densities are shown for four tissue planes of the same artery for axial strips in Figure 5.12 and circumferential

strips in Figure 5.13. To aid in viewing the fibres, the histology images shown here are enlarged portions of the original images. Further and more quantitative comparison of fibre structures in the different planes will follow in Section 5.4.3.

Figure 5.12A shows a histology image and corresponding fibre distribution of an axial-radial (AR) tissue plane, with fibres having low dispersion and a primary orientation near the axial direction. Even when a two-family system was assumed, the fibre structure was found by the fitting algorithm from Section 5.3.7 to have a one-family system (no separation between the two families of overdrawn lines). Most AR plane histology sections had this appearance, with the fibres equivalent to the sheets of tissues that were sketched in Figure 5.3. Some samples had higher dispersion in the AR plane, but generally the radial component of a fibre's 3D orientation was smaller than the axial or circumferential components.

An equivalent image and plot for an axial-circumferential (AC) plane are shown in Figure 5.12B. This plane has much higher fibre dispersion, and has been best fitted with a two-family distribution with π-periodic distribution peaks at 0° and ±90°. However, the two families in this particular distribution are quite dispersed, so could be considered an isotropic distribution of fibres.

For a circumferential-radial (CR) plane of the artery, a histology image and resulting orientation density are shown in Figure 5.13A. Fibres in this plane had low dispersion and were primarily oriented in the circumferential direction.

Figure 5.13B shows a histology image and orientation density of a circumferential-axial (CA) plane. Similar to the equivalent plane in the axial sample, this plane had a high fibre dispersion. The fibre structure of this particular sample was best represented by a two-family fibre distribution that had π-periodic distribution peaks at 0° and ±90°.

Discussion of Section

The texture of the AC and CR planes suggested the two fibre families, if present at all, were found within the same sheet of the tissue. This finding is counter to most previous models that alternating plies of tissue have opposing primary orientations [Clark and Glagov, 1985; Schriefl, 2013; Schriefl et al., 2012b]. If the histology was limited by only considering one ply of tissue, the structure

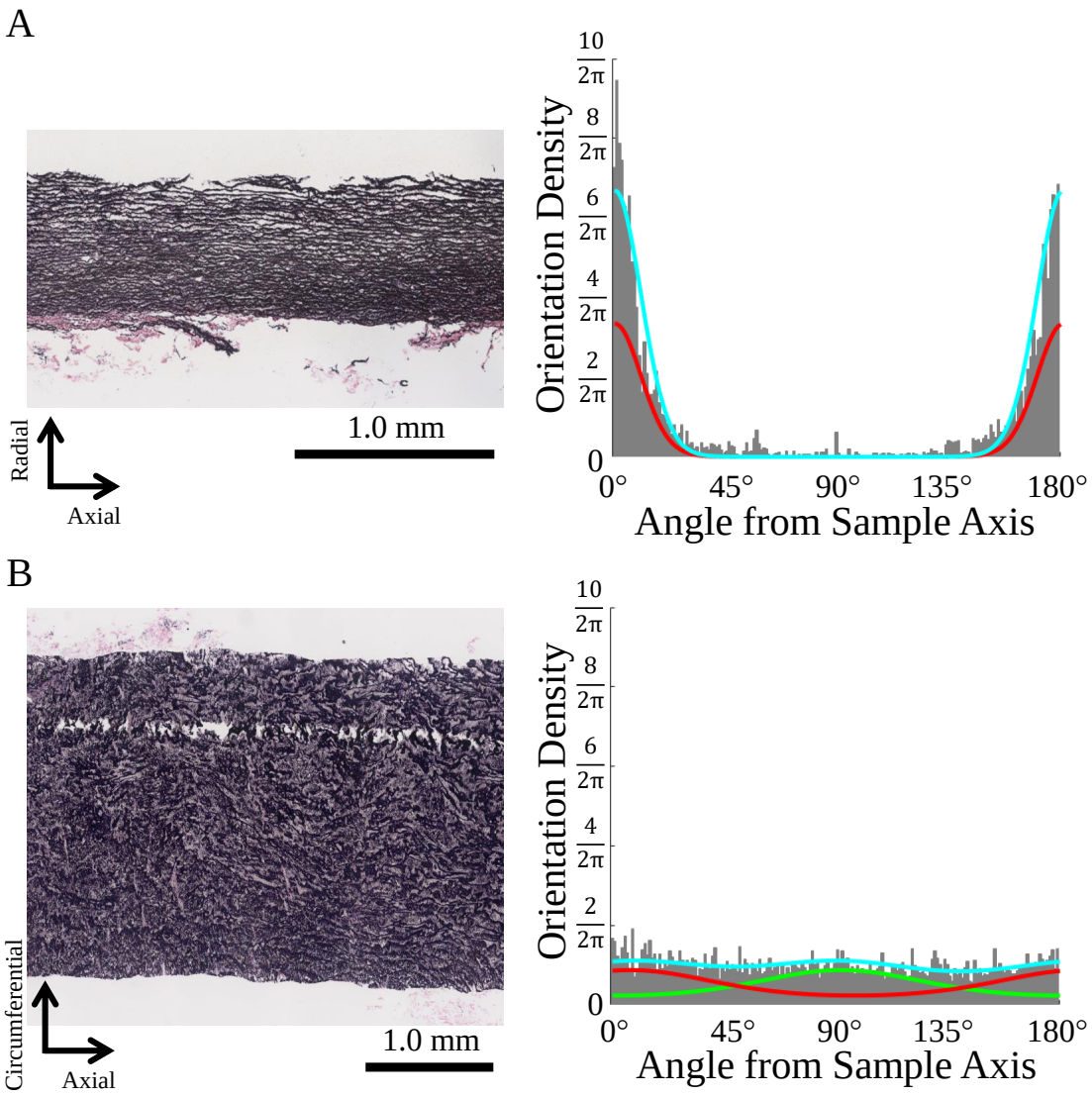

Figure 5.12: A.) An EVG histology image of an axial-radial plane of tissue (shows layers of fibre in artery thickness, fibres within layers are mainly oriented out of plane) and corresponding orientation density plot, and B.) EVG image of an axial-circumferential plane of tissue (image parallel to fibre layers, fibres mainly vertical) and corresponding orientation density plot. The scale of the vertical axis is relative to the normalisation condition (see Equation 5.6), where an isotropic distribution has a constant value of $\frac{1}{2\pi}$. The coloured lines over the plot are for a fitted two-family fibre distribution (see Section 5.3.7).

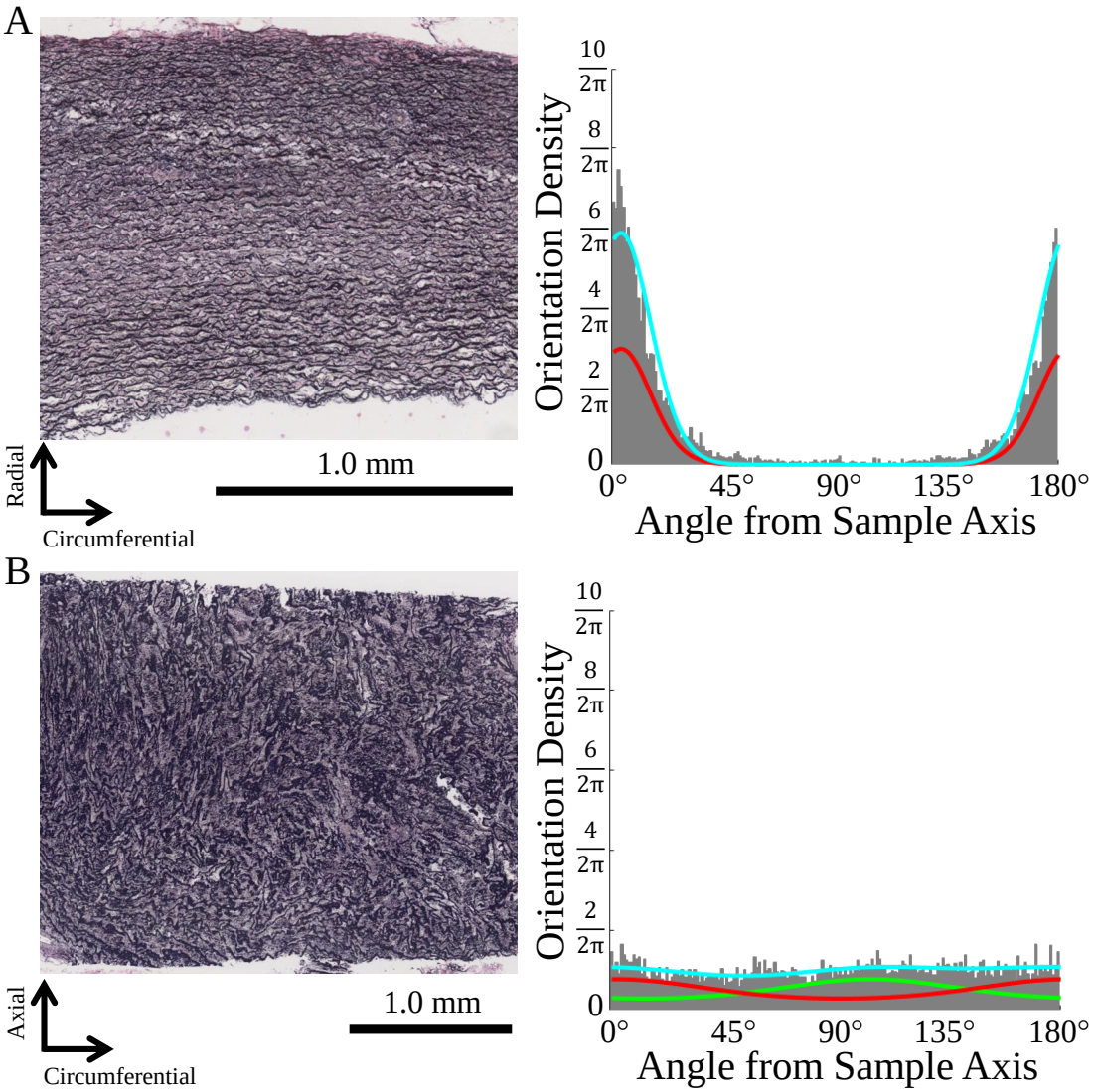

Figure 5.13: A.) An EVG histology image of a circumferential-radial plane of tissue (shows layers of fibre in artery thickness, fibres within layers are horizontal in the plane) and corresponding orientation density plot, and B.) EVG image of a circumferential-axial plane of tissue (image parallel to fibre layers, fibres mainly horizontal in image and corresponding orientation density plot.

proposed by these previous models would expect to find one family of fibres at an angle from the sample's axis, which was not seen here. Alternatively, patches of tissue within the histology section with different primary orientations might be expected, which also were not seen.

While these minor differences from previous models are interesting, the main finding of fibres being dispersed within the circumferential-axial plane remains. Furthermore, there was considerable variability to the tissue, even within the same artery, which will be further described in the following sections (see Figures 5.14 and 5.17). With high dispersion in this tissue plane and considerable variability between and within an artery, the precise fibre structure at a given location in the tissue may be less useful in determining mechanics.

Measurements of Fibre Structure in Different Planes

Figure 5.14 compares fibre properties between these different imaging planes, with Figure 5.14A and B assuming a one-family system (see Section 5.3.6) and Figure 5.14C and D assuming a two-family system (see Section 5.3.7).

One-Family Fibre Structure in Histology Images

Fibre structure should consider fibre orientation alongside dispersion. For example, the primary fibre orientation (Figure 5.14A) becomes more important with a lower fibre dispersion (Figure 5.14B). As an extreme case, the primary fibre orientation is meaningless for an isotropic fibre distribution ($\kappa{=}\frac{1}{3}$).

The bimodal mean fibre orientation (θ_i) of the different tissue planes are compared in Figure 5.14A. In both the AR and CR samples, θ_i was near 0° relative to the sample's axis (axial or circumferential) for all samples. The CA samples had θ_i values around 0°, but with a wider spread compared to images in the AR or CR planes. For the AC images, θ_i values were mainly at ±90°, with a few samples having a values near 0°. Recall that the AC and CA planes were the same, but had a different reference direction. Therefore, the AC samples with θ_i values at ±90° showed the same primary orientation as CA samples with $\theta_i{\approx}0°$ (i.e. primary orientations were in the circumferential direction).

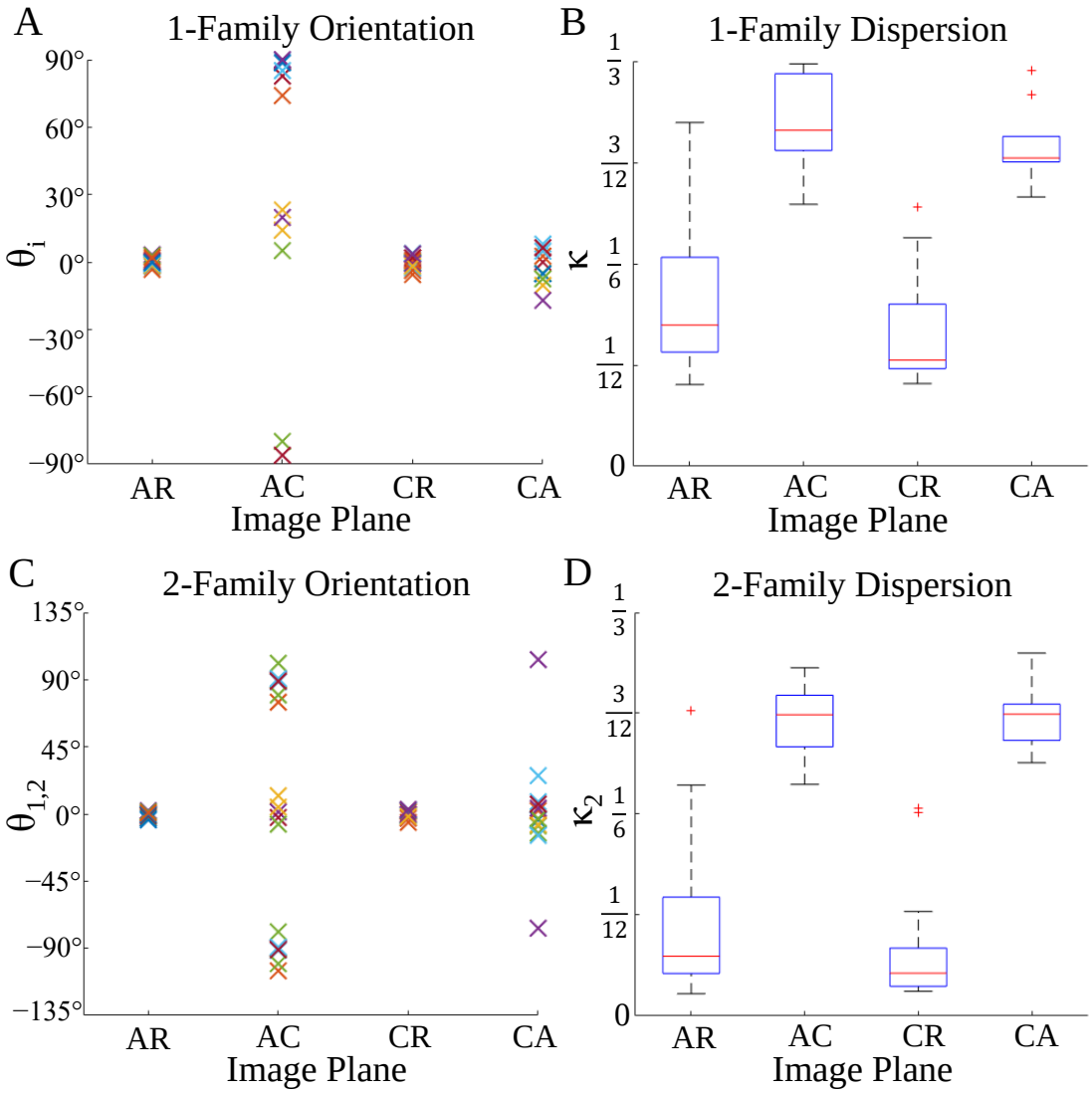

Figure 5.14: Fibre properties in histology images compared between planes of the tissue (defined in Figure 5.3) for: A.) Bimodal mean fibre orientation relative to the long axis of the sample (axial or circumferential axis, θ_i), B.) Fibre dispersion for a single-family distribution (κ), C.) π-periodic primary directions of each fibre family for a two-family fibre system ($\theta_{1,2}$), and D.) Equivalent fibre dispersion for each family for a two-family system (κ_2).

Figure 5.14B compares the single-family fibre dispersion (κ) by tissue plane. Dispersion was higher in the AC and CA planes, and lower in the AR and CR planes ($p<0.05$ using two-sample t-tests). There were no significant differences for the κ values between the AC and CA planes ($p=0.275$) or between the AR and CR planes ($p=0.080$).

Considering Figure 5.14A and B together, fibres in the AR and CR planes had relatively low fibre dispersion and primary fibre orientations that were well aligned with the respective axes of their sample strips (axial or circumferential). Fibres in the AC and CA planes had higher fibre dispersion, and primary fibre orientations were mostly towards the circumferential direction. Four (of twelve) AC samples had a primary fibre orientation toward the axial direction, but this may be explained by these samples having a two-family or isotropic fibre structure.

Two-Family Fibre Structure in Histology Images

The primary orientation of each fibre family in a two-family system is shown in Figure 5.14C. Fibres in the CR and AR planes were well represented as one-family systems, so the two-family system discussion will focus on the AC and CA planes.

Considering the fibre orientations were π-periodic, the vertical axis of the plot is extended to [-135°,135°] to better show primary directions in the CA and AC planes near ±90°. Four of the AC (from twelve total) and one of the CA samples (from ten total) were found to have primary fibre orientations around both 0° and ±90°. Therefore, these samples would have a split angle(θ_s) of about 90°, represented by the vertical gaps between the clusters in Figure 5.14C. The CA sample was from the same artery as one of the AC samples with a two-family system. Two additional CA samples had a split angle (θ_S) of about 5° and 20° each. The 20° sample was from the same artery as one of the AC samples with a two-family system.

The remainder of CA (7/10) and AC samples (8/12) had a very low split angle ($\theta_s \approx 0°$, $\theta_1 \approx \theta_2$). Of these, all had a primary orientation in the circumferential direction, except one AC strip that had an orientation near the axial direction.

The equivalent fibre dispersion for each family in a two-family orientation distribution (κ_2) is compared between imaging planes in Figure 5.14D. The CA

and AC planes had statistically higher dispersion compared to the radial planes ($p<0.05$ using two-sample t-tests). There were no significant differences between the CA and AC planes ($p=0.764$) or between the radial planes ($p=0.191$).

Discussion of Section

Fibres in the AR and CR planes were well aligned with the sample axes and had lower dispersion compared to those in the AC and CA planes. Viewed from these planes, the fibre structure resembles a one-family system. Since the fibre dispersion in these planes was lower than in the AC and CA planes, the tissue structure has been referred to as having sheets or plies that are stacked radially (see Figure 5.3). This model of stacked plies can be useful, particularly in describing tears in these planes see Section 5.4.1). However, the model is an approximation: 3D fibre orientation has a radial component and the AR and CR planes have a non-zero fibre dispersion. Indeed, some of the one-family fibre dispersion values in the AR plane were higher than some values in the AC plane.

Fibres in the AC and CA planes were generally oriented more towards the circumferential direction, but different samples resembled either a one-family, two-family, or isotropic fibre structure. Most of these (15/22) were found by the two-family fitting algorithm to have only one family. Of the remaining samples, two were reasonably approximated by a one-family system ($\theta_s \leq 20°$) and the remaining samples by an isotropic system ($\kappa_2 \geq 0.23$). Since an isotropic distribution can be represented by a one-family system with $\kappa=\frac{1}{3}$, a one-family system would reasonably model fibre structures in the AC and CA planes.

Previous studies have more frequently described artery tissue has having a two-family system in the AC and CA planes, but one-family systems have been reported for some artery types [Clark and Glagov, 1985; Schriefl, 2013; Schriefl et al., 2012b]. Also, a more general histology stain was used here compared to previous studies, where picrosirius red was used and is more specific for collagen.

5.5 Fibre Structure Versus Material Properties

Fibre dispersion (κ, assuming a single fibre family), tangent modulus, and tearing toughness (J_C) were compared to identify potential relationships. Linear regression models (as defined in Section 3.6) were used to identify significant relationships and evaluate strengths of relationships.

The material anisotropy ratio is derived from the tangent modulus of the axial and circumferential strips from the same artery (α), by Equation 5.10:

$$\alpha = \frac{E_a}{E_c} \tag{5.10}$$

where E_c is the circumferential tangent modulus and E_a is for axial (defined in Equation 5.5). Thus, arteries with a similar axial and circumferential tangent moduli had $\alpha \approx 1$. The material anisotropy ratio (α) is a phenomenological property, whereas fibre dispersion (κ) defines structural anisotropy.

5.5.1 Material Anisotropy Versus Tearing Toughness

Figure 5.15 compares the material anisotropy of an artery (α) with the tearing toughness of axial-radial (AR) and circumferential-radial (CR) trouser tear test strips (strips defined in Section 5.3.4).

Tearing toughness significantly increased with the material anisotropy ratio (p=0.035, R^2=0.25, slope=1.09 from linear regression modelling, see Section 3.6). While there were relatively few samples, there is a clear division between samples with higher toughness and those with lower toughness (around α=0.7).

Discussion of Section

In all but one artery, there was a higher tangent modulus in the circumferential direction than axial. As tears were observed to travel around fibres rather than break fibres (see Figure 5.9), a higher material anisotropy ratio may indicate features in the material structure that inhibit fracture progression.

A more anisotropic material may be responsible for the lateral fractures observed in the axial-radial trouser samples (see Figure 5.9D), which had some of the lowest tearing toughness values among these samples.

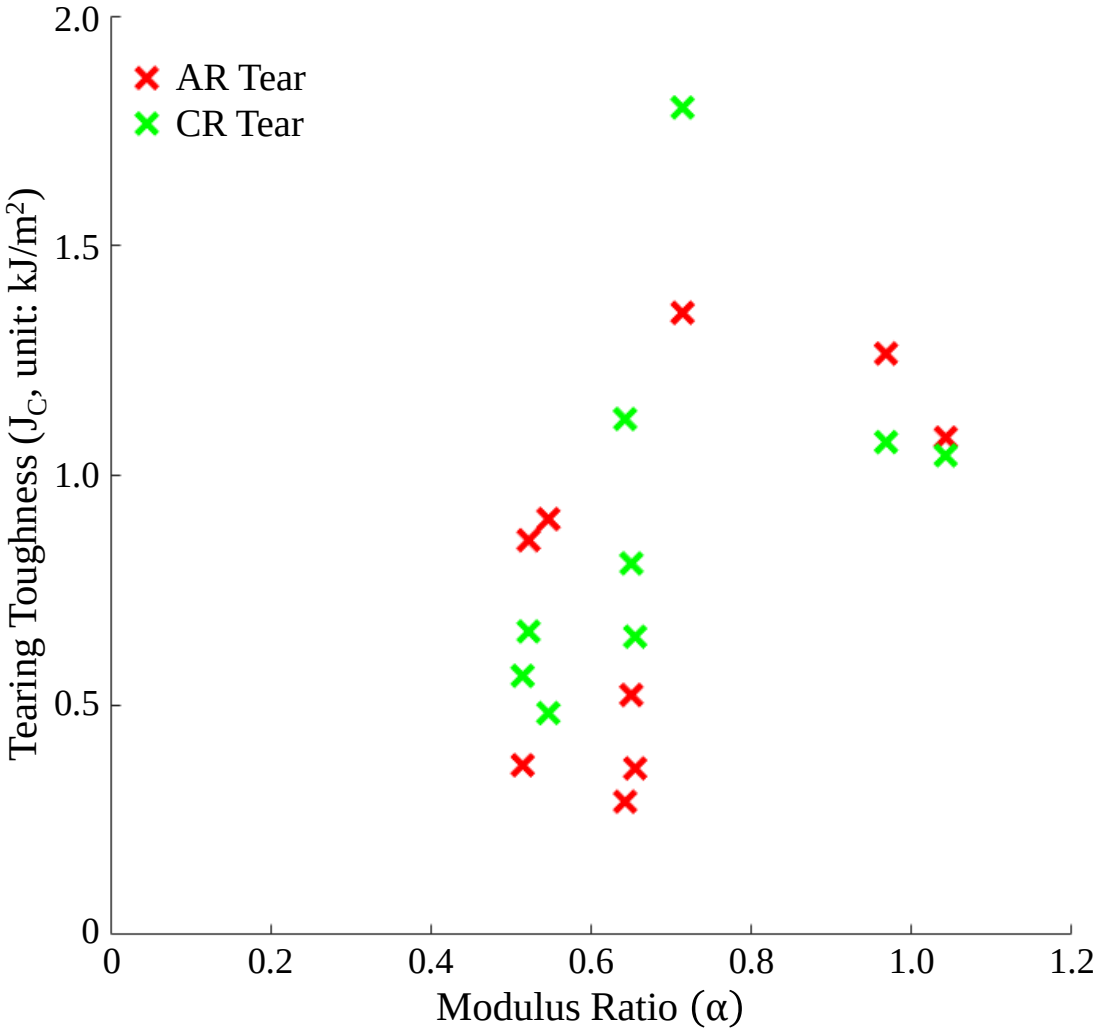

Figure 5.15: Plots comparing material anisotropy of an artery (α) with tearing toughness (J_C) in the axial-radial (AR) and circumferential-radial (CR) trouser tear tests from the same artery.

It was hypothesised that a higher stiffness normal to the tear progression would lead to a higher tearing force (higher E_c with higher AR J_C; higher E_a with higher CR J_C), but linear regression models found no relationships.

5.5.2 Fibre Dispersion Versus Tearing Toughness

To consider the role of structural anisotropy, tearing toughness (J_C) is compared to fibre dispersion (κ) in Figure 5.16.

Tearing planes and tissue structure planes in Figure 5.16 are labelled by marker colour, with the strips as defined in Section 5.3.4 and tissue planes defined in Section 5.3.2. Tearing toughness was assumed to be most affected by fibre dispersion (or κ) in the plane normal to tearing and in the direction the tear progressed (see legend of Figure 5.16). For example, an axial-circumferential tear progresses in the axial direction, and its progression was assumed to be mainly influenced by fibre structures in the axial-radial plane.

Linear regression modelling (using the methods described in Section 3.6) found tearing toughness significantly increased with fibre dispersion ($p<0.001$, $R^2=0.39$, slope=3.43). It should be noted that κ is a non-linear statistics-based parameter (see Equation 3.15), so a higher-order or exponential model would probably be more representative and give a better fit. Instead, a linear regression is used here to prove the statistical significance and direction of the relationship.

Differences in toughness between sample types mirrored differences in fibre properties, where the CA and AC tearing strips had a lower toughness and the AR and CR planes had a lower fibre dispersion.

Where results for tearing toughness, fibre dispersion, and tangent modulus are all available for a sample, the material anisotropy ratio (α) is indicated in Figure 5.16 for the AR and CR samples. As was shown in Figure 5.15, samples that were more isotropic (higher α) generally had a higher tearing toughness.

Discussion of Section

Four material groups are proposed from these comparisons of tearing toughness, tearing plane, fibre dispersion, and material anisotropy (indicated by dashed lines and labelled in Figure 5.16).

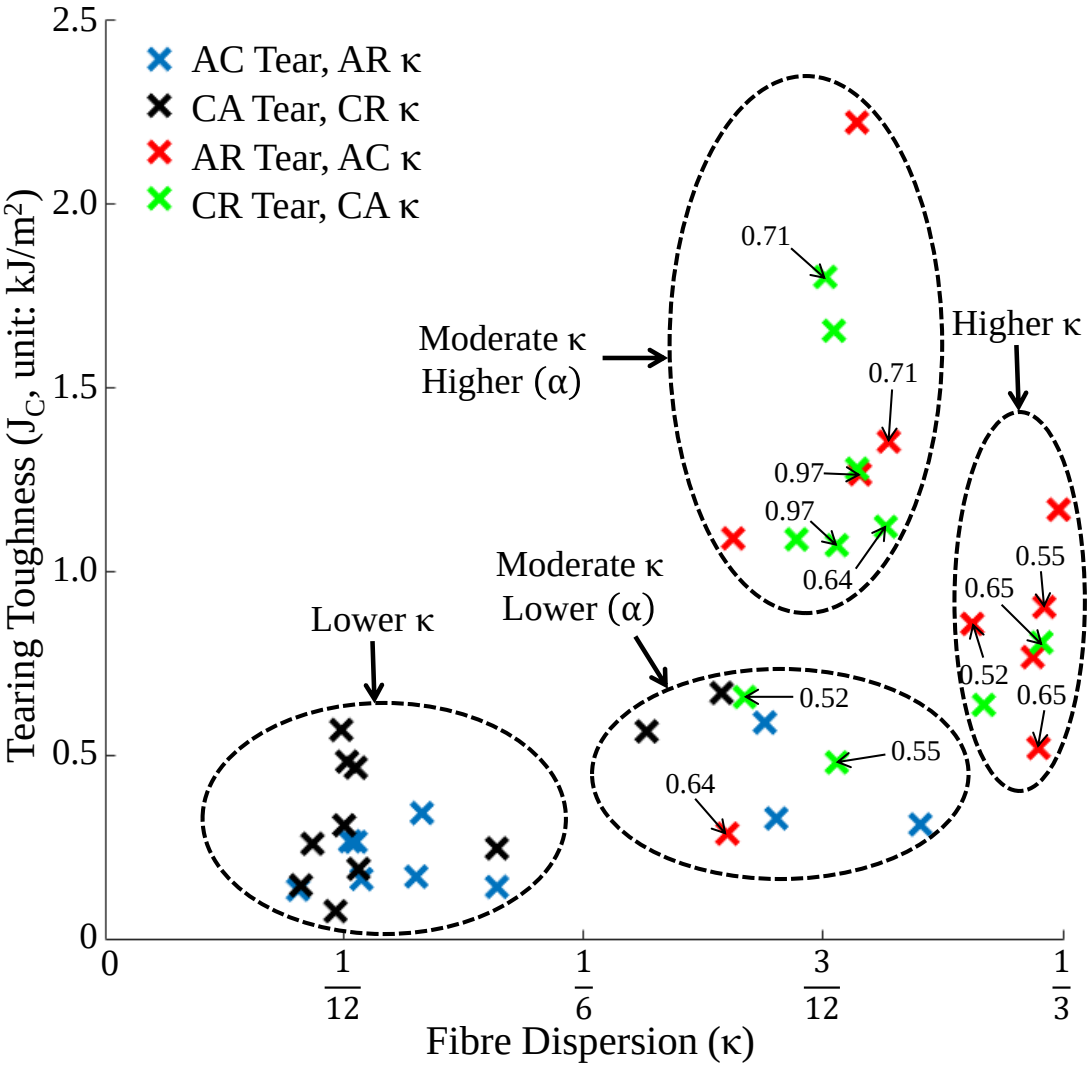

Figure 5.16: Plot comparing tearing toughness (J_C) with fibre dispersion (κ). Planes used for tearing type and κ are indicated by marker colour (see legend: axial-circumferential (AC), circumferential-axial (CA), axial-radial (AR), and circumferential-radial (CR)). The material anisotropy (α) is labelled where data existed. Dashed lines group samples with similar properties.

Firstly, the lower-right group of Figure 5.16 was AC and CA tearing tests with lower tearing toughness (J_C) and fibre dispersion (κ). To the right is a second group, which had a mix of tear types, a low-to-moderate J_C, and a moderate κ. In reviewing test videos, most of these tears involved two different tearing planes. Above this group in the figure, a third group has only AR and CR test strips, a high J_C, and a low-to-moderate κ. Compared to the CR and AR strips in the second group, those in the third group had a higher material anisotropy ratio (α). A fourth group (right of Figure 5.16) has only AR and CR strips, a high κ, a lower α, and a moderate J_C.

The strips with lower toughness had lower values of κ and α, so were more anisotropic in fibre structure and material stiffness (the second group). Samples with the highest toughness (the third group) had a relatively high κ and α, so had a more isotropic fibre structure as well as material stiffness.

These relationships suggest that the mechanics of fracture in the tissue are dependant on the degree of anisotropy of the tissue. Since tears were observed to progress around fibres (see Section 5.4.1), a fibre network with higher dispersion may be protective against fractures. In Chapter 6, multiphoton microscopy was used to observe *in situ* changes to the fibre structure during loading and tearing.

5.5.3 Fibre Dispersion Between Different Strips

In the histology images used for image processing, there were 23 pairs that were from the same artery and were in the same tissue plane. To test if fibre dispersion is similar in different strips of the same artery, values from pairs of strips are plotted in Figure 5.17.

Figure 5.17 shows 23 pairs of fibre dispersion that are from the same plane and same artery, but different test strips (see Section 5.3.2 for definition of planes). The pairs were typically located 10 mm or less from one another (see Section 5.3.3 for tissue preparation). A linear regression model (methods described in Section 3.6, with the intercept set as zero) found a strong but not perfect correlation between fibre dispersion (κ) found in each strip ($p<0.001$, $R^2=0.82$, slope=1.00).

Of the five pairs with the largest difference in κ, three pairs had at least one strip that was best represented by a two-family fibre structure (see Section 5.4.3).

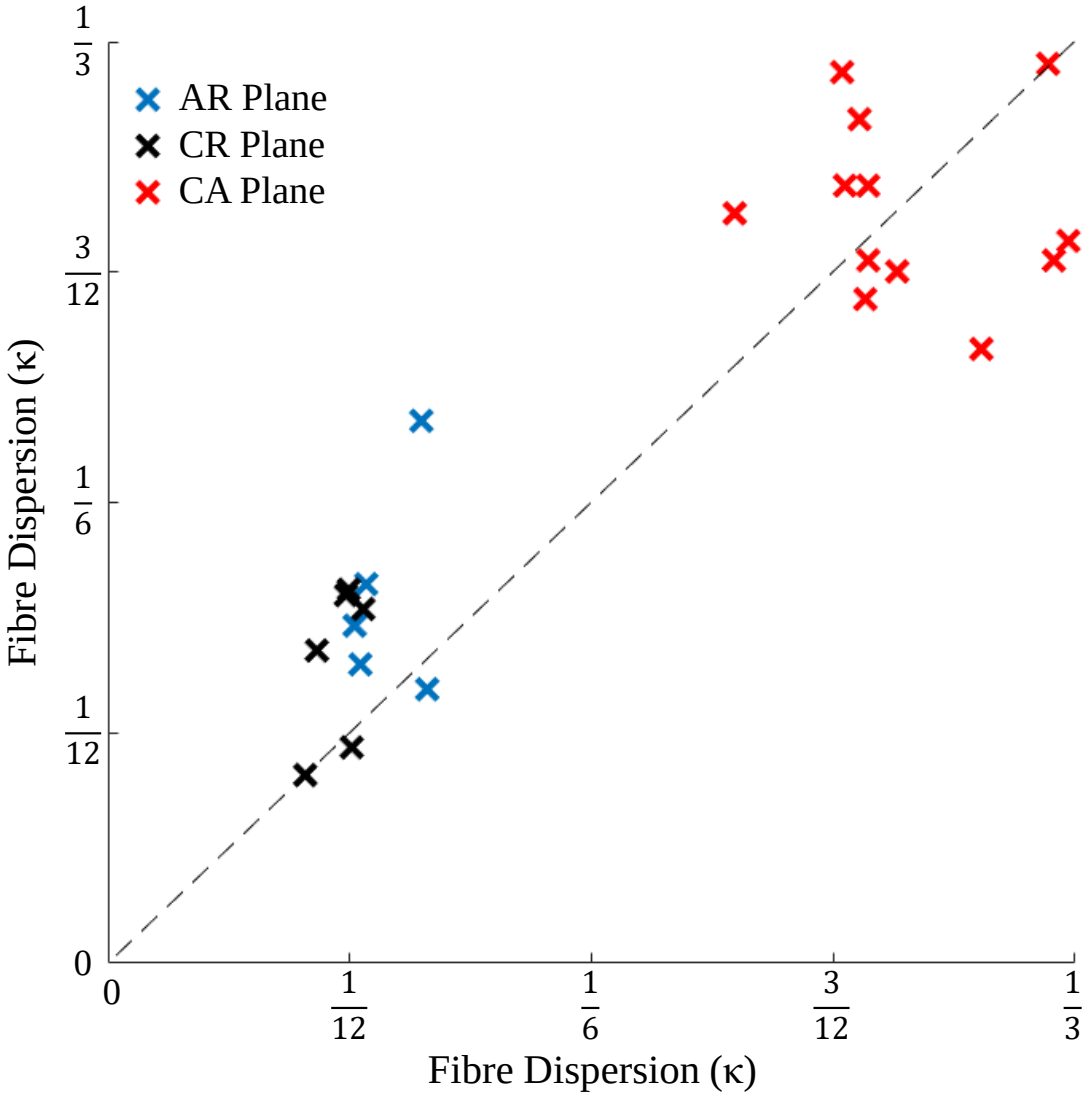

Figure 5.17: Plot comparing fibre dispersion (κ) in two different strips from the same artery. The dashed line indicates the expected positioning of points, where fibre dispersion is the same in both strips.

The remaining two pairs involved strips with atypical fibre structure (the highest AR plane and the lowest CA plane points in Figure 5.17).

Discussion of Section

These five pairs had a difference of at least 0.069 between their κ values, whereas the mean difference for the remaining 18 samples was 0.028. For reference, some representative values for κ are illustrated in Figure 3.10. Differences in fibre dispersion can be seen by the eye to a resolution of about 0.05. From a finite element study on sensitivity of fibre dispersion on stress in a plaque, changes to stress were relatively small for FE models having κ values within about 0.05 of one another. Calculating κ to within 0.05 would also be sufficient for determining which of the four groups a sample belonged to in Figure 5.16, if the material anisotropy ratio was also known. Since the samples having a two-family fibre system were often the ones outside this 0.05 tolerance, a two-family system might be needed to properly model fibre structure in some porcine carotid arteries.

Across the full range of values, there was a reasonable correlation between values of κ found in different strips from the same artery (R^2=0.82, and improves to R^2=0.92 with the five outliers removed). It is difficult to attribute what portion of κ variability is from changes with location in the tissue, from the image processing methodology, or from any damage sustained during testing. There is no gold standard to compare these κ values to, and it is not clear if there is benefit in calculating κ to a precision greater than 0.05. Future study could seek answers to these questions. Until then, studies should be designed to reduce any variability from location in the tissue or damage sustained from testing.

5.6 Discussion

5.6.1 Application of Results to the Mechanics of Plaques

These experiments were done on healthy porcine tissue, to have more controlled samples than atherosclerotic tissue would provide. However, many findings from this chapter can be interpreted in the context of atherosclerotic plaques.

Review of Tissue Changes Caused by Atherosclerosis

To provide background and context for applying these results to atherosclerotic tissues, differences between atherosclerotic and healthy artery tissue are reviewed.

Atherosclerosis causes the intima layer to thicken, grow inward, and become more fibrous. The composition of atherosclerotic tissue is more complex than healthy tissue, and can include zones with calcium, lipid, and intra-plaque haemorrhage deposited in or mixed with the fibrous components. A lipid-rich necrotic core is often present in atherosclerotic plaques, which is covered by a fibrous cap. The fibrous cap joins the fibrous intima on either side of the lipid core at the shoulder regions.

These changes to the structure and composition of the tissue are typically asymmetrical, so fibre structure in the radial planes of the tissue becomes more complex than for healthy tissue. In the healthy tissue considered in this chapter, fibres in the radial planes had low fibre dispersion (κ) and were parallel with one another as well as the luminal surface. In Chapter 3, the shoulder regions of atherosclerotic plaques were found to have a higher κ and a primary fibre orientation was less aligned with the luminal surface. Fibrous caps had fibre orientations that were well aligned with the luminal surface, and had a lower κ compared to the IT region, which was assumed to resemble healthier tissue.

Chapter 3 only considered fibre structure in the circumferential-radial plane, but the same plane had similar κ values for healthy tissue in this chapter (see Figure 5.14B and Table 3.6). Comparing κ values between the atherosclerotic and the CR plane of healthy tissue, the shoulder κ was similar to the healthy tissues' highest values, the fibrous cap κ was similar to the lowest values, and the IT κ was similar to the median value.

Comparing Finite Element Stresses and Experiment Stiffness Results

Finite element (FE) analysis in Chapter 4 found several links between fibre structure and mechanics. Firstly, significantly different stresses were predicted by isotropic (κ=0.333) and anisotropic (κ=0.136) FE plaque models (see Figures 4.6, 4.8, and 4.9). Linear regression models compared fibre misalignment and fibre dispersion to stresses. Instances of weak coupling were found for fibre struc-

ture with transverse stress, shear stress, and the stress transformation angle (see Table 4.10). Fibre orientation generally seemed to affect stresses more than κ, although local fibre orientation was assigned by element and local κ was only modelled indirectly by elemental orientation.

The FE study considered the fibre structure in the circumferential-radial (CR) plane, but assumed the fibre structure had spherically symmetric fibre dispersion (i.e. that the CR κ was the same as the CA κ). In this chapter, κ was shown to be considerably higher in the CA and AC planes, as has been reported by the group behind the material model that was used in Chapter 4 (Equation 4.1) [Holzapfel et al., 2015]. Therefore, future FE studies should consider the spherically asymmetric fibre dispersion as well as local or region-specific values for κ.

Comparing Finite Element Stresses and Experiment Toughness Results

In the experiments described in this chapter, tearing toughness (J_C) was higher in the AR or CR planes than the CA or AC planes. Conversely, fibre dispersion (κ) was lower in the AR and CR planes than the CA and AC planes. Tearing toughness was found to decrease with κ (see Figure 5.16), so tissues with low κ could be more vulnerable to tearing.

The 2D FE simulations in Chapter 4 considered fibre structures in the CR plane, which would be involved with CA plane tears. Relatively high shear stresses were predicted by the FE models, which is a loading mode that could cause CA plane tearing. Shear stress and κ were typically higher in the shoulders compared to the fibrous cap. Only a few plaque regions had both a lower κ and higher shear stresses. This uncommon combination of fibre structure and mechanics may explain why a relatively low proportion of plaques rupture [Akyildiz et al., 2014; Richardson et al., 1989; Versluis et al., 2006].

Previous analysis of rupture risk have typically considered the role of only one parameter at a time. However, rupture is likely the result of several risk factors interacting with one another, so coupling between factors should be considered.

The highest component of FE stress was in the direction of fibres, followed by shear stress, but transverse stresses were small. However, the trouser tear experiments in this chapter found the tissue failed between and around fibres rather

by fibres breaking (see 5.4.1). These observations suggest that shear loading is most likely to be responsible for fibrous cap rupture in atherosclerotic plaques.

Implications for Plaque Rupture

The FE studies in Chapter 4 only considered fibre structure and mechanics in the CR plane of the tissue (and therefore CA plane tears). From the experiments in this chapter, the tearing strength was two to three times lower for tears in the CA plane compared to those in the CR or AR planes (see Section 5.4.1). Higher fibre dispersion in the CR and AR planes may serve to distribute stresses and tearing loads more evenly.

The studies in Chapters 3 and 4 did not consider fibre structures in the CA and AC planes. Atherosclerosis was assumed to change fibre structure in the CA and AC planes less, because fibres viewed in these planes already have a higher dispersion. In healthy tissue, fibres in the CR and AR planes are concentric with the lumen. In atherosclerotic tissue, fibres are no longer parallel when viewed in these planes due to lipid, calcium, and intraplaque haemorrhage deposits. Further, these deposits could serve as initial defects, starting tears in the CA and AC planes (i.e. between fibres in the CR and AR planes).

While tearing toughness was higher in the CR and AR planes, tears in the CR and AR plane could still be considered as failure modes. For example, thin fibrous caps could fail through CR or AR plane tears due to having less material to support stresses. For this failure mode, thin fibrous caps with higher axial stresses in the 2D FE models from Chapter 4 would be at a higher risk.

Tearing energy could be used as a failure criterion in future FE studies. While the FE studies in Chapter 4 found axial stresses to be about ten times higher than shear stresses, shear strains were higher than axial strains by a similar factor. Therefore, the axial and shear components of strain energy would each have a similar magnitude, while tearing toughness between fibres (shear mode) was found to be three to four times weaker than for across fibres (axial mode).

5.6.2 Recommended Future Work

This study has motivated several directions for future work in understanding links between fibre structure and material properties of arterial tissue.

Similar to the recommendations in Chapter 3, additional fibre structure parameters such as fibre density, waviness, length, and diameter could have their mechanical roles considered alongside fibre orientation and dispersion. This study should be followed by one using atherosclerotic tissue to compare to these findings with healthy tissue.

5.7 Conclusions

The role of fibre structure in the material properties was considered using healthy porcine arterial tissue. Using trouser tear tests, tearing toughness was found to be three to four times higher for axial-radial (AR) and circumferential-radial (CR) tears compared to axial-circumferential (AC) and circumferential-axial (CA) tears (see Section 5.4.1). Differences in toughness can be explained by there being higher fibre dispersion in the AR and CR planes of the tissue compared to the AC and CA planes (see Figure 5.16).

Uniaxial tensile tests found the tissue was stiffer circumferentially than axially (see Section 5.4.2), which was explained by fibres in the CA plane being more circumferential (see Section 5.4.3). The material anisotropy ratio (α) was found to predict tearing toughness, with more anisotropic arteries having a lower tearing toughness in the AR and CR planes (see Figure 5.15).

Fibre structure was calculated from histology images using image processing (see Section 5.4.3). Fibres viewed in the AR and CR planes had fibre structures that were well represented by one-family systems of dispersed fibres around a primary direction. Viewed in the CA or AC planes, most samples were also well represented by a one-family fibre system. Several samples in these planes had fibre structures that more resembled a two-family fibre system or an isotropic distribution, but could be reasonably well approximated with a one-family system.

Fibre structure plays an important role in the material properties of artery tissue. Even in healthy tissue, there is considerable variability to material properties and fibre structure in different samples. In atherosclerotic tissue, variability would presumably be even higher and therefore is a critical consideration in assessing the rupture risk of plaques.

Chapter 6

Fibre Structure From Multiphoton Microscopy in Stretched Notched and Unnotched Artery Strips

6.1 Abstract

Uniaxial tensile tests using unnotched and notched strips from healthy porcine arteries were used to characterise changes to fibre structure with stretch. Fibres were imaged using multiphoton microscopy.

Distinct fibre structures were identified in each of the intima, internal elastic lamella (IEL), and media tissue layers. Fibres in the intima and IEL were oriented more in the axial direction of the artery, while fibres in the media were directed towards the circumferential direction. With increasing stretch in either the axial or circumferential direction, fibres in all three layers of the tissue rotated towards the direction of stretch. Fibre rotation could explain the strain stiffening behaviour of artery tissue.

In notched samples, fibres were recruited in response to the local mechanics around the crack. Fibres near the crack reorganised in different ways in the different tissue layers. In the intima and media, fibres near the crack would become

more distinct from one another, suggesting that the cross-links between fibres progressively failed with increasing stretch. The fibres themselves were not seen to break. The primary fibre direction relative to the notch determined fibre dispersion near the crack tip when the sample was loaded, and fibre dispersion was higher when the primary fibre direction and notch directions were similar. Therefore, the initial fibre structure relative to the crack influenced the toughening and fracture mechanisms of the tissue.

These findings show that not only does fibre structure affect material properties of artery tissue, but the mechanical state of the material affects the fibre structure. With disease, fibre structure is more varied though the tissue and may play an even more important role in artery biomechanics. Therefore, fibre structure is a critical consideration for future research on the mechanics and rupture risk of atherosclerotic plaques.

6.2 Introduction

Multiphoton microscopy is a unique technique that allows imaging of 3D microstructures without requiring stains, preservatives, or coatings, which would alter the mechanical properties of the sample [Chow et al., 2014; Zoumi et al., 2004]. In this chapter, unnotched and notched strips of healthy porcine carotid artery were stretched uniaxially, with 3D image stacks acquired at 500 μm increments of stretch. The unnotched tests were used to observe fibre reorganisation in different layers of the tissue with increasing strain. Tests with notched strips were used to identify mechanisms in the fibre structure that influenced fracture modes and material toughness of the tissue.

In multiphoton microscopy, excitation photons from the light source (here, a Galvo Ti:Sa excitation laser) undergo non-linear, molecule-dependent interaction with the sample [Zoumi et al., 2004, 2002]. This interaction produces emission photons through two mechanisms: second harmonic generation (SHG) and two photon fluorescence (TPF). SHG photons are produced by collagen (but not elastin) at a wavelength half that of the excitation photons. The SHG signal has a high intensity for a small bandwidth around this emission wavelength, but the signal intensity decays exponentially with sample depth [Zoumi et al., 2002].

In contrast, TPF has emission for both collagen and elastin, with a wide bandwidth of emission wavelengths (elastin peak at about 495 nm, combined material peak at about 510 nm) [Zoumi et al., 2004]. The TPF signal intensity is attenuated less with depth compared to SHG, and the peak emission wavelength of the TPF signal is relatively independent of the excitation wavelength.

The methodology of the multiphoton-based experiments is detailed in Section 6.3. Section 6.3.1 lists methods that were reused or adapted from those in Chapter 5. Methods specific to the notched specimen tests are detailed in Section 6.3.2. Equipment, techniques, and parameters used to acquire image stacks from the multiphoton microscope are described in Section 6.3.3. Methods to extract fibre structure from these image stacks are explained in Section 6.3.4.

Results of these experiments are reported in Section 6.4. Qualitative observations of fibre structure in different layers and at different stretches of unnotched samples are detailed in Section 6.4.1. Quantitative results for fibre structure in the unnotched samples are provided in plots of orientation against depth in Section 6.4.2. Section 6.4.3 plots fibre structure summary parameters (orientation and dispersion) against depth and stretch ratio for a one-family fibre system. Section 6.4.4 reports the same for a two-family fibre system.

The discussion section (Section 6.5) includes four sub-sections. First, the results are summarised into a general statement on the response of fibre structure in different layers to mechanical stretch in Section 6.5.1. Second, Section 6.5.2 suggests the role of fibre structure on mechanisms of fracture and the material toughness of the tissue. Thirdly, implications of these findings on biomechanical models of artery tissue are discussed in Section 6.5.3. Limitations and recommended future directions for multiphoton-based study of arterial tissue are listed in Section 6.5.4. Finally, conclusions of this chapter are stated in Section 6.6.

6.3 Experimental Methodology

Four carotid pig arteries were used for mechanical tests with *in situ* fibre imaging using a multiphoton microscope. Thus, the fibre structure was analysed at increasing stretch ratios (λ_1, as defined in Equation 5.2) in unnotched and notched strips.

The techniques used for these experiments have similarities to those used in Chapter 5, and will be referenced throughout this chapter. Section 6.3.1 reviews and details modifications to the apparatus, coordinate system, tissue preparation, and uniaxial tensile test methods that were used in Chapter 5. Notch specimen tests, which observed changes to fibre structure near a crack at increasing strain, are described in Section 6.3.2. Section 6.3.3 provides details and settings used for the multiphoton microscopy. Image processing of the 3D multiphoton stacks is reported in Section 6.3.4, borrowing techniques from Chapters 3 and 5.

6.3.1 Apparatus, Tissue Preparation, and Uniaxial Tests

Materials Test Apparatus

These experiments used a similar apparatus and parameters as described in Section 5.3.1, with modifications outlined here. Instead of the light microscope, cold lamp, and microscope camera, a multiphoton microscope was used (LaVision BioTec TriM Scope II, Bielefeld, Germany, with an Insight Deepsee light source, Spectra-Physics, Santa Clara, CA, USA). For the multiphoton experiments, loading was paused every 500 μm for about 90 seconds to scan the fibre structure of the sample. The pauses caused relaxation of the sample, which decreased stress by about 10% compared to the increase in stress between each pause.

Coordinate System and Tissue Plane Definition

The coordinate system and tissue planes in this chapter use the convention defined in Section 5.3.2. Stack images from the multiphoton microscope will use a similar definition. Slices of the stacks are nominally in the axial-circumferential plane of the tissue and from the horizontal plane relative to the microscope. This plane will be defined as axial-circumferential for strips stretched axially, and circumferential-axial for strips stretched circumferentially. The vertical direction of the multiphoton microscope and stack direction of images were the radial direction of the sample.

Tissue Source and Preparation

Tissue sourcing and preparation was as defined in Section 5.3.3, with differences described here. Four strips were cut from each pig artery used in the multiphoton tests, with two strips cut in each the circumferential and axial directions (see Table 5.1). One of the strips from each direction and artery was prepared as a notched specimen (further described in Section 6.3.2). Fibre rearrangement and fracture progression was observed at the tips of these notches.

Uniaxial Tests

Uniaxial tensile tests evaluated the stiffness of the tissue under multiphoton microscopy, using the methods described in Section 6.3.1. Sketches explaining the test strips used in the uniaxial tensile tests are shown in Figure 5.6.

6.3.2 Notched Specimen Tests

Four pairs of notched specimens strips were tested under multiphoton microscopy using the testing rig described in Section 5.3.1, with each pair having one circumferential and one axial strip. Sketches explaining the test strips used in the notched specimen tests are shown in Figure 6.1.

Figure 6.1A defines the orientation of axial and circumferential test strips relative to the artery coordinate system. An axial strip, as used in notched specimen tests, is sketched in Figure 6.1B. The notches in these strips were in the circumferential-radial tissue plane (see Figure 5.3B). Thus, the notch was in the same direction as the primary orientation of fibres in these strips. Figure 6.1C shows a sketch of a circumferential notched specimen test strip. These notches were in the axial-radial tissue plane (see Figure 5.3C), so were anti-aligned with the primary direction of fibres.

Strip Geometries

Figure 6.1D is a sketch of key geometry measurements for the notched specimen test strips. The strip thickness was the artery wall thickness, the length was the

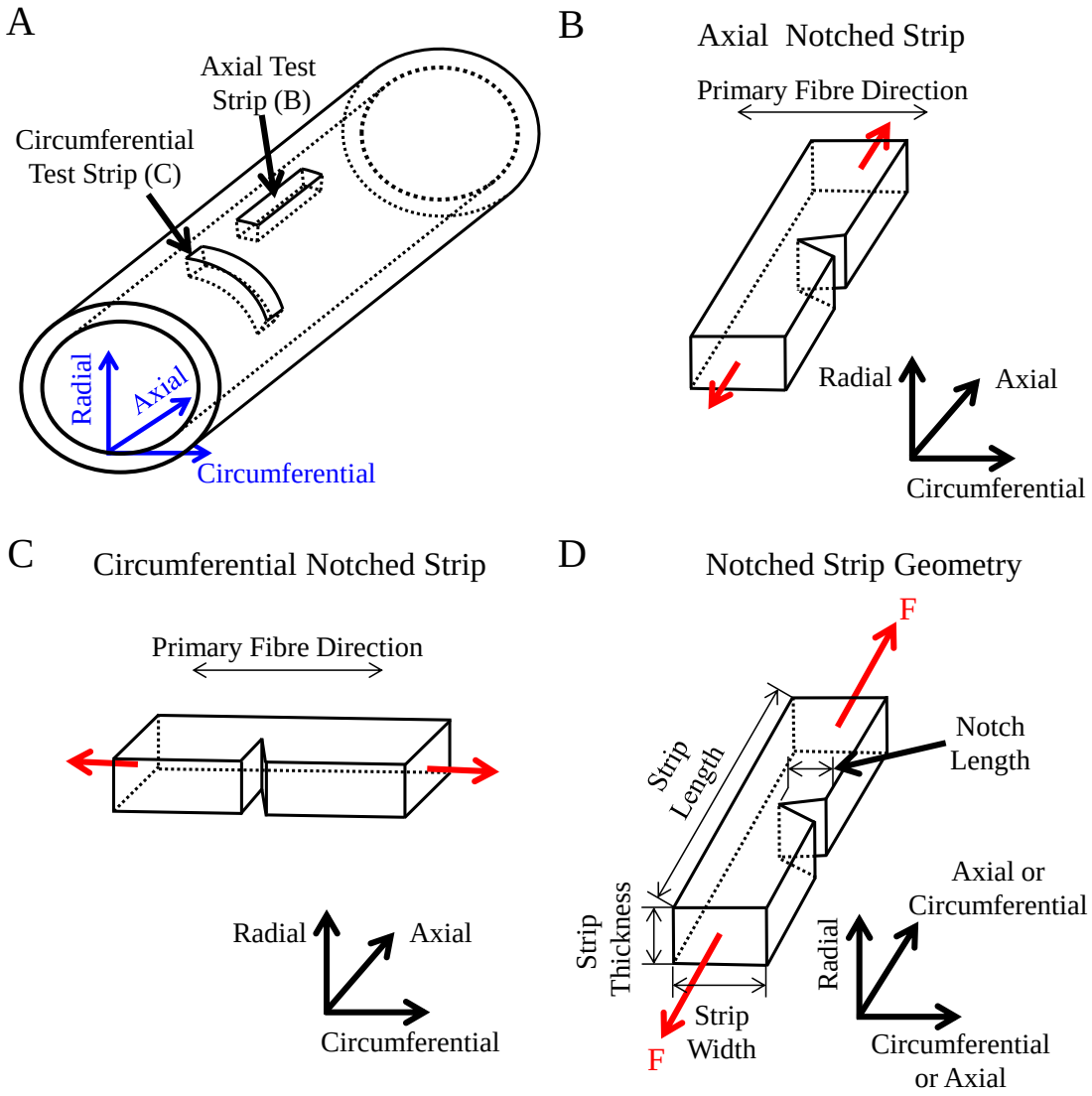

Figure 6.1: A.) Sketch of artery with coordinate system, showing relative orientations of axial and circumferential test strips, B.) Sketch of an axial test strip used for notched specimen tests, C.) Sketch of a circumferential test strip used for notched specimen tests, and D.) Geometry parameters labelled on a notched specimen test strip. These sketches are not to scale.

direction in which the strip was stretched, the strip width was the dimension the notch was in, and the notch length was for the lateral cut into the strip.

Using the image stacks from the multiphoton microscope, observations of damage and fibre reorganisation around the crack tip were compared between the different layers of the tissue (intima, internal elastic lamella, and media). These observation were also compared between the circumferential and axial strips. The stress and stretch at failure were also calculated for a simple comparison between axial and circumferential notches (see Appendix A.5).

6.3.3 Microscopy Preparation

In this study, the microscope's laser wavelength was 830 nm and used 4-6% transmission power. The power was selected to be as high as possible to allow deeper imaging, but not high enough to cause photodamage artefacts. The second harmonic generation (SHG, from collagen only) emission was therefore expected to be at around 415 nm and the two photon fluorescence emission (TPF, collagen or elastin) was expected to have a wide bandwidth and a peak near 510 nm.

A 400-700 nm band-pass filter was used to remove any reflected excitation photons or low-wavelength photons, which are not produced by either SHG or TPF. The microscope and signal acquisition were controlled by the TriM Scope's provided software. The following parameters or options used in the software: a gain of 70, a *Frequency* of 800, a *Line Average* of 2, a scanning region of 400×400 μm, and an image size of 505×505 pixels. Dr. Kevin O'Holleran of the Cambridge Advanced Imaging Centre advised and contributed to these imaging protocols.

At every 500 μm of linear stage displacement, the tests were paused and the multiphoton microscope was manually focussed on the sample. Note that since the sample moves and the microscope is manually re-focussed, image stacks from different stretches are typically of slightly different locations of the sample. Image stacks were acquired starting from the luminal surface, then at 5.0 μm increments of depth (into the radial direction) until the emission signal had attenuated to a degree it was indistinguishable from noise. Typically, this would be at a stack depth of about 200-300 μm.

6.3.4 Image Processing of Multiphoton Image Stacks

For both unnotched and notched tests, qualitative observations of fibre reorganisation with strain will be reported. Fibre structure was also calculated for the unnotched strips using methods adapted from Chapter 5, which will be further described in this section.

Stack Rotation to Artery Coordinate System

The 3D stack images were exported from the TriM Scope microscope software, and imported to the FIJI image processing application [Schindelin et al., 2012] through the *Bio-Formats Importer* module [Linkert et al., 2010].

To correct for any misalignment between the tissue and imaging planes, stacks were rotated using TransformJ [Meijering et al., 2001]. The horizontal plane of the image stack was rotated until it was the same as the axial-circumferential plane of fibres in the tissue (planes defined in Section 5.3.2). The rotated stack was resampled to have isotropic voxels with 0.79 μm edges, with *quintic B-spline interpolation* and the *Anti-alias boarders* options selected in TransformJ.

Representative sample images of detected fibres and their orientation relative to the sample axis (image horizontal and tissue circumferential) are shown in the left column of Figure 6.2 for slices in the intima (A), internal elastic lamella (IEL, B), and media (C). The other columns of the figure will be referenced as the image processing methodology is developed.

Fibre Detection and Fibre Orientation

Methods to calculate fibre structure in the histology images of test strips (as described in Section 5.3.6) were adapted to the multiphoton image stacks. For the multiphoton image stacks, fibre orientations were calculated in the circumferential-axial (CA) plane for each slice of the stack (plane defined in Section 5.3.2), relative to the direction of stretch. Since resolution in the radial direction of the original image stacks was lower (5.0 μm) than the resolution in the CA plane (0.79 μm), it was more difficult to reliably detect fibres in other tissue planes. Furthermore, fibres were primarily oriented in the CA plane, making it more challenging to detect edges in the radial direction by the gradient-based method used here.

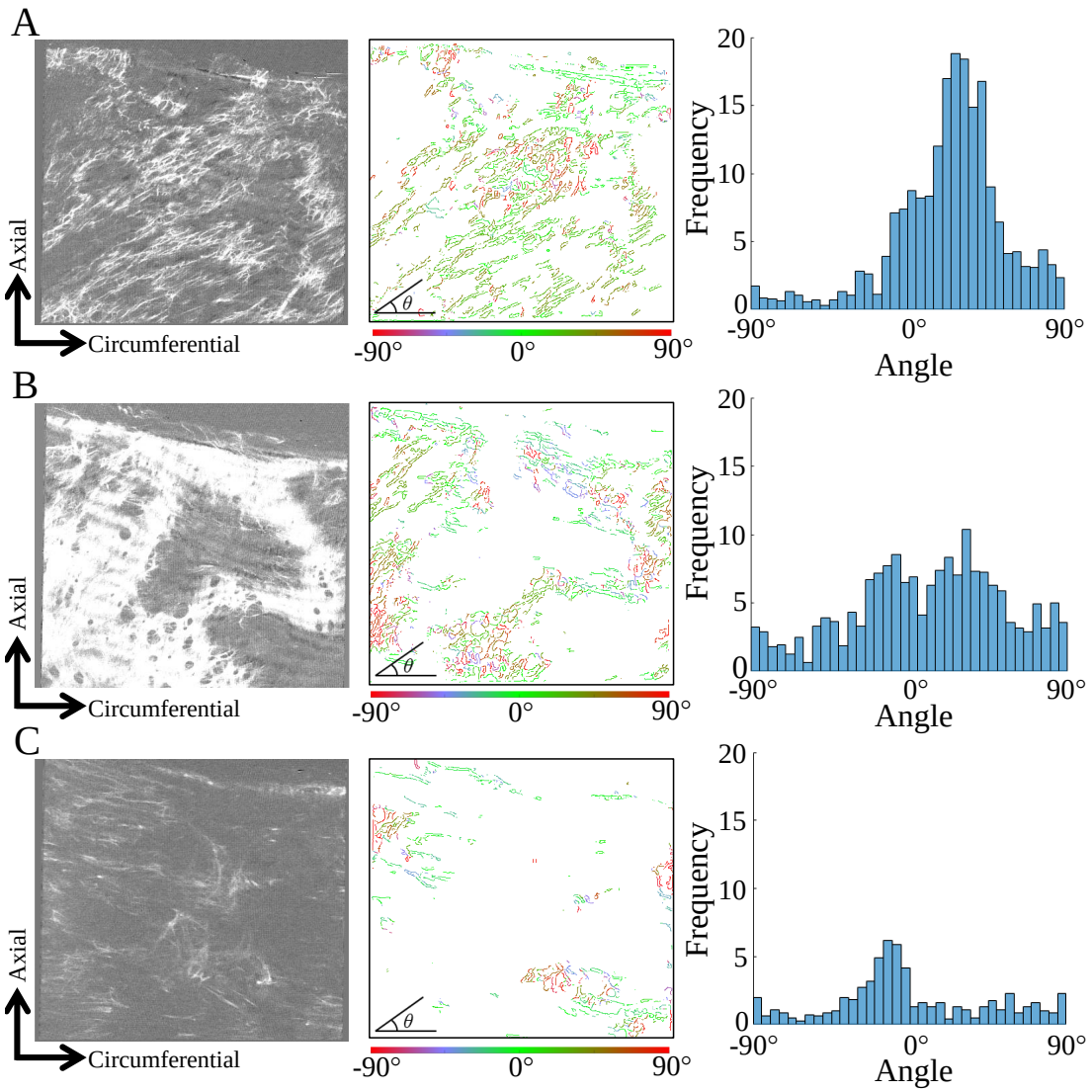

Figure 6.2: Validation study for fibre detection in multiphoton images, showing the image (left), detected fibres in the image and their orientation relative to the horizontal (centre), and frequency of fibre orientations found in the image (right), for slices from the: A.) Intima, B.) IEL, and C.) Media. Recall layers from Figure 1.3.

Section 3.4.2 described fibre detection by the Canny method for histology images, where 30% of pixels were strong edges. Strong edges were defined as having an intensity gradient above a high threshold value.

Here, the higher slices (in the radial direction) of the multiphoton image stacks were typically above the sample, so had fewer detected fibres. The signal from fibres deeper in the tissue was attenuated, and also had fewer detected fibres. Therefore, different slices of the image stack had different fibre densities, so needed a gradient threshold that was representative of the whole image stack.

Since the highest and lowest slices of the multiphoton image stacks had fewer fibres, the stacks had a lower overall fibre density compared to the histology images. For fibre detection in the multiphoton stacks, the high gradient threshold for the Canny edge detector was set so 2.5% of voxels were strong edges. This number of voxels was found iteratively, and confirmed on different stacks to have good precision in detecting fibres.

For more precision, the edge detector could be further tuned to the properties of each stack, such as the number of slices in a stack and the relative Canny gradients in each slice of the stack. In general, the balance is between being sensitive to deep fibres with a faint signal and detecting random noise as fibres, both of which had small but important differences between different image stacks. Dispersion calculations were particularly affected by falsely identified fibres, so these thresholds were set to favour under- rather than over-detecting fibres.

Because the multiphoton images were smaller than the histology images (in both pixels and μm), large fibres having more than 250 pixels were partitioned by a 50×50 grid in the multiphoton image stacks (compared to >500 pixel fibres split by a 75×75 grid in Section 5.3.6). All other methods for fibre detection and calculating fibre orientations were the same as described in Section 5.3.6.

In Figure 6.2, detected fibres (centre column) match well with the location and angle of true fibres in the multiphoton slices (left column). The frequency of fibre orientation for each slice is shown in the right column. The intima and media layer show one family of fibres with moderate dispersion, while the IEL has higher dispersion.

To correct for small undulations in the image stack, an algorithm was developed to reduce the degree to which different tissue layer types would be present in

the same slice of an image stack (see Appendix A.6). For example, the IEL layer in Figure 6.2B-left shows darker regions that are media. Thus, the intention of this algorithm was to shift portions of these images up or down, so that the slices of the shifted stack had fewer zones from different tissue layers (intima, IEL, or media). As fibres were detected and had their orientations calculated by stack slice, the stack shifting algorithm made each stack slice have a more homogeneous tissue layer type.

Methods for Summary Multiphoton Results

Summary fibre properties were calculated for each slice of the shifted stack, for a one-family fibre system and a two-family fibre system. To avoid edges of the sample being considered as fibres, only fibres within a 75 pixel border in each slice were used for summary fibre properties. For a one-family system, the bi-modal mean fibre orientation and fibre dispersion were calculated as described in Section 5.3.6. Fibre properties for a two-family distribution used the methods described in Section 5.3.7. Fewer fibres were present in the top slices of a stack (due to the slice being above the sample in what would be the lumen of the vessel) or in the lower slices (due to attenuated signal deeper into the tissue). To avoid reporting results based on few fibres, results are reported for stack slices between the upper- and lower-most slices to have more than 250 voxels with fibres (about 0.1% of the voxels in a slice).

In addition to calculating fibre properties as a function of depth, the fibre properties were calculated for each image stack, which were created at 500 μm increments of stretch. Similar to the correction for undulations within an image stack, results from different stacks were shifted to have a common depth. For example, the brighter signal from the IEL in Figure 6.2B-left should be all in the same slice. Similarly, the most superficial layer of the intima should start in one slice, and the signal should decay with attenuation independently of position in the slices. Therefore, plots of fibre structure parameters versus stretch would have a more similar depth for boundaries between the tissue layers (intima, IEL, and media).

6.4 Multiphoton Experimental Results

The results of the multiphoton-based experiments are reported in this section. Qualitative observations of fibre structure in the media, intima, and internal elastic lamella (IEL) at increasing stretch in unnotched strips are provided in Section 6.4.1. Section 6.4.2 reports fibre orientation with depth into the tissue, using heat maps at increasing stretch ratios. Summary fibre structure results (primary orientation and dispersion) are plotted by depth and stretch ratio for a one-family fibre system in Section 6.4.3 and a two-family system in Section 6.4.4.

6.4.1 Qualitative Uniaxial Multiphoton Results

This section uses maximum intensity projection (MIP) images to visualise the 3D volume of the multiphoton stack as 2D images. MIP was an early technique to render volumes from CT and MRI medical images. Here, MIP images are in the axial-circumferential plane, taking the maximum intensity from each radial column of voxels, from a manually-selected range of stack slices (see Section 5.3.2 for plane and coordinate definition). Thus, the MIP images combine about 20-40 stack slices (16-32 μm), which is similar to the diameter of the larger fibre bundles, into a single image with the same length and width as the image stack slices. Representative images are shown for one circumferential and one axial sample, detailing the intima, IEL, and media at a series of stretch ratios (λ_1).

Circumferential

Figure 6.3 shows MIP images of the intima, IEL, and media at uniaxial stretch ratios (λ_1) of 1.05, 1.25, 1.50, and 1.75 for an unnotched circumferential strip.

Fibres in the intima (left column of Figure 6.3) had a single family of fibres that was oriented nearer to the axial (vertical) than the circumferential direction (labelled as R1 in the figure). With increasing circumferential strain (lower rows of Figure 6.3), the intimal fibres rotated to be more aligned with the circumferential direction.

An artefact (labelled A1) was caused by the depth shift algorithm (described in Section 6.3.4) over-shifting deep fibres at the sample edge. Label A2 indicates

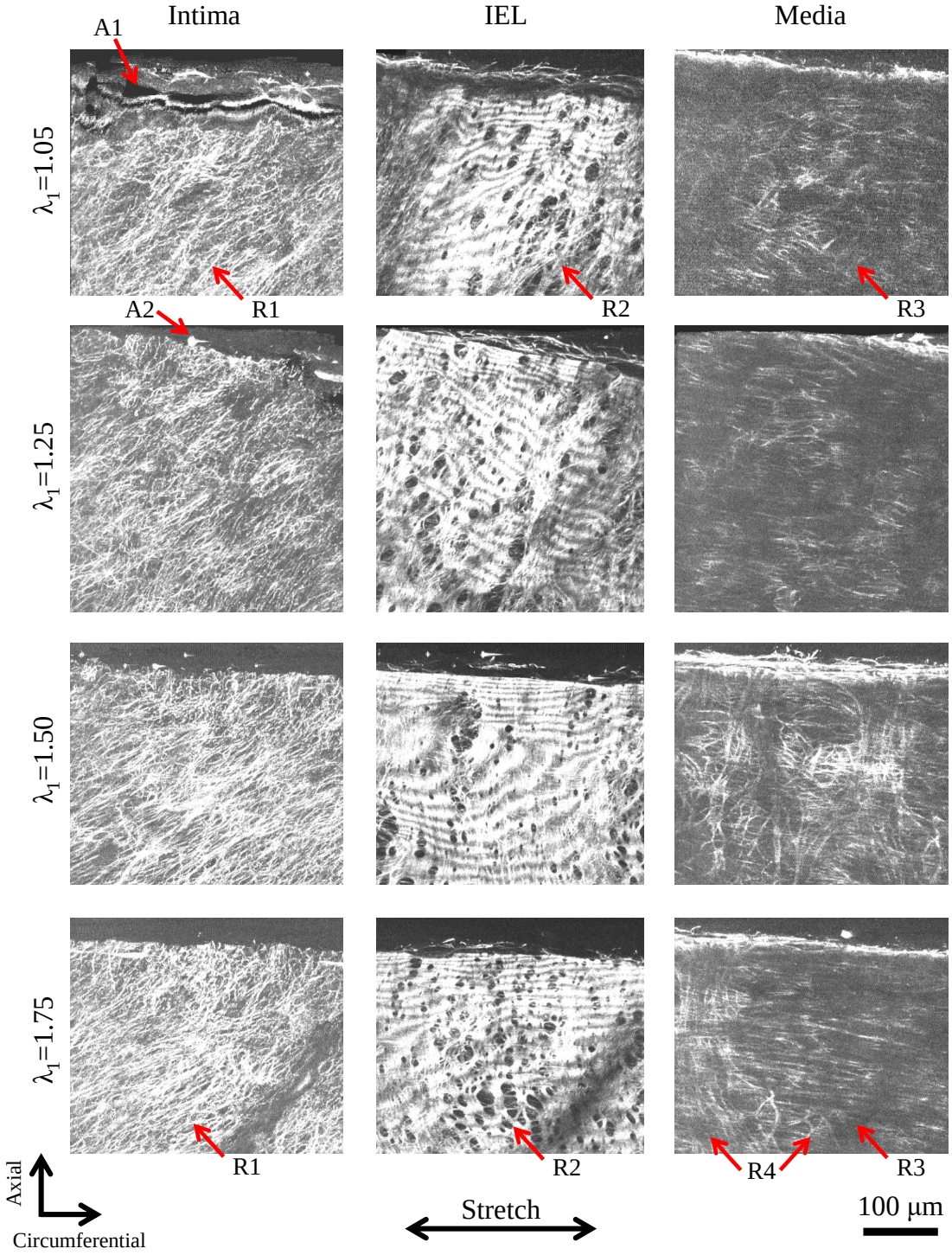

Figure 6.3: MIP images from a series of slices from a multiphoton image stack of a circumferential uniaxial test strip for the intima, IEL, and media (by column). Images are shown for a series of stretch ratios (by row): 1.05, 1.25, 1.50, and 1.75. Artefacts (A) and remarks (R) are discussed in the text.

an example of an artefact from debris or photodamage, which were mainly on the surface of the sample. These artefacts were relatively small compared to the total size of the image, so did not cause major limitations on calculated fibre structure.

The IEL had a stronger signal than other layers (centre column in Figure 6.3), here appearing as a sheet with oval-shaped pores (labelled as R2). The ovals were oriented to be longer in the axial direction, but became more circular with increased stretch. The banding artefacts in the IEL layers are from the image stacks being rotated to the artery coordinate system, where the brighter bands where more in focus with the microscope's laser in the original stacks.

Deeper in the tissue, the media had dispersed fibres at low stretches (right column of Figure 6.3), which were mainly oriented circumferentially (labelled as R3). At increasing strain, the fibres aligned and sometimes showed a fibre family in both the circumferential and axial directions (labelled R4).

Axial

An equivalent set of multiphoton slices are shown for an unnotched axial strip under uniaxial tension in Figure 6.4, where the horizontal direction is axial.

For the axial test strip, fibres in the intima (left column of Figure 6.4) were oriented diagonally but with a preferred direction towards the axial direction of the strip (labelled as R1). With increasing strain, intimal fibres rotated to be even more in the axial direction and dispersion of the fibres decreased. Label A1 is an artefact from incorrect shifting from the depth shift algorithm that was described in Section 6.3.4.

The IEL (centre column in Figure 6.4) had a similar appearance to that in the circumferential strip, and the oval-shaped voids were still aligned in the axial direction (labelled as R2). With increasing axial strain, the voids elongated in the axial direction.

The media of the axial test strips (right column of Figure 6.4) had fibres that were initially mainly oriented in the circumferential direction but highly dispersed (labelled as R3). Increasing strain caused fibres in the media to become more oriented in the axial direction. In this image, fibres appeared to have a two-family distribution, with one family primarily directed in each of the axial and

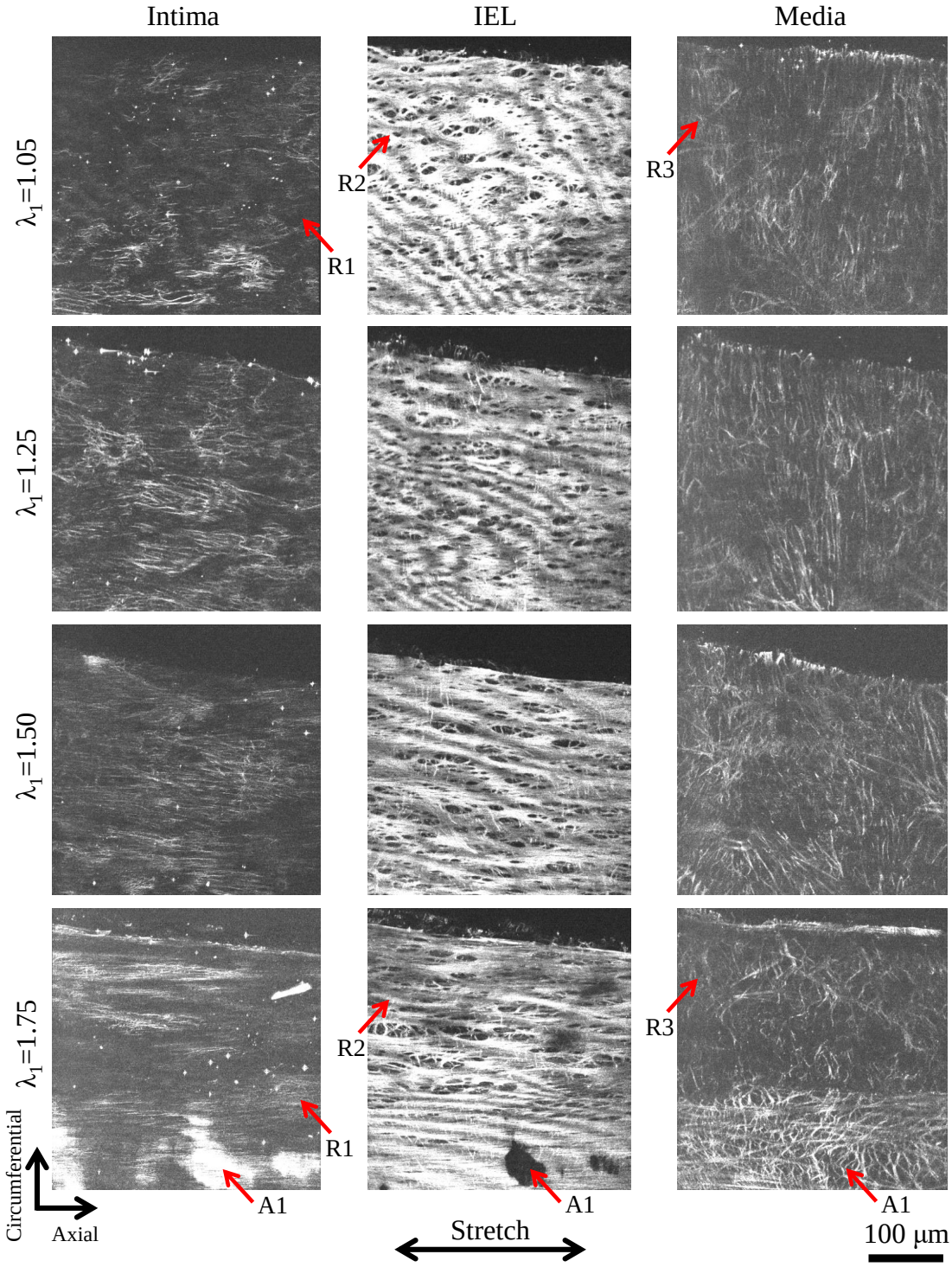

Figure 6.4: MIP images from a series of slices from a multiphoton image stack of an axial uniaxial test strip for the intima, IEL, and media (by column). Images are shown for a series of stretch ratios (by row): 1.05, 1.25, 1.50, and 1.75. Artefacts (A) and remarks (R) are discussed in the text.

circumferential directions. For the image in the lower right (media at λ_1=1.75), the apparent differences in contrast between fibres near the top of the image and those at the bottom of the image are probably due to the fibres being slightly less and more within the focus of the microscope's excitation laser, respectively. Recall that the sample may be slightly tilted relative to the horizontal plane of the microscope. Additionally, edge effects of the sample at higher stretches was observed to cause the tissue to curl slightly upwards or downwards. The differences in contrast should therefore be considered as an imaging artefact rather than being mechanically relevant or representative.

6.4.2 Uniaxial Fibre Orientation Versus Depth

Circumferential

Figure 6.5 shows a series of heat maps for fibre orientation of an unnotched circumferential sample, with the stretch ratio (λ_1) increasing to the right. These plots are for the same sample as the MIP images in Figure 6.3.

Each heat map in Figure 6.5 reports the orientation density function ($P(\theta)$) at different depths of the sample at the indicated stretch ratio. Therefore, each row of pixels in the heat map is equivalent to the orientation density function for one slice of the multiphoton stack. The orientation angles are relative to the stretch direction (circumferential here).

To avoid reporting unreliable fibre structure, the heat maps were truncated above and below regions where fibres were reliably detected.

At a low circumferential stretch (λ_1=1.00), $P(\theta)$ had a wider spread (higher fibre dispersion; indicated by red band in Figure 6.5 narrowing) compared to the distributions at higher stretches. The primary fibre direction in the intima (above 35 μm) was about 90° from that in the media (below 45 μm). Fibres in the intima were more aligned with the axial direction, whereas fibres in the media were more aligned with the circumferential direction. Fibres in the IEL (around 40 μm) had the widest distribution (highest fibre dispersion), but had a primary direction similar to that of the intima. With increasing stretch, the $P(\theta)$ distributions narrowed in all tissue layers (fibre dispersion decreased). Fibres in all layers rotated towards the direction of stretch (circumferential).

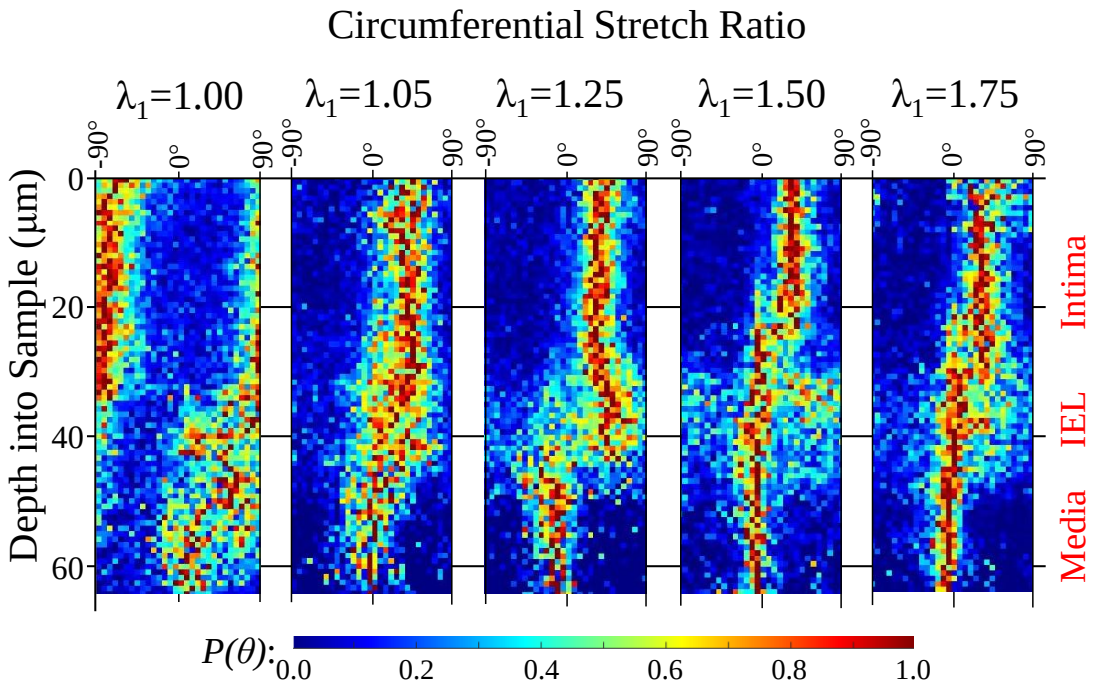

Figure 6.5: Heat maps showing orientation density function ($P(\theta)$) against depth into a circumferential sample for a series of stretch ratios: 1.00, 1.05, 1.25, 1.50, and 1.75. The fibre orientation (top axis label) is relative to the direction of stretch (circumferential). The approximate position of the intima, IEL, and media is labelled (right), as they are slightly different for each heat map.

Axial

Figure 6.6 shows a series of heat maps for fibre orientation of an unnotched axial sample. These plots are for the same sample as used for Figure 6.4. At a low stretch (λ_1=1.05), similar observations can be made for the axial sample $P(\theta)$ in Figure 6.6 as were made for the circumferential sample (Figure 6.5), recalling that the reference direction has rotated 90° (the 0° reference is to the stretch direction: axial). The primary fibre direction in the intima was towards the axial direction, and towards the circumferential direction in the media. Fibres in all layers had a relatively high dispersion.

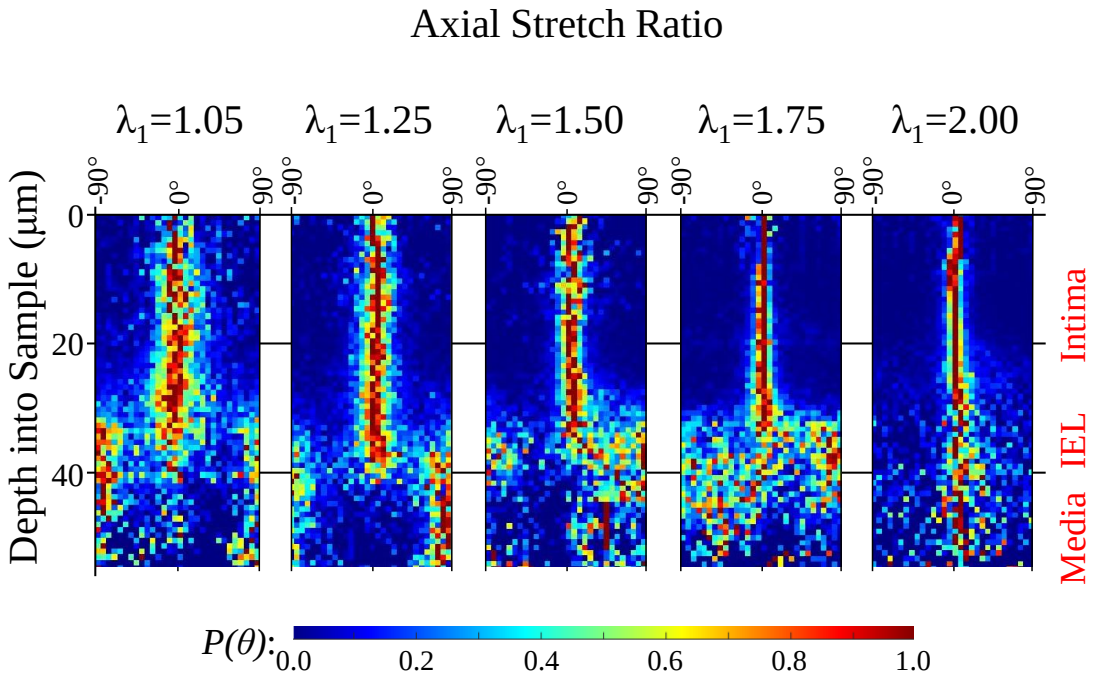

Figure 6.6: Heat maps showing orientation density function ($P(\theta)$) against depth into an axial sample for a series of stretch ratios (by column): 1.05, 1.25, 1.50, 1.75, and 2.00. See Figure 6.5 for further explanation of the figure's features. The 0° orientation is still referenced to the stretch direction, which was axial.

With increasing axial stretch, fibres in the intima and IEL remained in the axial direction and fibre dispersion decreased (red band in Figure 6.6 concentrates towards θ=0°). In the media, fibre dispersion initially increased with stretch, until

$P(\theta)$ was isotropic (red band becomes scattered). With further stretch, fibres in the media became primarily in the axial direction and fibre dispersion decreased (red band becomes more concentrated towards θ=0°).

Fibres in the intima would be well represented by a one-family fibre system. Fibres in the media sometimes would be better represented as a two-family fibre system, especially near the IEL and deeper into the tissue (where two red bands are present in Figures 6.5 and 6.6; also see R4 in Figure 6.3).

Fibre Orientation in All Four Samples

Figure 6.7 shows heat maps of $P(\theta)$ versus depth for the four unnotched circumferential strips at low stretch (λ=1.00, A) and moderate stretch (λ=1.50, B). Similar fibre structures were found for all four samples: the primary fibre orientation was towards the axial direction in the intima and the circumferential direction in the media. With increased stretch, fibres became more aligned in the circumferential direction. Fibres in the intima and media generally had less difference in their primary orientation, and this primary orientation became closer to the 0° reference. Differences between the figures can be partly attributed to the image processing methods being tuned for the left-most sample. In particular, the other samples had weaker signals from fibres in their media layers. A lower laser power was used for these samples, due to a concern of thermal damage to the sample surface from the higher laser power. Different tissue samples may have different fibre structures, with fibre dispersion being less consistent between samples (see Section 5.4.3). Heat maps in Figure 6.7 were trimmed manually to remove the top and bottom of each image stack, which contained few fibres (top: slices were above true sample, bottom: low signal from attenuation).

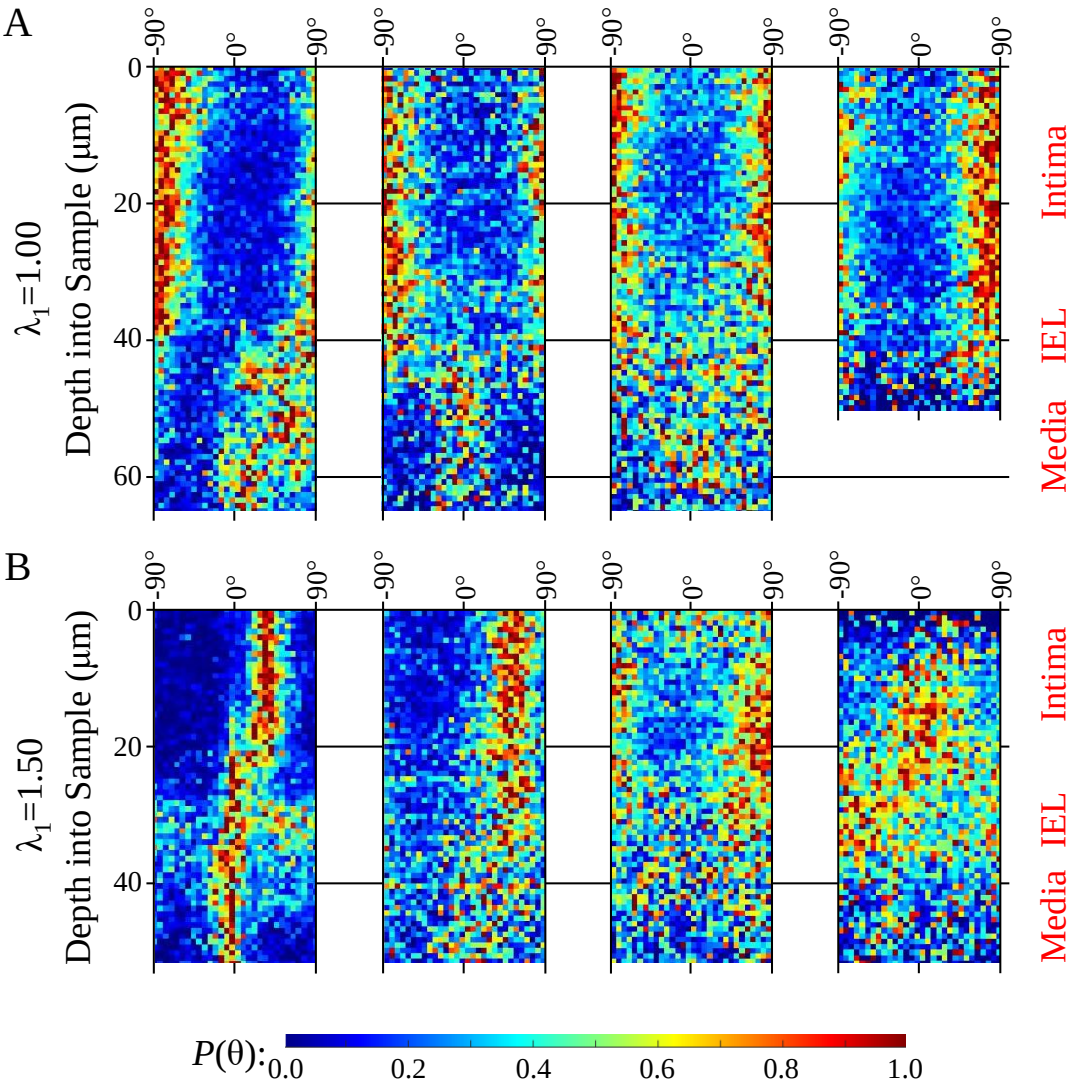

Figure 6.7: Heat maps showing orientation density function ($P(\theta)$) against depth into all four circumferential samples at a stretch ratio (λ) of A.) 1.05 and B.) 1.50. The left-most heat maps are from the sample used in Figure 6.5. See Figure 6.5 for further explanation of the figure's features.

6.4.3 Fibre Structure Versus Depth Versus Stretch

Circumferential

Summary fibre properties (orientation and dispersion, one-family system) are reported versus depth and stretch ratio for a circumferential sample in Figure 6.8.

Figure 6.8 is therefore a condensed representation of fibre structure against stretch as shown in the heat maps in Figure 6.5. The primary fibre orientation (left, similar to the angle red bands in Figures 6.5 and 6.6 are centred at) is aligned with the stretch direction in the media, indicated by green in Figure 6.8-left.

In the intima, fibres are initially oriented more towards the axial direction (red colours in Figure 6.8-left), but become more circumferential (green) with increasing circumferential stretch. Fibre dispersion (right, similar to the width of red bands in Figures 6.5 and 6.6) generally decreases with additional stretch (less red in Figure 6.8-right), except for the media near λ_1=1.3 where two fibre families appear to be present (see Figure 6.10).

Axial

Summary fibre properties (orientation and dispersion, one-family fibre system) are reported versus depth and stretch ratio for an axial sample in Figure 6.9.

For the summary fibre orientation of the axial sample (Figure 6.9-left), fibres were initially near the axial direction in the intima and the circumferential direction in the media (indicated by green colour).

With increased axial stretch, fibres became oriented more in the axial direction (more green in Figure 6.9-left). Fibre dispersion (Figure 6.9-right) was lower (less red) in the intima than the media. Generally, fibre dispersion decreased (less red) slightly with stretch.

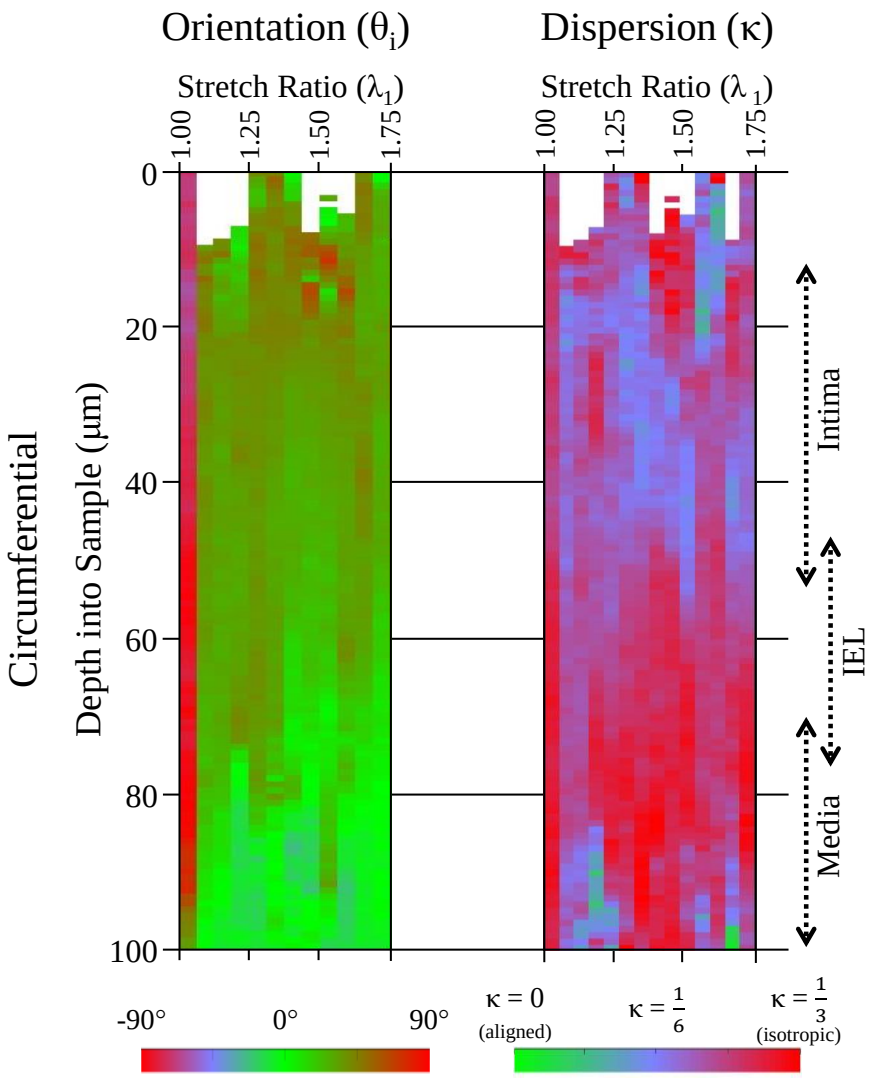

Figure 6.8: Left: heat map showing primary fibre orientation (θ_i, relative to stretch direction) against depth (vertical) and stretch (horizontal) for a circumferential sample. Right: heat map showing fibre dispersion (κ) against depth and stretch for the same sample. Combined, each column of pixels in the two plots represents one heat map stretch from Figure 6.5. The approximate depths of the intima, IEL, and media are labelled to the right.

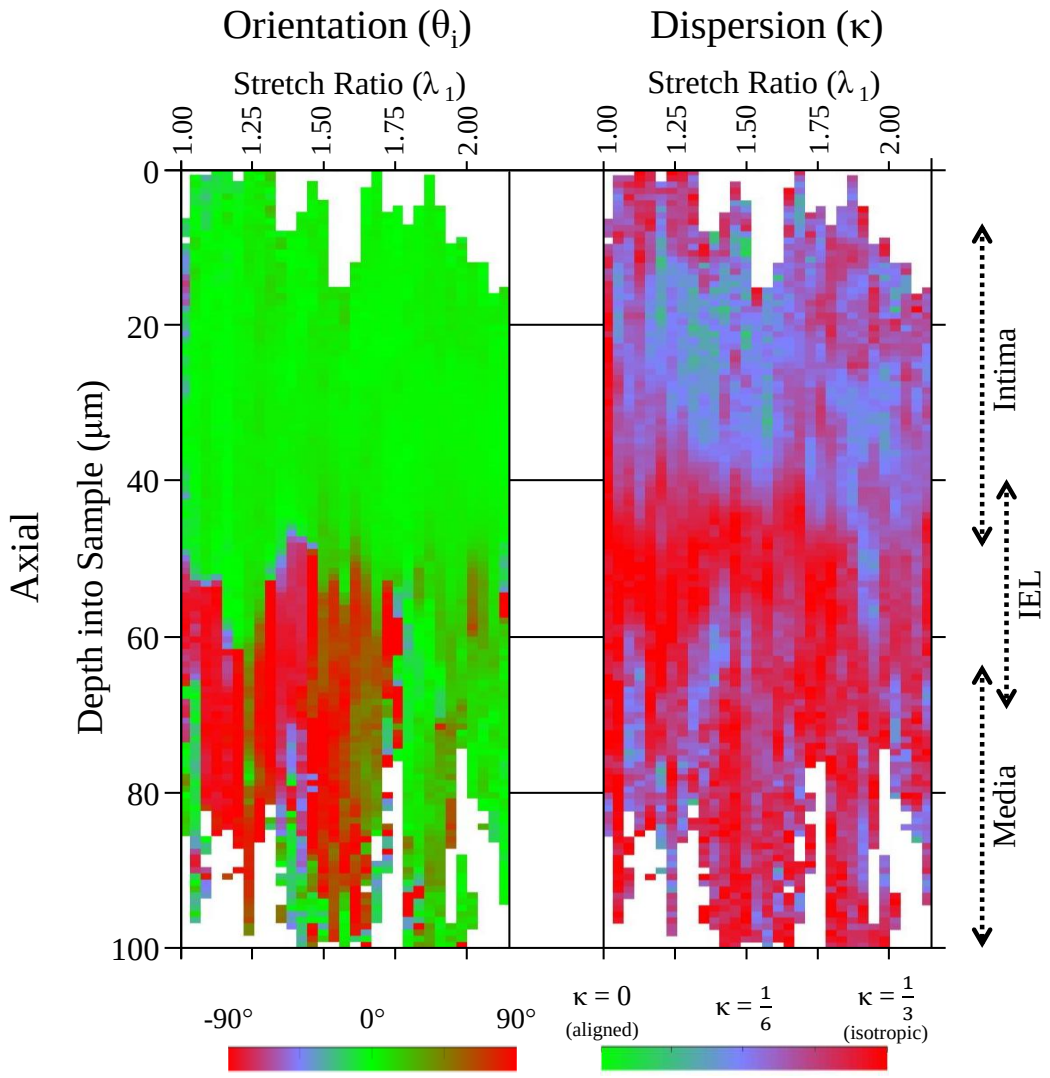

Figure 6.9: Left: heat map showing primary fibre orientation (θ_i, relative to stretch direction) against depth (vertical) and stretch (horizontal) for an axial sample. Right: heat map showing fibre dispersion (κ) against depth and stretch for the same sample. Combined, each column of pixels in the two plots represents one heat map stretch from Figure 6.6.

6.4.4 Two-Family Fibre Orientation, Depth, and Stretch

Circumferential

For a two-family fibre system, summary fibre properties (primary orientation of each family (θ_1 and θ_2) and fibre dispersion (κ_2)) are reported versus depth and stretch ratio for a circumferential sample in Figure 6.10.

A two-family fibre system is supported where θ_1 and θ_2 are different from one another in Figure 6.10. For example, the IEL below λ_1=1.4 and the media around λ_1=1.4 would be well represented by a two-family fibre system. For a two-family fibre system, there is a more clear decrease in fibre dispersion with increasing stretch compared to the one-family fibre system results (see Figure 6.8). In the heat maps of the fibre orientation density function versus depth (Figure 6.5), fibre dispersion decreased with increasing stretch.

Axial

For a two-family fibre system, summary fibre properties (primary orientation of each family (θ_1 and θ_2) and fibre dispersion (κ_2)) are reported versus depth and stretch ratio for an axial sample in Figure 6.11.

A two-family fibre system represents the fibre structure better than a one-family system at some regions of the IEL and media in Figure 6.11 (i.e. where θ_1 and θ_2 are different). Compared to a one-family system (Figure 6.9), two-family fibre dispersion more clearly decreases in the intima and increases before decreasing in the media with stretch. Therefore, the two-family plots better represent the observations made for some image slices in Figure 6.6.

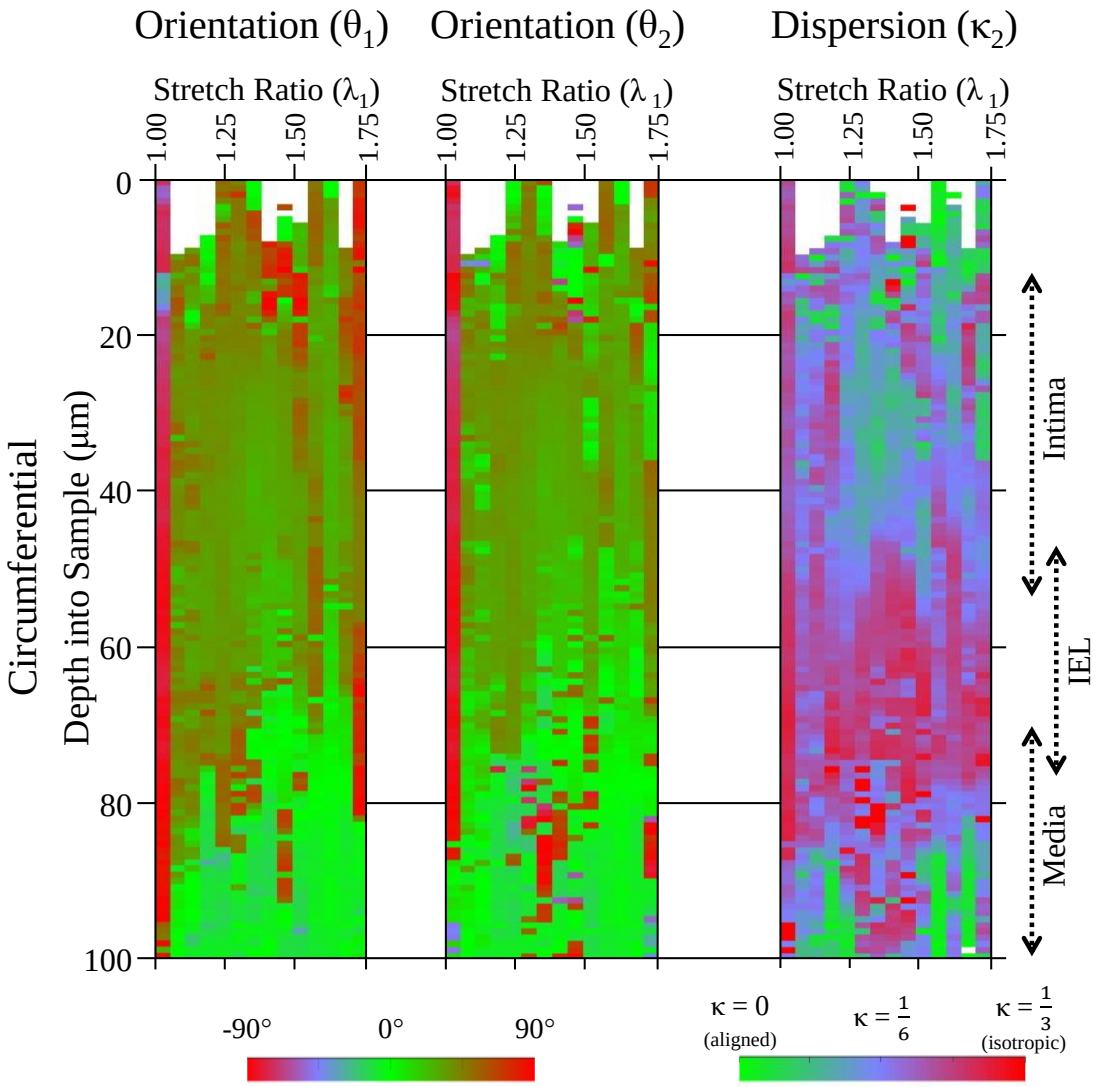

Figure 6.10: For a two-family fibre system; Left: heat map showing first primary fibre orientation (θ_1); Centre: heat map showing second primary fibre orientation (θ_2); Right: heat map showing fibre dispersion (κ), all against depth (vertical) and stretch (horizontal) for the same circumferential sample.

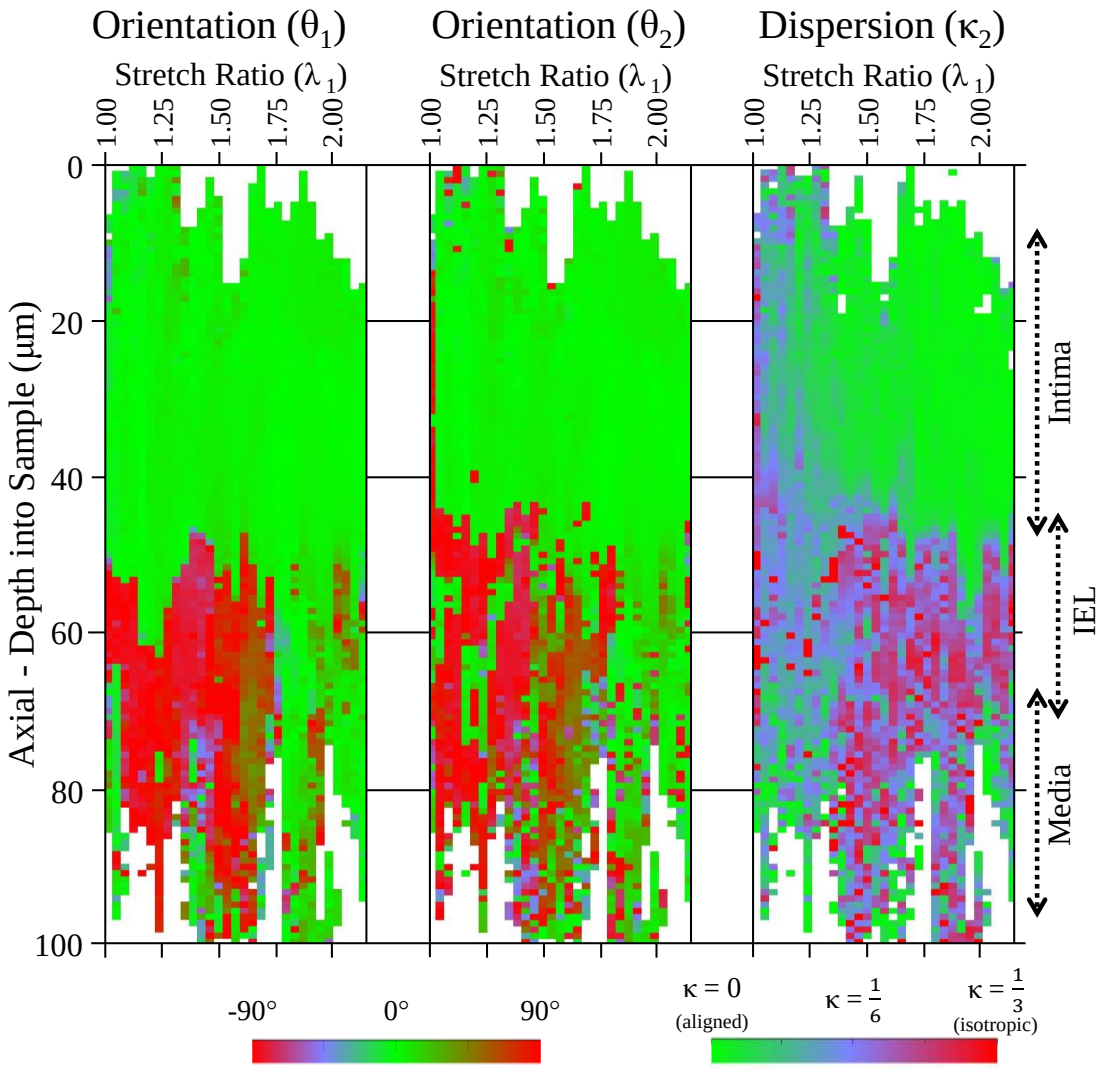

Figure 6.11: For a two-family fibre system; Left: heat map showing first primary fibre orientation (θ_1); Centre: heat map showing second primary fibre orientation (θ_2); Right: heat map showing fibre dispersion (κ), all against depth (vertical) and stretch (horizontal) for the same axial sample.

Discussion of Multiphoton Images of Uniaxial Strips

In summary, the intima, IEL, and media had distinctive fibre structures. The intima had relatively lower fibre dispersion and was made of a single family of fibres that were primarily directed in the axial direction. The IEL is probably best described as having dispersed fibres, oriented in a similar direction to the fibres in the intima. Fibres in the media appeared to be arranged into a primary family in the circumferential direction, with moderate-to-high fibre dispersion. The media sometimes had a fibre structure that would be better represented by a two-family fibre system than a one-family system.

Generally, there were no consistent changes in fibre properties with depth within a given tissue layer, although there was some variability between different image stack slices of the same layer. For example, the range of dispersion values in the media at a given strain was similar to the intra-quartile range of the histology image fibre dispersion in Figure 5.14B or D. Therefore, the range of values in the box-plots in Figure 5.14 may be affected by having sampled only a narrow slice of each tissue sample.

The multiphoton results at zero strain often had different values from results at different strains. Some of these differences could be explained by sag in the sample causing undulation of the tissue relative to the stack slices. For all layers, increasing strain resulted in fibres becoming more oriented toward the direction of stretch, representing considerable changes to the fibre microstructure of the tissue. This presents a challenge in that it is easier to image fibre structure at zero strain, but the structure might not represent the *in vivo* fibre structure. For example, the histology images in Chapters 3 and 5 were taken at zero stretch, which appears to have different fibre structures than at physiological stretches (approximately λ_1=1.1 for axial and λ_1=1.25 for circumferential).

At the highest stretches, the fibres were observed to de-bond from one another, which may explain why the orientation misalignment and fibre dispersion sometimes increased. In Section 6.4.5, fibres near a notch were seen to become more disordered as fibres de-bonded and the material approached failure.

6.4.5 Qualitative Notch Specimen Multiphoton Results

Notched specimen tests were used to observe and understand the mechanisms of tearing and fracture in the different layers of the tissue. This section will present one axial and one circumferential notched strip as cases, but the observations generally apply to all four strips, unless otherwise noted. Following these, three fracture observations from other samples will be presented. These three observations were only noted in one or two of the samples, but provide insight into failure mechanisms of the tissue.

Circumferential

Figure 6.12 shows sections of the intima, IEL, and media at a series of stretch ratios for a circumferential strip undergoing a notch specimen test.

The crack front was often ahead in the intima (left column) and IEL (centre column) compared to the media (right column; crack indicated by red ellipse at λ_1=1.05 in Figure 6.12). The IEL often fractured ahead of the intima as well. In the IEL, the tear propagated by jumping to subsequent pores or voids in the sheet-like layer, which also temporarily stopped the crack from progressing. Fibres in the intima and media bridged across the crack in the IEL, with thinner fibres separating from their bundles. Bridging fibres in both the intima and media were seen for about 50-100 μm behind the crack tip.

Fibres deformed and rotated with stretch in a similar way to those in the unnotched tests. Further, fibres within about 100 μm of the crack tip rotated in response to the local mechanical state (red arrows in Figure 6.12). Fibres in the intima and media were rarely observed to fracture, but became less bundled to one another with increasing stretch. This suggests the fibres themselves typically do not fail, and fracture comes from failure of the links between fibres.

Particularly as the crack tip blunted with increasing strain, several zones often developed of relatively more fibre disruption (pairs of red arrows in Figure 6.12).

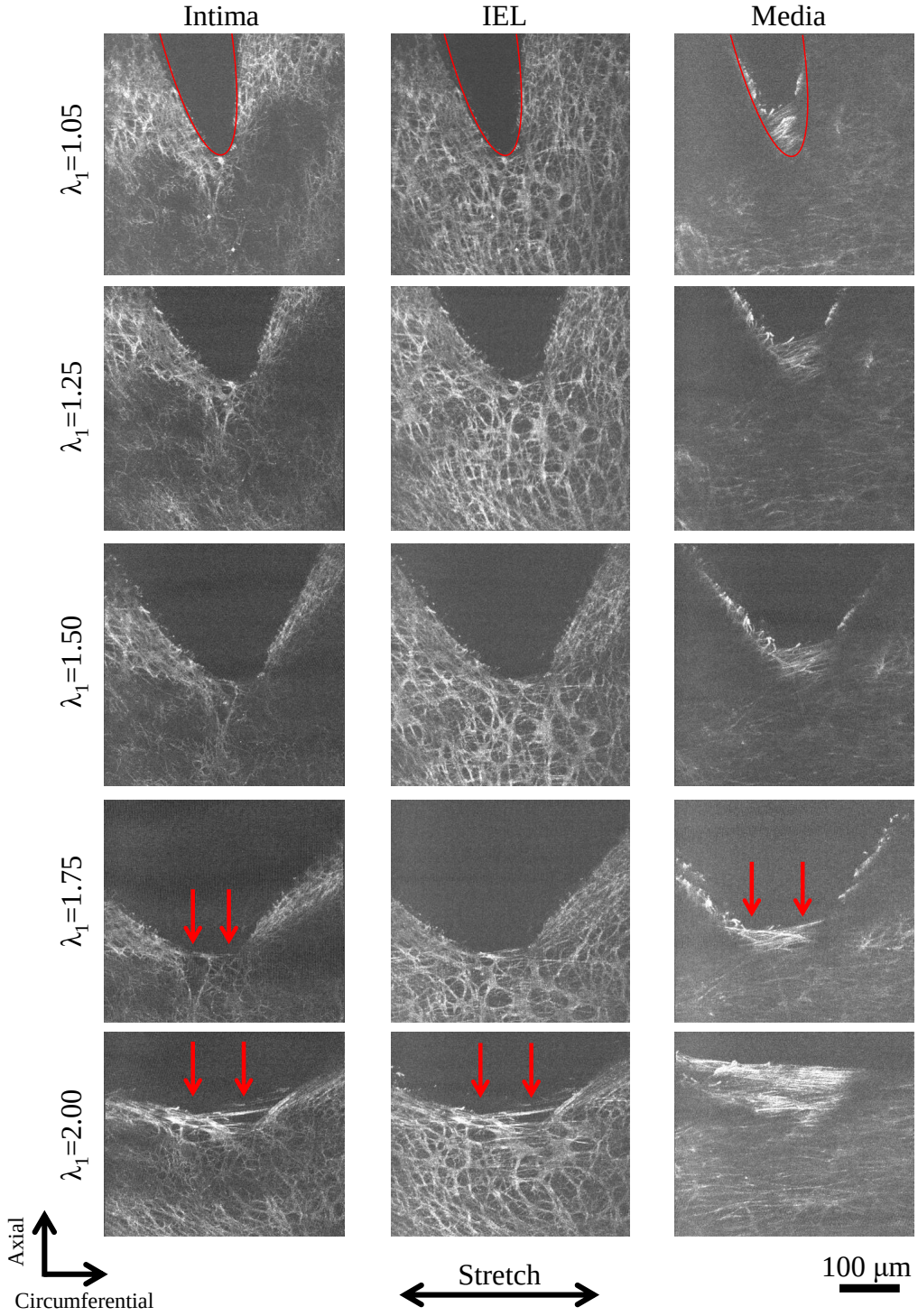

Figure 6.12: Slices from a multiphoton image stack of a circumferential notched specimen test strip for the intima, IEL, and media (by column). The stretch ratios (λ_1, by row) were 1.05, 1.25, 1.50, 1.75, and 2.00. The initial notch is indicated in red in the top figure. Red arrows are features referred to in the text.

Axial

Figure 6.13 shows sections of the intima, IEL, and media at a series of stretch ratios for an axial strip undergoing a notch specimen test.

In notched axial samples (Figure 6.13), the crack front was also ahead in the IEL, followed by the intima, and then the media (indicated by red ellipse). The sample in Figure 6.13 had a particularly dense IEL layer, in which progressive fractures occurred with increasing stretch (indicated by red arrows). Fibres in the intima (left column) bridge the IEL crack without fracturing themselves. In the media (right column), fibres were recruited to bridge the crack and rarely fractured. Instead, these fibres appeared to become more individual, suggesting the failure of links within and between fibre bundles.

Several smaller fronts would often develop from the main crack as it blunted with increasing stretch, with the new fronts or damaged regions typically being between fibres. Where the primary fibre direction was perpendicular to the notch direction, these zones could be behind and adjacent to the crack tip.

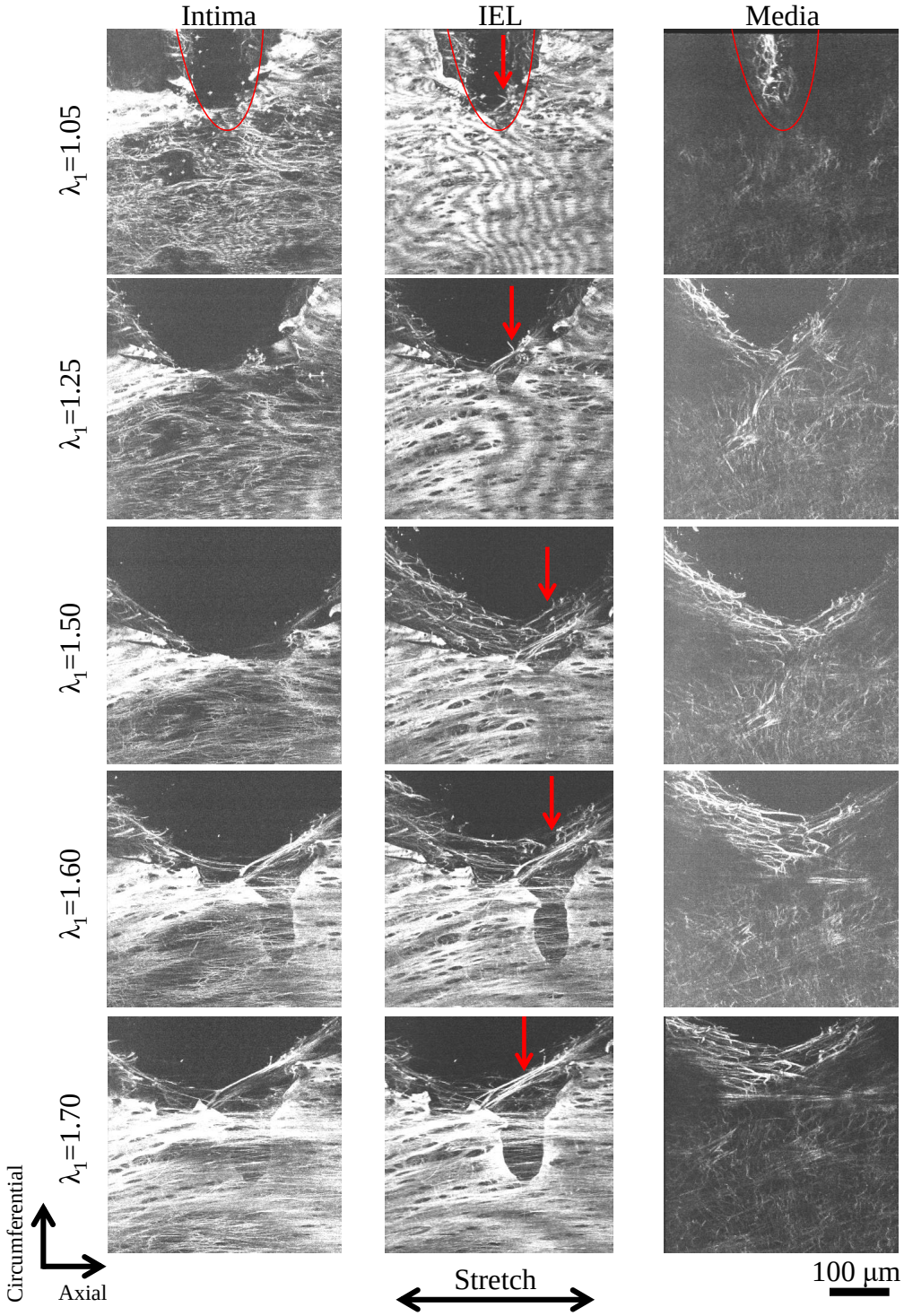

Figure 6.13: Slices from a multiphoton image stack of an axial notched specimen test strip for the intima, IEL, and media (by column). The stretch ratios (λ_1, by row) were 1.05, 1.25, 1.50, 1.60, and 1.70. The initial notch is indicated in red in the top figure. Red arrows are features referred to in the text.

Features of Particular Cracks

In addition to the two notched cases above, several interesting crack features were observed in some of the other notched samples.

Figure 6.14 shows a highly stretched (λ_1=1.9) circumferential notched sample (B), where the crack has formed separate fronts in the intima (C) and media (D). Delamination occurred in the axial-circumferential plane to connect the two notches (Figure 6.14A). In trouser tear tests in Section 5.4.1, tearing toughness in the axial-circumferential plane was found to be several times lower than in the axial-radial plane, as this notch originally was. Some other samples had different crack tip locations in the intima and media, but to a lesser degree.

In the same sample at a slightly further stretch (see Figure 6.15; λ_1=1.95), a lateral crack has developed about 250 μm ahead of the crack tip. The lateral crack split the intima, IEL, and some of the media. This was the only sample where a lateral fracture was observed ahead of the crack tip, and the sample completely fractured before the next pause in stretching for imaging (before λ_1=2.0). In trouser tear tests (see Section 5.4.1), lateral fractures (in the circumferential-radial plane) were frequently observed for tears initially in the axial-radial plane. The axial-radial trouser tears had the same initial tearing plane as circumferential notched samples (see Section 5.3.2 for plane definition).

In a different circumferential notched sample, a secondary fracture was observed to extend laterally from the initial notch (see Figure 6.16). The primary crack of this sample was more blunt than those in other samples. Several secondary cracks branched from the primary crack, of which this one was the most pronounced. This secondary crack (Figure 6.16B) did not elongate with increasing stretch of the sample, and the secondary crack was more pronounced in the intima and IEL, where it was in a similar direction to fibres, than it was in the media. It was not clear if this secondary crack was responsible for the eventual failure of the sample, or if the secondary crack was created when the initial notch was cut. Lateral secondary cracks of a similar size were observed in one other circumferential sample, and lateral cracks of a similar size to the voids in the IEL were observed in other samples.

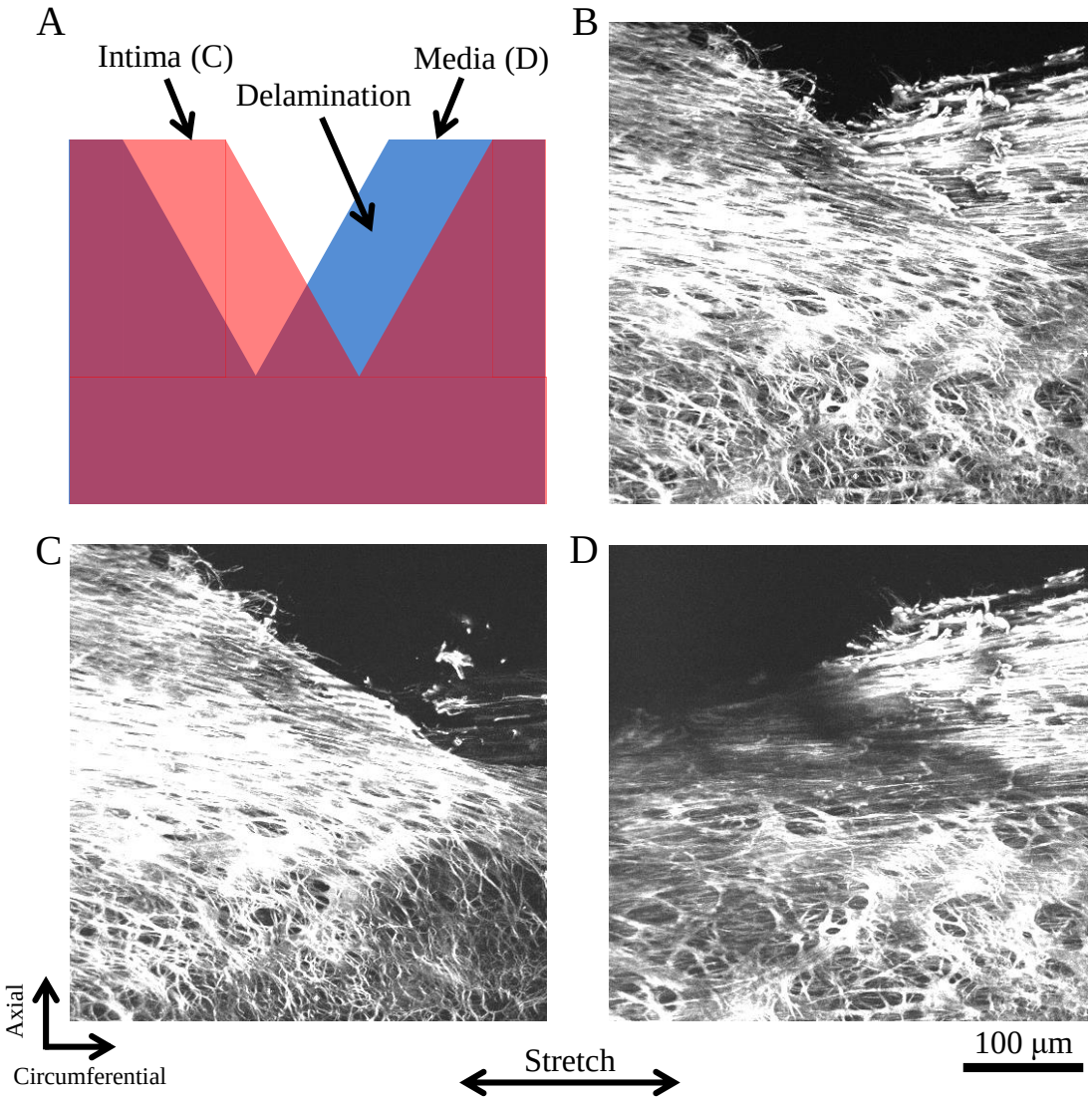

Figure 6.14: A circumferential notched sample (λ_1=1.9) where the initial axial-radial notch separated into two cracks by partial delamination in the CA plane. A.) Cartoon illustration of the intima layers (red), media layers (blue), and partial delamination, B.) MIP image of the intima and media of the sample, C.) MIP image of the intima, and D.) MIP image of the media.

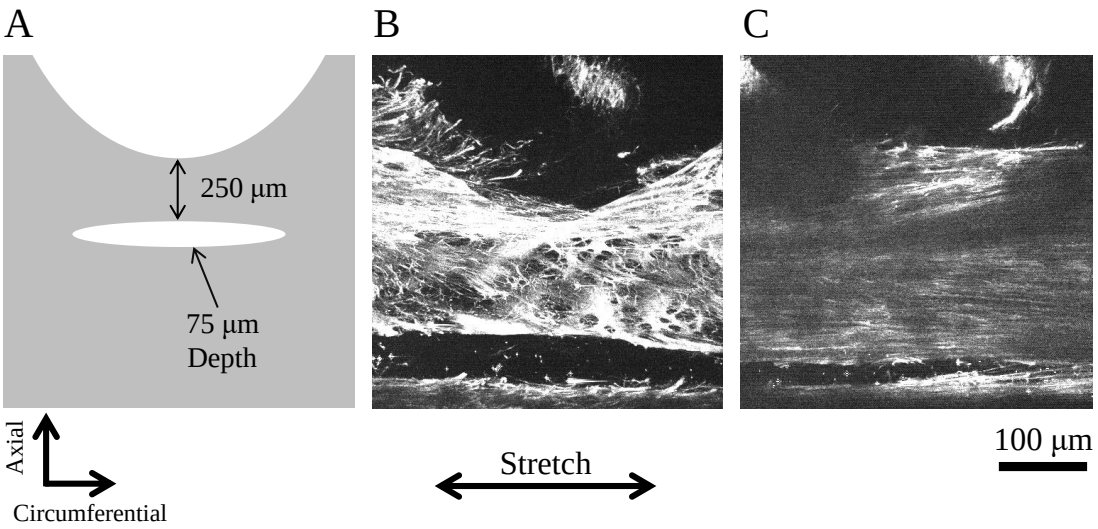

Figure 6.15: The circumferential notch sample from Figure 6.14 at λ_1=1.95, where a lateral crack has developed ahead of the original crack. A.) Cartoon illustration of the initial crack (top) and new lateral crack, which goes from the surface to a depth of about 75 μm, B.) MIP image of the intima and IEL, with the lateral crack at the bottom of the image, and C.) Maximum intensity projection of the same crack in the media (approximately depth of 45 μm).

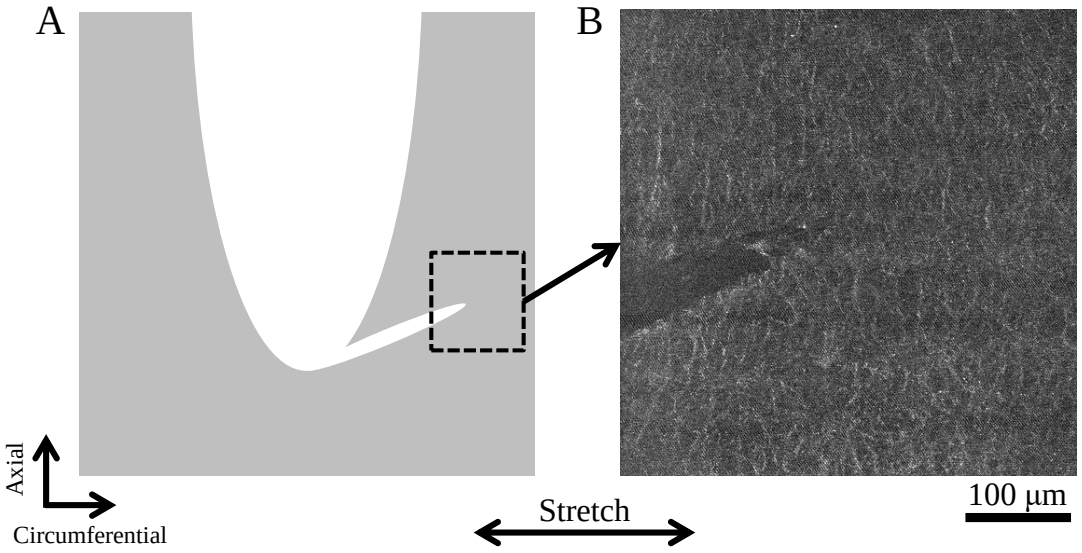

Figure 6.16: A circumferential notched sample where the crack tip was blunt, with smaller cracks branching from the initial notch as shown in: A.) By cartoon and B.) MIP image of the intima and IEL of the image stack.

Discussion of Notched Specimen Tests

Many features of tearing in the notch specimen tests were similar for both the circumferential and axial strips. The differences can be explained by the differences in fibre structure for each direction of the tissue. Fibres in the intima were oriented more in the axial direction, and seemed to contribute more to toughness in the axial strips (i.e. for circumferential-radial tears).

Fibres in the intima and media were more sparse and seemed to have less cross-linking, and those in the IEL were denser and seemed to be more tightly connected. In the notched tests, mechanisms of damage to the IEL depended on the direction of tearing relative to the fibres. For axial strips (Figure 6.13), sharp secondary tears propagated from a blunt primary tear in the IEL. Circumferential strips (Figure 6.12) had more opening between fibres in the intima and IEL, which were in a similar direction to the crack.

In the media layer, the axial strips (Figure 6.13) had fibres parallel to the crack, with more opening between fibres. The media of circumferential strips (Figure 6.12) had fibres perpendicular to the crack and had less opening between fibres. The media is thicker than the intima, and the circumferential notched strips had a higher failure stress and stretch than the axial notched strips (see Appendix A.5). This suggests the artery tissue has a higher tearing strength for planes of the tissue where more fibres cross the tearing plane.

In general, all three layers had mechanisms that increased material toughness. Fibres were recruited through rotation and deformation to distribute loads away from the crack tip. The material was ductile and the crack tips showed considerable blunting, which would reduce geometric stress concentrations. Tears propagated in jumps between voids in the material or by simultaneous failure of a group of fibres in the IEL. In the intima and media, links between fibres appear to fail, but without the fibres separating completely from the matrix.

In an artery, these mechanisms would lead to small but stable cracks. Failure would give local strain relief, distributing loads to adjacent tissues. These features explain clinical observations that partial tears in atherosclerosis plaques are common, but complete fractures are rare [Daemen et al., 2016; Falk et al., 2013].

6.5 Discussion

6.5.1 Response of Fibre Structure to Stretch

Three layers of tissue were observed in the multiphoton-based experiments: intima, IEL, and media. The intima was about 40 μm thick. Fibres in the intima were primarily in the axial direction and had a lower fibre dispersion than those in other layers. The IEL was thinner (about 10 μm). It had fibres that were in a similar direction as those in the intima, but with a higher density and more dispersion. The media was thicker, but the multiphoton signal was attenuated beyond about 20 μm of depth into the layer. Fibres in the media were primarily in the circumferential direction, but had a higher fibre dispersion than the intima. In some multiphoton stack images, the fibre structure would be better represented as a two-family fibre system.

With increasing stretch, fibres in all layers rotated towards the direction of stretch. Fibre structure changed considerably between an unloaded state and stretches at a physiological level. In notched samples, fibres were recruited to distribute loading away from the crack tip. At stretches approaching failure, fibre structure changed even more, particularly for fibres near crack tips.

In Chapter 4, fibre structure was shown to significantly influence stresses in FE models of atherosclerotic plaques. In Chapter 5, fibre structure was found to be a significant predictor of tearing toughness. However, fibre structure was calculated from histology images of unloaded tissue in both of those studies. In Section 6.4, it was shown that fibre structure without load may not be representative of the structure *in vivo*. This may explain why there was less influence of fibre dispersion on tearing toughness at higher fibre dispersions (see Figure 5.16). With a sufficiently high unloaded fibre dispersion, fibres could be recruited to have a similar structure by the failure load, irrespective of the initial fibre structure.

In addition to different samples having different fibre structures at no load (as found in Chapter 3), the rates at which fibre structure changes with stretch may be different in different samples. Further study should consider different rates of change in fibre structure in response to mechanical state in different tissues.

6.5.2 Mechanisms of Fracture and Toughening

The mechanisms of tissue failure and fracture that occur in plaque rupture are not well understood. Therefore, mechanical models such as those presented in Chapter 4 are limited by lack of failure criteria. In the notched specimen tests under multiphoton microscopy, failure features such as blunting of the crack tip, recruitment of fibres, and bridging of fibres across the crack were observed. Mechanisms of fibre reorganisation appear to be highly involved in the mechanisms of fracture and toughness of the tissue.

Where fibres had large rotations in response to stretch, fibres appeared to become less bonded to other fibres. This suggests local failure at a finer scale of cross-links between fibres, causing damage to the fibre structure at lower stretches than required to fracture the tissue. This served to increase toughness of the tissue, and warrants further study. In particular, any changes to the cross-links and their properties with disease should be considered.

As was observed in the trouser tear tests in Section 5.4.1, links holding fibres to one another were damaged more than the fibres themselves in the notched sample tests. In other words, fracture seems to be more from failure of bonds between fibres than the fibres themselves breaking. Therefore, toughness was found to be lower where the crack was more aligned with the fibres, as loads to separate fibres were more locally concentrated.

6.5.3 Implications for Biomechanical Models

In Chapters 4 and 5, fibre structure was shown to determine mechanics of artery tissue. In the multiphoton-based studies in this chapter, fibre structure was shown to change with mechanical state. While coupling between fibre structure and mechanics in artery tissue is almost certainly a critical parameter in biomechanical models, previous models have largely ignored fibre structure.

For example, the constitutive model used in Chapter 4 used a constant value for κ and an exponential function to account for strain-stiffening of the material. A more structurally motivated constitutive model could use a strain-dependent κ to account for strain-stiffening, as lower κ causes higher stiffness.

For predicting failure of the material, coupling between fibre structure and mechanics may be an even more important consideration than for stiffness or stress. Failure was observed in Section 5.4.1 and in the multiphoton-based experiments to be mainly between fibres, rather than the fibres themselves breaking. These observations motivate separating stresses into components relative to fibres, as was done in the finite element studies in Chapter 4. Because fibres are able to rearrange considerably with stretch and fracture appears to require the failure of many cross-links between fibres, strain and strain energy should also be considered as failure criteria. Small areas of locally high stress may fail, redistributing loads to surrounding tissue without causing complete fracture of the tissue. Failure criterion based on strain or strain energy may be less vulnerable to these concentrated areas.

6.5.4 Limitations and Recommended Future Work

Material tests under multiphoton microscopy provided a powerful way to link mechanics to fibre structure at different depths and stretches of the tissue. Constitutive material laws motivated by structure could be developed with data from this approach, with fibre reorganisation used to account for the non-linear strain-stiffening behaviour of the material.

Multiphoton techniques can distinguish between type of fibre (collagen or elastin), which should be considered in future study [Zoumi et al., 2004]. Samples could be scanned with higher depth-resolution, to allow assessment of fibre structure in the radial planes of the tissue. The light source power can be set to a depth-dependent profile, allowing for a stronger signal from deeper fibres without causing photodamage to the surface of the tissue.

The experiments reported in this chapter should be repeated using human atherosclerotic tissue to compare with these findings for healthy tissue.

6.6 Conclusions

Uniaxial tests under multiphoton imaging found distinct fibre structures for the intima, internal elastic lamella (IEL), and media layers. With increasing strain, fibres rotated towards the direction of applied stretch. Fibres rotating towards the direction of stretch explains the strain-stiffening properties of artery tissue.

In notched specimen tests of artery tissue with multiphoton imaging, fibres reorganised in response to the local mechanical environment. Mechanisms at the fibre-level increased the toughness and robustness of the material. The relative efficiency of fibre recruitment in different tissue planes and layers explained relative differences in tearing toughness between different tissue planes.

Chapter 7

Conclusions

Atherosclerotic plaque disruption is a mechanics-dominated aspect of cardiovascular disease progression, and is a key determinant for the fate of a plaque and its host [Falk et al., 1995; Halvorsen et al., 2008]. Plaque disruption is caused by the erosion or fracture of the fibrous cap, but the mechanisms involved in erosion and fracture have not been well understood. Although collagen and elastin fibres are the primary mechanical components in the fibrous cap, few previous studies have considered fibre structure in plaque mechanics or plaque disruption.

The studies described in this dissertation sought to understand changes to the fibre structure from atherosclerosis, determine the mechanical effects of these changes, and explain the role of fibre structure in material failure. Microscopic imaging, finite element based biomechanical models, and material tests were used independently and in combination to provide insight to fibre structure and plaque mechanics. Contributions from these studies will be detailed by revisiting the objectives that were posed at the beginning of this dissertation.

Characterise Changes to the Microstructure from Atherosclerosis

The fibre structures of atherosclerotic plaques were characterised by image processing (see Section 3.5). Compared to the healthier IT region, shoulder region fibres were less aligned with the luminal surface and had more fibre dispersion. The fibrous caps had lower fibre dispersion than the IT regions, but fibres in both regions were well aligned with the luminal surface. The fibrous cap, shoulders, and IT regions had similar fibre structures for carotid and coronary plaques.

Determine Effects of Fibre Structure on Stresses in Plaques

Finite element models were built with plaque-specific geometries and fibre structures, built from histology images of human carotid and coronary atherosclerotic arteries. Anisotropic finite element models (that included fibre structure) were found to have significantly different stresses than isotropic models (without fibre structure; see Section 4.5.2). Predicted stresses could be higher or lower in either model, and had extreme changes for some plaques. Anisotropic models had stress components calculated relative to fibre orientations: axial, transverse, and shear (see Section 4.5.3). Axial stresses were highest and transverse stresses were very low. Carotid plaques had significantly higher maximum principal stress in their fibrous caps compared to coronary plaques (see Section 4.5.1). This may explain clinical observations that coronary plaques rupture more frequently at their shoulders, while carotid plaques rupture more centrally in their fibrous caps [Redgrave et al., 2006; Richardson et al., 1989].

Relationships between Fibre Structure, Geometry, and Stress

Linear regression models were used to compare fibre structure, geometry, and FE stresses (see Chapters 3 and 4). The carotid plaques were significantly larger than the coronary plaques, and some geometry parameters were linked to fibre structure in key regions of coronary (but not carotid) plaques (see Section 3.6). Parameters related to shoulder geometry were more frequently linked to stresses in coronary plaques, while fibrous cap geometry was more linked to stresses in carotid plaques (see Section 4.6 for this relationship and those following). Fibre orientation predicted transverse and shear stress in the shoulders of carotid plaques, while fibre dispersion predicted transverse stress in the shoulders of coronary plaques. Fibre misalignment and dispersion also predicted the angle between fibres and the maximum principal stress in the fibrous cap and shoulders of carotid plaques. Isotropic maximum principal stress was only a moderate predictor of anisotropic stresses, so fibre structure must be considered to fully capture plaque mechanics.

Understand the Role of Fibre Structure in Artery Material Properties

Experiments tested stiffness and toughness of healthy porcine carotid arteries in different planes relative to the fibre structure in the tissue (see Chapters 5 and 6). Uniaxial tensile tests found the tissue to be stiffer circumferentially than axially, confirming findings from previous studies. Here, histological and multiphoton imaging suggested that fibre structure contributes to stiffness. Fibres were found to be more circumferential than axial in the thicker media layer, but more axial in the intima and internal elastic lamella. Fibre dispersion decreased with uniaxial strain, while stiffness increased (see Sections 5.4.2 and 6.4). Through trouser tear tests, the tissue had a higher tearing toughness within the sheet-like concentric layers of fibres compared to between these sheets (see Section 5.4.1). Samples with higher tearing toughness had higher fibre dispersion and more isotropic stiffness (see Section 5.5). While experiments in this study used healthy tissue, atherosclerotic tissue has a wider range of fibre dispersion values, so tearing toughness may be even more dependent on fibre structure.

Consider Microstructure-based Mechanisms in Plaque Disruption

SEM observations suggested that tissue fractures between fibres, rather than across them, and that partial fractures occur frequently without symptom or consequence (see Chapter 2). A triangle feature at the plaque shoulders was identified and proposed as a vulnerable plane for fractures. Triangle features are formed by fibre groups splitting between the fibrous cap, IT region, and tissue behind the lipid core. Finite element models found higher axial and shear stresses at similar locations to the boundaries between these fibre groups (see Section 4.5). Trouser tear and notched specimen tests, used alongside histological or multiphoton microscopy, confirmed that fractures extended around and between fibres, rather than by fracturing fibres (see Chapters 5 and 6). This suggests shear stresses should be considered with similar or even greater importance compared to axial and maximum principal stress. Fibres were recruited to redistribute loads from the crack tip, increasing toughness of the tissue. Fibres tended to fracture in groups (see Section 5.4.1 and 6.4.5), which increased the required tearing force, provided local strain relief, and limited the propagation distance of

each tear. The morphology of fibre recruitment and bridging depended on the original fibre orientation and dispersion, with considerable differences by layer and plane of tissue being fractured.

7.1 Future Directions

These findings motivate further and adjacent studies into the role of fibre structure on plaque mechanics.

Material Properties and Fibre Structure in Atherosclerotic Tissue

Experiments were done with healthy carotid arteries because they are more consistent than atherosclerosis plaques, which have more variable geometry, material composition, and fibre structure. With the influence of healthy fibre structure on material properties established, tests with diseased tissues can use this baseline to anticipate and interpret effects of these variabilities on test results. Any changes with atherosclerosis to the fibre recruitment, bridging, and joint failure mechanisms should be identified. Links between fibre structure and material properties could be compared by vessel type and plaque composition.

3D Fibre Structure Assessment and Biomechanical Models

2D sections in the circumferential-radial plane of atherosclerotic plaques were used to characterise the fibre structure and build finite element models. Mechanically-significant changes to fibre structure were found, motivating similar studies of the 3D fibre structure and mechanics. Ideally, such analysis would consider additional material and structure parameters such as fibre waviness, fibre dimensions, other plaque components (calcification, intra-plaque haemorrhage, and embedded lipid), type of fibre, and local relative density of components. Loading, boundary conditions, and material properties could consider the dynamic interactions of the plaque with blood flow and surrounding tissues.

Role of Scale in Plaque Micromechanics

SEM observations in Chapter 2 identified at least three levels of hierarchy to the fibre structure, while only the largest structures were considered in subsequent analysis. Fracture between these fibres and by shear suggests that structural failures actually occur at a smaller scale of the hierarchy. Smaller-scale fibre structures and material properties should be characterised, along with any change to these from disease. If structures and properties are found to change with disease, investigations should test if changes are consistent within a plaque or patient. If these smaller structures are consistent (or vary in predictable ways), then these features could be included in multiscale models or fracture models. Investigations at smaller scales will also help determine if structure-based biomechanical models are needed, or if continuum material models (that account for local fibre structure through statistics) can sufficiently capture the mechanics to predict failure.

Mechanobiology and Dynamics of Fibre Structure

Artery is a dynamic material, with cellular processes constantly changing the fibre structure and therefore mechanics. However, cellular activity is controlled in part by mechanical stimulus. Partial fractures were observed by SEM and results from material toughness tests suggested fractures may develop and propagate over time. Evidence of fracture healing was also seen in SEM images (Chapter 2). Cellular activity, fibre structure, and mechanics of a plaque probably evolve through complex interdependencies, which have not been well studied.

Clinical Assessment of Fibre Structure and Biomechanics

One ultimate goal in cardiovascular biomechanics is to build tools for clinical assessment and management of diseases. Medical imaging techniques are needed that can evaluate artery fibre structures in patients. To transition theory and models to clinical practice, accuracy and robustness must be validated with larger samples than is currently typical. Biomechanics must be matched to symptoms and outcomes. Since atherosclerosis is a complex disease, multifactorial assessment of plaques is needed, with consideration of coupling between factors.

Appendix A

Supplemental Material and Methodology

A.1 Dispersion by Vader Method

To validate the fibre dispersions calculated by the methods in Section 3.4.6, an alternative measure of fibre dispersion was considered [Vader et al., 2009]. As calculated through Equations A.1 and A.2, θ_{fibre} was the orientation of individual fibres and Ω was a tensor describing the local orientation, evaluated through a 51×51 pixel region of interest centred about each pixel on the plaque.

$$\Omega = \begin{pmatrix} \langle \cos^2(\theta_{fibre}) \rangle & \langle \cos(\theta_{fibre}) \sin(\theta_{fibre}) \rangle \\ \langle \cos(\theta_{fibre}) \sin(\theta_{fibre}) \rangle & \langle \sin^2(\theta_{fibre}) \rangle \end{pmatrix} \tag{A.1}$$

$$\chi = \text{Max}\{\text{Eigenvalues}(2\Omega - \mathbf{Id})\} \tag{A.2}$$

The Vader fibre dispersion (χ) was calculated from Ω and the identity matrix, **Id**. Here, χ=0 corresponds to a uniform (isotropic) distribution and χ=1 is for perfect fibre alignment [Vader et al., 2009].

For validation, the illustrative plaque (Figure A.1A) had its dispersion calculated by the Gasser (Figure A.1B, Section 3.4.6) and Vader methods (Figure A.1C, methods in this section). For both methods, fibre dispersion had considerable variability with location in the sample, but a reasonable match for zones of lower/ higher dispersion. Higher values of dispersion occurred near the lipid core (as would be expected for this disorganised and fibre-sparse region) and the shoulders. The fibrous cap and IT had relatively low dispersion.

Fibre dispersion was compared between the two methods on a pixel-by-pixel basis (Figure A.1D). While there is some scatter in the results, there is a quite strong linear relationship between the two methods of calculating fibre dispersion ($p<0.001$, $R^2=0.689$), despite neither method having a linear scale of dispersion. Similar results from each of the methods gave validation to dispersion being a repeatable and useful measure of fibre structure.

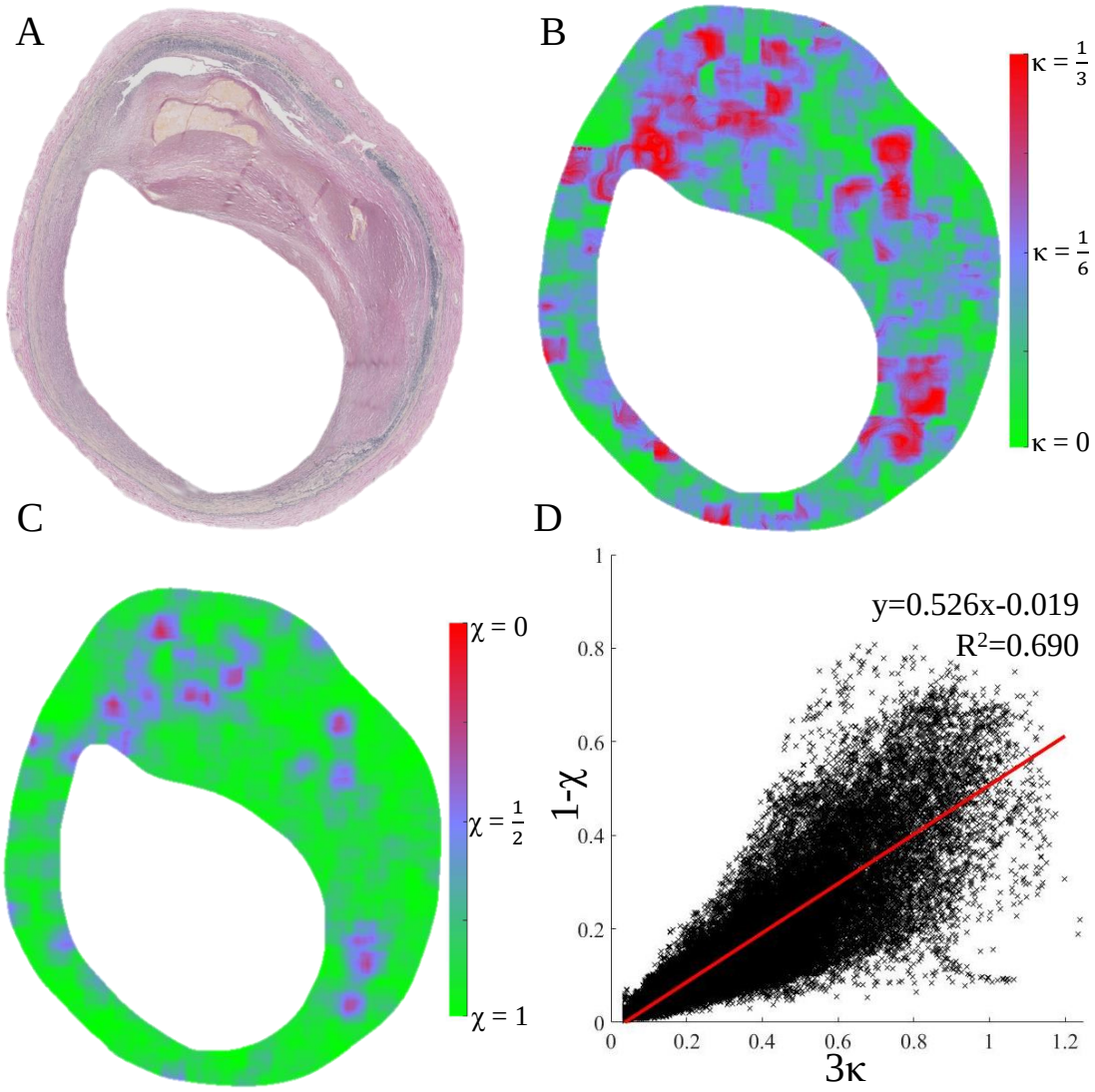

Figure A.1: A.) The illustrative coronary plaque, B.) Fibre dispersion calculated by the Gasser method (κ), C.) Fibre dispersion calculated by the Vader method (χ), and D.) Fibre dispersion compared between the two methods.

A.2 Finite Element Validation

A.2.1 Additional Probability Density Plots for FE Stresses

This section includes FE stress probability density plots to supplement the one for anisotropic maximum principal stress in Section 4.4.2.

Isotropic Maximum Principal Stress

Probability density plots of isotropic maximum principal stress within regions of the illustrative plaque are shown in Figure A.2. For all regions, most of the region had low stress, with the highest levels of stress being found in only a small portion of the region. In this plaque, the shoulder region (Figure A.2A) had the highest-stresses and relatively more area with higher stress. The IT (Figure A.2C) had a high median stress. The fibrous cap (Figure A.2B) and GEX regions (Figure A.2D) had mostly low stress.

Axial Stress

Probability density plots for axial stress are shown by region in Figure A.3. Like the stress visualisations in Figure 4.2B and C, the density distributions for anisotropic maximum principal (Figure 4.3) and axial stress were nearly identical. Along with the axial stresses being much higher than the transverse or shear stresses, this shows that stress was mainly in the direction of the fibres.

Transverse Stress

Probability density plots of transverse stress are shown in Figure A.4 for regions of the illustrative plaque. Transverse stresses were much smaller than isotropic maximum principal stress, anisotropic maximum principal stress, or axial stress (note change in scale from previous figures). Most transverse stress in the fibrous cap (Figure A.4B), IT (Figure A.4C), and GEX region (Figure A.4D) was negative (compressive). About half of the area within the shoulder regions (Figure A.4A) had tensile transverse stress.

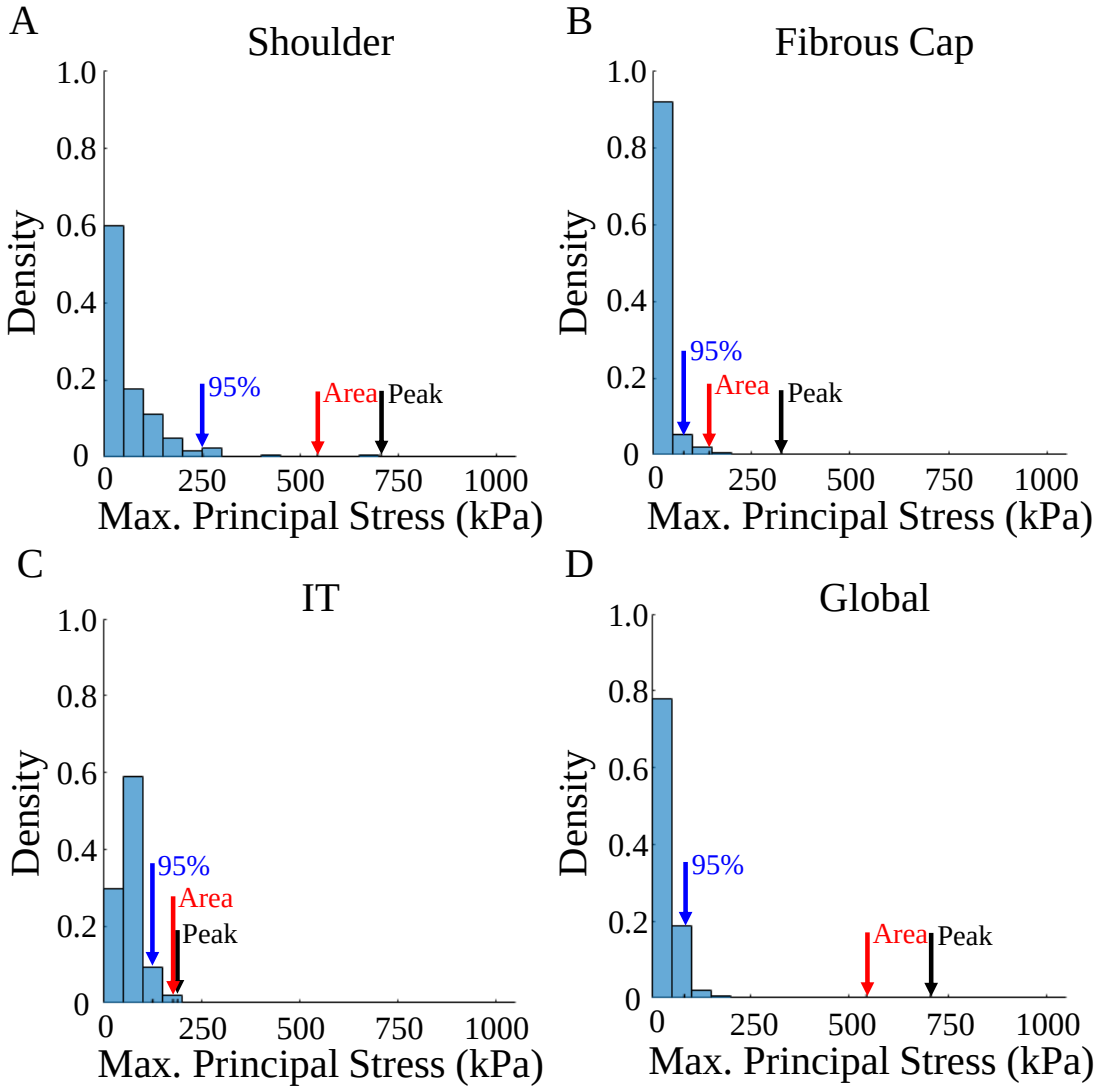

Figure A.2: Probability density plots for isotropic maximum principal stress by region: A.) Shoulder, B.) Fibrous cap, C.) IT, and D.) GEX. Labels indicate peak, area criterion, and 95% criterion stress.

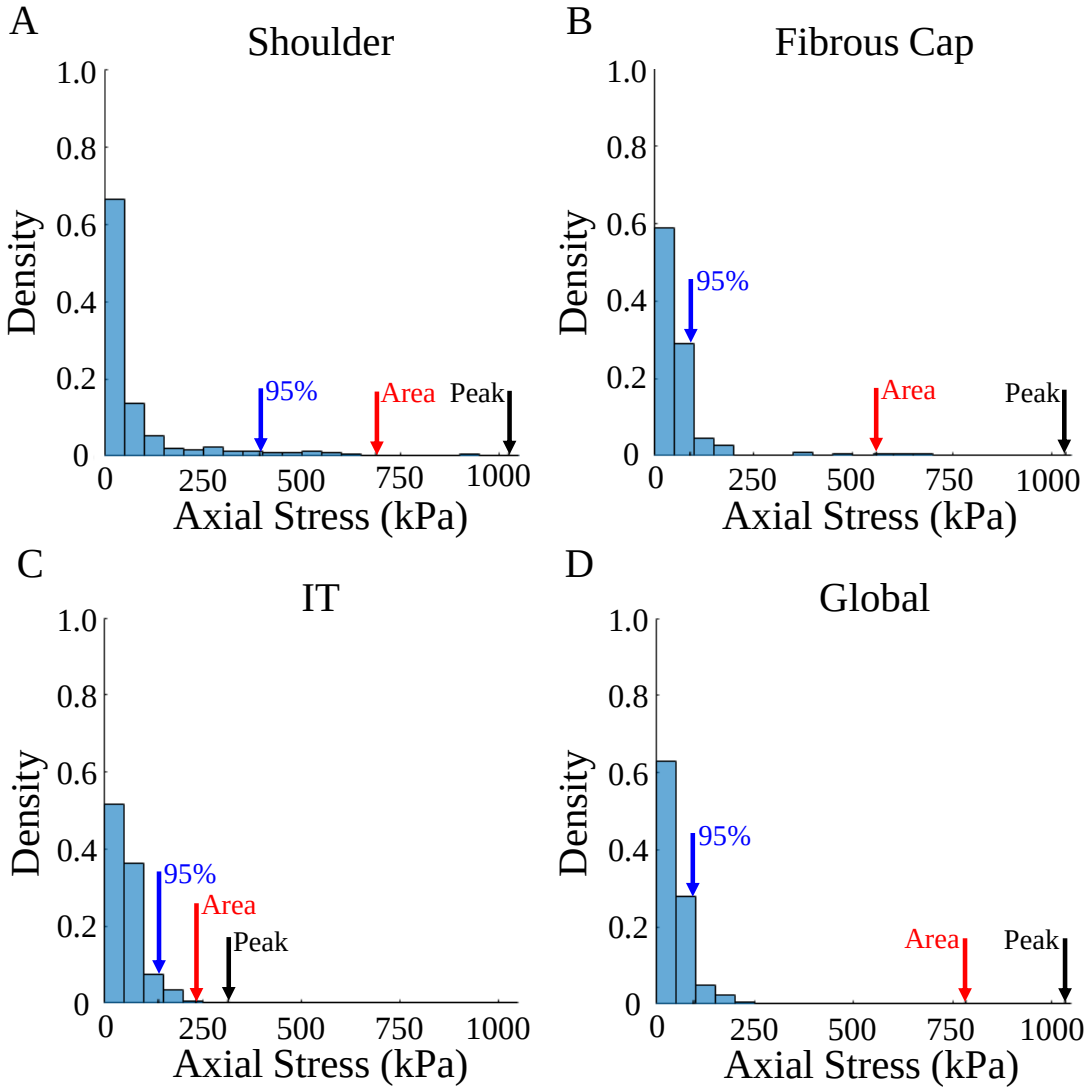

Figure A.3: Probability density plots for axial stress by region: A.) Shoulder, B.) Fibrous cap, C.) IT, and D.) GEX. Labels indicate peak, area criterion, and 95% criterion stress.

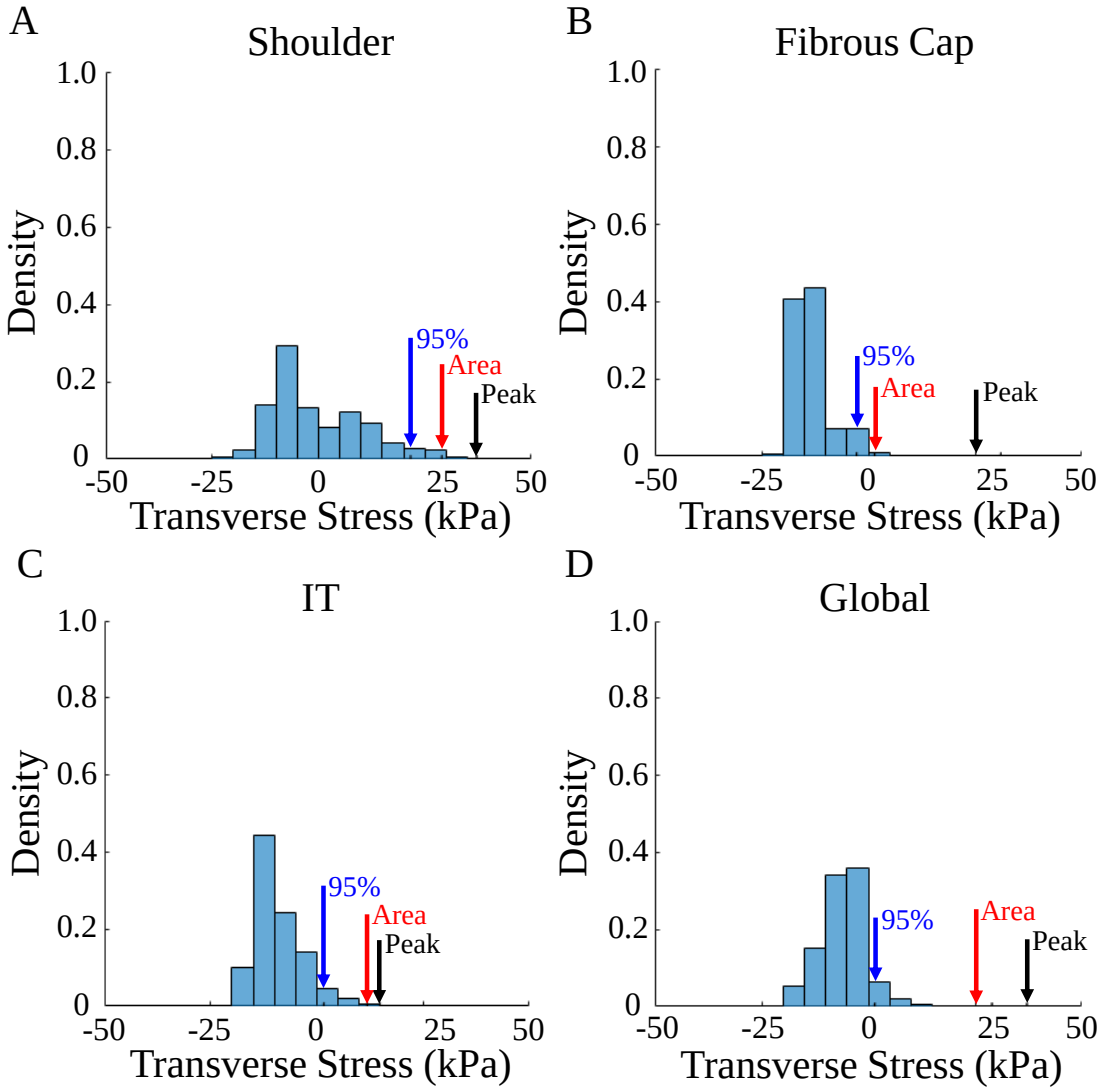

Figure A.4: Probability density plots for transverse stress by plaque region: A.) Shoulder, B.) Fibrous cap, C.) IT, and D.) GEX. Labels indicate peak, area criterion, and 95% criterion stress.

Shear Stress

Shear stresses in the representative plaque were higher than transverse stresses, but still low (see Figure A.5). Values are shown for magnitude of shear stress because the interpretation of shear direction would change with relative position in the plaque. The fibrous cap (Figure A.5B) had low shear stresses. The shoulder (Figure A.5A) had the highest shear stresses, and the IT region (Figure A.5C) had proportionally more elements with moderate (10-30 kPa) shear stresses.

Stress Transformation Angles

Probability density plots of stress transformation angles are shown by region in Figure A.6, with the median (Q2) and intra-quartile range (Q1 and Q3) labelled. Most stress transformation angles were near 0°, because axial stresses were highest. The shoulder region had a higher median stress transformation angle than the fibrous cap and IT, which had comparable median stress transformation angles.

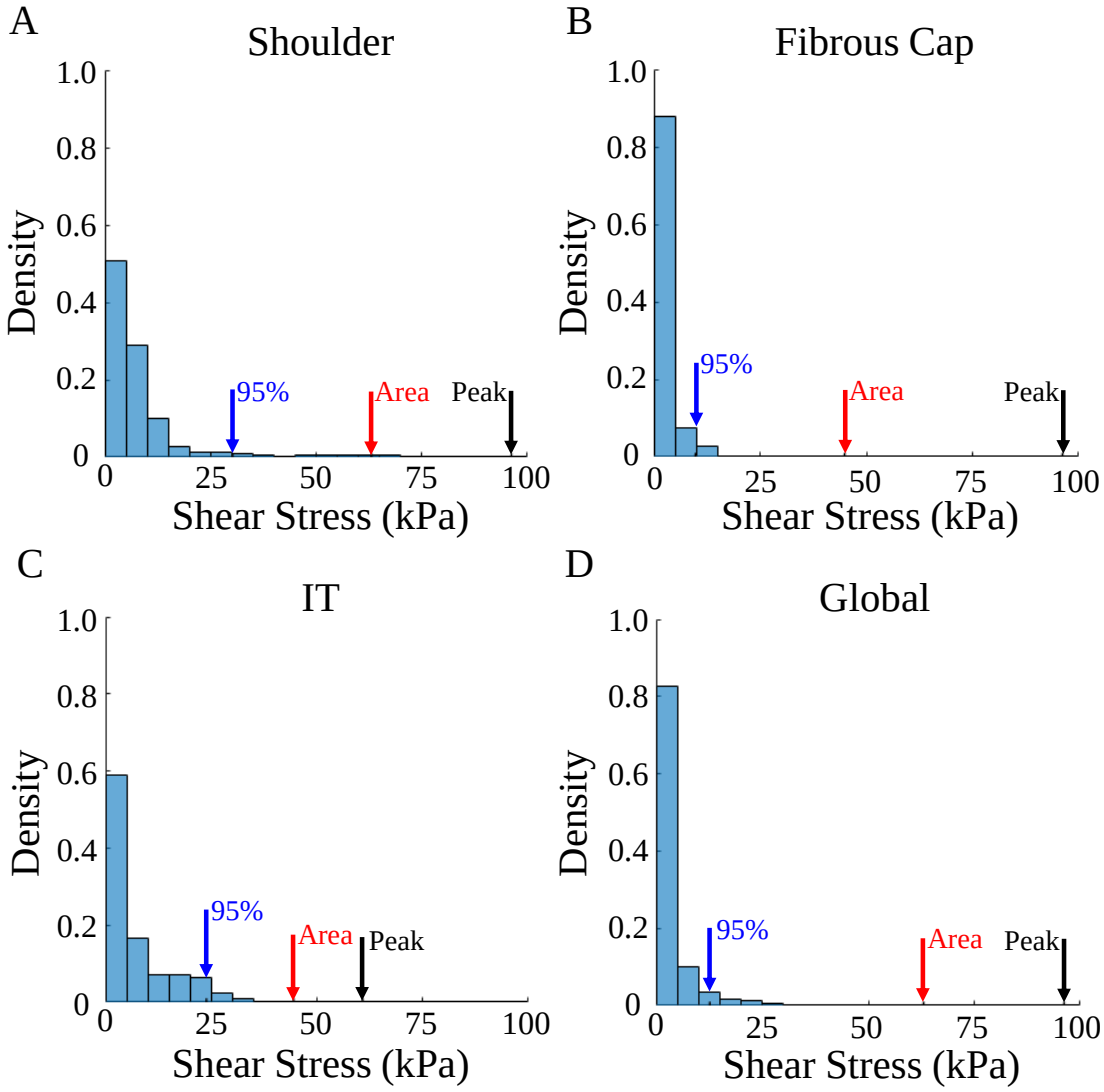

Figure A.5: Probability density plots for magnitude of shear stress, by region: A.) Shoulder, B.) Fibrous cap, C.) IT, and D.) GEX. Labels indicate peak, area criterion, and 95% criterion stress.

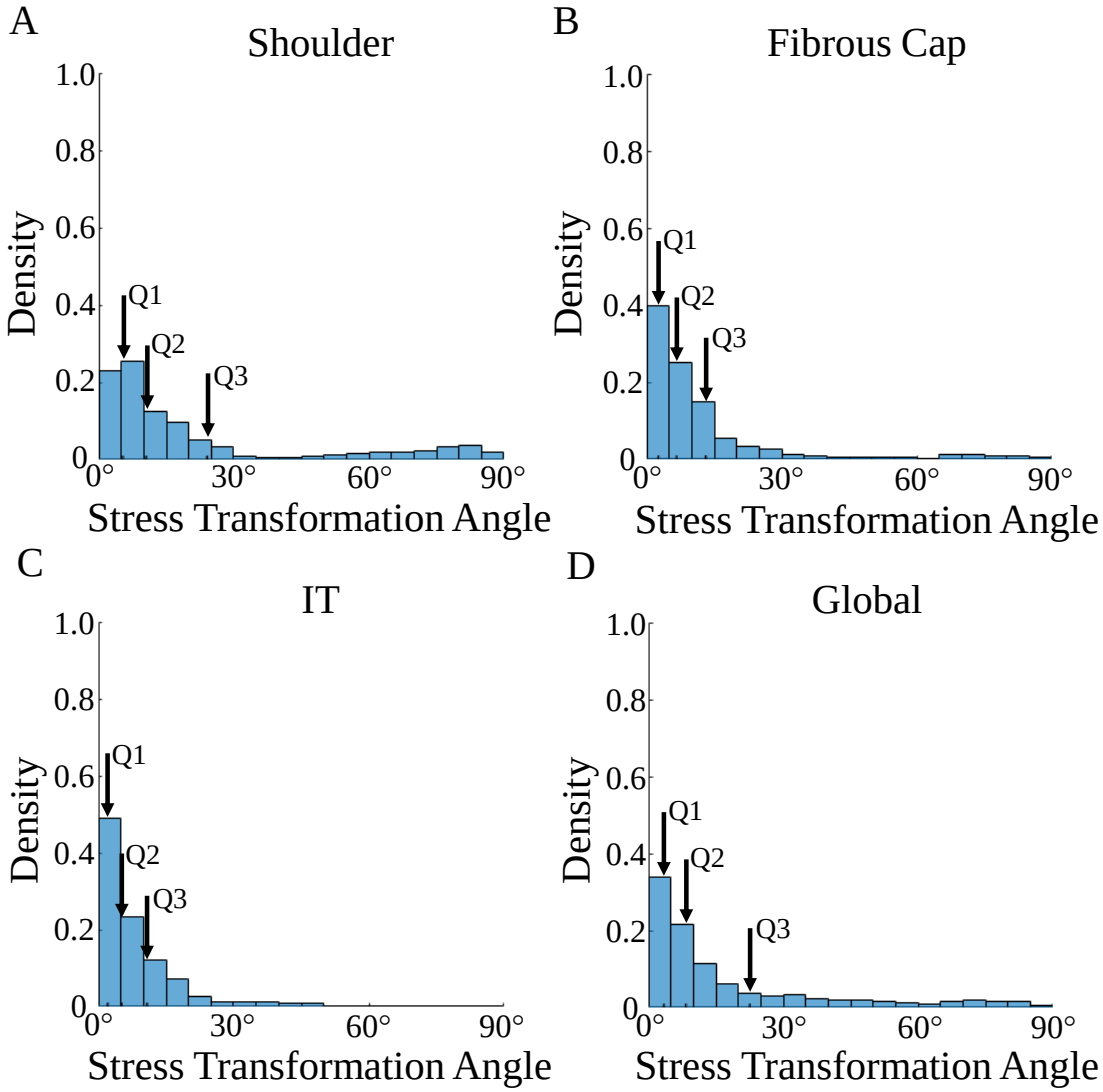

Figure A.6: Probability density plots for stress transformation angle by region: A.) Shoulder, B.) Fibrous cap, C.) IT, and D.) GEX. Labels indicate peak, area criterion, and 95% criterion stress; in degrees.

A.2.2 Orientation Sensitivity Study FE Band Plots

This section includes FE stress band plots for the orientation sensitivity study, to supplement Section 4.4.5.

FE band plots of transverse stress for the six FE models studying fibre misalignment sensitivity are shown in Figure A.7. The peak compressive and tensile transverse stresses both occur in the SH1 and are labelled. The tensile transverse stresses were small, but increased with the effective fibre misalignment. Subtle changes to transverse patterns near the SH1 can be seen (highlighted with red arrows), but transverse stresses away from the SH1 were relatively constant.

FE band plots for shear stress (magnitude) are shown in Figure A.8 for the FE models with different SH1 fibre orientations. Shear stresses near the SH1 changed with fibre rotations in SH1, particularly at the lumen near the fibrous cap and where the two bands of higher stress passed near to one another in Figure 4.5. Therefore, shear stresses may be involved with the mechanisms of loads splitting to the fibrous cap and to tissues behind the lipid core.

A.2.3 Dispersion Sensitivity Study FE Band Plots

This section includes FE stress band plots for the dispersion sensitivity study, to supplement Section 4.4.6.

FE band plots for shear stress (magnitude) for the FE models with six different κ values are shown in Figure A.9. Similar to the FE band plots for anisotropic maximum principal stress (see Figure 4.7), the largest changes to shear stresses in Figure A.9 were between the isotropic model (κ=0.333, Figure A.9A) and any of the other FE models. Most changes to shear stress with κ (indicated by red arrows) occurred in or near the shoulder regions.

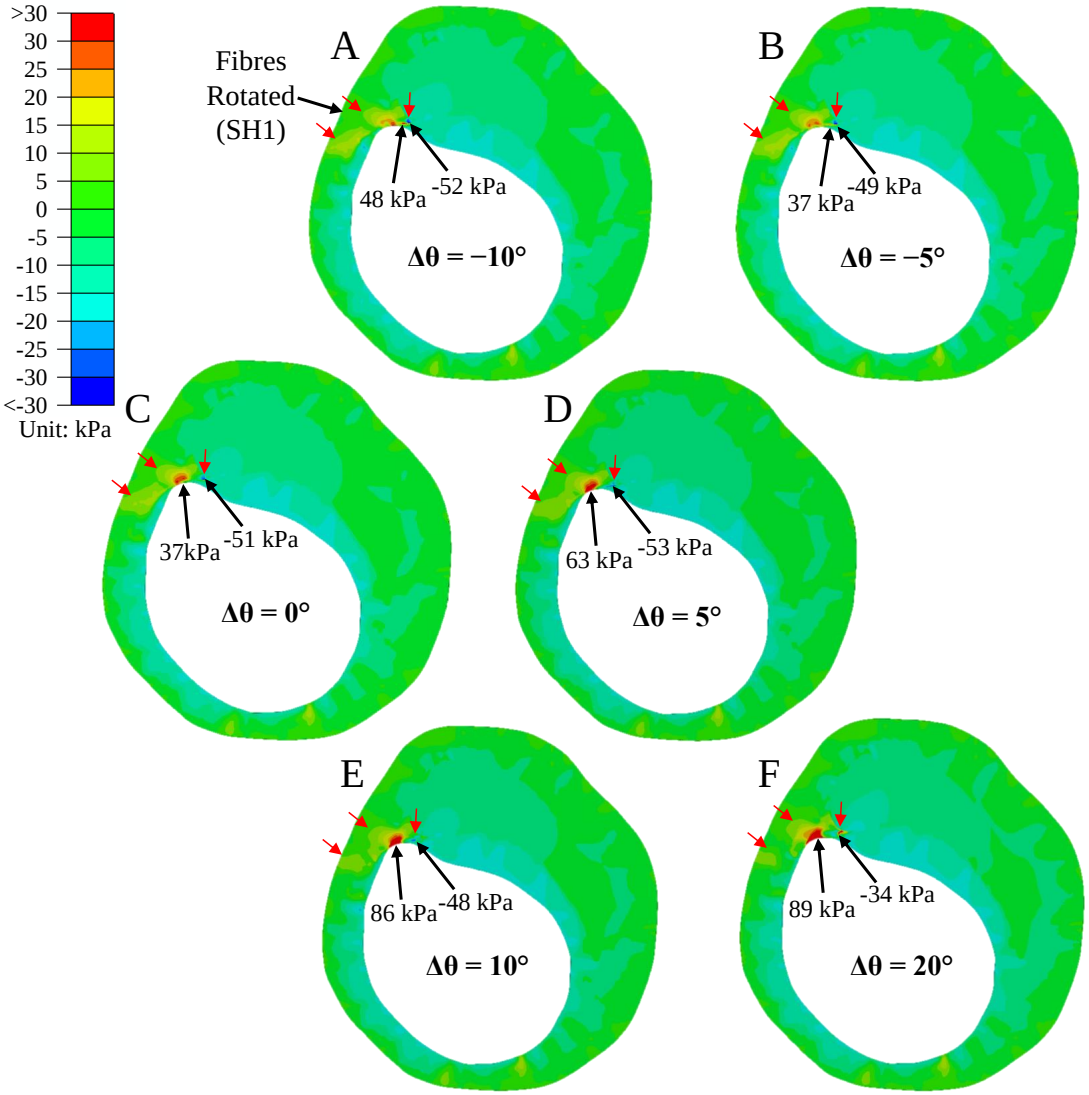

Figure A.7: Transverse stress for a study of FE sensitivity to fibre misalignment, by rotating fibres in the upper-left shoulder (SH1) counter-clockwise by: A.) -10°, B.) -5°, C.) 0° (non-rotated model), D.) +5°, E.) +10°, and F.) +20°; in kPa. Key changes to stress profiles are highlighted by red arrows, and the peak stress in SH1 is labelled.

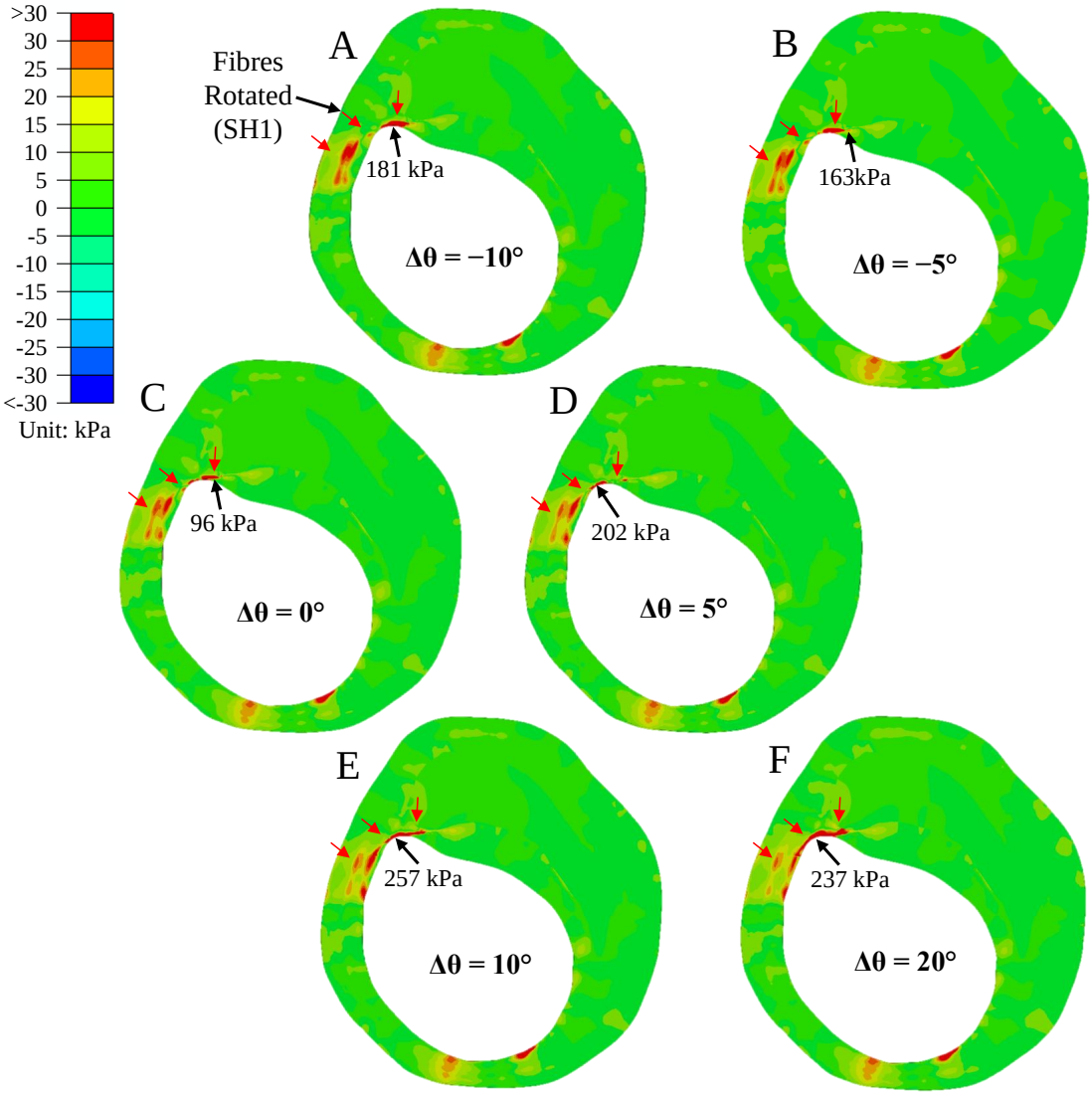

Figure A.8: Shear stress (magnitude) for a study of FE sensitivity to fibre misalignment, by rotating fibres in the left shoulder (SH1) counter-clockwise by: A.) -10°, B.) -5°, C.) 0° (non-rotated model), D.) +5°, E.) +10°, and F.) +20°; in kPa. Key changes to stress profiles highlighted by red arrows, and peak stress in SH1 is labelled.

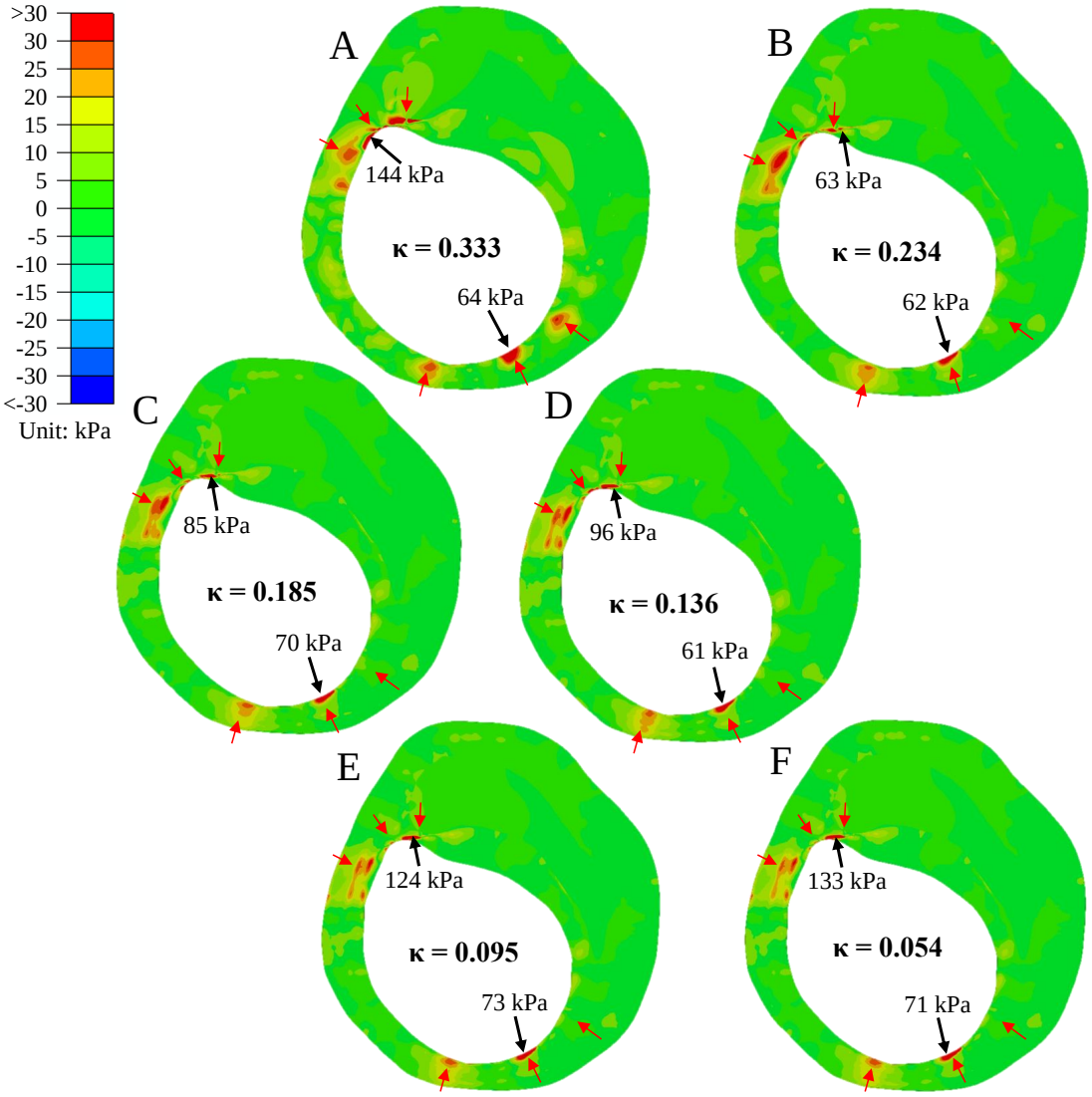

Figure A.9: Shear stress (magnitude) for a study of FE sensitivity to κ, using the following global values for κ: A.) 0.333 (isotropic), B.) 0.234, C.) 0.185, D.) 0.136 (the same as the anisotropic FE model in this chapter), E.) 0.095, and F.) 0.054; in kPa. Key changes to stress profiles are highlighted by red arrows, and the peak stresses in the SH1 and across the lumen from the SH1 are labelled.

A.3 95% Criterion Stress Results

The 95% criterion stress was calculated by region for each FE model and each reported stress type. Recall that the 95% criterion is the stress that exceeds the stress in 95% of a segmented region's area (see Section 4.3.5). This section supplements the FE results that used the area criterion in Section 4.5.

A.3.1 Summary Stress Results

For each stress type and plaque type, the median and intra-quartile ranges were calculated from the 95% criterion stress of each sample-region (see Table A.1). A two-sample t-test compared results for the carotid and coronary sets of plaques for each region and stress type, with $p<0.05$ considered significant.

A.3.2 Maximum Principal Stresses Compared

A pair-wise comparison between isotropic maximum principal stress and anisotropic maximum principal stress for the same region is shown in Figure A.10 for the coronary plaques. The p-value labelled on each region's plot is for a two-tailed, paired t-test indicating any significant difference between the isotropic maximum principal stress and anisotropic maximum principal stress for that region.

A pair-wise comparison of isotropic maximum principal stress and anisotropic maximum principal stress for the 95% criterion of stress in the same regions of carotid plaques is shown in Figure A.11.

A.3.3 Comparison of Anisotropic Stresses

Figure A.12 compares axial, transverse, and shear stress (95% criterion) from the coronary plaques by region. Figure A.13 shows the same for the carotid plaques.

Region	All Plaques	Carotid	Coronary	p
Isotropic Maximum Principal Stress (kPa)				
Fibrous Cap	62.3 [33.2, 81.6]	76.9 [46.5, 123]	44.5 [22.6, 74.5]	**0.026**
Shoulder	93.8 [57.8, 142]	67.3 [49.2, 96.7]	116 [82.2, 207]	**0.000**
IT	93.2 [71.9, 122]	87.0 [53.9, 106]	107 [83.6, 128]	0.384
Global	69.1 [60.5, 84.6]	65.2 [54.0, 91.1]	70.0 [60.8, 84.1]	0.416
GEX	85.5 [67.9, 98.9]	79.2 [65.7, 105]	86.7 [68.9, 98.8]	0.507
Anisotropic Maximum Principal Stress (kPa)				
Fibrous Cap	92.4 [42.2, 168]	134 [95.5, 204]	57.1 [0.4, 96.7]	**0.006**
Shoulder	123 [83.8, 185]	124 [83.8, 173]	120 [90.9, 217]	**0.036**
IT	130 [90.8, 154]	121 [73.6, 157]	142 [115, 153]	0.895
Global	96.8 [81.0, 118]	105 [79.4, 117]	91.3 [81.2, 118]	0.794
GEX	124 [105, 141]	127 [98.1, 141]	123 [106, 142]	0.828
Axial Stress (kPa)				
Fibrous Cap	91.0 [42.1, 168]	134 [93.5, 202]	56.3 [-0.3, 95.4]	**0.005**
Shoulder	122 [82.3, 184]	122 [81.7, 163]	119 [86.8, 210]	**0.044**
IT	127 [86.4, 149]	118[73.1, 155]	140 [111, 148]	0.866
Global	95.4 [79.5, 116]	103 [78.2, 115]	90.7 [79.5, 117]	0.802
GEX	123 [104, 139]	127 [96.2, 139]	122 [105, 140]	0.834
Transverse Stress (kPa)				
Fibrous Cap	-5.7 [-11.1, 0.6]	-2.0 [-6.8, 1.5]	-10.2 [-12.9, -3.4]	**0.018**
Shoulder	4.5 [-0.9, 8.0]	1.5 [-0.9, 5.6]	6.1 [-1.5, 11.5]	0.295
IT	1.6 [-4.9, 5.1]	-0.1 [-6.1, 5.8]	2.1 [-3.0, 4.8]	0.712
Global	1.3 [0.5, 2.5]	1.5 [0.6, 2.9]	1.2 [0.4, 1.7]	0.885
GEX	2.0 [1.3, 3.4]	2.1 [1.4, 3.3]	2.0 [1.2, 4.0]	0.713
Shear Stress (kPa)				
Fibrous Cap	11.6 [5.8, 16.6]	14.0 [11.8, 22.5]	8.9 [4.0, 12.9]	**0.023**
Shoulder	16.7 [12.3, 23.1]	16.7 [11.7, 19.5]	16.6 [12.8, 28.3]	0.101
IT	19.2 [12.9, 24.2]	15.8 [11.2, 22.5]	22.0 [18.1, 24.9]	0.080
Global	12.9 [10.2, 14.5]	13.3 [10.1, 14.3]	12.8 [10.7, 14.9]	0.316
GEX	15.4 [13.2, 17.1]	15.4 [13.1, 16.9]	15.9 [13.9, 17.1]	0.527

Table A.1: Median and intra-quartile range for 95% criterion FE stress within each combination of plaque region (rows), plaque type (columns), and stress type (grouped rows); in kPa. p-values compare carotid and coronary plaques.

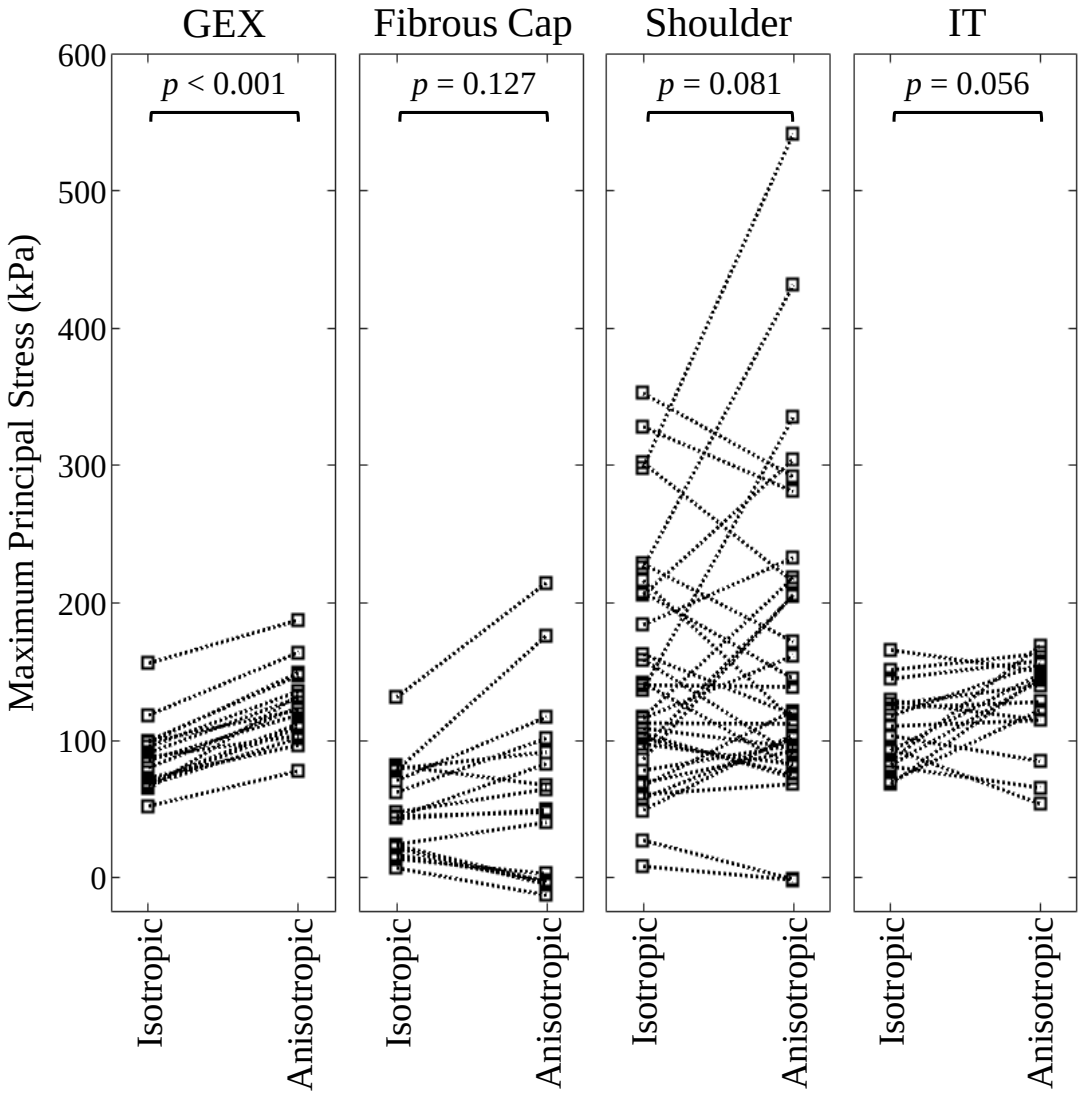

Figure A.10: For coronary plaques: pairwise comparison of maximum principal stress between the isotropic and anisotropic FE models, by plaque region using the 95% criterion.

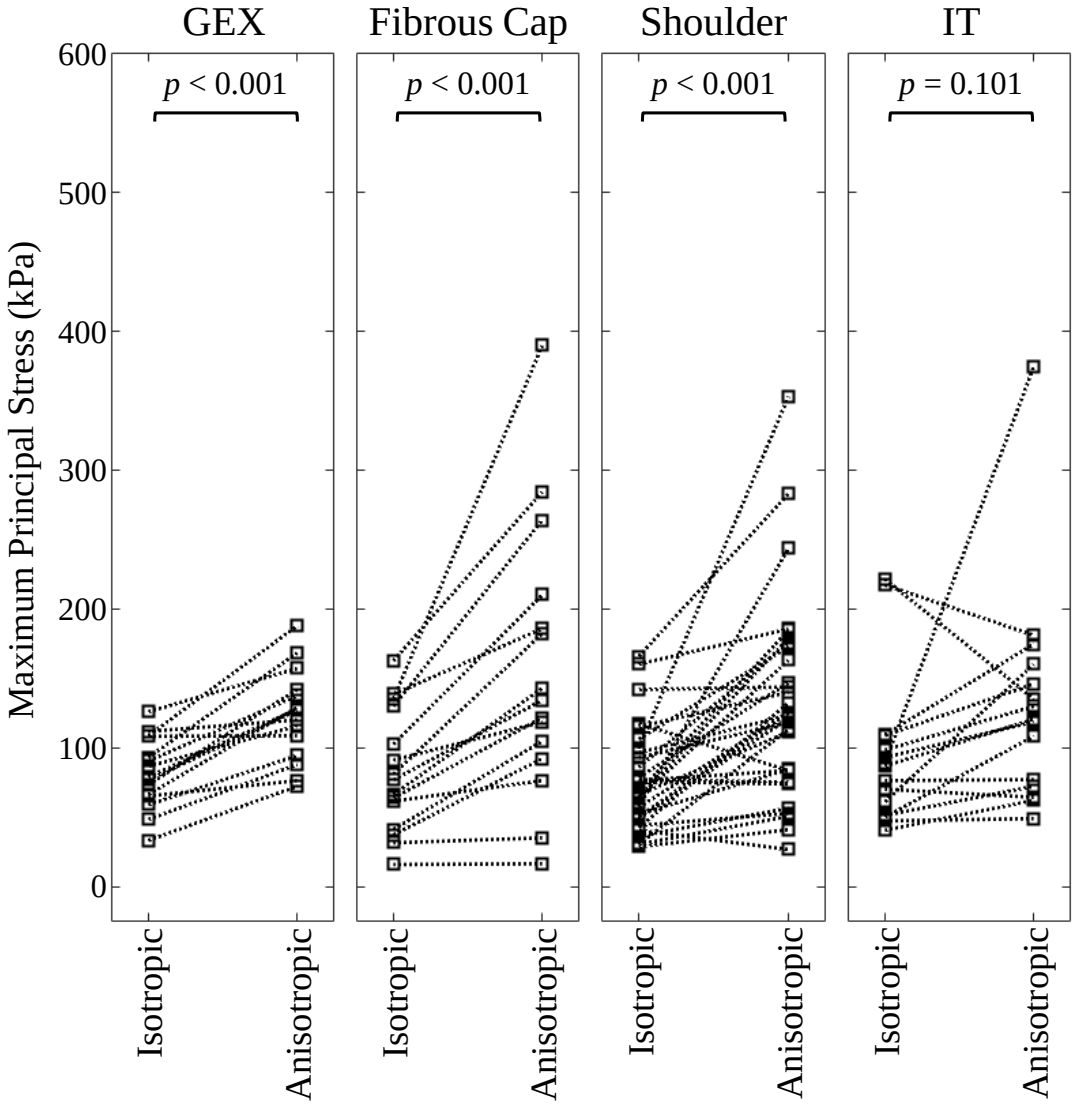

Figure A.11: For carotid plaques: pairwise comparison of maximum principal stress between the isotropic and anisotropic FE models, by plaque region using the 95% criterion.

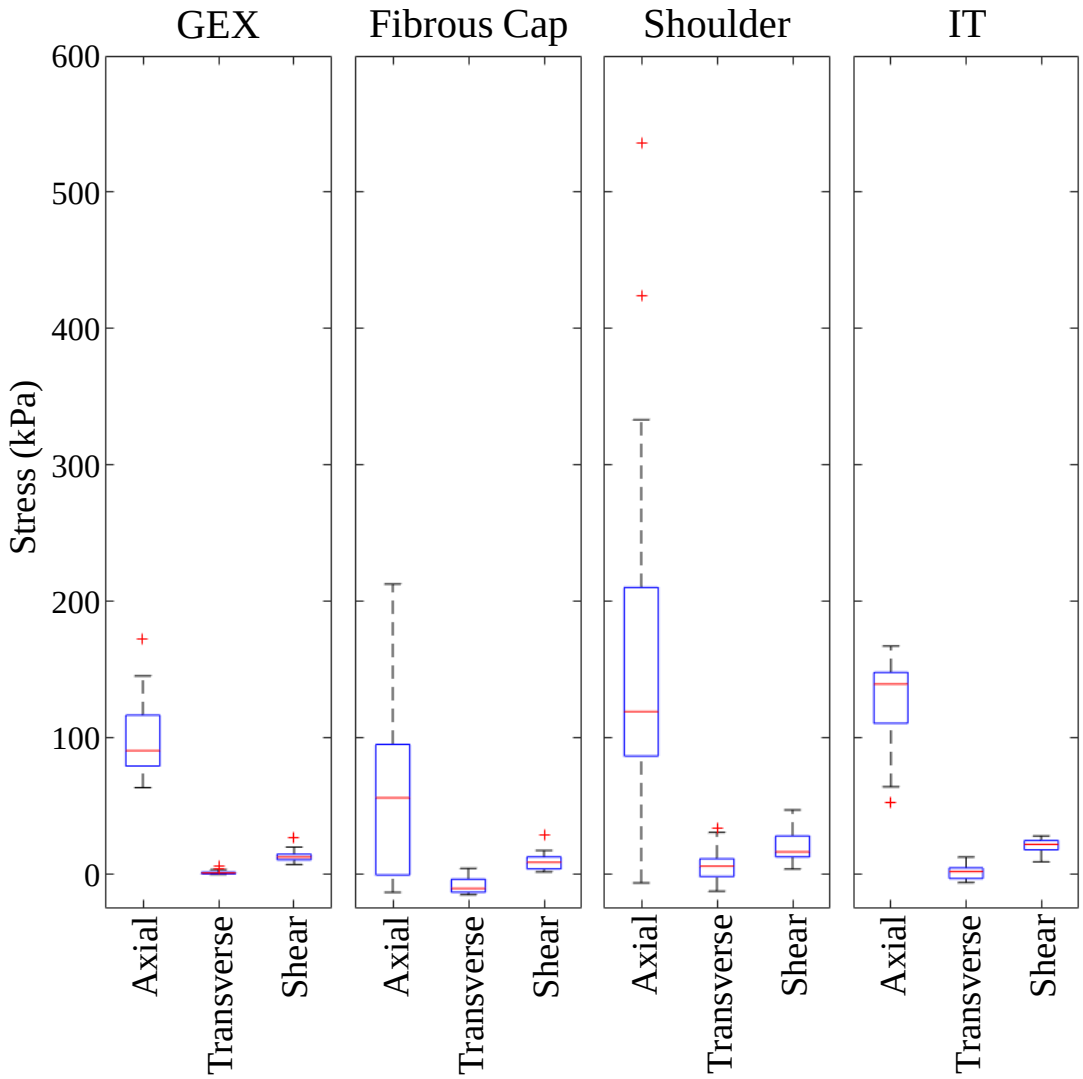

Figure A.12: For coronary plaques: box plots comparing axial, transverse, and shear stresses for each plaque region, using the 95% criterion.

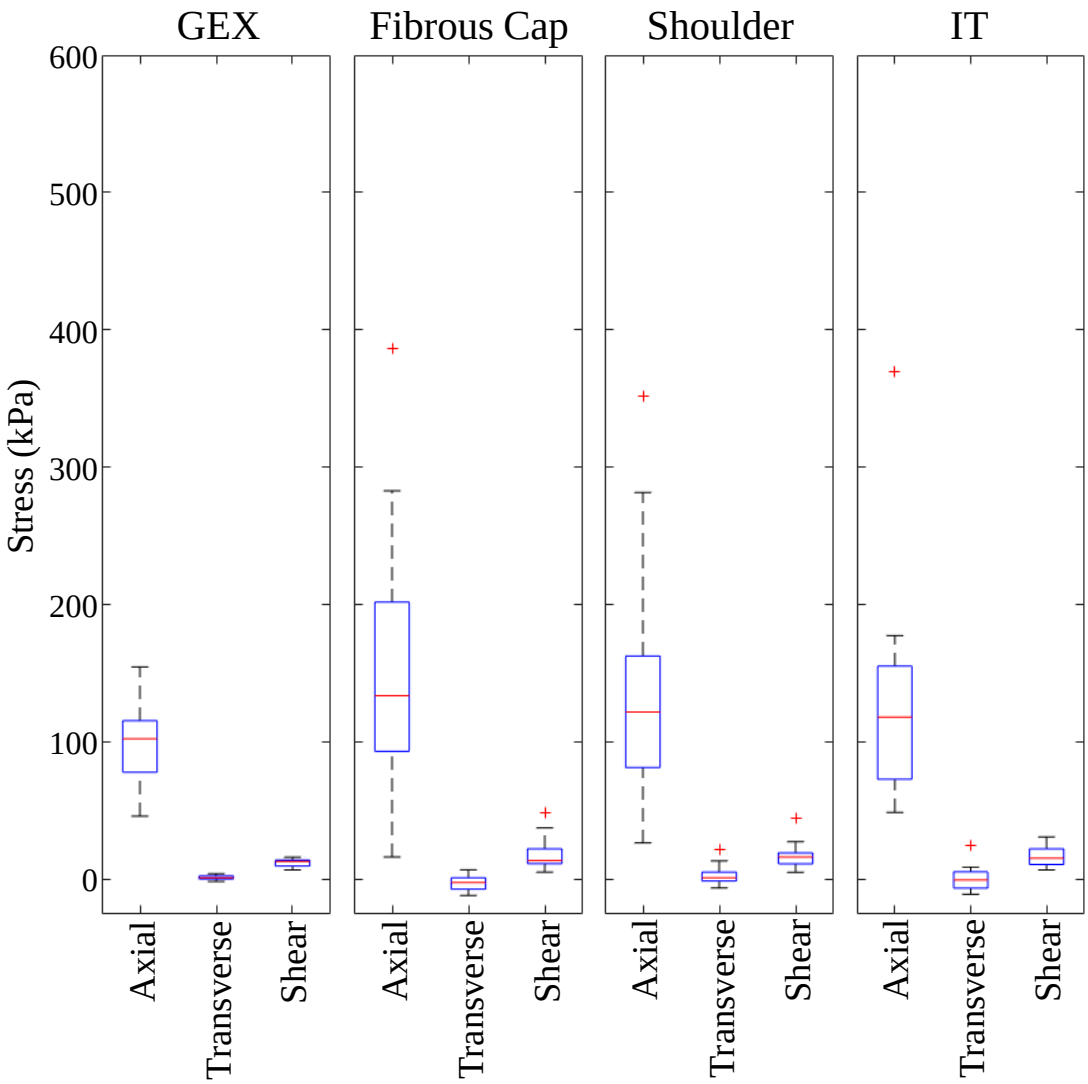

Figure A.13: For carotid plaques: box plots comparing axial, transverse, and shear stresses for each plaque region, using the 95% criterion.

A.3.4 Stresses Compared between Regions

Two-tailed, paired t-tests compared the 95% criterion of stress between different regions within a plaque, for all combinations of stress type and plaque type (see Table A.2 for p-values, and refer to Table A.1 for stress values).

Region 1	Region 2	All Plaques	Carotid	Coronary
Isotropic Maximum Principal Stress				
Fibrous Cap	Shoulder	**0.000**	0.517	**0.000**
Fibrous Cap	IT	**0.004**	0.532	**0.000**
Shoulder	IT	0.387	0.125	**0.036**
Fibrous Cap	GEX	**0.013**	0.956	**0.000**
Shoulder	GEX	**0.007**	0.454	**0.000**
IT	GEX	**0.011**	0.256	**0.008**
Anisotropic Maximum Principal Stress				
Fibrous Cap	Shoulder	**0.021**	0.256	**0.000**
Fibrous Cap	IT	0.331	0.476	**0.004**
Shoulder	IT	0.131	0.956	0.087
Fibrous Cap	GEX	0.338	0.137	**0.002**
Shoulder	GEX	0.055	0.454	0.0780
IT	GEX	0.616	0.650	0.837
Transverse Stress				
Fibrous Cap	Shoulder	**0.000**	**0.005**	**0.000**
Fibrous Cap	IT	**0.003**	0.349	**0.001**
Shoulder	IT	**0.023**	0.293	**0.039**
Fibrous Cap	GEX	**0.000**	**0.013**	**0.000**
Shoulder	GEX	0.071	0.695	0.067
IT	GEX	0.259	0.443	0.374
Shear Stress				
Fibrous Cap	Shoulder	**0.011**	0.639	**0.000**
Fibrous Cap	IT	**0.046**	0.740	**0.000**
Shoulder	IT	0.738	0.948	0.629
Fibrous Cap	GEX	0.336	0.306	**0.008**
Shoulder	GEX	**0.027**	0.257	0.061
IT	GEX	**0.008**	0.364	**0.006**

Table A.2: p-values from paired t-tests of stress between the two plaque regions specified in the left two columns, by set of plaque type (columns) and stress type (grouped rows), using the 95% stress criterion. Axial stress had similar results to anisotropic maximum principal stress, so is not shown.

A.4 Experimental Apparatus Photographs

Figure A.14 augments the description of the experimental apparatus described in Section 5.3.1.

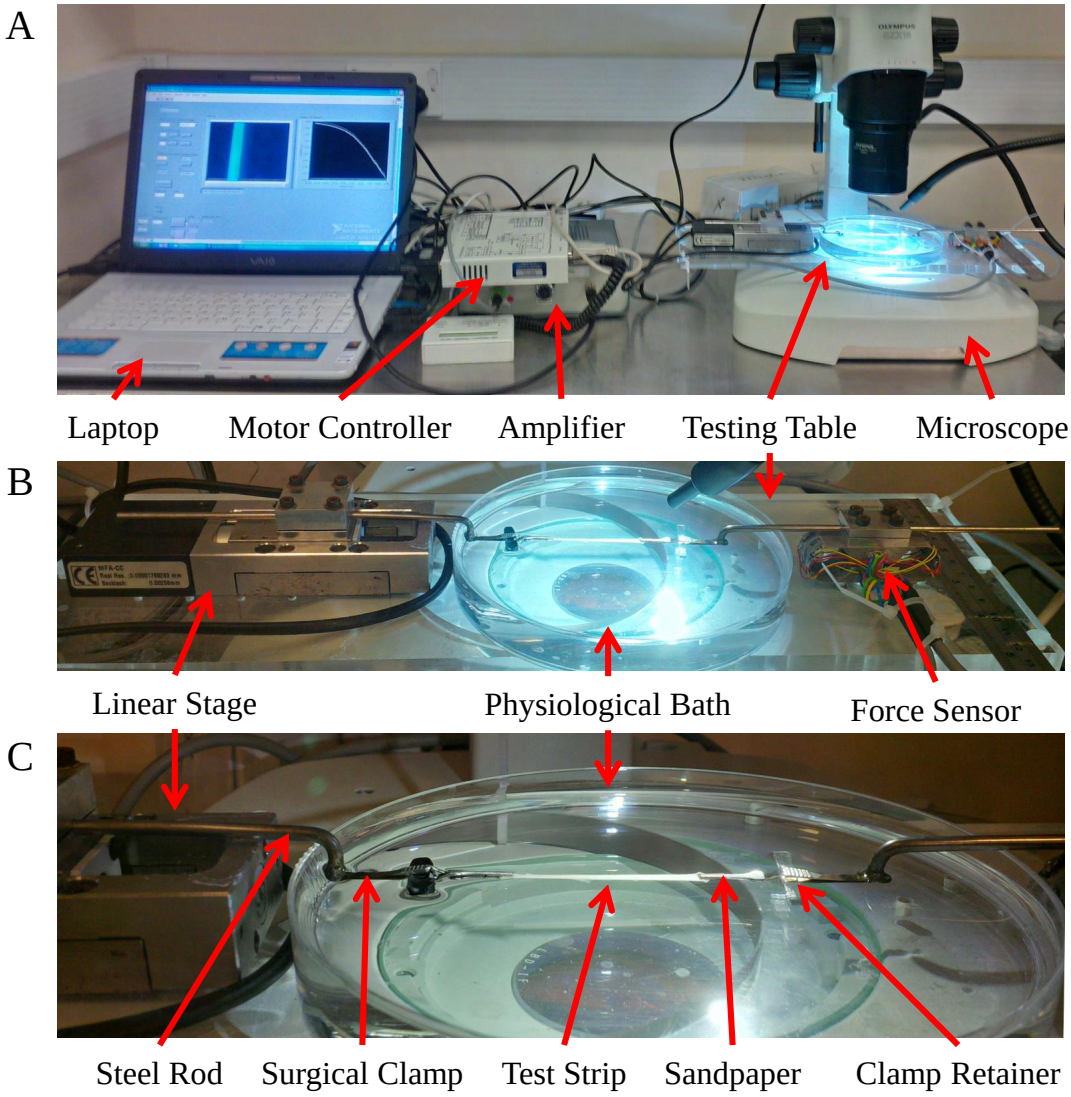

Figure A.14: Equipment used in the experiments: A.) Peripheral equipment from left to right: PC, motor controller, amplifier, material micro-testing table, and light microscope; B.) The material micro-testing table, from left to right: stepper motor and linear stage, physiological bath, and force sensor; and C.) The specimen and clamps, showing the right-angle rods, surgical clamps, clamp retainers, and sandpaper grips.

A.5 Notched Specimen Failure Stress and Stretch

This section is a supplement to the methods (Section 6.3.2) and results (Section 6.4.5) of the notched specimen tests under multiphoton microscopy.

Since only four samples of each strip direction were tested, a highly simplified model was used to give a measurement of failure for the test strips. For this, the engineering stress ($\sigma_{eng,f}$) and stretch (λ_f) at failure were calculated. The failure stress was calculated by Equation A.3:

$$\sigma_{eng,f} = \frac{F}{t_0(w_0 - w_c)} \tag{A.3}$$

where w_c was the initial length of the notch and other parameters were as defined in Equation 5.3. Failure stretch was calculated as in Equation 5.2. Thus, any influence from stress concentrations were ignored, along with changes to the cross-sectional area from incompressibility and crack propagation. Instead, the intention was to assess if the differences in fibre structures near the crack tip between the two strip types were likely to have mechanical significance. Summary geometry parameters are provided in Table A.3.

Sample Type	Width (mm)	Thickness (mm)	Length (mm)	Notch (mm)	Remaining (mm)	L:W Ratio
Circumferential	1.40	0.70	8.45	0.81	0.59	6.23
Axial	1.93	0.76	12.6	0.98	0.95	6.33
Combined	1.53	0.71	8.83	0.88	0.78	6.33

Table A.3: Geometry of the notched specimen test strips, with median results for the circumferential, axial, and combined sets of strips. Remaining width is for the uncut material adjacent to the notch.

A.5.1 Notched Specimen Failure Results

Estimated engineering stress and stretch at failure of the notched specimen test strips are shown in Table A.4.

Strip Type	Sample 1	Sample 2	Sample 3	Sample 4
Circumferential				
Stress (MPa)	5.64	1.37	2.59	3.66
Stretch	1.93	1.82	2.10	2.08
Axial				
Stress (MPa)	0.85	0.27	2.20	1.41
Stretch	1.71	1.60	2.06	1.86

Table A.4: Estimated stress and stretch at failure for notched specimen tests.

Since there were only four samples of each type, summary statistics and comparisons are not reported for these tests. Furthermore, the cracks from the initial notches progressed through the tissue with stretching, but before failure. However, cross-sectional area was not measured at different stretches, so true stress could not be calculated.

However, these results suggest the circumferential strips had a higher failure stress and stretch than the axial strips. Presumably, these differences were from the differences in crack direction relative to fibre structure. From the multiphoton images of the notch samples (see Section 6.4.5), the notch in the media of the circumferential samples was perpendicular to most of the fibres. In contrast, the notch was parallel to the dominant fibre family in the media of the axial strips. More efficient fibre bridging was seen in the circumferential strips, with bridges more directly across the crack and failing in larger groups than in the axial notched specimen strips.

A.6 Multiphoton Stack Depth Shift

Even with the stacks being rotated to align the circumferential-axial plane with the slices of the stacks, layers were found to have undulations, especially from sag before the sample began stretching. For example, the IEL in Figure A.15A was not completely planar, with the darker sections of the image having the IEL over 10 μm above or below the image plane.

To calculate fibre properties for the different layers of tissue (intima, IEL, and media), depths by column of the image stack were shifted to better separate layer types (as in Figure A.15B).

It was assumed that each column in the stack (radial direction) had a similar number of voxels containing fibres. Also, fibre density changed for different depths of the tissue, with the IEL in particular having a higher fibre density. Therefore, columns of the stack were shifted so the mid-depth of fibre density was the same for each column to make the layers of tissue more planar within the stack slices.

For shifting, the low gradient threshold from the Canny edge detector (which was 40% of the high gradient threshold) was used to select fibres. For each column, the median depth of fibres was calculated. Column median depths were referenced to the median fibre depth for the whole stack, resulting in a map of depth shifts required to make the stack planar.

A series of filters were applied to the depth shift map. First, columns having fewer than 20 fibres were ignored, as these were often at or beyond the edge of the sample. Outlier (as defined in Equation 4.7) depth shifts having very high shifts in either direction were also ignored. Thirdly, a 2D median filter with a 51×51 window was applied to the map, which also assigned shifts to the columns that had been ignored.

A filtered depth shift map is shown in Figure A.15C. The prescribed shift was usually than 5 μm, and very few were shifted by 10 μm or more. Figure A.15D shows plots of fibre orientation with depth without the depth shift (left) and with the depth shift (right). These plots are further explained in Section 6.4.2, and show the main features of the fibre distribution to be preserved and clarified by shifting column depths.

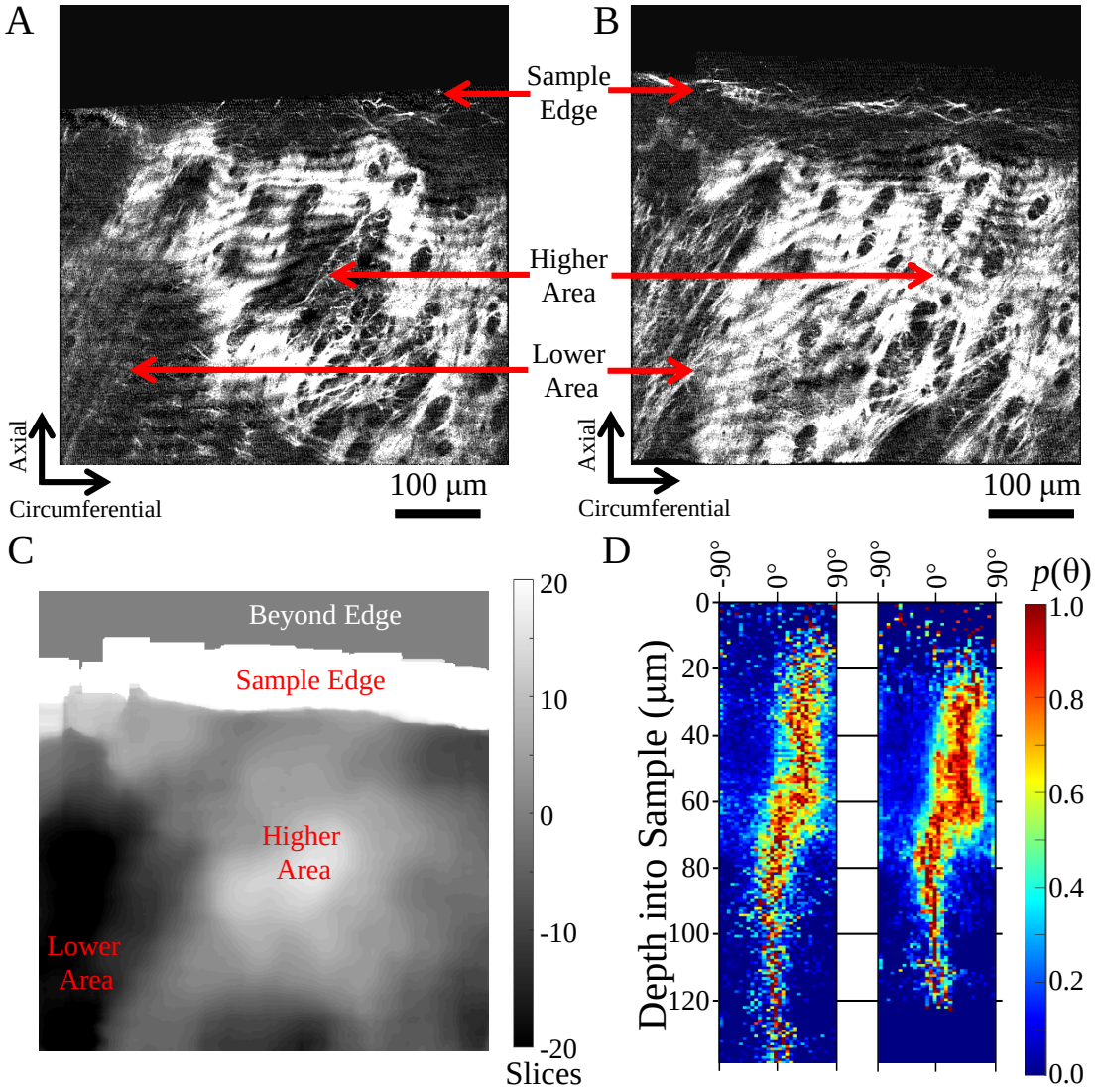

Figure A.15: A.) A multiphoton slice at the IEL layer, labelled with areas of tissue that are higher and lower than the imaging plane, B.) The same multiphoton slice with the depth shift correction applied, C.) Map of shifts, showing the local shifts from (A) to (B), and D.) Plot showing orientation density versus depth for this sample with no depth shifting (left) and with depth shifting (right).

References

Akyildiz, A. C., Speelman, L., and Gijsen, F. J. H. (2014). Mechanical properties of human atherosclerotic intima tissue. *Journal of Biomechanics*, 47(4):773–783. 1, 200

Alderman, E. L., Corley, S. D., Fisher, L. D., Chaitman, B. R., Faxon, D. P., Foster, E. D., Killip, T., Sosa, J. A., and Bourassa, M. G. (1993). Five-year angiographic follow-up of factors associated with progression of coronary artery disease in the Coronary Artery Surgery Study (CASS). *Journal of the American College of Cardiology*, 22(4):1141–1154. 50

Amiel, D., Woo, S. L., Harwood, F. L., and Akeson, W. H. (1982). The effect of immobilization on collagen turnover in connective tissue: a biochemical-biomechanical correlation. *Acta Orthopaedica Scandinavica*, 53(3):325–332. 11

Auer, M., Stollberger, R., Regitnig, P., Ebner, F., and Holzapfel, G. A. (2006). 3-D reconstruction of tissue components for atherosclerotic human arteries based on high-resolution MRI. *IEEE Transactions on Medical Imaging*, 25(3):345–357. 17

Azinfar, L., Ravanfar, M., Wang, Y., Zhang, K., Duan, D., and Yao, G. (2015). High resolution imaging of the fibrous microstructure in bovine common carotid artery using optical polarization tractography. *Journal of Biophotonics*. 17

Baldewsing, R. A., Schaar, J. A., Mastik, F., Oomens, C. W. J., and Van Der Steen, A. F. W. (2005). Assessment of vulnerable plaque composition by matching the deformation of a parametric plaque model to measured plaque deformation. *IEEE Transactions on Medical Imaging*, 24(4):514–528. 7, 17, 19

Barrett, S. R. H., Sutcliffe, M. P. F., Howarth, S., Li, Z.-Y., and Gillard, J. H. (2009). Experimental measurement of the mechanical properties of carotid atherothrombotic plaque fibrous cap. *Journal of Biomechanics*, 42(11):1650–5. 18, 19

Bennett, M., Yu, H., and Clarke, M. (2012). Signalling from dead cells drives inflammation and vessel remodelling. *Vascular Pharmacology*, 56(5-6):187–92. 8, 9

BHF (2013). British Heart Foundation: Cardiovascular disease statistics. 1

Brown, A. J., Obaid, D. R., Costopoulos, C., Parker, R. A., Calvert, P. A., Teng, Z., Hoole, S. P., West, N. E. J., Goddard, M., and Bennett, M. R. (2015). Direct comparison of virtual-histology intravascular ultrasound and optical coherence tomography imaging for identification of thin-cap fibroatheroma. *Circulation: Cardiovascular Imaging*, 8(10):e003487. 40

Cacho, F., Elbischger, P., Rodríguez, J., Doblaré, M., and Holzapfel, G. (2007). A constitutive model for fibrous tissues considering collagen fiber crimp. *International Journal of Non-Linear Mechanics*, 42(2):391–402. 14

Calvert, P. A., Obaid, D. R., O'Sullivan, M., Shapiro, L. M., McNab, D., Densem, C. G., Schofield, P. M., Braganza, D., Clarke, S. C., Ray, K. K., West, N. E. J., and Bennett, M. R. (2011). Association between IVUS findings and adverse outcomes in patients with coronary artery disease: the VIVA (VH-IVUS in Vulnerable Atherosclerosis) Study. *JACC. Cardiovascular Imaging*, 4(8):894–901. 7, 46, 48, 50

Canny, J. F. (1983). *Finding Edges and Lines in Images.* Masters thesis, Massachusetts Institute of Technology. 56

Chai, C.-K., Akyildiz, A. C., Speelman, L., Gijsen, F., Oomens, C., van Sambeek, M., van der Lugt, A., and Baaijens, F. P. T. (2014). Local anisotropic mechanical properties of human carotid atherosclerotic plaques. *Journal of the Mechanical Behavior of Biomedical Materials*, 43:59–68. 91, 146

Chen, H. and Kassab, G. S. (2016). Microstructure-based biomechanics of coronary arteries in health and disease. *Journal of Biomechanics*, 49(12):2548–2559. 15

Chen, H., Liu, Y., Zhao, X., Lanir, Y., and Kassab, G. S. (2011). A micromechanics finite-strain constitutive model of fibrous tissue. *Journal of the Mechanics and Physics of Solids*, 59(9):1823–1837. 15

Cheng, G. C., Loree, H. M., Kamm, R. D., Fishbein, M. C., and Lee, R. T. (1993). Distribution of circumferential stress in ruptured and stable atherosclerotic lesions. A structural analysis with histopathological correlation. *Circulation*, 87(4):1179–1187. 16, 46, 48, 91

Chow, M. J., Turcotte, R., Lin, C. P., and Zhang, Y. (2014). Arterial extracellular matrix: A mechanobiological study of the contributions and interactions of elastin and collagen. *Biophysical Journal*, 106(12):2684–2692. 13, 205

Chu, B., Gaillard, E., Mongrain, R., Reiter, S., and Tardif, J.-C. (2013). Characterization of fracture toughness exhaustion in pig aorta. *Journal of the Mechanical Behavior of Biomedical Materials*, 17:126–36. 22, 155

Clark, J. M. and Glagov, S. (1985). Transmural organization of the arterial media. The lamellar unit revisited. *Arteriosclerosis, Thrombosis, and Vascular Biology*, 5(1):19–34. 11, 37, 65, 160, 185, 191

Cleveland, W. S. (1979). Robust locally weighted regression and smoothing scatterplots. *Journal of the American Statistical Association*, 74(368):829–836. 45

Comley, K. and Fleck, N. A. (2010). The toughness of adipose tissue: measurements and physical basis. *Journal of Biomechanics*, 43(9):1823–6. 22, 167

Creane, A., Maher, E., Sultan, S., Hynes, N., Kelly, D. J., and Lally, C. (2011). Prediction of fibre architecture and adaptation in diseased carotid bifurcations. *Biomechanics and Modeling in Mechanobiology*, 10(6):831–843. 38, 91, 114, 162

Cunnane, E., Barrett, H., Kavanagh, E., Mongrain, R., and Walsh, M. (2016). The influence of composition and location on the toughness of human atherosclerotic femoral plaque tissue. *Acta Biomaterialia*, 31:264–275. 21

Daemen, M. J., Ferguson, M. S., Gijsen, F. J., Hippe, D. S., Kooi, M. E., Demarco, K., van der Wal, A. C., Yuan, C., and Hatsukami, T. S. (2016). Carotid plaque fissure: an underestimated source of intraplaque hemorrhage. *Atherosclerosis*, 254(October):102–108. 29, 87, 90, 102, 114, 147, 148, 152, 238

Davies, J. R., Izquierdo-Garcia, D., Rudd, J. H. F., Figg, N., Richards, H. K., Bird, J. L. E., Aigbirhio, F. I., Davenport, A. P., Weissberg, P. L., Fryer, T. D., and Warburton, E. a. (2010). FDG-PET can distinguish inflamed from non-inflamed plaque in an animal model of atherosclerosis. *The International Journal of Cardiovascular Imaging*, 26(1):41–8. 7, 8

Davis, L. A., Stewart, S. E., Carsten, C. G., Snyder, B. A., Sutton, M. A., and Lessner, S. M. (2016). Characterization of fracture behavior of human atherosclerotic fibrous caps using a miniature single edge notched tensile test. *Acta Biomaterialia*, 43:101–111. 21

de Boer, J. F., Milner, T. E., van Gemert, M. J., and Nelson, J. S. (1997). Two-dimensional birefringence imaging in biological tissue by polarization-sensitive optical coherence tomography. *Optics Letters*, 22(12):934–6. 8, 13, 17

de Korte, C. L., Pasterkamp, G., van der Steen, A. F. W., Woutman, H. A., and Bom, N. (2000). Characterization of plaque components with intravascular ultrasound elastography in human femoral and coronary arteries in vitro. *Circulation*, 102(6):617–623. 7, 17, 19

deBotton, G. and Oren, T. (2013). Analytical and numerical analyses of the micromechanics of soft fibrous connective tissues. *Biomechanics and Modeling in Mechanobiology*, 12(1):151–66. 15

deBotton, G. and Shmuel, G. (2009). Mechanics of composites with two families of finitely extensible fibers undergoing large deformations. *Journal of the Mechanics and Physics of Solids*, 57(8):1165–1181. 15

Deguchi, J.-O., Aikawa, E., Libby, P., Vachon, J. R., Inada, M., Krane, S. M., Whittaker, P., and Aikawa, M. (2005). Matrix metalloproteinase-13/collagenase-3 deletion promotes collagen accumulation and organization in mouse atherosclerotic plaques. *Circulation*, 112(17):2708–15. 8

Depre, C. (1996). Neovascularization in human coronary atherosclerotic lesions. *Catheterization and Cardiovascular Diagnosis*, 39:215–220. 6

ECSTGC Authors (1991). MRC European Carotid Surgery Trial : interim results for symptomatic patients with severe (70-99%) or with mild (0-29%) carotid stenosis. *The Lancet*, 337(8752):1235–1242. 2, 7

Falk, E. (1991). Coronary thrombosis: pathogenesis and clinical manifestations. *The American Journal of Cardiology*, 68(7):28B–35B. 1

Falk, E., Nakano, M., Bentzon, J. F., Finn, A. V., and Virmani, R. (2013). Update on acute coronary syndromes: the pathologists' view. *European Heart Journal*, 34(10). 5, 29, 34, 134, 148, 238

Falk, E., Shah, P. K., and Fuster, V. (1995). Coronary plaque disruption. *Circulation*, 92(3):657–671. 1, 2, 5, 7, 51, 52, 144, 243

Ferguson, G. G., Eliasziw, M., Barr, H. W. K., Clagett, G. P., Barnes, R. W., Wallace, M. C., Taylor, D. W., Haynes, R. B., Finan, J. W., Hachinski, V. C., and Barnett, H. J. M. (1999). The North American Symptomatic Carotid Endarterectomy Trial: surgical results in 1415 patients. *Stroke*, 30(9):1751–1758. 2, 7

Finlay, H. M., Whittaker, P., and Canham, P. B. (1998). Collagen organization in the branching region of human brain arteries. *Stroke*, 29(8). 12

Flamini, V., Kerskens, C., Simms, C., and Lally, C. (2013). Fibre orientation of fresh and frozen porcine aorta determined non-invasively using diffusion tensor imaging. *Medical Engineering and Physics*, 35(6):765–776. 13, 17, 88

Gasser, T. C. and Holzapfel, G. A. (2007). Modeling plaque fissuring and dissection during balloon angioplasty intervention. *Annals of Biomedical Engineering*, 35(5):711–23. 16, 91, 146

Gasser, T. C., Ogden, R. W., and Holzapfel, G. A. (2006). Hyperelastic modelling of arterial layers with distributed collagen fibre orientations. *Journal of the Royal Society Interface*, 3(6):15–35. 9, 14, 15, 23, 38, 66, 67, 69, 92, 96, 97, 160, 173

Gijsen, F. J. H. and Migliavacca, F. (2014). Plaque mechanics. *Journal of Biomechanics*, 47(4):763–764. 2

Gilpin, C. M. (2005). *Cyclic Loading of Porcine Coronary Arteries*. Masters thesis, Georgia Institute of Technology. 22

Halvorsen, B., Otterdal, K., Dahl, T. B., Skjelland, M., Gullestad, L., Øie, E., and Aukrust, P. l. (2008). Atherosclerotic plaque stability–what determines the fate of a plaque? *Progress in Cardiovascular Diseases*, 51(3):183–94. 1, 4, 5, 8, 144, 243

Hansen, H. H. G., Saris, A. E. C. M., Vaka, N. R., Nillesen, M. M., and de Korte, C. L. (2014). Ultrafast vascular strain compounding using plane wave transmission. *Journal of Biomechanics*, 47(4):815–823. 19

Haralick, R. M. and Shapiro, L. G. (1992). *Computer and Robot Vision, Vol. I, 1992*. Addison-Wesley Publishing Company, Inc. 58

Heiland, V. M., Forsell, C., Roy, J., Hedin, U., and Gasser, T. C. (2013). Identification of carotid plaque tissue properties using an experimental-numerical approach. *Journal of the Mechanical Behavior of Biomedical Materials*, 27:226–238. 96

Hobson, R. and Weiss, D. (1993). Efficacy of carotid endarterectomy for asymptomatic carotid stenosis. *New England Journal of Medicine*, 328(4):221–227. 7

Hodgkin, B. C., Burkett, D. E., and Smith, E. B. (1982). Noninvasive measurement of systolic and diastolic blood pressure in swine. *American Journal of Physiology - Heart and Circulatory Physiology*, 242(1). 170

Holzapfel, G. A. (2006). Determination of material models for arterial walls from uniaxial extension tests and histological structure. *Journal of Theoretical Biology*, 238(2):290–302. 20

Holzapfel, G. A. (2008). Collagen in arterial walls: biomechanical aspects. In Fratzl, P., editor, *Collagen: Structure and Mechanics*, chapter 11, pages 285–324. Springer Science+Business Media. xii, 10, 14

Holzapfel, G. A., Mulvihill, J. J., Cunnane, E. M., and Walsh, M. T. (2014). Computational approaches for analyzing the mechanics of atherosclerotic plaques: a review. *Journal of Biomechanics*, 47(4):859–869. 2, 7, 14, 16, 17, 18, 19, 20, 91, 99, 102, 144, 145, 146

Holzapfel, G. A., Niestrawska, J. A., Ogden, R. W., Reinisch, A. J., and Schriefl, A. J. (2015). Modelling non-symmetric collagen fibre dispersion in arterial walls. *Journal of The Royal Society Interface*, 12(106). 200

Holzapfel, G. A. and Ogden, R. W. (2010). Constitutive modelling of arteries. *Proceedings of the Royal Society A: Mathematical, Physical and Engineering Sciences*, 466(2118):1551–1597. 13, 14

Holzapfel, G. A., Sommer, G., and Regitnig, P. (2004). Anisotropic mechanical properties of tissue components in human atherosclerotic plaques. *Journal of Biomechanical Engineering*, 126(5):657. 18, 19, 20

Huang, Y. (2012). *Material Fatigue as a Possible Mechanism of Atherosclerotic Plaque Rupture*. Doctoral dissertation, University of Cambridge. 15

Karimi, R., Zhu, T., Bouma, B. E., and Mofrad, M. R. K. (2008). Estimation of nonlinear mechanical properties of vascular tissues via elastography. *Cardiovascular Engineering*, 8(4):191–202. 8, 17, 19

Kiousis, D. E., Rubinigg, S. F., Auer, M., and Holzapfel, G. A. (2009). A methodology to analyze changes in lipid core and calcification onto fibrous cap vulnerability: the human atherosclerotic carotid bifurcation as an illustratory example. *Journal of Biomechanical Engineering*, 131(12):121002. 17, 91, 146

Koh, C. T. (2013). *Fracture of Fibrous Tissue Membranes and Biomimetic Scaffolds*. Doctoral thesis, University of Cambridge. 22

Koh, C. T., Strange, D. G. T., Tonsomboon, K., and Oyen, M. L. (2013). Failure mechanisms in fibrous scaffolds. *Acta Biomaterialia*, 9(7):7326–34. 16, 22

Kolodgie, F. D., Gold, H. K., Burke, A. P., Fowler, D. R., Kruth, H. S., Weber, D. K., Farb, A., Guerrero, L. J., Hayase, M., Kutys, R., Narula, J., Finn, A. V.,

and Virmani, R. (2003). Intraplaque hemorrhage and progression of coronary atheroma. *The New England Journal of Medicine*, 349(24):2316–25. 6

Kroon, M. and Holzapfel, G. A. (2008). A new constitutive model for multi-layered collagenous tissues. *Journal of biomechanics*, 41(12):2766–71. 14

Kural, M. H., Cai, M., Tang, D., Gwyther, T., Zheng, J., and Billiar, K. L. (2012). Planar biaxial characterization of diseased human coronary and carotid arteries for computational modeling. *Journal of Biomechanics*, 45(5):790–798. 19

Lanir, Y. (1983). Constitutive equations for fibrous connective tissues. *Journal of Biomechanics*, 16(1):1–12. 15

Lendon, C. L., Davies, M. J., Born, G. V., and Richardson, P. D. (1991). Atherosclerotic plaque caps are locally weakened when macrophages density is increased. *Atherosclerosis*, 87(1):87–90. 20

Li, Z.-Y., Tang, T., U-King-Im, J., Graves, M., Sutcliffe, M., and Gillard, J. H. (2008). Assessment of carotid plaque vulnerability using structural and geometrical determinants. *Circulation Journal: Official Journal of the Japanese Circulation Society*, 72(7):1092–9. 17, 85, 91

Libby, P. (2013). Collagenases and cracks in the plaque. *Journal of Clinical Investigation*, 123(8):3201–3203. 8

Linkert, M., Rueden, C. T., Allan, C., Burel, J.-M., Moore, W., Patterson, A., Loranger, B., Moore, J., Neves, C., Macdonald, D., Tarkowska, A., Sticco, C., Hill, E., Rossner, M., Eliceiri, K. W., and Swedlow, J. R. (2010). Metadata matters: access to image data in the real world. *The Journal of Cell Biology*, 189(5):777–82. 211

Loree, H. M., Grodzinsky, A. J., Park, S. Y., Gibson, L. J., and Lee, R. T. (1994). Static circumferential tangential modulus of human atherosclerotic tissue. *Journal of Biomechanics*, 27(2):195–204. 18, 19

Loree, H. M., Kamm, R. D., Stringfellow, R. G., and Lee, R. T. (1992). Effects of fibrous cap thickness on peak circumferential stress in model atherosclerotic vessels. *Circulation Research*, 71(4):850–858. 46, 48

Maceri, F., Marino, M., and Vairo, G. (2010). A unified multiscale mechanical model for soft collagenous tissues with regular fiber arrangement. *Journal of Biomechanics*, 43(2):355–63. 15

Maher, E., Creane, A., Sultan, S., Hynes, N., Lally, C., and Kelly, D. J. (2009). Tensile and compressive properties of fresh human carotid atherosclerotic plaques. *Journal of Biomechanics*, 42(16):2760–7. 18

Martufi, G. and Gasser, T. C. (2012). Turnover of fibrillar collagen in soft biological tissue with application to the expansion of abdominal aortic aneurysms. *Journal of the Royal Society Interface*, 9(77):3366–77. 11

McCarthy, M. J., Loftus, I. M., Thompson, M. M., Jones, L., London, N. J. M., Bell, P. R. F., Naylor, A. R., and Brindle, N. P. J. (1999). Angiogenesis and the atherosclerotic carotid plaque: an association between symptomatology and plaque morphology. *Journal of Vascular Surgery*, 30(2):261–268. 6

McCord, B. (1992). *Fatigue of Atherosclerotic Plaque*. Doctoral thesis, Georgia Institute of Technology. 22, 23

Meijering, E. H., Niessen, W. J., and Viergever, M. A. (2001). Quantitative evaluation of convolution-based methods for medical image interpolation. *Medical Image Analysis*, 5(2):111–126. 211

Moreno, P. R., Purushothaman, K.-R., Sirol, M., Levy, A. P., and Fuster, V. (2006). Neovascularization in human atherosclerosis. *Circulation*, 113(18):2245–52. 6

Mulvihill, J. J., Cunnane, E. M., McHugh, S. M., Kavanagh, E. G., Walsh, S. R., and Walsh, M. T. (2013). Mechanical, biological and structural characterization of in vitro ruptured human carotid plaque tissue. *Acta Biomaterialia*, 9(11):9027–35. 20

Nadkarni, S. K., Pierce, M. C., Park, B. H., de Boer, J. F., Whittaker, P., Bouma, B. E., Bressner, J. E., Halpern, E., Houser, S. L., and Tearney, G. J. (2007). Measurement of collagen and smooth muscle cell content in atherosclerotic

plaques using polarization-sensitive optical coherence tomography. *Journal of the American College of Cardiology*, 49(13):1474–1481. 88

Nederveen, A. J., Avril, S., and Speelman, L. (2014). MRI strain imaging of the carotid artery: present limitations and future challenges. *Journal of Biomechanics*, 47(4):824–833. 19

NHS (2013). NHS Choices Atlas of Risk. 1

Pagiatakis, C., Galaz, R., Tardif, J. C., and Mongrain, R. (2015). A comparison between the principal stress direction and collagen fiber orientation in coronary atherosclerotic plaque fibrous caps. *Medical and Biological Engineering and Computing*, 53(6):545–555. 12, 91, 98

Pierce, D. M., Trobin, W., Raya, J. G., Trattnig, S., Bischof, H., Glaser, C., and Holzapfel, G. A. (2010). DT-MRI based computation of collagen fiber deformation in human articular cartilage: a feasibility study. *Annals of Biomedical Engineering*, 38(7):2447–63. 17

Plenz, G., Dorszewski, A., Breithardt, G., and Robenek, H. (1999). Expression of Type VIII collagen after cholesterol diet and injury in the rabbit model of atherosclerosis. *Arteriosclerosis, Thrombosis, and Vascular Biology*, 19(5):1201–1209. 11

Purslow, P. P. (1983). Measurement of the fracture toughness of extensible connective tissues. *Journal of Materials Science*, 18:3591–3598. 22, 155

Purslow, P. P. (1989). Fracture of non-linear biological materials: some observations from practice relevant to recent theory. *Journal of Physics D: Applied Physics*, 854. 167

Püspöki, Z., Storath, M., Sage, D., and Unser, M. (2016). Transforms and operators for directional bioimage analysis: A survey. *Advances in Anatomy Embryology and Cell Biology*, 219:69–93. 53

Redgrave, J., Lovett, J., Rothwell, P., and Gallagher, P. (2006). Response to letter regarding article, "Histological assessment of 526 symptomatic carotid

plaques in relation to the nature and timing of ischemic symptoms: the Oxford plaque study". *Circulation*, 114(21). 5, 128, 146, 149, 152, 244

Rezakhaniha, R., Agianniotis, A., Schrauwen, J. T. C., Griffa, A., Sage, D., Bouten, C. V. C., van de Vosse, F. N., Unser, M., and Stergiopulos, N. (2012). Experimental investigation of collagen waviness and orientation in the arterial adventitia using confocal laser scanning microscopy. *Biomechanics and Modeling in Mechanobiology*, 11(3-4):461–73. 12, 53, 88

Richardson, P. D. (2002). Biomechanics of plaque rupture: progress, problems, and new frontiers. *Annals of Biomedical Engineering*, 30(4):524–536. 2, 7, 18, 20

Richardson, P. D., Davies, M. J., and Born, G. V. R. (1989). Influence of plaque configuration and stress distribution on fissuring of coronary atherosclerotic plaques. *The Lancet*, 334(8669):941–944. 1, 5, 46, 48, 128, 146, 149, 152, 200, 244

Ritter, M. C., Jesudason, R., Majumdar, A., Stamenovic, D., Buczek-Thomas, J. A., Stone, P. J., Nugent, M. A., and Suki, B. (2009). A zipper network model of the failure mechanics of extracellular matrices. *Proceedings of the National Academy of Sciences*, 106(4):1081–6. 15

Rodriguez, J. F., Alastrue, V., and Doblare, M. (2008). Finite element implementation of a stochastic three dimensional finite-strain damage model for fibrous soft tissue. *Computer Methods in Applied Mechanics and Engineering*, 197(9-12):946–958. 17

Rodríguez, J. F., Cacho, F., Bea, J. A., and Doblaré, M. (2006). A stochastic-structurally based three dimensional finite-strain damage model for fibrous soft tissue. *Journal of the Mechanics and Physics of Solids*, 54(4):864–886. 17

Rodríguez, J. F., Ruiz, C., Doblaré, M., and Holzapfel, G. A. (2008). Mechanical stresses in abdominal aortic aneurysms: influence of diameter, asymmetry, and material anisotropy. *Journal of Biomechanical Engineering*, 130(2):021023. 91

Rothwell, P. M. and Goldstein, L. B. (2004). Carotid endarterectomy for asymptomatic carotid stenosis: asymptomatic carotid surgery trial. *Stroke*, 35(10):2425–7. 7

Sadat, U., Li, Z.-Y., Graves, M. J., Tang, T. Y., and Gillard, J. H. (2009). Noninvasive imaging of atheromatous carotid plaques. *Nature Clinical Practice Cardiovascular Medicine*, 6(3):200–9. 6, 7, 16

Sadat, U., Teng, Z., and Gillard, J. H. (2010). Biomechanical structural stresses of atherosclerotic plaques. *Expert Review of Cardiovascular Therapy*, 8(10):1469–81. 2, 13, 17, 91, 146

Sadat, U., Teng, Z., Young, V. E., Graves, M. J., Gaunt, M. E., and Gillard, J. H. (2011). High-resolution magnetic resonance imaging-based biomechanical stress analysis of carotid atheroma: A comparison of single transient ischaemic attack, recurrent transient ischaemic attacks, non-disabling stroke and asymptomatic patient groups. *European Journal of Vascular and Endovascular Surgery*, 41(1):83–90. 17

Sáez, P., Peña, E., and Martínez, M. A. (2014). A structural approach including the behavior of collagen cross-links to model patient-specific human carotid arteries. *Annals of Biomedical Engineering*, 42(6):1158–1169. 15

Schindelin, J., Arganda-Carreras, I., Frise, E., Kaynig, V., Longair, M., Pietzsch, T., Preibisch, S., Rueden, C., Saalfeld, S., Schmid, B., Tinevez, J.-Y., White, D. J., Hartenstein, V., Eliceiri, K., Tomancak, P., and Cardona, A. (2012). Fiji: an open-source platform for biological-image analysis. *Nature Methods*, 9(7):676–82. 211

Schrauwen, J. T. C., Vilanova, A., Rezakhaniha, R., Stergiopulos, N., van de Vosse, F. N., and Bovendeerd, P. H. M. (2012). A method for the quantification of the pressure dependent 3D collagen configuration in the arterial adventitia. *Journal of Structural Biology*, 180(2):335–342. 88

Schriefl, A. J. (2013). *Quantification of Collagen Fiber Morphologies in Human Arterial Walls*. Doctoral dissertation, Graz University of Technology. 53, 160, 172, 185, 191

Schriefl, A. J., Reinisch, A. J., Sankaran, S., Pierce, D. M., and Holzapfel, G. A. (2012a). Quantitative assessment of collagen fibre orientations from two-dimensional images of soft biological tissues. *Journal of the Royal Society Interface*, 9(76):3081–93. 12

Schriefl, A. J., Zeindlinger, G., Pierce, D. M., Regitnig, P., and Holzapfel, G. A. (2012b). Determination of the layer-specific distributed collagen fibre orientations in human thoracic and abdominal aortas and common iliac arteries. *Journal of the Royal Society Interface*, 9(71):1275–86. 12, 53, 160, 172, 185, 191

Sellaro, T. and Hildebrand, D. (2006). Effects of collagen fiber orientation on the response of biologically derived soft tissue biomaterials to cyclic loading. *Jounal of Biomedical Materials Research Part A*, pages 194–205. 20

Shekhonin, B. V., Domogatsky, S. P., Muzykantov, V. R., Idelson, G. L., and Rukosuev, V. S. (1985). Distribution of Type I, III, IV and V collagen in normal and atherosclerotic human arterial wall: immunomorphological characteristics. *Collagen and Related Research*, 5(4):355–368. 11, 12, 38, 70

Sluimer, J. C., Kolodgie, F. D., Bijnens, A. P. J. J., Maxfield, K., Pacheco, E., Kutys, B., Duimel, H., Frederik, P. M., van Hinsbergh, V. W. M., Virmani, R., and Daemen, M. J. A. P. (2009). Thin-walled microvessels in human coronary atherosclerotic plaques show incomplete endothelial junctions relevance of compromised structural integrity for intraplaque microvascular leakage. *Journal of the American College of Cardiology*, 53(17):1517–27. 6

Sommer, G., Gasser, T. C., Regitnig, P., Auer, M., and Holzapfel, G. A. (2008). Dissection properties of the human aortic media: an experimental study. *Journal of Biomechanical Engineering*, 130(2):021007. 21, 155

Sommer, G. and Regitnig, P. (2009). Biaxial mechanical properties of intact and layer-dissected human carotid arteries at physiological and supraphysiological loadings. *American Journal of Physiology Heart Circulation Physiology*, 298:898–912. 18, 19, 20

Speelman, L., Bosboom, E., Schurink, G., Hellenthal, F., Buth, J., Breeuwer, M., Jacobs, M., and van de Vosse, F. (2008). Patient-specific AAA wall stress analysis: 99-percentile versus peak stress. *European Journal of Vascular and Endovascular Surgery*, 36(6):668–676. 99

Stone, G. W., Maehara, A., Lansky, A. J., de Bruyne, B., Cristea, E., Mintz, G. S., Mehran, R., McPherson, J., Farhat, N., Marso, S. P., Parise, H., Templin, B., White, R., Zhang, Z., and Serruys, P. W. (2011). A prospective natural-history study of coronary atherosclerosis. *New England Journal of Medicine*, 364(3):226–235. 46, 48

Störk, S., van den Beld, A. W., von Schacky, C., Angermann, C. E., Lamberts, S. W., Grobbee, D. E., and Bots, M. L. (2004). Carotid artery plaque burden, stiffness, and mortality risk in elderly men a prospective, population-based cohort study. *Circulation*, 110(3):344–348. 50

Svensson, R. B., Mulder, H., Kovanen, V., and Magnusson, S. P. (2013). Fracture mechanics of collagen fibrils: influence of natural cross-links. *Biophysical Journal*, 104(11):2476–84. 21

Tang, D., Yang, C., Kobayashi, S., Zheng, J., Woodard, P. K., Teng, Z., Billiar, K., Bach, R., and Ku, D. N. (2009). 3D MRI-based anisotropic FSI models with cyclic bending for human coronary atherosclerotic plaque mechanical analysis. *Journal of Biomechanical Engineering*, 131(6):1–27. 14

Taviani, V., Sutcliffe, M. P. F., Wong, P., Li, Z.-Y., Young, V., Graves, M. J., and Gillard, J. H. (2008). In vivo non-invasive high resolution MR-based method for the determination of the elastic modulus of arterial vessels. In *30th Annual International IEEE EMBS Conference*, pages 5569–5572, Vancouver, Canada. IEEE. 17, 19

Taylor, C. A. and Humphrey, J. D. (2009). Open problems in computational vascular biomechanics: hemodynamics and arterial wall mechanics. *Computer Methods in Applied Mechanics and Engineering*, 198(45-46):3514–3523. 7, 13

Taylor, D. W. (1991). Beneficial effect of carotid endarterectomy in symptomatic patients with high-grade carotid stenosis. *New England Journal of Medicine*, 325(7):445–453. 7

Teng, Z. (2011). Lumen irregularity dominates the relationship between mechanical stress condition, fibrous-cap thickness, and lumen curvature in carotid atherosclerotic plaque. *Journal of Biomechanical Engineering*, 133(3):034501. 2, 7, 48, 91

Teng, Z., Feng, J., Zhang, Y., Sutcliffe, M. P., Huang, Y., Brown, A. J., Jing, Z., Lu, Q., and Gillard, J. H. (2015a). A uni-extension study on the ultimate material strength and extreme extensibility of atherosclerotic tissue in human carotid plaques. *Journal of Biomechanics*, 48(14):3859–3867. 20

Teng, Z., He, J., Degnan, A. J., Chen, S., Sadat, U., Bahaei, N. S., Rudd, J. H. F., and Gillard, J. H. (2012). Critical mechanical conditions around neovessels in carotid atherosclerotic plaque may promote intraplaque hemorrhage. *Atherosclerosis*, 223(2):321–6. 16, 91, 146

Teng, Z., Sadat, U., and H. Gillard, J. (2013a). Translational application of combining magnetic resonance imaging and biomechanical analysis in carotid plaque vulnerability assessment. *Recent Patents on Medical Imaging*, 3(1):3–13. 6, 7, 16

Teng, Z., Sadat, U., Wang, W., Bahaei, N. S., Chen, S., Young, V. E., Graves, M. J., and Gillard, J. H. (2013b). Intraplaque stretch in carotid atherosclerotic plaque - an effective biomechanical predictor for subsequent cerebrovascular ischemic events. *PLoS ONE*, 8(4):e61522. 14, 102

Teng, Z., Yuan, J., Feng, J., Zhang, Y., Brown, A. J., Wang, S., Lu, Q., and Gillard, J. H. (2015b). The influence of constitutive law choice used to characterise atherosclerotic tissue material properties on computing stress values in human carotid plaques. *Journal of Biomechanics*, 48(14):3912–3921. 14

Teng, Z., Zhang, Y., Huang, Y., Feng, J., Yuan, J., Lu, Q., Sutcliffe, M. P. F., Brown, A. J., Jing, Z., and Gillard, J. H. (2014). Material properties of com-

ponents in human carotid atherosclerotic plaques: A uniaxial extension study. *Acta Biomaterialia*, 10(12):5055–5063. 19, 97

Thim, T., Hagensen, M. K., Wallace-Bradley, D., Granada, J. F., Kaluza, G. L., Drouet, L., Paaske, W. P., Bøtker, H. E., and Falk, E. (2010). Unreliable assessment of necrotic core by virtual histology intravascular ultrasound in porcine coronary artery disease. *Circulation Cardiovascular Imaging*, 3(4):384–91. 8

Thunes, J. R., Pal, S., Fortunato, R. N., Phillippi, J. A., Gleason, T. G., Vorp, D. A., and Maiti, S. (2016). A structural finite element model for lamellar unit of aortic media indicates heterogeneous stress field after collagen recruitment. *Journal of Biomechanics*, 49(9). 15

Tong, J., Cohnert, T., Regitnig, P., and Holzapfel, G. A. (2011). Effects of age on the elastic properties of the intraluminal thrombus and the thrombus-covered wall in abdominal aortic aneurysms: biaxial extension behaviour and material modelling. *European Journal of Vascular and Endovascular Surgery*, 42(2):207–19. 21

Tranfield, E. M. and Walker, D. C. (2013). The ultrastructure of animal atherosclerosis: What has been done, and the electron microscopy advancements that could help scientists answer new biological questions. *Micron*, 46:1–11. 12, 26

Tsamis, A., Phillippi, J. A., Koch, R. G., Pasta, S., D'Amore, A., Watkins, S. C., Wagner, W. R., Gleason, T. G., and Vorp, D. A. (2013). Fiber micro-architecture in the longitudinal-radial and circumferential-radial planes of ascending thoracic aortic aneurysm media. *Journal of Biomechanics*, 46(16):2787–94. 13

Vader, D., Kabla, A., Weitz, D., and Mahadevan, L. (2009). Strain-induced alignment in collagen gels. *PloS ONE*, 4(6):e5902. 248

Versluis, A., Bank, A. J., and Douglas, W. H. (2006). Fatigue and plaque rupture in myocardial infarction. *Journal of Biomechanics*, 39(2):339–347. 1, 91, 146, 200

Walsh, M. T., Cunnane, E. M., Mulvihill, J. J., Akyildiz, A. C., Gijsen, F. J. H., and Holzapfel, G. A. (2014). Uniaxial tensile testing approaches for characterisation of atherosclerotic plaques. *Journal of Biomechanics*, 47(4):793–804. 18, 19, 20, 21, 128, 145, 155, 169, 184

Weisbecker, H., Pierce, D. M., Regitnig, P., and Holzapfel, G. A. (2012). Layer-specific damage experiments and modeling of human thoracic and abdominal aortas with non-atherosclerotic intimal thickening. *Journal of the Mechanical Behavior of Biomedical Materials*, 12:93–106. 20

Wenk, J. F., Papadopoulos, P., and Zohdi, T. I. (2010). Numerical modeling of stress in stenotic arteries with microcalcifications: a micromechanical approximation. *Journal of Biomechanical Engineering*, 132(9):091011. 91, 146

Wilson, J. S., Baek, S., and Humphrey, J. D. (2013). Parametric study of effects of collagen turnover on the natural history of abdominal aortic aneurysms. *Proceedings of the Royal Society A*, 469(2150):20120556. 11

Yang, C., Tang, D., Kobayashi, S., Zheng, J., Woodard, P. K., Teng, Z., Bach, R., and Ku, D. N. (2008). Cyclic bending contributes to high stress in a human coronary atherosclerotic plaque and rupture risk: in vitro experimental modeling and ex vivo MRI-based computational modeling approach. *Molecular & Cellular Biomechanics*, 5(4):259–274. 14

Yu, H., Clarke, M. C. H., Figg, N., Littlewood, T. D., and Bennett, M. R. (2011). Smooth muscle cell apoptosis promotes vessel remodeling and repair via activation of cell migration, proliferation, and collagen synthesis. *Arteriosclerosis, Thrombosis, and Vascular Biology*, 31(11):2402–9. 6, 8

Zoumi, A., Lu, X., Kassab, G. S., and Tromberg, B. J. (2004). Imaging coronary artery microstructure using second-harmonic and two-photon fluorescence microscopy. *Biophysical Journal*, 87(4):2778–2786. 13, 205, 206, 241

Zoumi, A., Yeh, A., and Tromberg, B. J. (2002). Imaging cells and extracellular matrix in vivo by using second-harmonic generation and two-photon excited fluorescence. *Proceedings of the National Academy of Sciences of the United States of America*, 99(17):11014–9. 13, 205